

Lawrence Berkeley National Laboratory

Recent Work

Title

LEED CRYSTALLOGRAPHY STUDIES OF THE STRUCTURE OF CLEAN AND ADSORBATE COVERED Ir, Pt AND Rh CRYSTAL SURFACES

Permalink

<https://escholarship.org/uc/item/3xd953tv>

Author

Koestner, R.J.

Publication Date

1982-08-01



Lawrence Berkeley Laboratory

UNIVERSITY OF CALIFORNIA

RECEIVED

Materials & Molecular Research Division

LAWRENCE
BERKELEY LABORATORY

JAN 11 1983

LIBRARY AND
DOCUMENTS SECTION

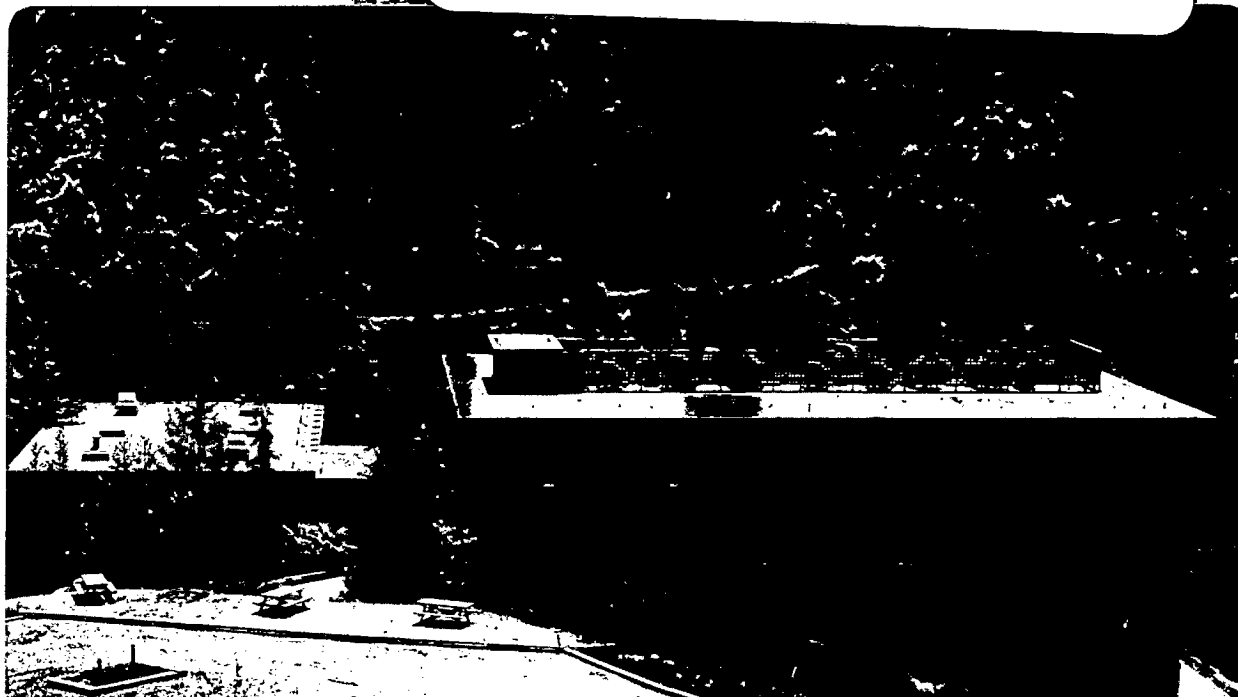
LEED CRYSTALLOGRAPHY STUDIES OF THE STRUCTURE OF CLEAN
AND ADSORBATE COVERED Ir, Pt AND Rh CRYSTAL SURFACES

Roland John Koestner
(Ph.D. thesis)

August 1982

TWO-WEEK LOAN COPY

*This is a Library Circulating Copy
which may be borrowed for two weeks.
For a personal retention copy, call
Tech. Info. Division, Ext. 6782.*



LBL-14766
e.2

DISCLAIMER

This document was prepared as an account of work sponsored by the United States Government. While this document is believed to contain correct information, neither the United States Government nor any agency thereof, nor the Regents of the University of California, nor any of their employees, makes any warranty, express or implied, or assumes any legal responsibility for the accuracy, completeness, or usefulness of any information, apparatus, product, or process disclosed, or represents that its use would not infringe privately owned rights. Reference herein to any specific commercial product, process, or service by its trade name, trademark, manufacturer, or otherwise, does not necessarily constitute or imply its endorsement, recommendation, or favoring by the United States Government or any agency thereof, or the Regents of the University of California. The views and opinions of authors expressed herein do not necessarily state or reflect those of the United States Government or any agency thereof or the Regents of the University of California.

LBL-14766

**LEED CRYSTALLOGRAPHY STUDIES OF THE STRUCTURE OF
CLEAN AND ADSORBATE COVERED Ir, Pt AND Rh CRYSTAL SURFACES**

Roland John Koestner

(Ph.D. Thesis)

Materials and Molecular Research Division
Lawrence Berkeley Laboratory
University of California
Berkeley, California 94720

August 1982

This work was supported by the Director, Office of Energy Research,
Office of Basic Energy Sciences, Materials Science Division of the
U.S. Department of Energy under Contract No. DE-AC03-76SF00098.

TABLE OF CONTENTS

	Page
ABSTRACT	ix
I. INTRODUCTION AND ACKNOWLEDGMENTS	1
References for Chapter I	6
II. LEED CRYSTALLOGRAPHY: OVERVIEW	8
A. HISTORY	8
B. INSTRUMENTATION	11
i) Faraday Cup	13
ii) Spot Photometer	14
iii) Photography	15
iv) TV Camera	15
v) CEMA/Phosphor and TV Camera	16
vi) CEMA/RANICON	17
C. ANALYSIS	18
i) LEED Theory	18
ii) Reliability Factors	27
References for Chapter II	30
III. EXPERIMENTAL DETAILS	34
A. APPARATUS	34
B. SAMPLE PREPARATION	36
i) Metal Samples (Ir, Pt, Rh)	36
ii) Gas Samples	37
C. LEED INTENSITY MEASUREMENT	38

Reference for Chapter III	41
Figure Captions for Chapter III	41
Figures	42
IV. Ir, Au, AND Pt(100) SURFACE RECONSTRUCTIONS	44
PART 1: EXPERIMENTAL OBSERVATIONS AND POSSIBLE STRUCTURE MODELS	44
A. INTRODUCTION	44
B. PREVIOUS OBSERVATIONS OF THE Ir, Pt AND Au(100) RECONSTRUCTIONS	46
i) LEED Observations	46
ii) Observations of Ir, Pt and Au(100) Reconstructions by Other Techniques	49
iii) The Depth of Reconstruction	50
iv) Unreconstructed Metastable Surface Structures of the (100) Faces of Ir, Pt and Au	51
v) Previous Structural Analyses	51
C. LEED INTENSITY MEASUREMENTS	52
D. INTERPRETATION OF THE DIFFRACTION PATTERNS	53
i) Ir(100)	53
ii) Au(100)	53
iii) Pt(100)	55
iv) Au(111)	56
E. SURFACE STRUCTURAL MODELS	58
i) The Hexagonal Model	58
ii) The Missing Row Hexagonal Model	63

iii) The Shifted Row Models	63
iv) The Charge-Density Wave (CDW) Model	66
F. LASER SIMULATION	67
i) Ir(100)	68
ii) Pt(100) and Au(100)	69
iii) Au(111)	70
iv) Conclusions	70
G. SUMMARY	71
ACKNOWLEDGMENTS	72
References for Chapter IV, Part 1	73
Figure Captions for Chapter IV, Part 1	77
Figures	80
PART 2: STRUCTURE DETERMINATION OF THE Ir AND Pt(100)	
FACES	93
A. INTRODUCTION	93
B. DYNAMICAL LEED THEORY	93
i) Methods Used	93
ii) Physical Parameters	94
iii) Geometrical Aspects	95
C. RESULTS	99
i) The Reconstructed Ir(100) Surface	102
ii) The Reconstructed Pt(100) Surface	104
D. DISCUSSION	105
i) Summary of Results	105
ii) Other Reconstructions	105
iii) Bond Lengths	106

iv)	Mechanisms of Reconstruction	109
v)	Layer Rotation	110
vi)	Correlations with Material Constants	111
vii)	Reconstructions and Adsorbates	112
viii)	Prospects For Finding Other Metal Surface Reconstructions	114
	References for Chapter IV, Part 2	117
	Figure Captions for Chapter IV, Part 2	129
	Figures	132
V.	CO AND CO ₂ ADSORPTION ON RH(111)	138
	PART 1: RH(111)-($\sqrt{3}\times\sqrt{3}$)R30°-CO, CO ₂ STRUCTURE DETERMINATION	138
	A. INTRODUCTION	138
	B. EXPERIMENTAL	140
	C. LEED THEORY	145
	D. RESULTS AND DISCUSSION	147
	E. SUMMARY	152
	References for Chapter V, Part 1	154
	Figure Captions for Chapter V, Part 1	158
	Figures	159
	PART 2: Rh(111)-(2×2)-3CO STRUCTURE DETERMINATION	169
	A. INTRODUCTION	169
	B. EXPERIMENTAL	171
	C. RESULTS AND DISCUSSION	173
	i) Structural Models	173
	ii) LEED Theory	174

iii)	Structure Determination with Dynamical LEED	175
iv)	Comparison between Kinematic and Multiple Scattering Calculations	178
D.	SUMMARY	180
	References for Chapter V, Part 2	182
	Figure Captions for Chapter V, Part 2	183
	Figures	184
VI.	THE ADSORPTION OF C_3H_4 , C_3H_6 , AND CIS- OR TRANS-2- C_4H_8	188
A.	INTRODUCTION	188
B.	EXPERIMENTAL	191
C.	RESULTS	192
i)	LEED Patterns	192
ii)	Comparison of I-V Curves	194
D.	DISCUSSION	196
i)	Metastable Methylacetylene ($H_3C-C\equiv CH$)	197
ii)	Stable Propylene ($CH_3-CH=CH$)	198
iii)	Stable Methylacetylene ($CH_3-C\equiv CH$)	199
iv)	Low (~10 L) and High (~1000 L) Exposure 2-Butenes ($CH_3-CH=CH-CH_3$)	199
v)	Intermediate Exposure (~100 L) 2-Butenes	202
E.	SUMMARY	202
	References for Chapter VI	204
	Figure Captions for Chapter VI	207
	Figures	209

VII. ETHYLENE ADSORPTION ON THE Rh(111) SURFACE	222
A. INTRODUCTION	222
B. EXPERIMENTAL	224
C. LEED THEORY	227
D. RESULTS	228
E. DISCUSSION	230
F. SUMMARY	235
References for Chapter VII	236
Figure Captions for Chapter VII	246
Figures	247
VIII. C ₂ H ₂ , C ₃ H ₄ , and C ₃ H ₆ ADSORPTION ON THE Rh(111) SURFACE	254
A. INTRODUCTION	254
B. EXPERIMENTAL	256
i) Apparatus and Intensity Measurement	256
ii) Preparation of the c(4×2) Overlayer	257
iii) Preparation of the (2×2) Layer of Adsorbed Propylene	258
iv) Preparation of the (2×2) Layer of Adsorbed Methylacetylene	258
v) Coadsorption of Background H ₂ and CO	259
C. RESULTS	261
i) c(4×2) Layer	261
a) Domain Preference	261
b) Comparison of Intensity Curves	263

ii)	$2\sqrt{3}\times 2\sqrt{3}$)R30° Propylene Layer	263
a)	Comparison of Half-Order Intensity Curves for Ethylene and Propylene Structures	263
b)	$(2\sqrt{3}\times 2\sqrt{3})$ R30° Structure Determination by LEED	264
iii)	$(2\sqrt{3}\times 2\sqrt{3})$ R30° Methylacetylene Layer	266
D.	DISCUSSION	266
i)	c(4×2) Layer	267
a)	Comparison of Intensity Curves	267
b)	LEED Analysis	268
ii)	$(2\sqrt{3}\times 2\sqrt{3})$ R30° Propylene Layer	271
a)	Comparison in Intensity Curves	271
b)	$(2\sqrt{3}\times 2\sqrt{3})$ R30° Propylene Structure Determination	272
c)	The Disorder-Order Transition	273
iii)	$(2\sqrt{3}\times 2\sqrt{3})$ R30° Methylacetylene Layer	276
E.	SUMMARY	278
	References for Chapter VIII	281
	Figure Captions for Chapter VIII	282
	Figures	285
IX.	ETHYLENE ADSORPTION ON Rh(100)	302
A.	INTRODUCTION	302
B.	ORGANOMETALLIC ANALOGUES	303
C.	RESULTS AND DISCUSSION	306
i)	Ethylene Adsorption on Rh(100) at 220 K	306
ii)	Ethylene Dehydrogenation on Rh(100) at 700 K	310

References for Chapter IX	312
Figure Captions for Chapter IX	314
Figures	315
X. BENZENE AND NAPHTHALENE ADSORPTION ON THE Rh(111) SURFACE	316
A. INTRODUCTION	316
B. EXPERIMENTAL	318
C. RESULTS AND DISCUSSION	320
i) Preparation of the Benzene Adlayers	320
ii) Preparation of the Naphthalene Overlayers	322
iii) Interpretation of LEED Patterns	323
a) Benzene	323
b) Naphthalene	326
iv) Thermal Desorption Spectra	329
a) Benzene	329
b) Naphthalene	332
D. SUMMARY	333
References for Chapter X	335
Figure Captions for Chapter X	338
Figures	339
APPENDIX I. EXPERIMENTAL INTENSITY CURVES	346
Figures	347
APPENDIX II. LIST OF PUBLICATIONS	399

LEED CRYSTALLOGRAPHY STUDIES OF THE STRUCTURE
OF CLEAN AND ADSORBATE COVERED Ir, Pt AND Rh CRYSTAL SURFACES

Roland John Koestner

(Ph.D. Thesis)

Materials and Molecular Research Division
Lawrence Berkeley Laboratory
University of California
Berkeley, California 94720

ABSTRACT

There have only been a few Low Energy Electron Diffraction (LEED) intensity analyses carried out to determine the structure of molecules adsorbed on metal surfaces; most surface crystallography studies concentrated on the structure of clean unreconstructed or atomic adsorbate-covered transition metal faces. The few molecular adsorption systems already investigated by dynamical LEED are CO on Ni(100), Cu(100) and Pd(100) as well as C₂H₂ and C₂H₄ adsorbed on Pt(111).

The emphasis of my thesis research has been to extend the applicability of LEED crystallography to the more complicated unit cells found in molecular overlayers on transition metals or in the reconstructed surfaces of clean transition metals. The reconstruction of the Ir(100) surface was the first structure considered. The top layer of this surface rearranges into a hexagonal mesh with six-atoms in the overlayer unit cell. In contrast to semiconductor surfaces, the Ir reconstruction appears to be limited to only the top layer. Next, we examined the structure of the $(\sqrt{3}\times\sqrt{3})R30^\circ$ -CO and (2x2)-3CO overlayers

that form on the Rh(111) surface. We find that one CO stands above an atop site in the $(\sqrt{3}\times\sqrt{3})R30^\circ$ unit cell, while two CO molecules occupy near-atop sites and the other CO chooses a bridge site in the (2×2) cell.

The adsorbed phases of C_2H_2 , C_2H_4 , C_3H_4 , and C_3H_6 on Rh(111) as well as cis- and trans-2- C_4H_8 on Pt(111) produced a family of very similar structures. All the alkenes (C_nH_{2n}) yielded alkylidyne layers ($\equiv C(CH_2)_nCH_3$) on these surfaces near room temperature, while the alkynes (C_nH_{2n-2}) required the presence of coadsorbed hydrogen before the alkylidyne layer formed. Propylidyne on Rh(111) and butylidyne on Pt(111) ordered into a (2×2) adsorption lattice and also gave a $(2\sqrt{3}\times 2\sqrt{3})R30^\circ$ superlattice of methyl and ethyl groups, respectively. The superlattice formation is probably driven by the Van der Waals forces acting between neighboring admolecules.

We are presently studying benzene and naphthalene adsorption on the Rh(111) surface as well as ethylene and acetylene adsorption on the Rh(100) face. The aromatics appear to π -bond to the metal with their carbon ring parallel to the surface. Dynamical LEED should be able to determine the overlayer geometry for these large hydrocarbons since only one molecule seems to be present in most of the surface unit cells. It will be interesting to see how important Van der Waals forces are in determining the overlayer geometry of these aromatics. Finally, our study of ethylene and acetylene adsorption on the Rh(100) face should allow us to examine the dependence of metal-adsorbate bonding on the metal substrate structure (i.e., (100) vs. (111) faces).

I. INTRODUCTION AND ACKNOWLEDGEMENTS

With the advent of modern surface science, a number of techniques have recently been developed and employed to study the structure and bonding at surfaces. In Table 1, we list the more commonly used methods¹⁻³ and stress the strengths and weaknesses of each technique since they are very complementary in nature. We have relied primarily on Low Energy Electron Diffraction (LEED) to determine the structure of clean and adsorbate covered transition metal surfaces. LEED has been fairly successful in determining the structure of clean unreconstructed and atomic adsorbate-covered surfaces in the past, but our main objective has been to extend its applicability to more complicated surface unit cells.

In the case of clean metal surfaces, we studied the (111) face of Rh and the (100) faces of Ir, Pt, and Au. Unlike most transition metals, Ir, Pt, and Au exhibit surface reconstructions; that is, the topmost layer of metal atoms occupy very different lattice positions than predicted from a mere termination of the bulk structure. Our LEED intensity analyses (Chapter IV) of the Ir and Pt(100) surfaces support the popular model that the first metal layer rearranges into a buckled hexagonal lattice, while the lower layers maintain the square lattice expected from the (100) planes of face centered cubic crystals. Recently a larger set of intensity curves were obtained for the reconstructed Ir(100) surface where the buckled hexagonal structure is strongly favored with a Zanazzi-Jona R-factor of 0.34 and a Pendry R-factor of 0.45.⁴ This reconstruction may well be driven by the

higher in-plane coordination number of the hexagonal layer that outweighs the mismatch energy between the hexagonal and square lattices.

There have been only a few LEED crystallography studies carried out to determine the structure of molecules adsorbed on metal surfaces. The few adsorption systems already investigated by dynamical LEED are CO on Ni,⁵ Cu,⁵ and Pd(100)⁶ as well as C₂H₂ and C₂H₄ on Pt(111).⁷ We began our study of molecular adsorption by considering the bonding of CO and CO₂ to the Rh(111) surface [Chapter V]. Both molecules order into a progression of overlayer lattices with increasing coverage. We examined the $(\sqrt{3}\times\sqrt{3})R30^\circ$ and (2×2) structures (with a coverage $\theta = 1/3$ and $3/4$, respectively) that form with either CO or CO₂. The adsorption site of CO in the $(\sqrt{3}\times\sqrt{3})R30^\circ$ layer is largely determined by the metal-adsorbate interaction; however, adsorbate-adsorbate interactions become significant in the highly compressed (2×2) lattice. So a compromise must be reached between the adsorption above a high symmetry metal site and the formation of an hexagonal overlayer of CO. These high coverage phases are particularly important to study since they more closely approximate the crowded adsorbate layers encountered in the metal surface reactions that are used in industry. The structure determination of the $(\sqrt{3}\times\sqrt{3})R30^\circ$ -CO overlayer gave a Zanazzi-Jona R-factor of 0.40 and a Pendry R-factor of 0.50, while the (2×2) -3CO overlayer had a Zanazzi-Jona R-factor of 0.25 and a Pendry R-factor of 0.47.

The focus of our molecular adsorption studies however has been the bonding of straight-chain and aromatic hydrocarbons to the low-miller index faces of Rh and Pt. The C₂, C₃ and C₄ unsaturated hydrocarbons produce alkylidyne ($\equiv C(CH_2)_n CH_3$) species on Pt(111)

[Chapter VI] and Rh(111) [Chapters VII, VIII] near room temperature. (Our LEED determination of the Rh(111)-(2x2)-C₂H₃ layer gave a Zanazzi-Jona R-factor of 0.49 and a Pendry R-factor of 0.52.) Below 200K these alkenes (C_nH_{2n}) and alkynes (C_nH_{2n-2}) probably di-σ bond to the metal via the unsaturated carbon atoms; upon warming, an interesting hydrogen shift reaction occurs which produces the alkylidyne group. This group must be fairly stable because we believe it also forms on the (100) faces of Rh [Chapter IX] and Pt.⁸ An analogous species, (CCH₃)Co₃(CO)₉, is found in Organometallic Chemistry and is very resistant to thermal decomposition and oxidation; yet the best evidence for the thermodynamic stability of these alkylidyne clusters is the large number of very different synthetic pathways that are available for their preparation.⁹

The most interesting feature of these hydrocarbon studies is that propylidyne ($\equiv\text{C}(\text{CH}_2)\text{CH}_3$) on Rh(111) [Chapter VIII] as well as butylidyne ($\equiv\text{C}(\text{CH}_2)_2\text{CH}_3$) on Pt(111) [Chapter VI] each exhibit two distinct lattice periodicities. The α and β carbon atoms fit into a (2x2) unit cell above the metal, while the γ (and also δ in the case of butylidyne) carbon atoms produce a larger (2√3x2√3)R30° periodicity. The most convincing evidence for this geometry comes from our LEED intensity analysis of the (2√3x2√3)R30-3C₃H₅ layer that considers only kinematic scattering in the overlayer; and we are presently doing a full dynamical calculation to confirm this structure. This is the first example to our knowledge where a single ad molecule has two

separate periodicities. The formation of this $(2\sqrt{3}\times 2\sqrt{3})R30^\circ$ superlattice is probably driven by Van der Waals forces acting between the alkylidyne chains.

Although the adsorption of aromatic hydrocarbons on transition metal surfaces has been fairly well-studied to date, little surface structural information is really available for this important class of molecules. We have begun a systematic study of benzene (C_6H_6) and naphthalene ($C_{10}H_8$) adsorption on the Rh(111) surface [Chapter X]. Both molecules produce two different ordered structures as a function of temperature. At present, we believe benzene occupies two different C_{3v} metal sites (atop, hcp hollow, or fcc hollow) in the two observed unit cells; naphthalene seems to parallel benzene adsorption. These structural models will be tested by dynamical LEED intensity calculations presently underway. Once again adsorbate-adsorbate interactions may play a considerable role in determining the surface structure, since the naphthalene and benzene cells are very crowded in most of these overlayers.

This section would not be complete without a proper explanation of my use of the first person plural throughout the manuscript. This thesis would not be possible without the help of Gabor Somorjai and Michel Van Hove. Gabor's enthusiasm to do research, his clear and quick way of thinking, and his concern for my scientific career have made a deep impression on me that I will always be grateful for. Michel did all the LEED calculations necessary in the intensity analyses and has been a constant source of encouragement, guidance, and advice to me. He has also written sections of this manuscript which

have already been published (most notably, all of Chapter IV). All the Pt(111) work that I present has been done in collaboration with Jonathan Frost and Peter Stair; Jonathan Frost was also largely responsible for the set of computer programs used to generate the experimental intensity spectra. Rong-Fu Lin should be credited for most of the aromatic adsorption experiments that I will discuss; and Frank Ogletree has been of considerable help in the methylacetylene on Rh(111) experiments. Finally, Greg Lewis as an undergraduate in the Chemistry Department helped me analyze most the Rh(111) intensity data.

References for Chapter I

1. a) M. A. Van Hove and S. Y. Tong, Surface Crystallography by LEED (Springer-Verlag, NY, 1979).
b) J. B. Pendry, Low Energy Electron Diffraction (Academic Press, NY, 1974).
2. H. Ibach, ed., Electron Spectroscopy for Surface Analysis (Springer-Verlag, NY, 1977).
3. G. Margaritondo and J. E. Rowe, J. Vac. Sci. Tech. 17 561 (1981).
4. E. Lang, K. Muller, K. Heinz, M. A. Van Hove, R. J. Koestner, and G. A. Somorjai, submitted to Surface Science.
5. a) S. Anderson and J. B. Pendry, Phys. Rev. Lett. 43 363 (1979).
b) M. Passler, A. Ignatiev, F. Jona, D. W. Jepsen, and P. M. Marcus, Phys. Rev. Lett. 43 360 (1979).
c) S. Y. Tang, A. Maldonado, C. H. Li and M. A. Van Hove, Surf. Sci. 94 73 (1981).
6. R. J. Behm, K. Christmann, G. Ertl, M. A. Van Hove, P. A. Thiel, and W. H. Weinberg, Surf. Sci. 88 L59 (1979).
7. L. L. Kesmodel, L. H. Dubois and G. A. Somorjai, J. Chem. Phys. 70 2180 (1979).
8. A. M. Baro and H. Ibach, "Proc. Conf. on Vibrations in Adsorbed Layers," Julich, Germany (1978).
9. D. Seyferth, Adv. Organomet. Chem. 14 97 (1976).

Table 1. Commonly used structural methods in surface science.

Acronym	LEED ¹	HREELS ²	SEXAFS ³	NPD ³	UPS ³
<u>Full Name:</u>	Low energy electron diffraction	High resolution electron energy loss spectroscopy	Surface extended X-ray absorption fine-structure spectroscopy	Normal photoelectron diffraction	(Angle - integrated) Ultraviolet photoemission spectroscopy
<u>Sensitive to:</u>	Atomic positions	Molecular configuration	Atomic positions	Atomic positions	Electronic structure
<u>Underlying Principle:</u>	Electron diffracts from atomic cores	Electron energy gain or loss by interaction with the dynamic dipole moment or short-range forces of surface vibrations	Emitted electron backscattered from nearby atomic cores	Photoelectron diffracts from nearby atomic cores	Photoelectron emission from molecular orbitals
<u>Advantages:</u>	Measures bond distances ($\pm 0.05-0.1\text{\AA}$) and bond angles ($\pm 10-15^\circ$)	Identifies molecular species present on surface and its adsorption site; detects hydrogen	Measures bond distances ($\pm 0.03\text{\AA}$)	Measures bond distances ($\pm 0.05-0.1\text{\AA}$) and bond angles ($\pm 10-15^\circ$), also probes bond symmetry	Measures binding energy of molecular orbitals
<u>Disadvantages:</u>	Requires long range order; complicated multiple scattering occurs	Not quantitative; difficult to assign vibrational modes	Synchrotron radiation required	Synchrotron radiation required	d-band emission and relaxation effects complicate interpretation of spectra

II. LEED CRYSTALLOGRAPHY: OVERVIEW

A. HISTORY

The potential of Low Energy Electron Diffraction (LEED) as a surface structural probe was recognized more than a half-century ago. As early as 1921, Davisson and Kunsman¹ noticed anisotropies in the angular distribution of backscattered electrons from a polycrystalline Ni target, while the more decisive experiment that supported de Broglie's² wave theory of matter came accidentally in 1927³ when a polycrystalline Ni sample was inadvertently recrystallized via high temperature oxygen and hydrogen treatments by Davisson and Germer. The resulting single crystal Ni surface produced a dramatic variation in the backscattered electron angular distribution that could only be explained by diffraction from the Ni surface. They then went on to discuss the ordered adsorbate structures that could be detected by LEED.

In 1936, Farnsworth⁴ clearly determined that most of the diffracted electrons originate from the first few atomic layers of the crystal since only three or four layers of gas were sufficient to completely mask the pattern of the underlying crystal. The large inelastic scattering cross-sections [$\sim 10\text{\AA}^2$] that Farnsworth observed had established LEED as a surface sensitive technique; on the other hand, Davisson and Germer³ had anticipated the need for a complicated multiple scattering to model the diffraction of electron through a metal lattice due to the large elastic scattering cross-section. So both the strengths and weaknesses of LEED as a structural tool were recognized from the very start.

Unfortunately, even with this encouraging beginning, the method was largely ignored until the early 1960's when two groups working at Bell Laboratories^{5,6} built an easy-to-use LEED spectrometer. This machine energy-analyzed the backscattered electrons with a retarding field grid and accelerated them onto a display-type fluorescent screen. This mode of diffraction beam detection suggested by Ehrenberg in 1934⁷ made it easy to determine the size and symmetry of the surface unit cell and avoided the need for the time-consuming Faraday cup measurements employed by earlier workers.

The limited interest in LEED prior to 1960 may also have been caused by the relatively poor vacuum technology available then. All glass vacuum chambers that were sealed with rubber gaskets and evacuated with sorption and getter pumps could only achieve 10^{-8} torr at best; such ambient pressures would contaminate the surfaces under investigation fairly rapidly. However, the space science program in the early 1960's introduced Ultra High Vacuum components that now routinely insure base pressures of 10^{-10} - 10^{-9} torr.

With the necessary experimental sophistication at hand, a dynamical or multiple scattering theory had to be developed to model the diffraction process before LEED could be used to measure the equilibrium positions of atoms in the surface unit cell. During 1969-71 the quantitative determinations of clean metal surface structures (where only the interlayer spacing was different from the bulk value) began to appear.⁸ It was found that surface atoms with fewer nearest neighbors would show a larger interlayer spacing contraction in accordance

with long established principles⁹ and in accordance with electron diffraction studies of 12-92 Å radius metal clusters.¹⁰ Most contractions were about 4% of the bulk value, but there are some notable exceptions such as Al(110) (5-15%) and Mo(100) (11-12%).

In 1972, Pendry and Andersson¹¹ reported the structure of sodium chemisorbed on the Ni(100) surface; this was the first atomic adsorbate studied with dynamical LEED. In 1976, L. L. Kesmodel et al.,¹² presented a LEED determination of a molecular adsorbate, namely acetylene chemisorbed on Pt(111). Up to now, more than a hundred structure determinations of clean and adsorbate covered surfaces have been published with peak activity periods occurring in 1973 and more so in 1977.

Presently, substantial progress is still being made in both LEED theory and experiment. More efficient approximation schemes are used to model the multiple scattering in the substrate and adlayer so that larger and more complicated surface unit cells can be considered. In this way, LEED can be applied to stepped metal surfaces, to the chemisorption of large molecules, and to crowded (6 atoms or more) or large (>25 Å²) overlayer unit cells. On the experimental front, a new generation of LEED spectrometers are available that improve the precision, resolution, and speed of LEED intensity measurements. In the remainder of this chapter we will consider the instrumentation presently used to measure LEED intensities and outline the basic ingredients in the theory of LEED.

B. INSTRUMENTATION

In the LEED experiments, a well characterized single crystal with or without an adsorbed overlayer is illuminated with an electron beam, typically having a 1 μ amp current and a 1 \AA wavelength. The steady state back-diffracted electron current is energy-analyzed to remove the inelastically scattered electrons and then measured; the normalized current in each diffraction beam is then plotted versus the incident electron energy. These intensity-voltage (I-V) curves are compared to theoretical curves that assume a particular model geometry for the surface unit cell; that model geometry which gives best agreement between theory and experiment is considered to be the correct one.

The level of agreement between theory and experiment is already approaching the agreement among experimental curves obtained from different laboratories for the same surface. This has been observed¹³ quite convincingly for the W(100)-(1 \times 1) system. Normal incidence curves were measured by six different groups over the past decade; the reliability factors for the best and worst agreement between theory and the separate experiments are 0.07 and 0.27, respectively. (The Zanazzi-Jona reliability factor¹⁴ used is a measure of the agreement between theory and experiment just as in the X-ray crystallography analogue.) The difference between the 0.07 and 0.27 values is considerable and indicates the need, at least for this case of more accurate intensity measurements.

There are a number of experimental difficulties that could affect the accuracy of the LEED intensity measurement. Here we consider three

major problems that are encountered before discussing the recent developments made in LEED spectrometers.¹³ The incident electron current in most measurements is about 1 μ amp with a beam diameter of roughly 1 mm; this high electron current can lead to decomposition or desorption of the adsorbate due to local heating and to space charging of poorly conducting surfaces. The LEED structural analysis of the Ni(100)-c(2x2)-CO overlayer by Andersson and Pendry¹⁵ as well as by other authors^{15b-f} serves as a good example of this problem. It demonstrates the sensitivity of the molecular overlayer to electron beam damage.

Long data collection times could lead to residual gas coadsorption and also does not permit the observation of time dependent processes on surfaces. For example, the clean Ni(100) surface I-V profiles were collected within 20 sec in one experiment¹⁶ and within one hour in another;¹⁷ the resulting curves were shown to be significantly different.

The present electron guns provide beams which have a transfer width (or less precisely, a coherence length) of only 50-150 \AA .¹⁸ This severely limits the ability of LEED to examine the domain and defect structure of surfaces. Thus an ordering on the scale of ~ 100 \AA or longer would be difficult to detect with the present generation of LEED spectrometers. Conversely, only very extensive disorder on the surface, causing a domain size of ~ 100 \AA or smaller, can be detected by LEED at present. If a lower current gun could be used in the LEED experiment, the electron beam would be better collimated and could produce a significantly larger transfer width. A number of different

LEED spectrometers were built to avoid some of the above mentioned difficulties. We will now describe these machines and consider their relative merits; a chronological order will be followed. A summary of the important characteristics of these different spectrometers appears in Table 1.

i) Faraday Cup^{1,3,4,13}

This is the oldest device used and is the only one that gives an absolute intensity. It involves a carefully shielded, movable cup with a small aperture for detecting the back-diffracted electrons. The cup is shielded to repel inelastically scattered electrons and to avoid secondary emission. The sensitivity of the method is limited only by the leakage current of the cup which is roughly 10^{-14} A; this should, in principle, allow incident beam currents as low as 10^{-8} A to be used.

The major advantages of this method is that absolute intensities are measured. Since relatively low incident currents may be used, the probability of electron beam induced decomposition/desorption is reduced; a better collimation of the beam is also possible which could increase the transfer width. The dynamic range of the Faraday cup is about 10^3 which permits fairly weak intensities to be measured.

The important disadvantages are long and tedious measuring times, and the inability to quickly view the size, shape and symmetry of the diffraction pattern due to the surface unit cell under study. Typically, a single intensity-energy point requires 10 sec to record; this means that one diffraction beam intensity vs energy (I/V) curve ranging from 20-120 eV (in 1 eV intervals) would take ~15 min to measure. Even

with the fastest Faraday cups designed to date, it would take more than an hour to record the 20 intensity spectra (at a given incidence angle) that are needed in the fit with theoretical curves.

ii) Spot Photometer

Here spherical retarding-field grid optics and postacceleration onto a luminescent spherical screen are used. The design is very similar to the spectrometer built by Lander et al.⁶ The phosphorescent intensity displayed on the screen is strictly proportional to the impinging electron current; the light intensity of each Bragg beam is measured with the telephotometer. The incident beam current is 10^{-6} - 10^{-7} A so that the backscattered current can adequately excite the phosphor. Each light spot must be tracked individually as the incident electron energy is varied; this leads to fairly long measurement times. Typically, each intensity-energy point requires a 10 sec measurement time; thus about 15 min is again required for a single spectrum of 100 intensity points and about 5 hours for 20 spectra.

The method has a large dynamic range ($>10^3$) and allows easy identification of the shape, size, and symmetry of the unit cell. Since the telephotometer measures the integrated intensity in an area on the screen significantly larger than the LEED beam cross section, this is the only method described that does not adequately remove the background intensity present on the LEED screen. This was shown to be a serious problem for the $c(2 \times 2)-0$ and $p(2 \times 2)-0$ structures on Ni(100).¹⁶

iii) Photography^{20,21}

This method was first used in 1975^{20a} and also relies on the postaccelerated display screen. Here all the intensity information on the LEED screen is recorded at once by photographing the entire screen image; the photograph is then digitized with a microdensitometer²⁰ or a vidicon system.²¹ The film has a linear response over 3 orders of magnitude yielding a sufficiently large dynamic range. Typically, all the intensity spectra (~20 beams) each containing 100 energy points can be recorded in a few minutes. The off-line scanning of 100 frames of film can be performed in less than 10 min with the microdensitometer.^{20b} The resulting density grids are then analyzed by a set of computer programs that yield the desired I-V profiles. In the best of cases, only a few hours in real time are needed to run these programs. Similarly, with the vidicon system, a TV camera digitizes the photographic image and evaluates a single I-V profile containing 100 intensity points in about 50 min.

iv) TV Camera^{22,23}

This method was developed in Erlangen^{22a,b} in the past five years and is now commercially available.²³ A CdSe vidicon camera views and digitizes the image of the phosphor display screen; with the advent of very fast Analog to Digital Converters (ADC's), the video signal of the entire LEED screen can be acquired at the TV rate of 1/50-1/60 sec. The vidicon camera rasters the screen image while a 13.5 MHz ADC with 8 bit resolution digitizes the image in only 18 msec. The data can then be dumped onto magnetic tape for off-line

evaluation or it may be submitted to a suitable interface in the preliminary data reduction for on-line evaluation.

In the off-line mode, the intensity data for 100 energy points and ~20 diffraction beams is collected in 2 sec which is $\sim 10^2$ times faster than the photographic method. The resulting intensity information can be analyzed with a similar set of computer programs that were used to evaluate the microdensitometer output. In the on-line mode, a special interface accepts only one LEED beam and discards the remaining intensity information contained in the screen image. The LEED beam intensity evaluation (~ 2 msec) along with the LEED screen digitization (18 msec) can be performed at the TV data acquisition rate (~ 20 msec, or 1/50-1/60 sec). A single I-V curve of 100 intensity-energy points can then be measured on-line in 2 sec; while all the diffraction intensity information on the LEED screen (~ 20 I-V curves) takes about 40 sec. The dynamic range of this method is also sufficiently large ($\sim 10^3$).

v) CEMA/Phosphor and TV Camera^{24,25}

In this method the back diffracted electrons are again energy-analyzed with spherical, retarding field grid optics, but the back-diffracted current is then amplified (10^2 - 10^3) by a flat channel electron multiplier array (CEMA). A flat grid at ground potential is placed just in front of the high voltage CEMA to insure that the back-scattered electrons maintain a radial trajectory. Yet since the LEED pattern is projected onto a flat detector the LEED beam spots on the detector will appear oval shaped and the LEED pattern will be slightly

distorted. These simple geometric distortions can be easily corrected during the data analysis.

After leaving the CEMA, the LEED beams are again accelerated onto a phosphor screen. A vidicon camera²⁵ coupled to an optical multi-channel analyzer, OMA, digitizes the resulting image displayed on the fluorescent screen. Each frame containing all the intensity information on the screen is measured and stored within 4 sec; the time needed to collect I-V profiles with 100 intensity points is about 8 min, comparable to the photographic technique. The I-V profiles are then evaluated off-line as in the photographic technique. The major advantage of this spectrometer is the very low incident current ($\sim 10^{-9}$ A) used; all the earlier phosphor screen detectors required a 1 μ amp incident current to adequately excite the phosphor. The dynamic range is again about 10^3 .

vi) CEMA/RANICON²⁶

Here the spherical, retarding field grid optics are coupled to a two-stage CEMA and a resistive anode image convertor (RANICON). The back-to-back channel plates amplify the electron current by about 10^6 ; however, the electron pulse shape is severely distorted in the process. The electron current is then further accelerated onto the resistive anode that records both the position and the intensity of the electron pulse. Although the pulse is distorted, its centroid can still be accurately determined. The resistive anode acts as a current divider; by measuring the charge collected at the sides of the resistive anode, the position as well as the total charge of an arriving electron pulse is determined. Since the detection electronics can

measure each event within 5-10 μ sec, a 50 kHz count rate can be achieved without a severe pulse pileup. In this way, a full set of I-V profiles (~20 beams) containing 100 intensity points can be measured in less than 10 minutes.

The major advantage of this spectrometer is the extremely low incident current (10^{-12} A) that would allow a much better collimation of the electron beam. The dynamic range is probably slightly less than $\sim 10^3$, while the pin cushion distortion caused by the flat detector can be easily corrected in the beam intensity evaluation programs.

C. ANALYSIS

In this section, I will describe the method used to extract structural information from the experimental intensity data. In the first step, theoretical I-V curves are calculated that assume particular model geometries for the surface unit cell.²⁷ These theoretical curves are then compared to the experimental ones; the model geometry that gives best agreement between theory and experiment is considered to be the correct one. Since a large computational effort is needed to generate the theoretical spectra, only a few probable structures can be tested in this way. Reliability factors are used to gauge the degree of certainty in any given determination.

i) LEED Theory

The calculation of intensity spectra is complicated by the high elastic cross-section of a low energy electron propagating through a crystal lattice. To reduce the computational effort involved, a number

of approximation schemes have evolved over the last 10-15 years that consider only the more important multiple scattering events in the diffraction process. We have relied mostly on the straightforward kinematic approximation that includes only single-scattering and on a perturbative method called Renormalized Forward Scattering (RFS) that includes full multiple scattering in the forward direction and a perturbative scheme for the weaker backscattering.

Let's consider the kinematic diffraction of an incident plane wave, $\phi_k = Ae^{ik \cdot r}$, from a two dimensional array of point scatterers. The total wave function is given by

$$\psi(R) = \phi_k(R) + \frac{Ae^{ik' \cdot R}}{R} F(\Delta k) \quad (1)$$

$$F(\Delta k) = \sum_j^{N^2} f_j(\theta, \phi) e^{i(\Delta k \cdot r_j)} \quad (2)$$

The summation is taken over the N^2 scatterers with positions, r_j , in the 2-D array; and the scattered term in $\psi(R)$ has the expected form with F -squared equalling the cross section.

The Bragg condition results from interference among the scatterers that are present in the lattice with translation vectors a, b as shown below.

$$\begin{aligned}
 F &= f \sum_{j=0}^{N-1} e^{i(\Delta k \cdot a_j)} \sum_{j=0}^{N-1} e^{i(\Delta k \cdot b_j)} \quad (\text{assume } f = f_j) \\
 &= f \frac{1 - e^{i\Delta k \cdot aN}}{1 - e^{i\Delta k \cdot a}} \frac{1 - e^{i\Delta k \cdot bN}}{1 - e^{i\Delta k \cdot b}} \quad (3)
 \end{aligned}$$

$$I \propto F \cdot F^* = |f|^2 \frac{\sin^2(\Delta k \cdot a N/2)}{\sin^2(\Delta k \cdot a)} \frac{\sin^2(\Delta k \cdot b N/2)}{\sin^2(\Delta k \cdot b)} \quad (4)$$

The intensity, I , has maxima when $\Delta k \cdot a = 2\pi m$ and $\Delta k \cdot b = 2\pi n$ ($m, n =$ integer); the height of the maxima is proportional to N^2 and its width is proportional to $1/N$.

A strong energy dependence in the diffraction intensities arises when these layers are stacked to form a surface. If they are stacked in a periodic manner, the condition $\Delta k \cdot c = 2\pi r$ ($r =$ integer) appears, where c indicates the translation vector in the stacking direction; the peak width in the intensity vs. energy curves is proportional to $(1/N)$ where N represents the number of stacked layers. Typically, low energy electrons have a penetration depth of only ~ 5 atomic layers; so the resulting I - V curves should show fairly broad peaks (3-15 eV) that are centered at energies where Bragg diffraction perpendicular to the surface is satisfied. Even if the inelastic cross-section for low energy electrons were very low, the high elastic cross-section (metal reflectivities of 50% occur at energies of 10 eV or lower) would open up wider band gaps that cause peak widths in the I - V curves of ~ 5 eV.

Unfortunately this kinematic approximation does not model the electron diffraction in a metal lattice very well; yet it is useful in calculating the diffraction in atomic or molecular overlayers. The C, O, and H atoms that usually occupy the overlayer unit cells in our structural determinations are fairly weak scatterers and are placed fairly far apart from one another. The multiple scattering that occurs in the metal lattice requires a more complicated formalism. We start by considering the Schrodinger equation for an electron in the metal lattice:

$$\left(-\frac{\hbar^2}{2m} \nabla^2 + V(r)\right) \psi(r) = E\psi(r) \quad (5)$$

or

$$(\nabla^2 + k_0^2)\psi(r) = U(r)\psi(r) = f(r)$$

where

$$E = \frac{\hbar^2 k_0^2}{2m}, \quad U(r) = \frac{2m}{\hbar^2} V(r)$$

The homogeneous solution to Eq. (5) (i.e., when $f(r) = 0$) is the set of plane waves $\phi_{k_0} = 1/\sqrt{V} e^{ik_0 \cdot r}$; the inhomogeneous solution can be found by using the Green's function for a single electron, $G_{k_0}(r, r')$. The Green's function itself is the inhomogeneous solution to the source Eq. (6).

$$(\nabla^2 + k_0^2) G_{k_0}(r, r') = \delta(r-r') \quad , \quad (6)$$

where

$$G_{k_0}(r, r') = \frac{\phi_k(r) \phi_k^*(r')}{k_0^2 - k^2} \quad ,$$

So

$$\begin{aligned} \psi(r) &= \phi_{k_0} + \int G_{k_0}(r, r') f(r') d^3r' \\ &= \phi_{k_0} + \int G_{k_0}(r, r') U(r') \psi(r') d^3r' \\ &= \phi + GU\psi \end{aligned} \quad (7)$$

Unfortunately $\psi(r)$ appears on both sides of Eq. (7); so we need to solve for $\psi(r)$ self-consistently. This leads to an expansion of $\psi(r)$ in terms of $\phi_{k_0}(r)$.

$$\psi(r) = \phi + GU\phi + GUGU\phi + \dots \quad (8)$$

Each term in this expansion corresponds to a different number of scattering events that the low energy electron could experience in the metal lattice. If only the first term, ϕ_{k_0} , is considered in the sum, we exclude all scattering and effectively ignore the potential, $U(r)$. If the second term is included, we arrive at the Born approximation where only single scattering events are taken into account. Since we know a low energy electron feels a very strong scattering potential in a metal, the expansion in Eq. (8) should include a large number of terms.

The solution of $\psi(r)$ in Eq. (7) is usually put in a slightly different form for the LEED intensity calculations.

$$\psi = \phi + GU\psi = \phi + GT\phi \quad (9)$$

where

$$T = U + UGU + \dots$$

Combining Eqs. (6) and (9), a more detailed expression for $\psi(r)$ can be written

$$\psi(r) = \phi_{k_0}(r) + \int d^3k \frac{\phi_k(r)}{k_0^2 - k^2} \left(\int d^3r' \phi_k^*(r') T(r', r) \phi_{k_0}(r) \right) \quad (10)$$

when the periodic crystal potential is inserted into the T matrix, we obtain

$$\psi(r) = \phi_{k_0}(r) + f_{k_g}(\theta, \phi) \phi_{k_g} \delta(k_{i\parallel} - k_{g\parallel} + g) \quad (11)$$

The intensity of a particular diffraction beam is equal to the square amplitude, $|f_{k_g}|^2$.

Different approximation schemes are available to calculate the amplitude, f_{k_g} . I will only briefly describe the method used in our work, namely Renormalized Forward Scattering (RFS). This method was first used by Pendry in 1972.²⁷ In this scheme, the propagation of a low energy electron through a metal lattice is considered in two steps. First, the electron is scattered by a single layer of atoms; this scattering redistributes the initial plane wave, ϕ_{k_0} , among all the available diffraction beams, $\{\phi_{k_g}\}$. Second, these plane

waves should propagate to the next layer of metal atoms; the electrons will then experience a phase change, $e^{ik_g \cdot c}$, in the process.

The scattering of the low energy electrons within a metal layer is best described using a partial wave expansion in an angular momentum representation, while the propagation from one metal layer to the next is carried out in a linear momentum representation. This picture of the crystal being composed of many independently scattering layers is only useful when the layers are separated by a distance large enough to allow just a few evanescent plane waves to reach neighboring layers. At small interlayer spacings ($< 1 \text{ \AA}$), too many evanescent waves need to be considered and this approximation scheme is not very efficient. An evanescent wave has an imaginary momentum perpendicular to the surface; this happens with the ϕ_{kg} beams that have large g values since energy conservation must be satisfied.

The scattering amplitudes for a single layer, $f_g^\alpha(\theta, \phi)$, calculated from Eq. (10) have the following form:

$$\begin{aligned} \text{in forward scattering: } f_g^\alpha(\theta, \phi) &= (I + M_{go}^{++}) \\ \text{in reverse scattering: } f_g^\alpha(\theta, \phi) &= M_{go}^{-+} \end{aligned} \tag{12}$$

where

$$M_{gg'}^{\pm\pm} = \frac{\gamma_0}{k_{lg}} \sum_{LL'} Y_L(k_g^\pm) T_{LL'} Y_{L'}(k_{g'}^\pm)$$

Y_L is a spherical harmonic, (\pm) indicates forward (+) or reverse (-) directions, γ_0 is a constant, and $k_{g'}$, k_g are the incoming and outgoing plane wave momenta, respectively. The $T(k, k_0)$ matrix shown

in Eq. (10) is given in a linear momentum representation, while the T_{LL} matrix in Eq. (12) is given in an angular momentum representation.

As mentioned earlier, the multiple scattering that occurs in the forward direction is fully treated by RFS, while reverse scattering is described by a perturbation scheme. This approach works down to low energies (< 10 eV) where the cross-section for reverse scattering then becomes too large. Let's first follow the diffraction of an incident plane wave, ϕ_{k_0} , through the metal. We can represent the amplitudes for all the forward-scattered Bragg beams, $\{\phi_{k_g}\}$, by a column vector $A(g)$; so the incident beam can be described by setting $A^0(g=(0,0))$ equal to one and leaving all the other elements of the column vector, $A^0(g)$, equal to zero. After scattering by the first layer, a new column vector $A'(g)$ will give the redistribution of intensity (the intensity is just the square amplitude) among all the transmitted Bragg beams.

$$A'(g) = \sum_{g'} P_g^+ (I + M_{gg'}^{++}) P_{g'}^+ A^0(g') \quad (13)$$

where

$$P_g^+ = e^{ik_g^+ \cdot c/2}$$

The matrix, $I + M_{gg'}^{++}$, is calculated by Eq. (12) and the phase changes P_g^+ , $P_{g'}^+$, take into account the propagation from one layer to the next. Equation (13) can be iterated for subsequent layers until the term, $A^n \cdot A^n$, is arbitrarily small. Typically n is equal to five atomic layers due to the strong electron damping in the metal.

The reverse scattering is now treated perturbatively. The electron first backscatters from the n^{th} layer,

$$B^n(g) = \sum_{g'} P_{g'g}^- M_{gg'}^{-+}, P_g^+, A^{n-1}(g') \quad (14)$$

The column vector, $(B^n(g))$, gives the amplitudes for plane waves moving toward the surface and the matrix $M_{gg'}^{-+}$, indicates the probability for turning the electron around. Next we should consider the back-scattered wave at the $(n-1)$ layer; this will have two contributions. The first term in Eq. (15) represents

$$B^{n-1}(g) = \sum_{g'} [P_{g'g}^- M_{gg'}^{-+}, P_g^+, A^{n-2}(g') + P_{g'g}^- M_{gg'}^{--}, P_g^-, B^n(g')] \quad (15)$$

the reverse scattering of the plane waves $(A^{n-2}(g'))$ moving into the bulk and the second gives the forward scattering of the plane waves $(B^n(g'))$ already moving toward the surface. This process can be repeated until the amplitudes in the backscattered beams above the first layer, $(B^1(g))$, is calculated.

In this way, all single back-scattering events are included in the intensity calculation; to consider higher-order back-scattering, the outgoing plane waves with amplitudes, $(B^2(g))$, can be reflected from the first layer and can make a second pass through the metal. Generally, only two or three passes are required to reach convergence in the outgoing plane wave intensities. These intensities are then plotted as a function of energy for later comparison with the experimental spectra.

ii) Reliability Factors^{14,28}

X-ray crystallographers use reliability factors (R-factors) to measure the fit between calculated and experimental curves and it should really come as no surprise that LEED crystallographers try to do the same. R-factors in the LEED analysis have three major advantages:

- 1) In most of our structural determinations, 50 experimental beam profiles were obtained and about 100-200 distinct model geometries were tested. This leads to almost 10^4 individual comparisons between theoretical and experimental I-V curves. Visual inspection of the curves would be a very lengthy and error-prone process; so the use of R-factors can easily be justified.
- 2) R-factors also are more easily standardized. The fit between theory and experiment can be measured on a common scale so that crystallographers can gauge the relative certainty of their proposed structures.
- (3) R-factor contour plots also can be used in structural searches. We can graph the R-factor value vs two structural parameters on a two-dimensional contour plot. The contours give the direction where a local minimum (lower R-factor means better fit) could be and in this way we can more efficiently determine the best values for the structural parameters in question. The contour plots also show the precision or resolution in the bond distances obtained in the analysis. A steep minimum in the R-factor contour

plot indicates a very precise measurement of the relevant bond distances, and a broad minimum would imply a poorer resolution.

R-factor contour plots are now used on practically a routine basis with most LEED crystallography studies, but it should be kept in mind that any given R-factor will be sensitive to different features of the correlation between the calculated and experimental intensity curves.²⁸ We have actually used five different R-factors in most of our structural determinations. In our study of the Rh(111)-($\sqrt{3}\times\sqrt{3}$)R30°-CO surface, the popular Zanazzi-Jona R-factor predicted bridge-bonded CO using only the normal-incidence data, yet the average of five R-factors chose the more likely adsorption site which is CO linearly bonded to the metal surface. This adsorption site was then clearly favored in the analysis of our off-normal incidence data.

The Zanazzi-Jona R-factor¹⁴ is shown as an example in Eq. (16).

$$R = \frac{1}{\int_{E_s}^{E_f} I_{obs} dE} \int_{E_s}^{E_f} w(E) |cI'_{calc} - I'_{obs}| dE \quad (16)$$

$$w(E) = \frac{cI''_{calc} - I''_{obs}}{I'_{obs} - (I'_{obs})_{max}} ; \quad c = \frac{\int_{E_s}^{E_f} I_{obs} dE}{\int_{E_s}^{E_f} I_{calc} dE} ,$$

The factor measures the difference in the first derivatives (I'_{calc} , I'_{obs}) for the correlated intensity spectra and is thereby sensitive to their shape. Using the difference between the intensities (I_{calc} , I_{obs}) instead would give an R-factor that is only sensitive to peak areas and not the peak shapes. The weighting factor, $w(E)$, emphasizes the regions of high curvature in the curves where the second derivatives (I'') are large and the first derivatives (I') are small.

References for Chapter II

1. C. J. Davisson and C. H. Kunsman, *Science*, 52 522 (1921).
2. L. de Broglie, *Phil. Mag.* 17 446 (1973).
3. C. J. Davisson and L. H. Germer, *Phys. Rev.* 30 705 (1927).
4. H. E. Farnsworth, *Phys. Rev.*, 49 605 (1936).
5. E. J. Scheibner, L. H. Germer and C. D. Hartman, *Rev. Sci. Instrum.*, 31 112 (1959).
6. J. J. Lander, J. Morrison and F. Unterwald, *Rev. Sci. Instrum.*, 33 782 (1962).
7. W. Ehrenberg, *Phil. Mag.* 18 878 (1934).
8. See tabulation in: J. A. Strozier, Jr., D. W. Jepsen and F. Jona, in Surface Physics of Materials, Vol. I, ed. J. M. Blakely, (Academic, London).
9. L. Pauling, The Nature of the Chemical Bond, 3rd Ed. Cornell University Press, 1960.
10. H. J. Wasserman and J. S. Vermaak, *Surf. Sci.*, 32 168 (1972).
11. S. Andersson and J. B. Pendry, *J. Phys.* C5 L41 (1972).
12. L. L. Kesmodel, P. C. Stair, R. C. Baetzold and G. A. Somorjai, *Phys. Rev. Lett.* 36 1316 (1976).
13. K. Heinz and K. Muller, LEED Intensities--Experimental Progress and New Possibilities of Surface Structure Determination, Springer, Heidelberg, 1980.
14. E. Zanazzi and F. Jona, *Surf. Sci.*, 62 1977.
15. a) S. Andersson and J. B. Pendry, *Surf. Sci.*, 71 75 (1978).
b) M. Passler, A. Ignatiev, F. Jona, D. W. Jepsen and P. M. Marcus, *Phys. Rev. Lett.* 43 360 (1979).

- c) S. Andersson and J. B. Pendry, Phys. Rev. Lett. 43 363 (1979).
 - d) S. Andersson and J. B. Pendry, J. Phys. C. (in press).
 - e) S. Y. Tong, A. Maldonado, C. H. Li and M. A. Van Hove, Surf. Sci. 99 73 (1980).
 - f) K. Muller, E. Lang, P. Heilmann and K. Heinz (to be published).
16. G. Hanke, E. Lang, K. Heinz and K. Muller, Surf. Sci., 91 551 (1980).
17. J. E. Demuth and T. N. Rhodin, Surf. Sci., 42 261 (1974).
18. a) R. L. Park, J. E. Houston and D. G. Schreiner, Rev. Sci. Instrum. 42 60 (1971).
- b) G. C. Wang and M. G. Lagally, Surf. Sci., 81 69 (1979).
- c) D. G. Welkie and M. G. Lagally, Appl. Surf. Sci., 3 272 (1979).
19. J. E. Demuth and T. N. Rhodin, Surf. Sci., 45 249 (1974).
20. a) P. C. Stair, T. S. Kaminska, L. L. Kesmodel and G. A. Somorjai, Phys. Rev., B11 623 (1975).
- b) J. C. Frost, R. J. Koestner, M. A. Van Hove and G. A. Somorjai (unpublished).
21. a) D. C. Frost, K. A. R. Mitchell, F. R. Sheperd and P. R. Watson, J. Vac. Sci. Technol., 13 1196 (1976).
- b) T. N. Tommet, G. B. Olszawski, P. A. Chadwick and S. L. Bernasek, Rev. Sci. Instrum. 50 147 (1979).
22. a) P. Heilmann, E. Lang, K. Heinz and K. Muller, Appl. Phys. 9 247 (1976).

- b) E. Lang, P. Heilmann, G. Hanke, K. Heinz and K. Muller, Appl. Phys. 19 287 (1979).
- c) D. G. Welkie, M. G. Lagally, Appl. Surf. Sci. 3 272 (1979).
23. Vacuum Generators, GmbH, Wiesbaden, Data LEED System.
24. M. D. Chinn and S. C. Fain, Jr., J. Vac. Sci. Technol. 14 314 (1977).
25. S. P. Weeks, J. E. Rowe, S. B. Christman and E. E. Chabran, Rev. Sci. Instrumen. 50 1249 (1979).
26. P. C. Stair, Rev. Sci. Instrumen., 51 132 (1980).
27. a) J. B. Pendry, Low Energy Electron Diffraction (Academic Press, New York, 1974).
- b) M. A. Van Hove and S. Y. Tong, Surface Crystallography by LEED (Springer-Verlag, New York, 1979).
28. M. A. Van Hove and R. J. Koestner, Proc. Conf. on Determination of Surface Structure by LEED, Plenum Press (New York) 1981.

Table 1. Important characteristics of the various data collection systems reviewed.

System	On/Off Line	Incident Beam Current A	Typical Measurement Times		Typical Evaluation Times		Dynamic Range	Distortion?
			1 beam	20 beams	1 beam	20 beams		
Faraday cup	on	10^{-6} - 10^{-8}	15 min	5 hrs	0	0	$>10^3$	no
Spot photometry	on	10^{-6}	15 min	5 hrs	0	0	$>10^3$	no
Photography: microdensitometer	off	10^{-6}	10 min	10 min	-	5 hrs	10^3	no
vidicon	off	10^{-6}	10 min	10 min	50 min	15 hrs	10^3	no
TV camera	off	10^{-6}	2 sec	2 sec	2 sec	40 sec	10^3	no
CEMA / phosphor +TV camera	off	10^{-9}	2 sec	40 sec	0	0	10^3	no
			8 min	8 min	-	?	10^3	yes
CEMA / RANICON	off	10^{-12}	8 min	8 min	to be done	to be done	$<10^3$	yes

III. EXPERIMENTAL DETAILS

A. APPARATUS

Figure 1 diagrams the apparatus used in almost all the experimental work described in later chapters. The apparatus can be divided into three separate sections: the Ultra-High Vacuum (UHV) chamber, the manifold, and the roughing line. The UHV chamber was maintained at $5-10 \times 10^{-10}$ torr during adsorption experiments using an Ultek 200 liter/sec ion pump and a water cooled titanium sublimation pump. The manifold was used to introduce gases into the UHV chamber via a Varian leak valve; a rotary mechanical pump and a molecular sieve sorption pump kept the base pressure below about $1\mu (=10^{-3}$ torr). The roughing line had a base pressure of about 5×10^{-9} torr using a small 75 liter/sec ion pump (Varian). This section could pump the manifold down to much lower base pressures than 1μ by opening a Viton valve and would thereby avoid contamination problems that arise when the manifold is filled with successively different gases. The roughing line also ion-pumped the Ar and O₂ from the main chamber after sample cleaning treatments.

The UHV chamber is equipped with four-grid LEED/Auger optics, an ion sputtering gun (Varian), and a mass spectrometer head (UTI 100 C). An off-axis LEED gun (Varian) is mounted on the back 8" flange; this gun uses a directly heated tungsten ribbon filament as shown in Fig. 2a. A glancing incidence electron gun (not shown in Fig. 1) is also mounted on a 2-3/4" flange for use in Auger Electron Spectroscopy.

The Auger and LEED electrons (see Fig. 2b) are energy analyzed with the standard four-grid optics. A phosphorescent screen biased by +8 kV displays the diffraction pattern of the sample surface in the LEED mode; it is also biased by +300 V and used as a current collector in the Auger mode. Mu metal shielding is wrapped cylindrically around the LEED gun and sample to avoid deflection of the low energy electrons by reducing the magnetic flux through the chamber; the magnitude of the transverse component of the magnetic field along the incident beam trajectory is 50 milligauss with the shielding present and about 600 milligauss without the mu metal. The angle between the sample normal and incident LEED beam would change by less than 0.25° over the relevant energy range when the transverse magnetic field strength is kept below 50 milligauss.

The ion gun is directed at the sample to sputter clean its surface; the well-focussed Ar^+ beam would deliver a 1-4 μ amp current to the sample. The mass spectrometer head is used to monitor the residual gases in the main UHV chamber and to detect the desorption of gases from the sample as its temperature is raised (Thermal Desorption Spectroscopy). In order to orient the sample with respect to the incident LEED beam, a Varian "flip" manipulator was modified slightly to allow both polar and azimuthal rotations. The polar rotation axis lies along the manipulator shaft, while the azimuthal axis is parallel to the crystal normal. The crystal is spot welded onto 4 mil Ta foil and can be heated resistively to 1200°C . The sample can also be cooled to -50°C (220K) by immersing in LN_2 filled dewars the copper bars that are thermally attached to the sample via copper braids.

The major difficulty with the main chamber design is the poor conductance from the sample region to the ion pump. The mu metal shielding that surrounds the sample area has only a few small apertures so the effective pumping speed near the sample may be quite low. This implies that the background pressure near the sample is significantly higher than that measured at the ion gauge which is located very near the mouth of the large ion pump.

B. SAMPLE PREPARATION

i) Metal Samples (Ir, Pt, Rh)

The Ir(100) [10 ppm impurities, Orion Chemical] and Pt(100) [1 ppm impurities, Materials Research Corp.] crystals were oriented and spark cut to the proper crystallographic plane; they were then polished with a sequence of finer emery grits and finally with a 0.5 μm diamond paste. The Ir sample was within a $1/2^\circ$ of the (100) face, but the Pt crystal was misaligned slightly and a (012) facet could be observed in the LEED pattern. This facet was removed by prolonged Ar^+ ion sputtering and annealing at 900°C .¹

Both crystals were cleaned of carbon and sulfur impurities by a combination of Ar^+ bombardments and oxygen treatments. Calcium proved to be the most troublesome impurity and was depleted from the near surface region only after many short heating (occasionally in the presence of O_2) and Ar^+ sputtering cycles (for 2-3 days). Heating the crystal would draw Ca to the surface; and in the presence of oxygen, this Ca segregation could be dramatically enhanced. The calcium was probably present as an oxide on the surface and produced a large number of different ordered superlattice structures. We also found

that the concentration of Ca varied significantly across the metal surface.

The Rh(111) [1000 ppm impurities, MRC], Pt(111) [1 ppm impurities, MRC], and Rh(100) [100 ppm impurities, MRC] samples were similarly oriented and spark cut. The Rh(111) sample was only polished down to a 0.5 μm diamond paste, while the Rh(100) and Pt(111) samples were further polished with a 0.05 μm alumina slurry. The Rh(111) LEED spots were noticeably larger than those for either the Rh(100) or Pt(111) surface; this suggests that the Rh and Pt metals should be fine polished to remove most of the surface damage present after facing and rough polishing.

The Pt(111) sample was easily cleaned of trace amounts of calcium, phosphorous, and carbon by oxygen treatments (5×10^{-7} torr O_2 , 10 min, 700°C with a subsequent flash to 1000°C) and Ar ion bombardments (with subsequent annealing at 800°C for 5 min). The Rh(111) crystal had small sulfur, chlorine, and carbon contamination as well as a major boron impurity. Only after two weeks of continuous Ar^+ bombardments (1-3 μ amps, 1.2 kV) with 5 min annealing at 800°C and O_2 treatments (flowing 5×10^{-7} torr O_2 , 700°C) was boron largely depleted from the near surface region. The Rh(100) sample (with a much lower bulk impurity level) required only one or two such treatments to become reasonably clean.

ii) Gas Samples

The carbon monoxide, carbon dioxide, ethylene, propylene, and cis- and trans-2-butene samples (Matheson, nominally 99+%) were drawn

directly from lecture bottles without further purification. Methylacetylene (99.9%) purchased from Air Products was used similarly. Acetylene (Matheson, 99.8%) was trapped with a solid CO₂/ethanol bath to remove any acetone that could be present. (The acetylene is stored in an acetone solution to prevent an explosion but the acetone concentration in the gas phase will increase dramatically as the acetylene pressure drops.)

Reagent grade benzene (Mallinckrodt) was degassed by a few freeze-pump-thaw cycles; its vapor pressure at room temperature (~100 torr) was high enough to fill the manifold without substantial contamination from background gases. Solid naphthalene (reagent grade, J. T. Baker) was also degassed by freeze-pump-thaw cycles (m.p. ~80°C); both the manifold and the naphthalene sample were heated to ~80°C to obtain a reasonable vapor pressure (~10 torr) above the background gases. In order to reduce desorption of contaminants from the manifold walls, the manifold was first heated to 80°C and ion pumped for an hour before introduction of the naphthalene vapor.

C. LEED INTENSITY MEASUREMENT

The photographic technique (see Chapter II.B and Ref. 1) was used to collect all the intensity vs. voltage curves presented in later chapters. In this method, photographs of the LEED patterns displayed on the fluorescent screen are taken at 2 eV intervals; a typical energy range stretches from 20-150 eV. The electron beam, however, still may damage molecular overlayers during the 5 min interval needed to record all the intensity information; in the molecular systems we studied, the crystal was translated during the course of photography to reduce the

total electron beam exposure of any area on the surface to less than 25 or 60 μ amp-sec. A more extensive discussion of possible electron beam effects will be presented for each molecular structure individually.

A Beattie Varitron view camera (fitted with a Bencher external shutter and an 85 mm, f 1.8 Nikon lens) was adjusted for the maximum aperture and a 1/2 sec exposure time. The camera was loaded with a high speed Kodak film (Panchromatic 2484); the 150 ft roll of film (1200 exposures) was advanced frame by frame with high precision. This precision ($< 1/64$ in) is necessary for the subsequent reduction of the intensity data. After exposure, the film was spray developed with Dupont's extra fast X-ray developer. The developing, fixing, and working times were all 150 secs at 28.5°C.

The processed film was scanned using a computer controlled, digital output, stepping microdensitometer with the measured densities stored on a magnetic tape. The microdensitometer is a home-built device attached to a DEC-10 computer. The densitometer digitized the LEED image using a (120 \times 120) density grid with about 500 effective gray levels; a typical diffraction spot would encompass between 10-100 points on the density grid. Usually, 10^6 density points (corresponding to 100 frames of film) could be measured and stored on tape in a 5-10 minute scan time.

A set of computer programs were written by Jonathan Frost to analyze the digital output from the microdensitometer; these programs find each diffraction beam on the density grid and then calculate its intensity at that energy. In order to transform the measured density into an intensity, a calibration wedge should also be analyzed. The

wedge is prepared by changing the log of the intensity linearly along a length of film (using a neutral density filter); the variation in the optical density along the length of the wedge is then measured. This produces a calibration table mapping measured density into exposing intensity that is used by our computer programs.

Once the intensity of each diffraction beam is measured at each energy, the resulting intensity vs. voltage curves are normalized for constant incident beam current, averaged over degenerate diffraction beams and independent runs, and smoothed twice by a three-point formula before they are compared to theoretical spectra.

Reference for Chapter III

1. P. C. Stair, PhD Thesis (University of California, Berkeley, 1977).

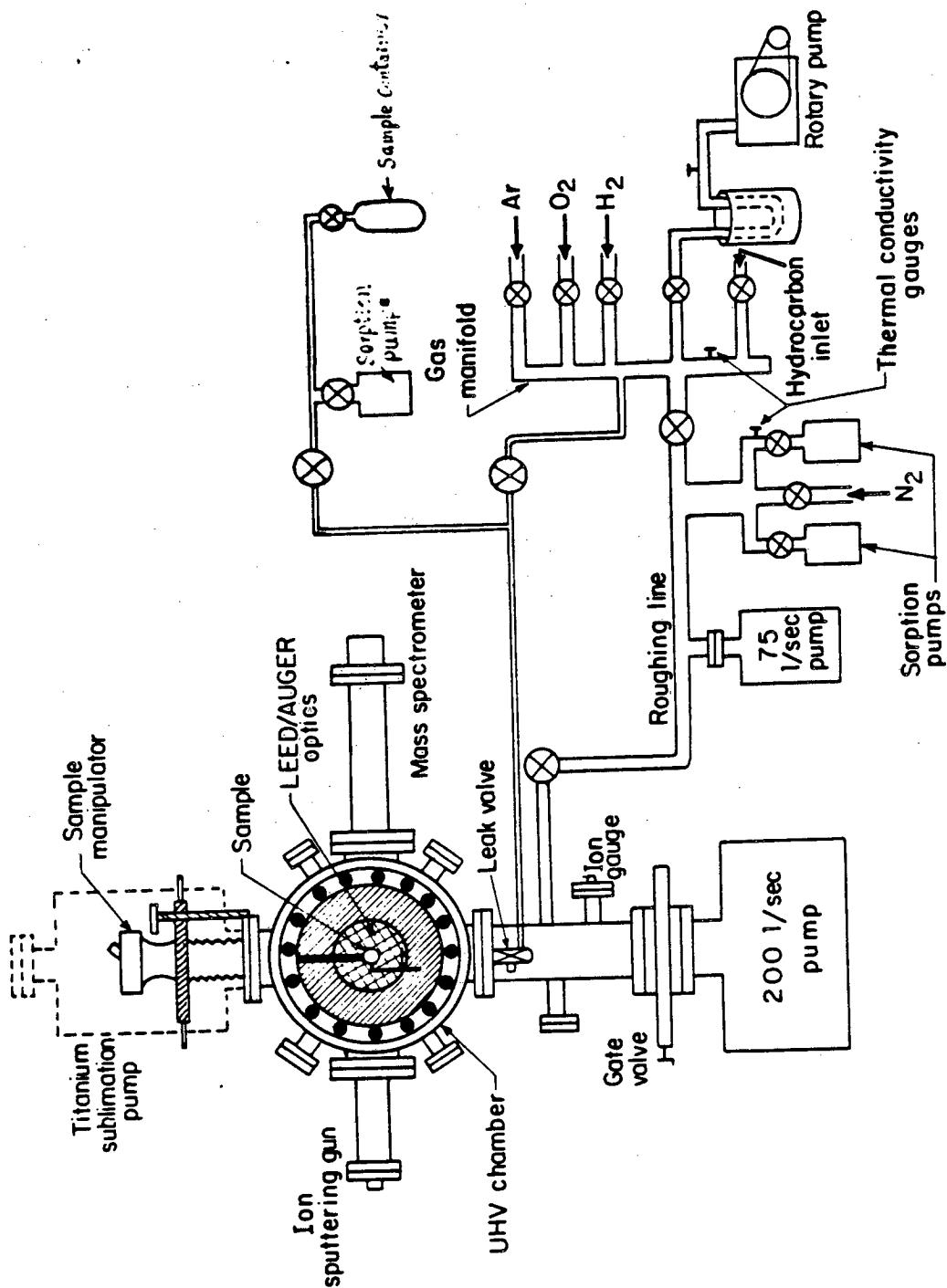
Figure Captions for Chapter III

Fig. 1. Diagram of vacuum chamber used for most of the experiments described in this thesis.

Fig. 2. (a) Schematic of sample mount and LEED spectrometer.

(b) Distribution of electrons scattered from the sample.

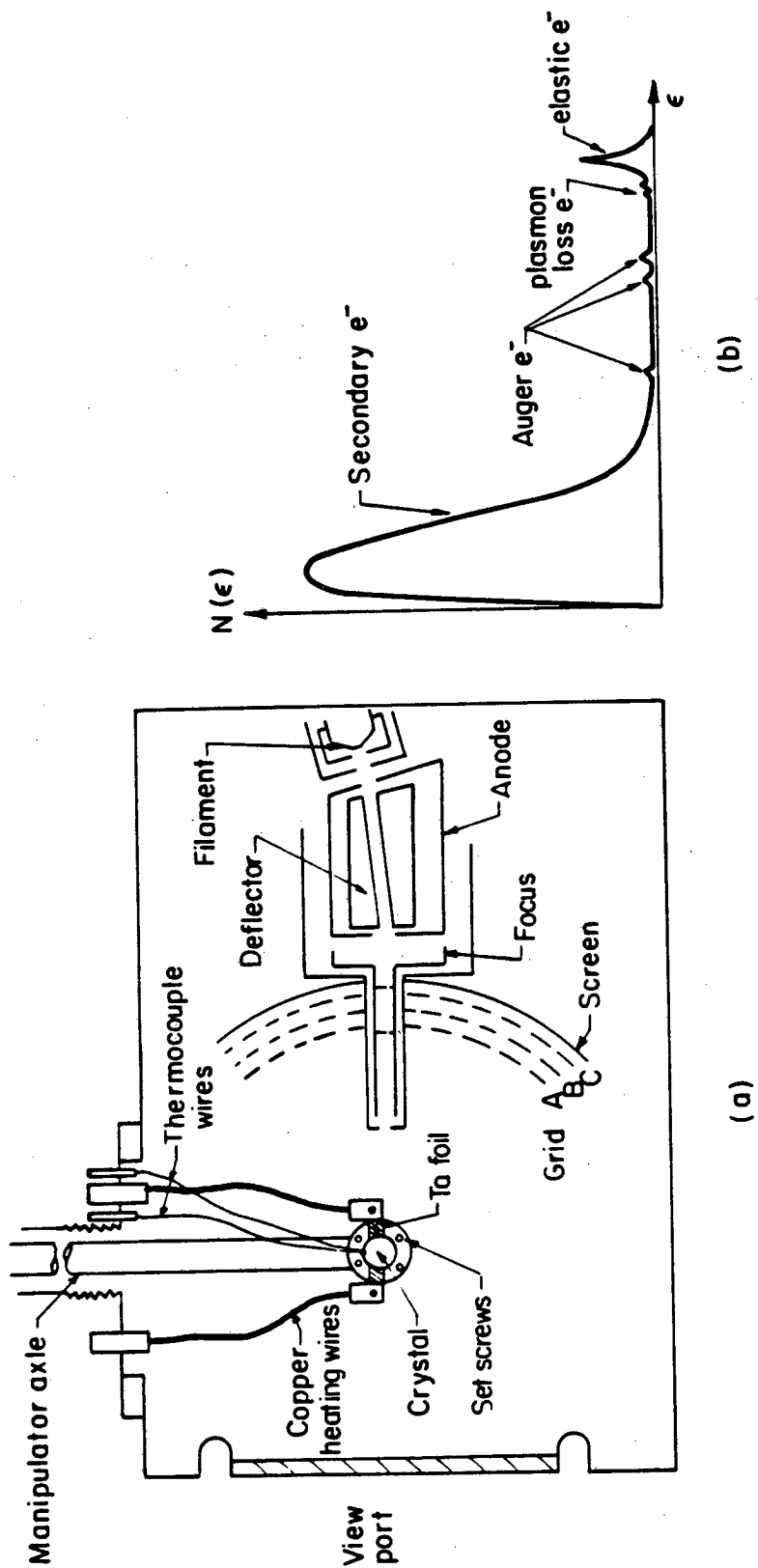
The LEED electrons are elastically scattered.



Schematic of apparatus

XBL 791-5654

Fig. 1



XBL791-5655

Fig. 2

IV. Ir, Au, AND Pt(100) SURFACE RECONSTRUCTIONS

PART 1: EXPERIMENTAL OBSERVATIONS AND POSSIBLE STRUCTURE MODELS

A. INTRODUCTION

It has been known for many years, from low energy electron diffraction (LEED) studies, that clean metal surfaces may reconstruct, that is, may have a structure that is not a simple termination of the bulk structure. At present the clean metal surfaces known to reconstruct are the (100) faces of Ir,¹ Pt,² Au,³ V,⁴ Cr,⁵ Mo,⁶ W,⁷ the (110) faces of Ir,⁸ Pt,⁹ and Au¹⁰ and the (111) face of Au.¹¹ Since many metal surfaces have not been subjected to surface structural studies, surface reconstruction may well be a more widespread occurrence than is apparent at present. Also, only a few surfaces have been studied at low temperatures where the chances for reconstruction are greater than at room temperature (e.g., clean W(100) reconstructs only when cooled). It has been found that some surfaces reconstruct under the influence of adsorbates, such as W(100)¹² and Ni(100)¹³ when hydrogen is present. The precise location of atoms in the reconstructed metal surface has been determined only for clean W(100)¹⁴ (which exhibits a c(2x2) superlattice), Ir(110)¹⁵ and Au(110)¹⁶ (both of which have (1x2) superlattices).

The knowledge of the surface structure is of particular importance in studies of surface and bulk phase transitions. The surface structure could correspond to a phase different from the bulk structure,

or the surface may act as the nucleation site for a bulk phase transition, just as other defects can. Determination of the reconstructed surface structure is also important for the understanding of the mechanism of phase transitions and to test the theories (such as the soft-phonon theory) proposed to explain their occurrence. Some surface reconstructions have been suggested to be caused by charge density waves [on W(100),¹⁷ Mo(100),¹⁷ Si(111),¹⁸ and 1T-TaS₂(0001)¹⁹], in which the conduction electron density has periodic fluctuations with a wavelength a few times the lattice constant; thereby inducing a static wavelike deviation of the atomic equilibrium positions with that same wavelength.

The precise location of atoms in the reconstructed surface must also be known for the analysis of the electronic structure of the metal surface. The existence and the characteristics of surface states depend on the surface structure which also controls the surface density of states. The importance of the surface structure of metals is also evident in the fundamental steps of heterogeneous catalysis since many chemical reactions are known to be surface-structure sensitive. The surface structure also plays an important role in crystal growth and in epitaxy.

In this two part contribution we report a surface structure analysis of the intriguing (100) surface reconstructions of Ir, Pt and Au. We have studied in detail the sometimes complicated LEED patterns for these surfaces, and performed a dynamical LEED intensity analysis of the Ir and Pt(100) reconstructions to determine the atomic locations.

B. PREVIOUS OBSERVATIONS OF THE Ir, Pt AND Au(100) RECONSTRUCTIONS

i) LEED observations

The first clean metal surface reconstruction was reported in 1965 for the Pt(100) crystal by Hagstrom et al.² This metal surface exhibits a so-called "(1x5)" LEED pattern because of the appearance of diffraction beams in (or near) 1/5th order positions. In 1967, a Au(100)"(1x5)" reconstruction was observed by Fedak and Gjostein³ and soon after by Mattera et al.²⁰. Later in 1967, Fedak and Gjostein resolved a splitting in the LEED spots for Au, leading to a "(20x5)" rather than "(1x5)" superstructure; they were the first to propose a hexagonal overlayer on the square substrate mesh as a model for the surface rearrangement.²¹ In 1969 Palmberg²² similarly resolved split spots in the LEED pattern of reconstructed Pt(100) and decomposed the pattern into four equivalent domains, each having a $\begin{pmatrix} 13 & 1 \\ -2 & 1 \end{pmatrix}$ unit cell. A single domain was formed by thermal stressing while heating the crystal to or above 1000°C, yielding a straightforward determination of the unit cell. Also in 1969, Grant found that the Ir(100) surface reconstructed and gives a sharp (1x5) LEED pattern without splittings,¹ cf. Fig. 1.

In 1977, Stair²³ studied the Pt(100) surface reconstruction, arriving at the somewhat different unit cell $\begin{pmatrix} 14 & 1 \\ -1 & 5 \end{pmatrix}$ cf. Fig. 2, where the number 14 is an average over values ranging from 13 to 15; a closer look at the diffraction patterns favors a matrix element of about -1.5 rather than -1, yielding a unit cell close to $\begin{pmatrix} 14 & 1 \\ -3 & 10 \end{pmatrix}$. In fact,

Blakely reported²⁴ in 1976 that the reconstruction unit cell in the (100) terraces of a few stepped Pt surfaces depends on the particular stepped surface; in addition, fewer domains are present simultaneously on stepped surfaces. For example, the Pt(13,1,1) surface, with 6-atom wide (100) terraces separated by 1-atom high steps of (111) orientation, has a $\begin{pmatrix} 13.5 & 1 \\ -3 & 6 \end{pmatrix}$ unit cell, better written as $\begin{pmatrix} 27 & 2 \\ -3 & 6 \end{pmatrix}$; the number 6 is possibly due to the width of the 6-atom wide terraces. In the presence of only about 0.02 monolayers of O₂, the Pt(13,1,1) surface facets into a (100) face with a $\begin{pmatrix} 12 & 1 \\ -3 & 5 \end{pmatrix}$ reconstruction unit cell and a (311) facet. The stepped Pt(911) surface, that has 4-atom wide (100) terraces and 1-atom high (111) steps, yields terraces with a $\begin{pmatrix} 12 & 1 \\ -3 & 5 \end{pmatrix}$ reconstruction unit cell. The stepped Pt(510) surface, that also has 4-atom wide (100) terraces but 1-atom high steps of (100) orientation, facets to a (100) face again with a $\begin{pmatrix} 12 & 1 \\ -3 & 5 \end{pmatrix}$ reconstruction unit cell and a (210) facet.

Other slightly different surface structures are reported by Heilman et al.,²⁵ and by Norton and co-workers²⁶ on the clean Pt(100) crystal face. The first authors report a "Pt(100)-hex-R0.7°" reconstruction which we identify with the $\begin{pmatrix} 14 & 1 \\ -1 & 5 \end{pmatrix}$ structure, on the basis of the published LEED pictures which closely resemble those of Stair in the presence of all four domains. They also report a "Pt(100)-hex" structure. If we decompose the published diffraction pattern into four equivalent domains we arrive at a $\begin{pmatrix} 14 & 1 \\ 0 & 5 \end{pmatrix}$ structure,

also observed by the second authors. Some of these patterns with their corresponding unit cells are shown in Fig. 3. The fact that steps seem to affect the reconstruction unit cell suggests that the detailed form of the reconstruction is influenced by the presence, and especially by the orientation, of surface defects. Similar orientational effects were obtained after sputtering the Pt(100) surface at an angle to the surface normal.²³

The Au(100) diffraction patterns from the (20×5) structure exhibit some triplets of split spots that are not aligned, but have a V shape with an obtuse angle at the apex of the V. Because it was only weakly discernible, this feature was included in a few drawn renditions of the diffraction pattern but not commented upon,²¹ although it implies a unit cell different from (20×5). More recent photographs^{27,28} obtained when a more collimated electron beam was used, show additional split-off spots that clearly have a V or W or longer zigzag arrangement, cf. Figs. 4 and 5. Our best estimate for the unit cell of this structure is a large centered cell labelled c(26×68). Here the number 26 comes from direct measurement of spot separations and is uncertain by about ±1. The number 68 follows from the angle of the V shape and should be about $10/4 \times (26+1) = 68 \pm 2.5$; however, the five partly unequal distances between visible spots along the line from the (00) to the (01) spot must be in the proportion $n+1:n+1:n:n+1:n+1$ with suitable n to produce a coincidence lattice; one then obtains the possible numbers $2(5n+4)$, among which the one closest to 65 is 68 with $n=7$. The number $26/2 = 13$ corresponds to the often quoted and probably overestimated period 20 in the (noncentered) notation (20×5).

A different structure has also been observed on stepped surfaces of Au with reconstructed (100) terraces. Melle and Menzel²⁹ report a $\begin{pmatrix} 14 & 1 \\ -1 & 5 \end{pmatrix}$ structure on several such stepped surfaces (observed by RHEED).

Here a comment is necessary concerning the above unit cell designations such as $\begin{pmatrix} 14 & 1 \\ -1 & 5 \end{pmatrix}$ or $c(26 \times 68)$. These designations assume that there is a finite unit cell, that is exclude structures obtained by superposing two incommensurate lattices. The diffraction patterns do not exclude incommensurate lattices, however. The only well-defined quantities are the numbers 5 and 1 in the matrix $\begin{pmatrix} p & 1 \\ q & 5 \end{pmatrix}$ for Pt(100) and in the designation (1×5) for Ir(100) since these are obtained by simple counting of the number of extra spots. All other quantities, such as p and q , and the Au(100) designation, are based on the measured ratio of two lengths in photographs and are therefore uncertain. Only if all these numbers are integers does one obtain a finite unit cell. (Note: the distinction between incommensurate and commensurate lattices becomes pointless from the point of view of LEED for coincidence unit cells larger than the coherence length of the electron beam, which is typically 100Å, but larger in the case of Fig. 4.)

ii) Observations of Ir, Pt and Au(100) Reconstructions
by Other Techniques

Several studies using techniques other than LEED have monitored the Ir, Pt and Au(100) reconstructions. High energy ion scattering has been applied to Pt(100)³⁰ and Au(100),³¹ yielding the information

that about one monolayer of the surface atoms are positioned well away from their ideal unreconstructed positions. Also, an ultraviolet photoemission study³² reveals that the UPS spectrum of the unreconstructed Ir(100) surface resembles more that of Ir(111) than that of unreconstructed Ir(100). Similar results have been obtained on Au(100).³³ Observations with electron energy loss spectroscopy have been made²⁷ for Au(100) and (111) which also show great similarity between the reconstructed (100) and the unreconstructed (111) surfaces.

It is interesting to note that field ion microscopy studies on Ir, Pt or Au tips have not reported the reconstructions of the (100) surfaces,³⁴ although a $c(2 \times 2)$ reconstruction on clean W(100) has recently been observed with FIM.³⁵ This may be due to field effects or to the fact that atomic arrangements are made obvious by FIM only near terrace edges where a reconstruction may either not take place or may not be readily detectable. As pointed out above, reconstructions do occur on some 4-atom wide terraces according to LEED observations.

iii) The Depth of Reconstruction

There is a certain amount of evidence that only the topmost layer of Ir, Pt and Au(100) reconstructs. First, the LEED patterns can be interpreted as a combination of a rearranged top layer and the unmodified square substrate lattice. This presupposes that the attenuation of the substrate contribution by the reconstructed surface layer is not too large; given known electron mean free paths, this can only be true for less than two layers, that is presumably for one reconstructed monolayer. Second, the HEIS results,^{28,30} which count

the number of displaced atoms, are not consistent with more than one reconstructed monolayer. Of course one cannot exclude small deviations from the substrate geometry in the second layer due to the modified top layer geometry. However, we shall ignore these.

iv) Unreconstructed Metastable Surface Structures of the (100) Faces of Ir, Pt and Au

Clean, metastable, unreconstructed (100) (1x1) surfaces have been prepared for Ir,³⁶ Pt,³⁷ and Au²⁷ and the temperatures needed to produce an irreversible order-order transition to a reconstructed state has been measured. The unreconstructed Ir(100) surface gradually and continuously reconstructs as the temperature is varied from about 700K to about 1200K.^{32,36} The resulting (1x5) pattern is stable from 55 to 2100 K.³⁸ The metastable Au(100)(1x1) surface is converted into the "(20x5)" structure at 373 K.²⁷ The metastable Pt(100)(1x1) surface transforms into the "(20x5)" structure at 400K,^{37,39} but upon further heating to 1100-1150 K it is converted into the "Pt(100)-hex-R0.7" structure mentioned above.³⁹ The latter structure is stable from 77 to 1450 K.³⁹

v) Previous Structural Analyses

No full dynamical LEED analysis of the reconstructed Ir, Pt or Au(100) surface structures has been published. However, a double-diffraction LEED calculation has been attempted in the case of Pt(100), that assumed the presence of a hexagonal top monolayer. A certain degree of agreement between experiment and theory has been achieved.³⁹ Dynamical (spin-polarized) LEED calculations have been

performed for the unreconstructed metastable surface structures of Pt and Au(100)⁴⁰ which yield good agreement with experimental IV curves when an ideal, unrelaxed surface was assumed; no relaxations of the surface atoms were considered. From past experience with similar studies one may assume that for this case the topmost layer spacing has the bulk value within about 5%. A HEIS result for metastable Pt(100)(1×1) indicates a minimal outward relaxation of this spacing by $0.5 \pm 0.5\%$.³⁰

C. LEED INTENSITY MEASUREMENTS

Photographs of the Pt(100) $\begin{pmatrix} 14 & 1 \\ -1 & 5 \end{pmatrix}$ and Ir(100)-(1×5) LEED patterns were taken within a 10 minute interval at a base pressure $\sim 1 \times 10^{-9}$ torr with the crystal temperature falling from $\sim 50^\circ\text{C}$ to $\sim 30^\circ\text{C}$. (CO had just been flashed off the crystal by heating to 600°C (for Ir) or 900°C (for Pt).) A Nikon F camera equipped with 85 mm lens, K2 + K3 + K4 extension rings, and motor drive was used; the film used was Kodak's Pan-X 2484. The Pt LEED pattern was photographed at polar angles $\theta = 0^\circ, 4^\circ, 10^\circ, 16^\circ$ with an azimuth $\phi = 45^\circ$ ($\theta=0^\circ$ being defined as a [011] direction) in 2 eV steps stretching from 10 - 100 eV; the components in the Pt(100) $\begin{pmatrix} 14 & 1 \\ -1 & 5 \end{pmatrix}$ split spots were measured separately. The Ir LEED pattern was photographed at polar angles $\theta = 0^\circ, 10^\circ, 20^\circ$ with an azimuth $\phi = 0^\circ$ in 2 eV steps from 20 - 200 eV. Only photographs of LEED patterns for one crystal orientation (for example $\theta = 10^\circ, \phi = 0^\circ$) with the specified energy range (for example, 20 - 200 eV) were taken during the 10 minute interval. The crystal was then recleaned before another set of

photographs were taken; the major contaminant after photography was C, probably produced by LEED beam fragmentation of the adsorbed CO from the ambient.

Comparing the Ir and Pt I-V profiles, the Ir curves have more gaps, appear noisier, and have larger scaling factors; the major reason for the discrepancy is the shutter speed being limited to about 1/4 sec in the Ir data, rather than 1 sec as in the Pt data.

D. INTERPRETATION OF THE DIFFRACTION PATTERNS

i) Ir(100)

The diffraction pattern of the reconstructed Ir(100) surface implies the presence of a (1×5) unit cell. There are no systematic absences or weaknesses of any of the (1×5) spots. This fact puts some restrictions on possible models, such as the absence of glide symmetry planes or domain structures (within the electron coherence length). However, it leaves open many options for the relative positions of the surface atoms within the unit cell since the unit cell has an area that is sufficient to accommodate up to 6 atoms in one plane. One possibility is a hexagonal top layer, as illustrated in Fig. 6. The hexagonal layer, if it is planar, must be contracted in the 5-fold direction by 3.92% to be discussed in the next section.

ii) Au(100)

The reconstructed Pt(100) and Au(100) diffraction patterns are more complicated. Figure 5 shows a diagram of the diffraction pattern^{27,28} due to one domain of reconstructed Au(100). It implies a c(26×28) unit

cell structure of the surface which is approximated by a (20×5) unit cell in poorly resolved LEED patterns. Many of the possible diffraction spots, based on the $c(26 \times 68)$ unit cell, are not detected. Such a large unit cell can be understood as one large domain that consists of many (1×5) units identical to those of $\text{Ir}(100)(1 \times 5)$. The regular repetition of the domains produces the splitting of the $1/5$ th order spots due to the (1×5) units. It is necessary to assume (1×5) units within the domain to obtain significant intensity near the $1/5$ th order positions of the diffraction pattern. If we indeed have a domain structure, the individual split-off components of each $1/5$ th order spot should have an almost identical energy dependence of their intensities, except for constant factors. This is because such split spots can be regarded as the product of the (1×5) diffraction pattern, with its complicated energy dependence of intensities, and the $c(26 \times 68)$ superlattice pattern, which in itself produces only a smooth energy dependence of intensities. However, one can observe in the experiment that the split spots do not exhibit similar intensity changes as the electron energy is varied; for example, there are reversals in the intensities of neighboring split spots. Therefore, the simple domain model of (1×5) units is incorrect.

A different interpretation of the $c(26 \times 68)$ periodicity comes about when one tries to understand the diffraction pattern with its many absent spots in terms of multiple scattering effects. The combination of a suitable hexagonal lattice and the square lattice of the unreconstructed surface would produce the observed diffraction pattern, with single-scattering spots the most intense and multiple diffraction

spots weaker or absent, depending on the order of multiple scattering. In Fig. 5 some first-order hexagonal spots are indicated, one of which lies at $(1+1/16, 3/5+1/68)$, the other at $(0, 6/5+2/68)$ in terms of the substrate lattice. By multiple scattering one obtains all other observed extra spots with intensities that are smaller when the reciprocal lattice vectors needed to reach them are longer (Long reciprocal lattice vectors produce evanescent waves that contribute less intensity). Relative to bulk bond lengths, this hexagonal layer is contracted by $1/26 = 3.85\%$ in one direction, and by 6.47% in the direction perpendicular to that.

Other models besides the hexagonal surface layer model could also reproduce the observed $c(26 \times 68)$ diffraction pattern and we discuss one such model in Section E in connection with the shifted-row model for Ir(100).

iii) Pt(100)

Figure 3 shows some of the observed diffraction patterns of reconstructed Pt(100), assuming single domains. Here, as with Au(100) $c(26 \times 68)$, the absence of many spots can be interpreted as large domains containing many identical (1×5) units. In this case the two different intense parts of any split diffraction spot appear to have almost identical energy dependences so that a domain structure of (1×5) units is a possibility. However, a suitable hexagonal model as proposed by Palmberg²² can also explain the observed pattern. Figure 3 shows this interpretation by inclusion of first-order hexagonal diffraction spots. All other spots follow in a manner similar to Au(100)

discussed above and the observed spots with relatively short reciprocal lattice vectors are obtained by multiple diffraction. The above-mentioned nearly identical energy dependences of the split spots are then a result of the near-symmetry of the pattern.

In the $\begin{pmatrix} 14 & 1 \\ -1 & 5 \end{pmatrix}$ case, cf. Fig. 6, one thus obtains a hexagonal layer that is contracted by about 3.5% (nearly isotropically) and rotated by about 0.7° with respect to perfect alignment with the substrate; for the other unit cells shown in Fig. 3, hexagonal layers with slightly different contractions and torsions by about 2° are required.

Here also, other models can reproduce the observed diffraction pattern but the particular absence of many spots puts limitations on the possible models. Laser simulation is an effective method of studying such effects since a suitable general theory of two-dimensional diffraction patterns is not available to accurately specify those limitations.

iv) Au(111)

Because of its close relationship with the metal surface reconstructions that are the main topic of this work, the Au(111) reconstruction^{11,27,28} deserves special attention. No structural model for this surface has been published to our knowledge. The observed diffraction pattern is shown in Fig. 7. It can be interpreted as the superposition of three 120° rotated domains, each domain consisting of rectangular $(\sqrt{3}\times 22)$ unit cells which we designate $(\sqrt{3}\times 22)$ rect for convenience.

A model consisting of a 4.55% uniaxially contracted hexagonal top layer, cf. Fig. 8, satisfies the observed diffraction pattern in terms of single and double diffraction, the contraction direction being a [110] direction. Interestingly, a transmission electron microscope study of Au(111) layer growth in ultrahigh vacuum observed "fringes" (not seen with other metals in (111) orientation) of about 63Å periodicity with just the characteristics expected from the model just described; three 120° rotated domains of the correct orientation. The 63Å periodicity corresponds to about a rectangular ($\sqrt{3}\times 22$) unit cell and a with recent HEIS results.²⁸

A domain-structure model can also be proposed for this reconstruction, involving alternate strips 11 atoms wide of different bulk structure terminations. An interesting possibility is that half the strips have the normal fcc termination, while in the other strips an hcp termination occurs through slippage of the topmost layer to different hollow sites of the second layer. For this model to be stable the two types of termination should have only a small difference in surface energies.

Another possibility for this reconstruction is a charge density wave with an unusually long wavelength of about 22 lattice constants.

E. SURFACE STRUCTURAL MODELS

In any LEED analysis, one must postulate plausible surface structural models and test each against experiment. In this section we discuss plausible models for the Ir, Pt and Au(100) reconstructions.

i) The Hexagonal Model

The most popular model for the Ir, Pt and Au(100) reconstructions assumes that the topmost atomic layer takes a hexagonal close-packed arrangement over the square-net substrate,²¹ cf., Fig. 6. There are three main reasons for this idea. First, the hexagonal (111) face of face-centered cubic materials (the three metals studied here have an fcc bulk structure) is known to have the lowest surface energy among the possible crystal faces and it is the closest-packed.⁴²⁻⁴³ Therefore, a close packed reconstruction of the (100) face may conceivably lower its surface energy despite the resulting mismatch between the hexagonal layer and the substrate that would increase the strain energy at the surface. Because of the balance of these different surface forces, reconstruction would then happen only for certain metals under certain conditions of cleanliness and temperature. Second, a number of epitaxially grown metallic layers have a crystallographic orientation that corresponds to the building up of hexagonally close packed layers on the substrate surface often independently of the substrate orientation.⁴⁴ Thus such a structure appears to have some thermodynamic advantage over others. Third, the reconstruction unit cell of approximately (1×5) dimensions strongly suggest a hexagonal top layer. This was first apparent²¹ with

Au(100) where the diffraction pattern is such that spots corresponding to a hexagonal layer were clearly identified together with weaker multiple-scattering spots due to combinations of the substrate and hexagonal reciprocal lattices. Furthermore, it is easy to recognize that such a layer, in order to match the substrate mesh exactly, need only contract in one direction (the direction of 5-fold periodicity) by 3.9% with respect to its bulk size; this implies a bond length reduction of only 2.9%. This reduction of bond length is further minimized if one allows the hexagonal layer to buckle, which it surely must do since different top layer atoms must have different registries and therefore different heights (d-spacings) with respect to the underlying square-net substrate. Thus if one assumes backbond lengths (bond lengths between the top layer and the next layer) equal to the bulk value, the bond lengths parallel to the surface need be contracted by only 0.7 to 1.0%, depending on the registry of the hexagonal layer as a whole. Such contractions seem quite reasonable since analogous contractions have been observed to have values of 1 to 4% for other metal surfaces, namely for backbond lengths on fcc (110), fcc (311), bcc (100) and bcc (111) surfaces.⁴⁵

How much buckling occurs is an important question. An absence of buckling implies the flattest surface (minimum surface area), but maximum buckling (as described above) provides the most constant and bulklike backbond lengths. Surface flatness and constancy of bond lengths are both energetically favorable and so a compromise between the two may be best.

Another interesting question concerns the registry of the hexagonal layer with respect to the substrate. Figure 9 shows the two high-symmetry possibilities. The first involves bridge sites for 2/5 of the atoms which we call "two bridge registry" while the other has 1/5 of the atoms in top sites and 1/5 in center sites which we call "top/center registry". The remaining atoms have less symmetrical sites. Clearly the amount of buckling could depend on the registry. Assuming bulk bond lengths between the top and next layers, the buckling in the top/center registry is $\sim 0.8\text{\AA}$, that is $\pm 0.4\text{\AA}$ deviations about the middle plane, while for the two-bridge registry it reduces to $\sim 0.5\text{\AA}$ ($\pm 0.25\text{\AA}$ deviations). Thus the two-bridge registry provides for a smoother surface. In addition, it gives a more even distribution of the number of nearest neighbors than the top/center registry (that is a more constant coordination number between each surface atom and its neighbors, thereby more evenly spreading the mismatch among the atoms).

The differences between the LEED patterns of Ir, Pt and Au(100) can be explained conveniently with the hexagonal reconstruction model if one allows the top layer to contract slightly by different amounts, in both directions parallel to the surface, and/or to rotate about the surface normal. A hexagonal layer and a square layer, because of the inherent misfit between a hexagon and a square which essentially provides a slip fault, should have relatively little difficulty in translating or rotating with respect to each other. There is experimental⁴⁶ and theoretical evidence⁴⁷ for such rotation in Ar overlayers on the basal plane of graphite.

Thus the LEED patterns can be explained by hexagonal reconstruction such as those shown in Fig. 6. Ir(100) (1x5) has the simplest structure, a uniaxially contracted hexagonal layer aligned with the substrate orientation (no rotation) as described above. The Pt(100) $\begin{pmatrix} 14 & 1 \\ -1 & 5 \end{pmatrix}$ structure can be explained by a slightly rotated ($\sim 0.7^\circ$), biaxially contracted ($\sim 3.55\%$, not allowing for buckling) hexagonal layer with a coincidence lattice spanned by the vectors $(14,1)a$ and $(-1,5)a$ (a being the substrate square edge). A very slight distortion by an angle of about 2° of this layer produces the observed $\begin{pmatrix} 14 & 1 \\ 0 & 5 \end{pmatrix}$ structure spanned by the vectors $(14,1)a$ and $(0,5)a$. Other contractions and distortions and/or rotations can produce the other observed structures.

Instead of a simple rigid rotation of the hexagonal layer as discussed above, one may also imagine an unrotated (1x5) hexagonal structure to have dislocations every 14 atomic rows apart,²⁴ producing a $\begin{pmatrix} 14 & 1 \\ -1 & 5 \end{pmatrix}$ or similar superstructure. The dislocation need not be abrupt, it may be spread out over several atomic rows. An abrupt dislocation would be rather jagged and thus energetically unfavorable unless a $\begin{pmatrix} 14 & 1 \\ -3 & 5 \end{pmatrix}$ were adopted. This is shown in Fig. 10. The dislocations follow the rows of atoms, avoiding any jaggedness. A spread-out rather than abrupt dislocation as illustrated in Fig. 10 is also consistent with the $\begin{pmatrix} 14 & 1 \\ -1 & 5 \end{pmatrix}$ and $\begin{pmatrix} 14 & 1 \\ 0 & 5 \end{pmatrix}$ geometries. Such a spread-out dislocation can also be regarded as just a relaxation of the rotated hexagonal models if one allows atoms to have preferences for some adsorption sites over others,

thereby letting atoms move as much as they can toward the nearest preferred sites.

Finally, the Au(100) $c(26 \times 68)$ surface would have a hexagonal layer without rotation but with 3.85% and 6.47% contractions in the 26-fold and 68-fold periodicity directions, respectively, corresponding to the 20-fold and 5-fold directions, respectively, in the (20×5) notation.

A difficulty with the hexagonal model is the 20% higher concentration of atoms in the topmost layer of such a reconstructed surface as compared with the unreconstructed (1×1) surface: about 6 rows of atoms in a hexagonal layer fit over five rows of atoms of the square substrate. The transition between the unreconstructed and reconstructed states occurs experimentally quite easily. Where do the 20% more atoms come from? Apart from the presumably insufficient number of defect atoms (metal adatoms migrating along the surface), the always present steps on the surface can provide the answer. A terrace bounded by a step may contract parallel to the surface with the step retreating over the terrace below it. Of course, all successive steps would retreat in this way by similar amounts leaving the step-to-step distance constant, but each retreating step exposes formerly unexposed second-layer atoms which provides the additional 20% surface atoms. Because the terraces should be at least a few hundred Angstroms wide to give the observed sharp LEED patterns, the step edges would then have to retreat by at least several tens of Angstroms in a reconstruction.

ii) The Missing Row Hexagonal Model

To avoid the problem of 20% higher surface concentration in the hexagonal model one may imagine that the hexagonal model is formed in strips five atoms wide with one vacancy row between such strips. We may call this the missing row hexagonal model. The formation of such a surface, however, would increase the surface energy. In considering this model in our analysis, we assume that the missing rows are in symmetry planes, such as the row of top-site atoms for the top/center registry, or a row of bridge-site atoms for the two bridge registry. This way we keep high symmetry in the surface structure.

To produce the Pt(100) and Au(100) structures one would have to imagine a suitable domain structure to match the large observed unit cells. However, it is not clear what physical mechanism could produce the necessary ordering of missing rows.

iii) The Shifted Row Models

Another set of (1×5) structures which do not require a 20% higher surface concentration we call shifted row models. This type of model was originally proposed by Burton and Jura.⁴⁸ Here two of the five atoms in each (1×5) unit cell are shifted⁴⁹ as indicated in Fig. 11; depending on the choice of shift, three basic structures are possible. One obtains a greater degree of close-packing than in the unreconstructed surface at the price of opening up channels with broken bonds. Compared with the hexagonal model, the shifted row models have less misfit between the top layer and the substrate, but more misfit within

the top layer. An advantage over the hexagonal model is that no bond length contraction is needed and that less movement of atoms is required in the reconstruction process. Also, this model provides an explanation for the decrease of the work function upon transition from an unreconstructed to a reconstructed Ir(100) surface. The work function decreases since the roughness of the surface increases. One expects a higher work function with a (111)-type top layer in analogy with the unreconstructed (111) face, neglecting effects due to the hexagon-square interface. There is no fundamental preference in this model for the observed 5-fold periodicity. Other periodicities could occur as well. A 7-fold periodicity has been observed in one experiment^{44a} supporting the plausibility of this model; this occurs when three or four layers of gold are deposited on a (100) surface of palladium (although here the lattice constant of the gold substrate may be affected by the palladium substrate below the gold). Also, streaks have been observed in [110] directions when gold is deposited in certain coverages on Pt(100), indicating a disorder in the 5-fold period.⁵⁰

One of the main arguments against the model proposed originally by Burton and Jura is that the atoms of the shifted rows are in bridge sites and, therefore, probably in an unstable situation. Surface phonon calculations have been carried out in the case of a (2x1) reconstruction involving a shift of every other row, showing that there is indeed an instability for low frequency phonons in this configuration.⁵¹ Figure 11 shows that in fact the model proposed here is slightly different since each atom of the shifted rows is moved to the

3-fold site formed by two of the unshifted atoms and one atom of the second layer.

To explain the Pt(100) and Au(100) reconstructions, regularly spaced defects have to be introduced in the shifted rows model. Figure 12 shows a sketch of a possible model associated with the reconstruction of platinum. Here the shifted atoms form rows of a finite length (14 atoms long) instead of the infinite length rows of iridium. Similar dislocations can also produce the various other observed unit cells.

The length of 14 for the shifted rows could be explained by a contraction or expansion of the atomic size by a factor $1/14$; then each shifted row would contain 15 or 13 atoms, respectively. This would permit a smooth transition at the ends of each shifted row. It would also remove the criticism raised for Au(100) that all split parts of a spot should have a similar energy dependence since we no longer have a simple domain structure.

A suitable model for the Au(100)_c(26×68) reconstruction involves dislocations in two directions instead of one for platinum. Figure 12 shows a sketch of a possible structure. In one of the directions the type of defect is similar to that of platinum (finite chains of 14 shifted atoms), but platinum shows no defects in the other direction. For Au(100) there is a different interaction between chains and there appears a stacking fault of chains after every 34 chains. In Figure 12, we have represented the models with three unshifted rows followed by two shifted ones, corresponding to Fig. 11c. A similar model can be built with the structures shown in Figs. 11d and 11e.

This model for Au(100) explains the difference in the nature of the spot splittings. On the one hand, the doublet formation many authors have observed and which gives rise to the designation (20×5) is associated with the first type of defect (finite length of shifted rows), while the V-shaped triplet formation which few experiments show^{27,28} is associated with the second type of defect, such as interaction between chains. This second type requires a much better ordering of the surface since first the chains have to be formed and then ordered.

Such dislocations are very common in three dimensions with polytype crystals, and it would not be surprising if a similar effect could exist at surfaces. In the preceding section we proposed a model of this type for the Au(111) reconstruction as well.

An argument against the shifted row models is the HEIS observation that about one full monolayer is shifted out of alignment with chains of substrate atoms for Pt(100), Au(100), and Au(111).

iv) The Charge-Density Wave (CDW) Model

Several clean surface reconstructions have been described as charge density waves (CDW's), including W(100)_c(2×2)¹⁷ for which a LEED analysis gives a structure consistent with a CDW, Mo(100),¹⁷ Si(111)(7×7),¹⁸ and 1T-TaS₂(0001)¹⁹ with various superstructures, among them ($\sqrt{13}\times\sqrt{13}$). In a CDW⁵¹ atoms are displaced from their ideal position in a wavelike pattern by no more than about 0.1 Å. A (1×5) structure on fcc(100) can be obtained with a CDW that has a wavelength 5a (a=bulk bond length) and direction parallel to rows of

close-packed atoms, such as [011]. The $\begin{pmatrix} 14 & 1 \\ -1 & 5 \end{pmatrix}$, $c(26 \times 68)$ and similar structures can be obtained with pairs of CDW's of different wave vectors. The Au(111) structure can also be interpreted as a long wavelength CDW.

Many other surface models in addition to those discussed here can be imagined which will fit the (1×5) and other observed unit cells (missing rows, additional rows above the surface, etc.) but none that we considered seemed intuitively more plausible than the models described above.

F. LASER SIMULATION

Laser simulation of LEED patterns has been frequently used in the past to test various types of surface structure models, especially when large unit cells, domain structures, or disorder are involved. The basis of this technique is described by Ellis.⁵³ Fedak et al.,⁵⁴ have applied this technique to the reconstruction of Au(100), supporting their conclusion of a hexagonal top-layer model with some modulation. Laser diffraction was also used in a recent study of the Pt(100) reconstruction.²⁵ We have used this approach to study many more models for these reconstructions than has been done previously.

Our implementation of laser simulation is quite simple. The surface atoms are represented by arrays of dots (usually small dots for the first substrate layer and large dots for the top layer), computer drawn directly onto microfiche or 35 mm film with a basic lattice constant of typically 30 μm . This produces convenient diffraction spot separations on a screen a few meters away and an overall size comparable to the laser beam diameter of about 1 mm. Since the coherence

length across the laser beam is about equal to its diameter, we effectively simulate a LEED beam coherence length of about 100\AA , a realistic result. For simplicity we have not attempted to include different domain orientations simultaneously since one domain orientation is sufficient for the purposes of the following discussion. Atomic displacements perpendicular to the surface (such as in a layer buckling) are simulated by dot displacements of proportional magnitude parallel to the plane of the film.

We now consider what laser diffraction can teach us concerning the surface models proposed in Section E in relation to the observed LEED patterns for the reconstructed Ir, Pt and Au(100) surfaces. For convenience, we shall term the integral-order spots (those present without reconstruction) substrate spots, while those due to a hexagonal array by itself are called hexagonal spots, even though the hexagon may be somewhat distorted.

i) Ir(100)

Starting with the simple nonbuckled (1×5) structure of the hexagonal model (cf. Figs. 6 and 9), we find that only the substrate and hexagonal spots have strong intensity in laser diffraction, as seen in Fig. 13c. To obtain an intensity in the other extra spots comparable to the intensity of the substrate and hexagonal spots, as required by the experimental observation for Ir, it is necessary to include a modulation of the top-layer atomic positions in the 5-fold direction. This suggests that the real Ir(100) (1×5) surface also has such a modulation. The obvious choice is a buckling perpendicular to the surface already described in Section E. Laser simulation leads to

the same conclusion for the Pt and Au structures based on the hexagonal model; a buckling is also likely there. Note that with such buckling the extra spots are already present in the kinematic limit; multiple scattering is not required to produce them.

We find that laser diffraction puts few limitations on the missing row and shifted rows models for the (1×5) structure. Some typical patterns are shown in Figs. 13b and 13c. However, the charge-density-wave model does not produce adequate intensity in the extra spots, cf. Fig. 13e.

ii) Pt(100) and Au(100)

Concerning the $\begin{pmatrix} 14 & 1 \\ -1 & 5 \end{pmatrix}$, c(26×68) and similar surface structures, the simple hexagonal model produces realistic laser diffraction patterns, but it is necessary, in order to obtain sufficient intensity in the split spots away from the (1×5) spot positions, to include a modulation of atomic positions in the 14-fold and 26-fold directions, respectively. This comes in addition to the modulation needed in the 5-fold direction. The effect is seen in Figs. 13g and 13h. As above, this may be indicative of buckling. Buckling would be reasonable in this direction as well, since different atoms would have different registries as a result of the contraction of the layer by factors of 1/14 and 1/26, respectively. Sufficient intensity in the split spots for Pt(100) may also be obtained by the spread-out dislocation model of Fig. 10, which includes not only a possible buckling, but also a position modulation parallel to the surface. It is interesting to observe what happens as the dislocation becomes more localized; more

and more spots appear which extend from one row of 1/5th order spot positions to the next, cf. Fig. 13. If the dislocation were of the domain boundary type, all these additional spots would disappear again. Thus patterns very similar to those of Figs. 13g and 13h could also be produced (not shown) with the dislocation model of the shifted rows structure (Fig. 12).

The Au(100)c(26×68) unit cell is so large that it was not possible to perform the laser diffraction satisfactorily in this case. However, by approximating the structure with a (20×5) unit cell, we obtain with the hexagonal model the same effects due to position modulations as with the Ir and Pt structures shown in Figs. 13j and 13k. The V shape of the diffraction multiplet observed in LEED could also be produced (not shown) with suitably reduced unit cells. This is possible with both the hexagonal and the shifted-rows models.

iii) Au(111)

In Fig. 13 we show a laser diffraction pattern for Au(111)($\sqrt{3}\times 22$) rect, modeled in Fig. 8, without position modulations. Inclusion of such modulations would multiply the number of split-off spots, reproducing the appearance of Fig. 7. A charge-density-wave structure for Au(111)($\sqrt{3}\times 22$) rect would also be capable of producing the observed diffraction pattern, especially if a few higher harmonics of the basic periodicity are included.

iv) Conclusions

We reach the following conclusions based on laser simulation. The hexagonal model is realistic and probably requires buckling or a similar position modulation. The missing row and shifted rows models

are also compatible with the LEED patterns. However, no abrupt dislocations other than domain boundaries should occur as one moves in the direction perpendicular to the 5-fold direction. Also the charge-density wave model can be ruled out for the (100) reconstructions.

G. SUMMARY

In this part we have brought together and analyzed the various observed reconstructions of the Ir(100), Pt(100), Au(100) and Au(111) surfaces. Ir(100) shows a simple (1×5) structure (no spot splittings) indicating a relatively small unit cell. Pt(100) exhibits a variety of patterns, including $\begin{pmatrix} 14 & 1 \\ -1 & 5 \end{pmatrix}$, $\begin{pmatrix} 14 & 1 \\ 0 & 5 \end{pmatrix}$, $\begin{pmatrix} 12 & 1 \\ -3 & 5 \end{pmatrix}$ and $\begin{pmatrix} 27 & 2 \\ -3 & 6 \end{pmatrix}$, some of which occur on stepped Pt(100) surfaces. According to high quality diffraction patterns Au(100) has a c(26×68) reconstruction which, in lower quality patterns, appears approximately as a (20×5) structure. On stepped Au(100) surfaces a $\begin{pmatrix} 14 & 1 \\ -1 & 5 \end{pmatrix}$ structure has also been observed. Au(111) reconstructs with a rectangular ($\sqrt{3}$ ×22) unit cell.

This part also describes the measurement of LEED intensities for Ir(100) and Pt(100). These are to be used in a detailed structural analysis with dynamical calculations (see part 2); but first we interpret the LEED patterns in terms of possible structural models and do a laser simulation to test those models and some of their parameters. The hexagonal top-layer model can explain all observed diffraction patterns with varying contractions and rotations of the top layer. The laser simulation indicates that this model probably requires a buckling perpendicular to the surface. The missing row hexagonal model and the

shifted row models cannot be ruled out by laser diffraction, but have to include suitable domain structures to explain the more complicated LEED patterns. Models based on charge density waves can be ruled out, however, for the (100) faces.

Acknowledgments

We are thankful to Drs. D. M. Zehner and J. F. Wendelken for kindly providing us with photographs of Au(100) and (111) diffraction patterns.

References for Chapter IV, Part 1

1. J. T. Grant, Surface Sci. 18 (1969) 228.
2. S. Hagstrom, H. B. Lyon and G. A. Somorjai, Phys. Rev. Lett. 15 (1965) 491.
3. D. G. Fedak and N. A. Gjostein, Phys. Rev. Lett. 16 (1966) 171.
4. P. W. Davies and R. M. Lambert, subm. to Surface Sci.
5. G. Gewinner, J. C. Peruchetti, A. Jaegle, and R. Riedinger, Phys. Rev. Lett. 43 (1979) 935.
6. T. E. Felter, R. A. Barker and P. J. Estrup, Phys. Rev. Lett. 38 (1977) 1138.
7. K. Yonehara and L. D. Schmidt, Surface Sci. 25 (1971) 238.
8. K. Christmann and G. Ertl. Z. Naturforsch. 28a (1973) 1144.
9. H. P. Bonzel and R. Ku, Surface Sci. 33 (1972) 91.
10. D. G. Fedak and N. A. Gjostein, Acta Met. 15 (1967) 827.
11. J. Perdereau, J. P. Biberian and G. E. Rhead, J. Phys. F4 (1974) 798.
12. P. J. Estrup and J. Anderson, J. Chem. Phys. 45 (1966) 2254.
13. a) C. A. Haque and H. E. Farnsworth, Surface Sci. 1 (1964) 378.
b) J. E. Demuth, J. of Colloid and Interface Sci. 58 (1977) 184.
14. R. A. Barker, P. J. Estrup, F. Jona and P. M. Marcus, Sol. St. Comm. 25 (1978) 375.
15. C.-M. Chan, M. A. Van Hove, W. H. Weinberg and E. D. Williams, Sol. St. Comm. 30 (1979) 47.
16. W. Moritz and D. Wolf, Surface Sci. 88 (1979) L29.
17. a) J. E. Inglesfield, J. Phys. C11 (1978) L69.
b) E. Tosatti, Sol. St. Comm. 25 (1978) 637.

18. E. Tosatti and P. W. Anderson, Jpn. J. Appl. Phys. Suppl. 2, Pt. 2 (1974) 381.
19. B. J. Mrstik, R. Kaplan, T. L. Reinecke, M. Van Hove and S. Y. Tong, Il Nuovo Cimento 38B (1977) 387; the notation 1T specifies a particular layer stacking of this layer compound.
20. A. M. Mattera, R. M. Goodman and G. A. Somorjai, Surface Sci. 7 (1967) 26.
21. D. G. Fedak and N. A. Gjostein, Surface Sci. 8 (1967) 77.
22. P. W. Palmberg, in The Structure and Chemistry of Solid Surfaces, ed. G. A. Somorjai, John Wiley & Sons, Inc., New York, 1969, p. 29-1.
23. P. C. Stair, PhD. Thesis, University of California, Berkeley, 1977.
24. D. W. Blakely, PhD. Thesis, University of California, Berkeley, 1976.
25. K. Heinz, P. Heilmann, and K. Muller, Z. Naturforsch., 32a (1977) 28.
26. P. R. Norton, private communication.
27. J. F. Wendelken and D. M. Zehner, Surface Sci. 71 (1979) 178.
28. D. M. Zehner, private communication.
29. H. Melle and E. Menzel, Z. Naturforsch. 33a (1978) 282.
30. P. R. Norton, J. A. Davies, D. P. Jackson and N. Matsunami, Surface Sci. 85 (1979) 269.
31. D. M. Zehner, B. R. Appleton, T. S. Noggle, J. W. Miller, J. H. Barrett, L. H. Jenkins and O. E. Schow III, J. Vac. Sci. Technol. 12 (1975) 454.

32. J. Koppers and H. Michel, *Appl. Surface Sci.* 3 (1979) 179.
33. P. Heimann, J. Hermanson, H. Miosga, and H. Neddermeyer, *Phys. Rev. Lett.* 43 (1979) 1757.
34. E. W. Muller and T. T. Tsong, Field Ion Microscopy, American Elsevier Publ. Co., New York, 1969.
35. A. J. Melmed, R. T. Tung, W. R. Graham and G. D. W. Smith, *Phys. Rev. Lett.* 43 (1979) 1521.
36. T. N. Rhodin and G. Broden, *Surface Sci.* 60 (1976) 466.
37. H. P. Bonzel, C. R. Helms and S. Kelemen, *Phys. Rev. Lett.* 35 (1975) 1237.
38. A. Ignatiev, A. V. Jones, and T. N. Rhodin, *Surface Sci.* 30 (1972) 573.
39. P. Heilmann, K. Heinz, and K. Muller, *Surface Sci.* 83 (1979) 487.
40. R. Feder, *Surface Sci.* 68 (1977) 229.
41. K. Tagi, K. Takayanagi, K. Kobayashi, N. Osakabe, Y. Tanashiro and G. Honjo, *Proc. 9th Intern'l. Congr. on Electron Microscopy*, Toronto, 1978, J. M. Sturgess, ed., Vol. I, p. 458.
42. a) W. L. Winterbottom, in Surfaces and Interfaces, J. J. Burke et al., eds. Syracuse Univ. Press, Syracuse, New York, 1967.
b) C. Herring, in Structure and Properties of Solid Surfaces, R. Gomer and C. S. Smith, eds. Univ. of Chicago Press, Chicago, 1972.
43. T. N. Rhodin, P. W. Palmberg and E. W. Plummer, in Structure and Chemistry of Solid Surfaces, ed. G. A. Somorjai, John Wiley & Son, Inc., New York, 1969.

44. See, for example: a) P. W. Palmberg and T. N. Rhodin, J. Chem. Phys. 49 (1972) 134; and A. J. Henrion and G. E. Rhead, Surface Sci. 29 (1972) 20.
45. a) M. A. Van Hove and S. Y. Tong, Surface Crystallography by LEED, Springer-Verlag, Heidelberg, 1979.
b) G. A. Somorjai and M. A. Van Hove, in Adsorbed Monolayers on Solid Surfaces, Structure and Bonding, Vol. 38 (1979) 1.
46. C. G. Shaw, S. C. Fain, Jr., and M. D. Chinn, Phys. Rev. Lett. 41 (1978) 955.
47. A. D. Novaco and J. P. McTague, Phys. Rev. Lett. 38 (1977) 1286.
48. J. J. Burton and G. Jura, in Structure and Chemistry of Solid Surfaces, Ed. G. A. Somorjai, John Wiley & Sons, Inc., New York, 1969.
49. J. P. Biberian, to be published.
50. J. W. A. Sachtler, private communication.
51. C. Annett, W. R. Lawrence and R. E. Allen, Phys. Rev. B10 (1974) 4184.
52. J. A. Wilson, F. J. DiSalvo and S. Mahajan, Adv. in Phys. 24 (1975) 117.
53. W. P. Ellis, in Optical Transforms, H. S. Lipton, ed., Academic Press, New York, 1972.
54. D. G. Fedak, T. E. Fischer and W. D. Robertson, J. Appl. Phys. 39 (1968) 5658.

Figure Captions for Chapter IV, Part 1

- Fig. 1. LEED patterns for clean reconstructed Ir(100).
- Fig. 2. LEED patterns for clean reconstructed Pt(100). Four domains are present in (a); only two domains are present in (b).
- Fig. 3. Unit cells and schematic LEED patterns for different reconstructions of Ir and Pt(100). Dot size is roughly proportional to average spot intensity. Triangular dots represent "hexagonal spots" due to a hexagonal layer.
- Fig. 4. LEED patterns for clean reconstructed Au(100). (Courtesy of J. F. Wendelken and D. M. Zehner).
- Fig. 5. Schematic LEED pattern for clean reconstructed Au(100), with unit cell in reciprocal space. Conventions as in Fig. 3.
- Fig. 6. Hexagonal models for Ir(100)(1×5) and Pt(100) $\begin{pmatrix} 14 & 1 \\ -1 & 5 \end{pmatrix}$ reconstructions. Top layer atoms are shown as thick circles, next layer as thin circles. The two-bridge registry is assumed.
- Fig. 7. LEED diffraction patterns for clean reconstructed Au(111). (Courtesy of J. F. Wendelken and D. M. Zehner).
- Fig. 8. Hexagonal model for Au(111) ($\sqrt{3}\times 22$) rect reconstruction. Conventions as in Fig. 6.
- Fig. 9. Detail of hexagonal model for Ir(100)(1×5) with two registries. Side views, parallel to the surface, are shown at top, exhibiting full buckling. Views from the top are shown at bottom. Thick circles represent atoms closer to the viewer than thin circles.

Fig. 10. Hexagonal-layer dislocation model for Pt(100) $\begin{pmatrix} 14 & 1 \\ -3 & 5 \end{pmatrix}$ compared to Ir(100)(1×5) model shown in (a). (b) gradual dislocation, (c) abrupt dislocation.

Fig. 11. Five models in top view for the reconstruction of Ir(100)(1×5). (a) hexagonal model with two-bridge registry, (b) hexagonal model with center/top registry, (c) shifted rows model with 5-atom clusters, (d) as (c) with 4-atom clusters, and (e) as (c) with 3-atom clusters.

Fig. 12. Sketched domain structure of the shifted rows model for Pt(100) $\begin{pmatrix} 14 & 1 \\ -1 & 5 \end{pmatrix}$ and $\begin{pmatrix} 14 & 1 \\ 0 & 5 \end{pmatrix}$ (left) and for Au(100)c(26×68) (right) assuming clusters. Only the top layer is shown. Unshifted rows of atoms are represented by continuous line segments; shifted rows (possibly contracted or expanded) are represented by dashed lines.

Fig. 13. Laser diffraction patterns for various models of the (100) reconstructions of Ir (a-f), Pt (g-i), and Au (j,k) and of the (111) reconstruction of Au(l) (only one domain is included in each pattern). Substrate spots are sometimes weak in these patterns.

(a,b) Ir(100)(1×5) hexagonal model, (a) without and (b) with a position modulation in the 5-fold direction.

(c) Ir(100)(1×5) hexagonal model with missing rows.

(d) Ir(100)(1×5) shifted rows model (3-atom) clusters.

(e,f) Ir(100)(1×5) charge density wave model with 0.1Å and 0.4Å amplitudes, respectively.

(g,h) Pt(100) $\begin{pmatrix} 14 & 1 \\ -1 & 5 \end{pmatrix}$ hexagonal model with one (g) or two (h) sine-wave position modulations in the 14-fold direction. A modulation in the 5-fold direction is included in both cases.

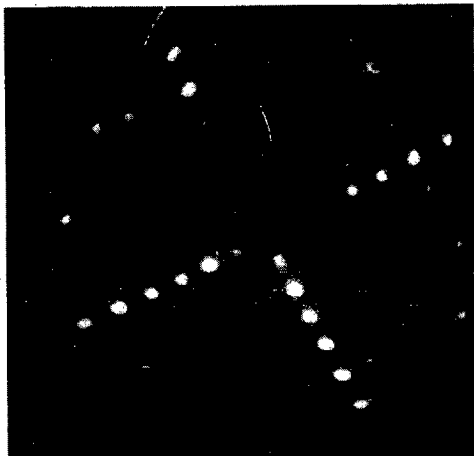
(i) Pt(100) $\begin{pmatrix} 14 & 1 \\ -3 & 5 \end{pmatrix}$ hexagonal model with abrupt dislocations as in Fig. 10.

(j,k) Au(100)(20×5) hexagonal models (j) without and (k) with (k) position modulations in both the 5-fold and 20-fold directions. Pattern (k) is very similar to low resolution LEED patterns. (l) Au(111)($\sqrt{3}\times 22$) rect hexagonal model without position modulation.

IR (100) - 5x1

$\theta = 0, \phi = 0$

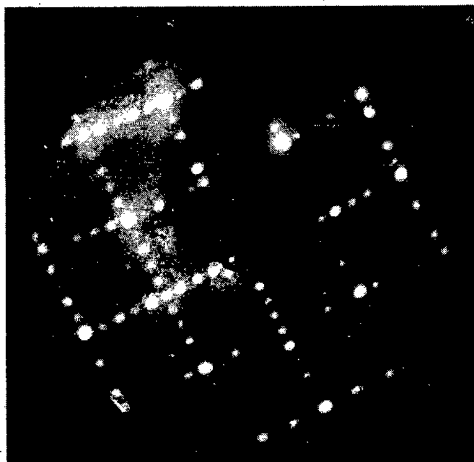
T = 300 K



48 eV



100 eV



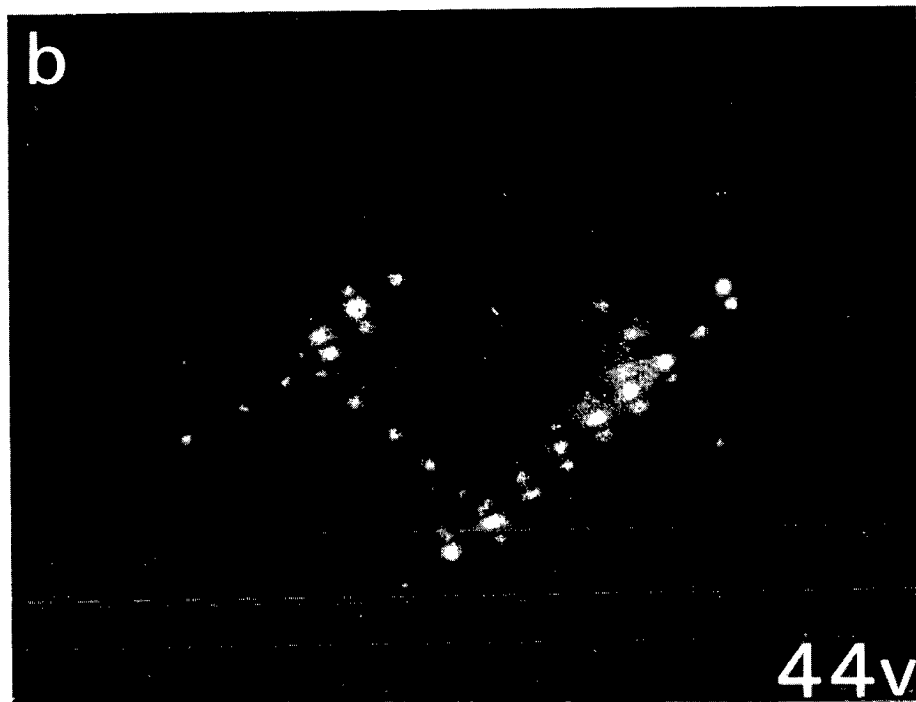
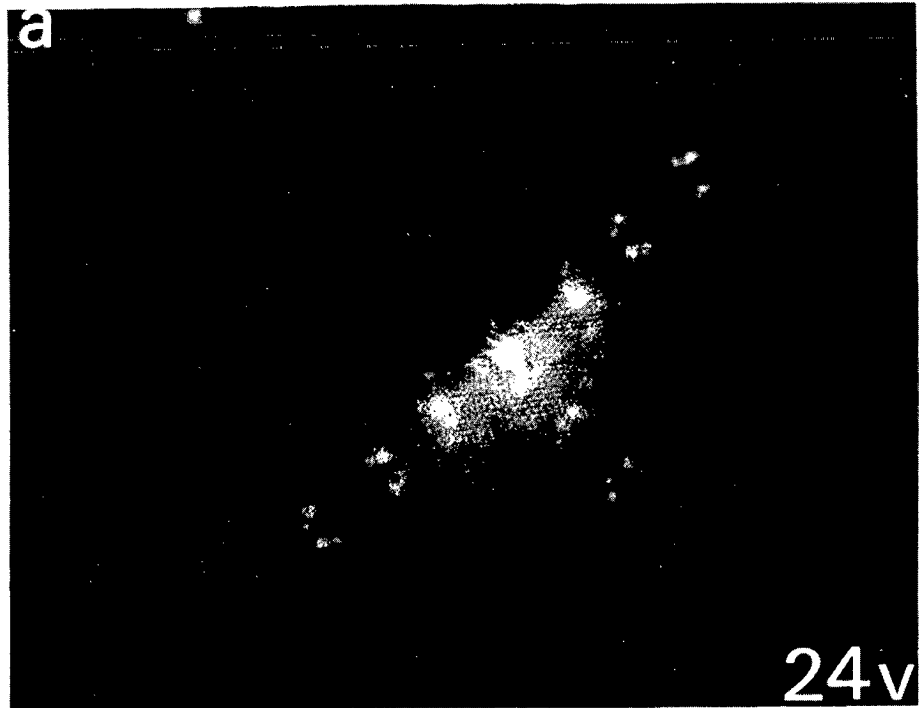
175 eV



XBB 790-16403

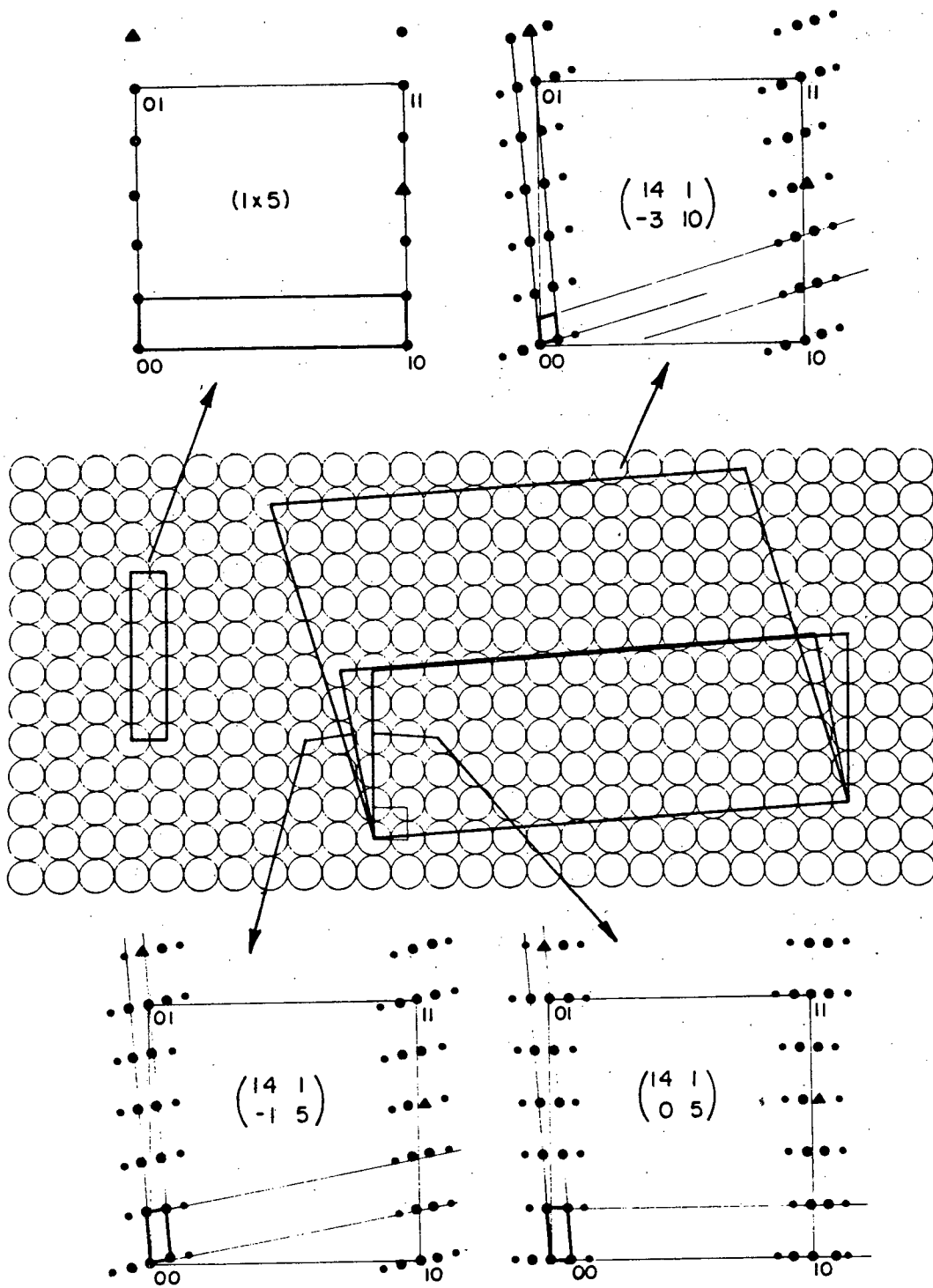
273 eV

Fig. 1



XBB 774-2914

Fig. 2



XBL 7911-14542

Fig. 3

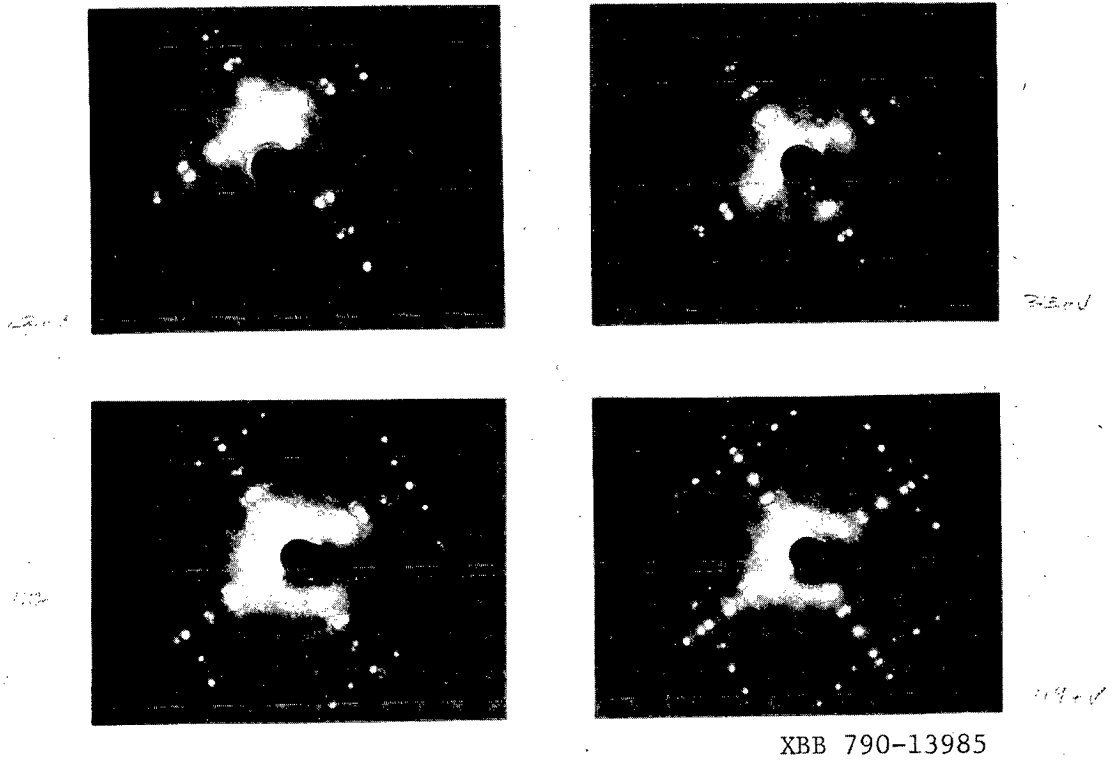
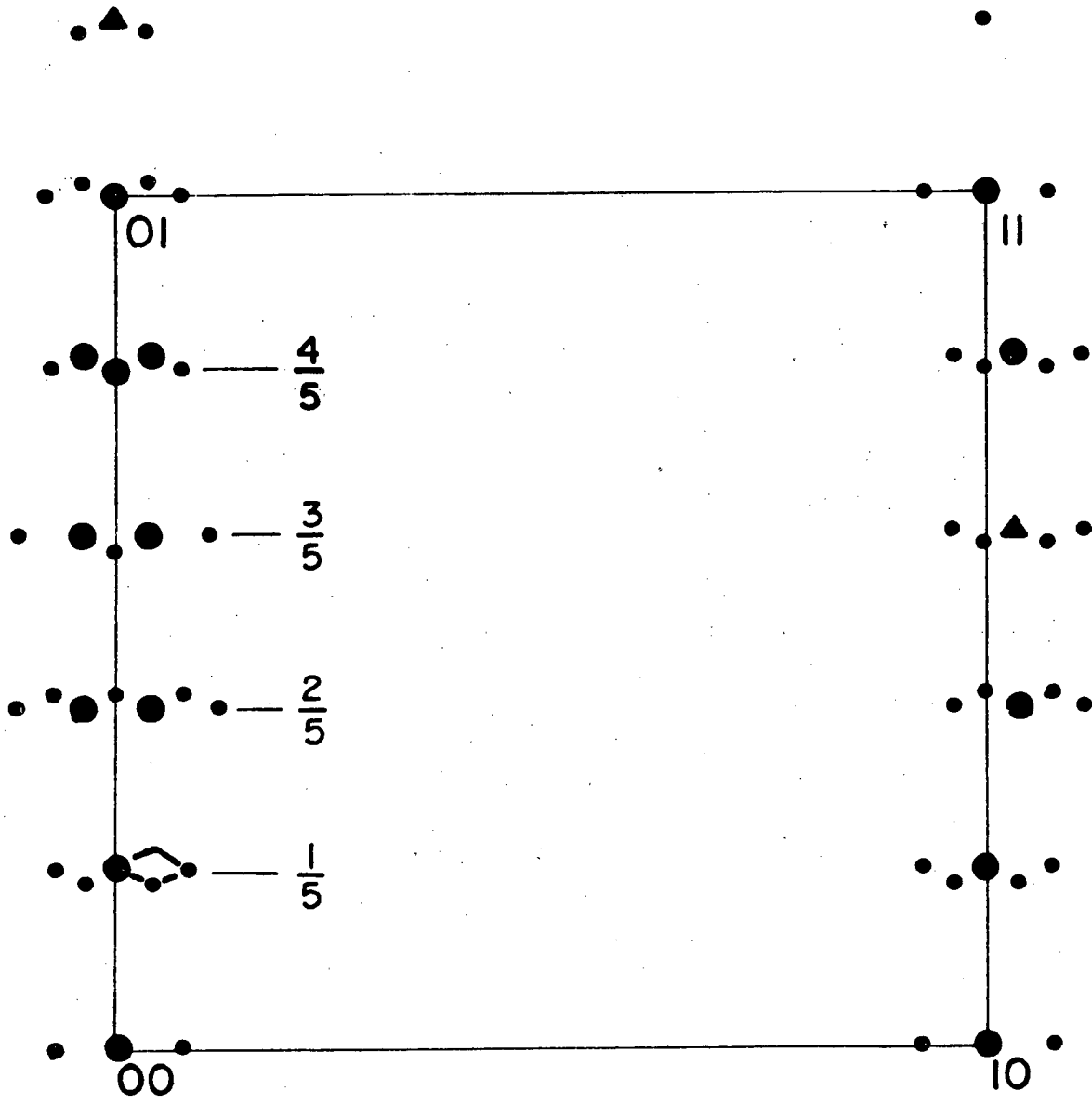


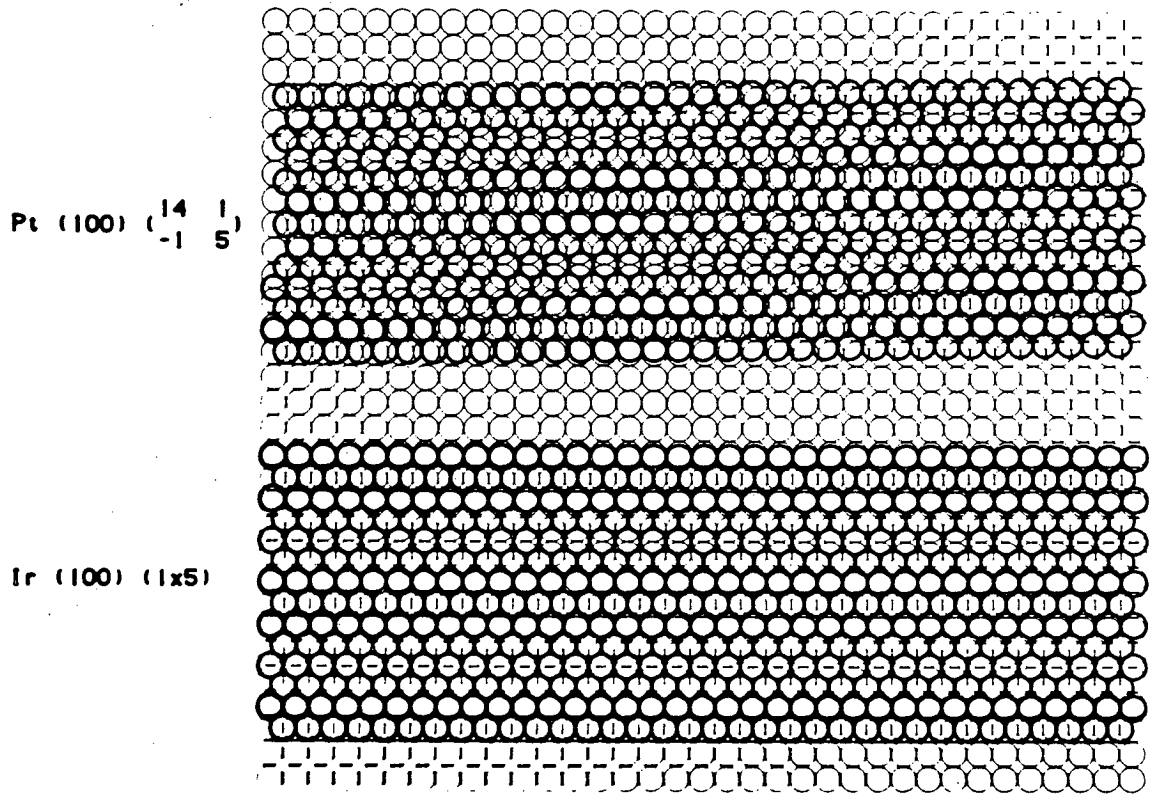
Fig. 4



Au (100) c (26x68)

XBL 7911-14543

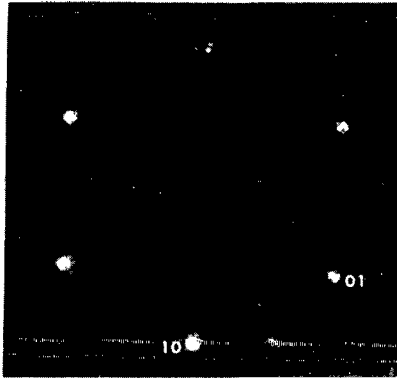
Fig. 5



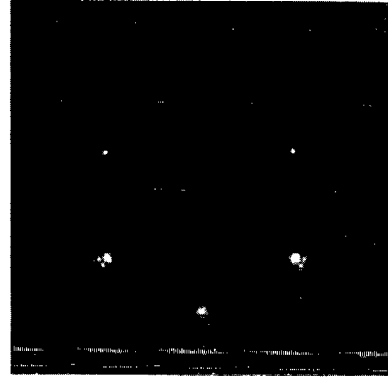
XBL 7912-13736

Fig. 6

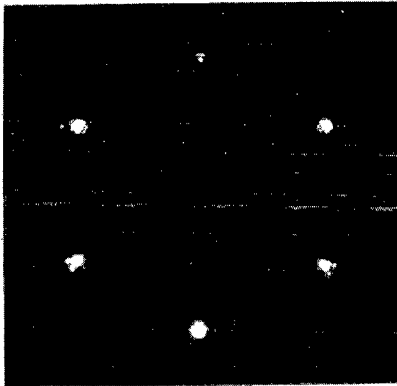
Au(111)



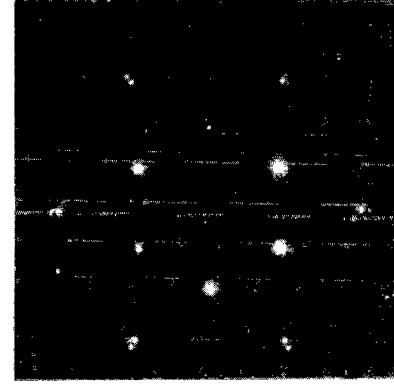
46V



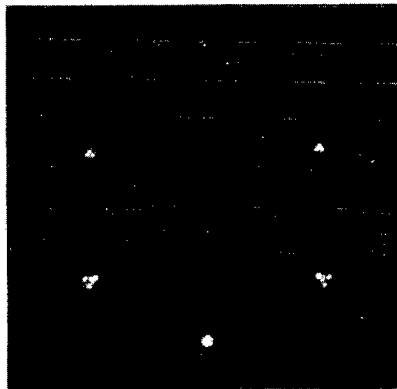
80V



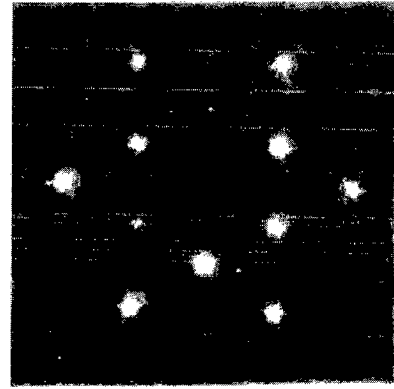
54V



133V



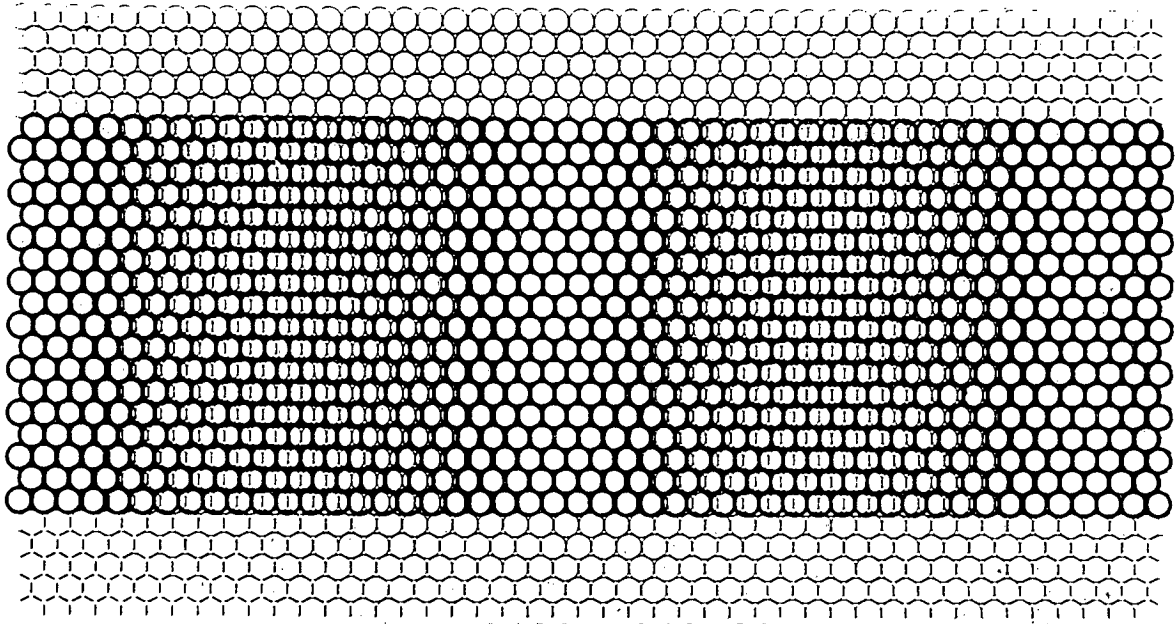
64V



145V

XBB 790-13988

Fig. 7



Au (111)(R3x22)rect

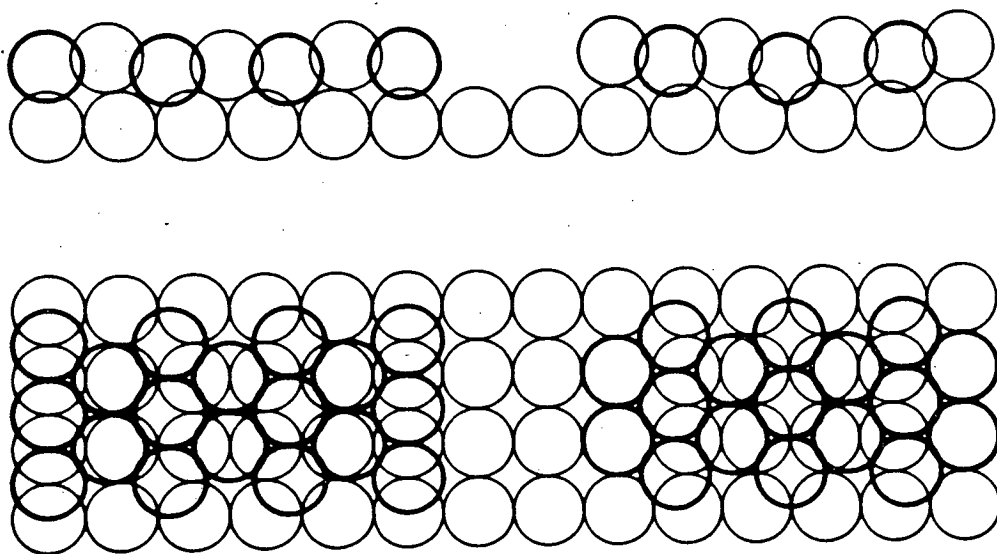
XBL 7912-13738

Fig. 8

fcc (100) : buckled hexagonal top layer

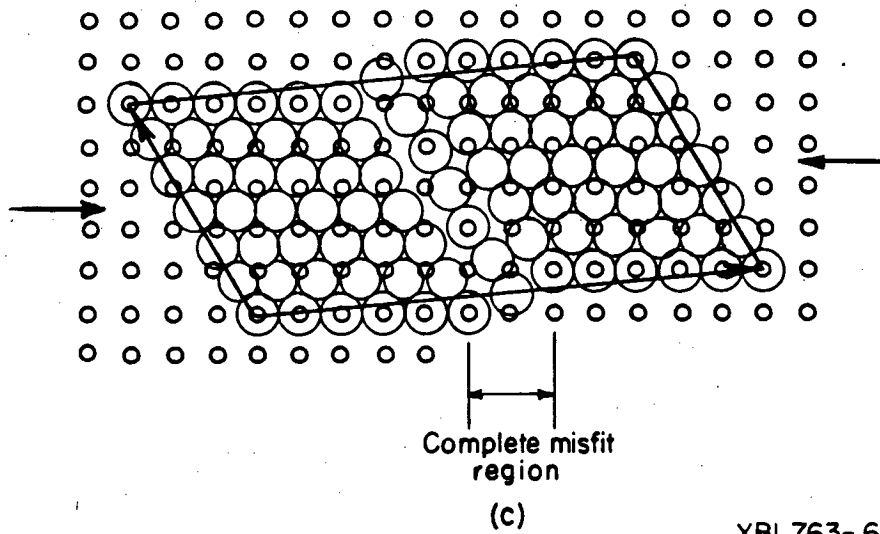
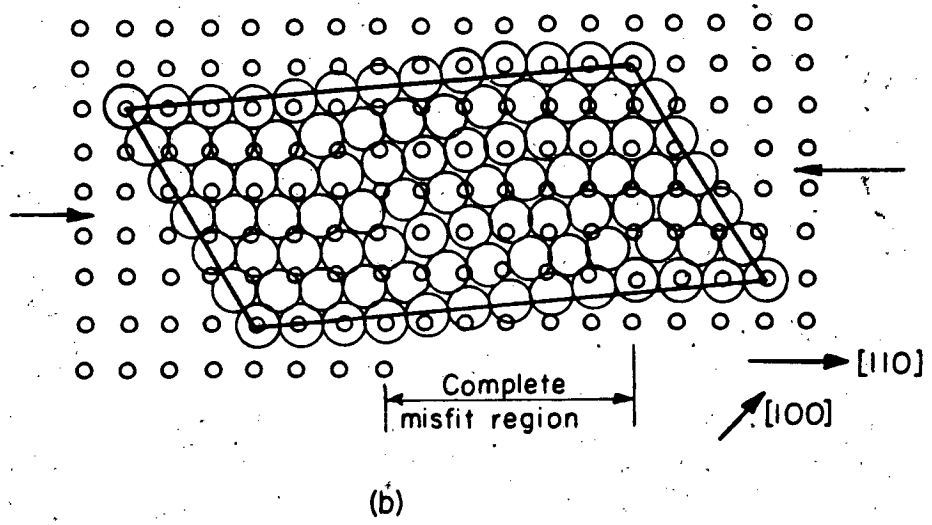
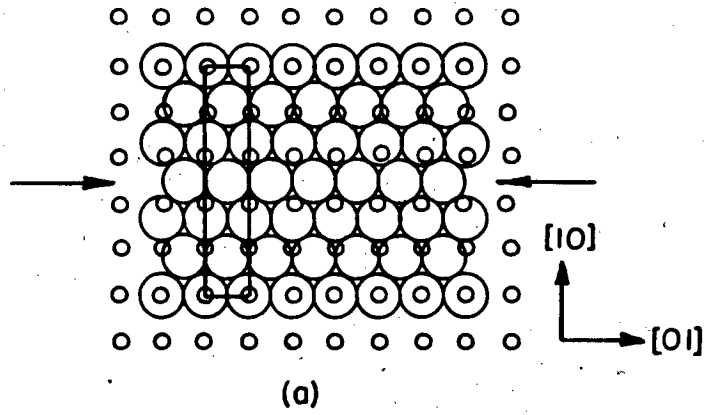
two-bridge

top/center



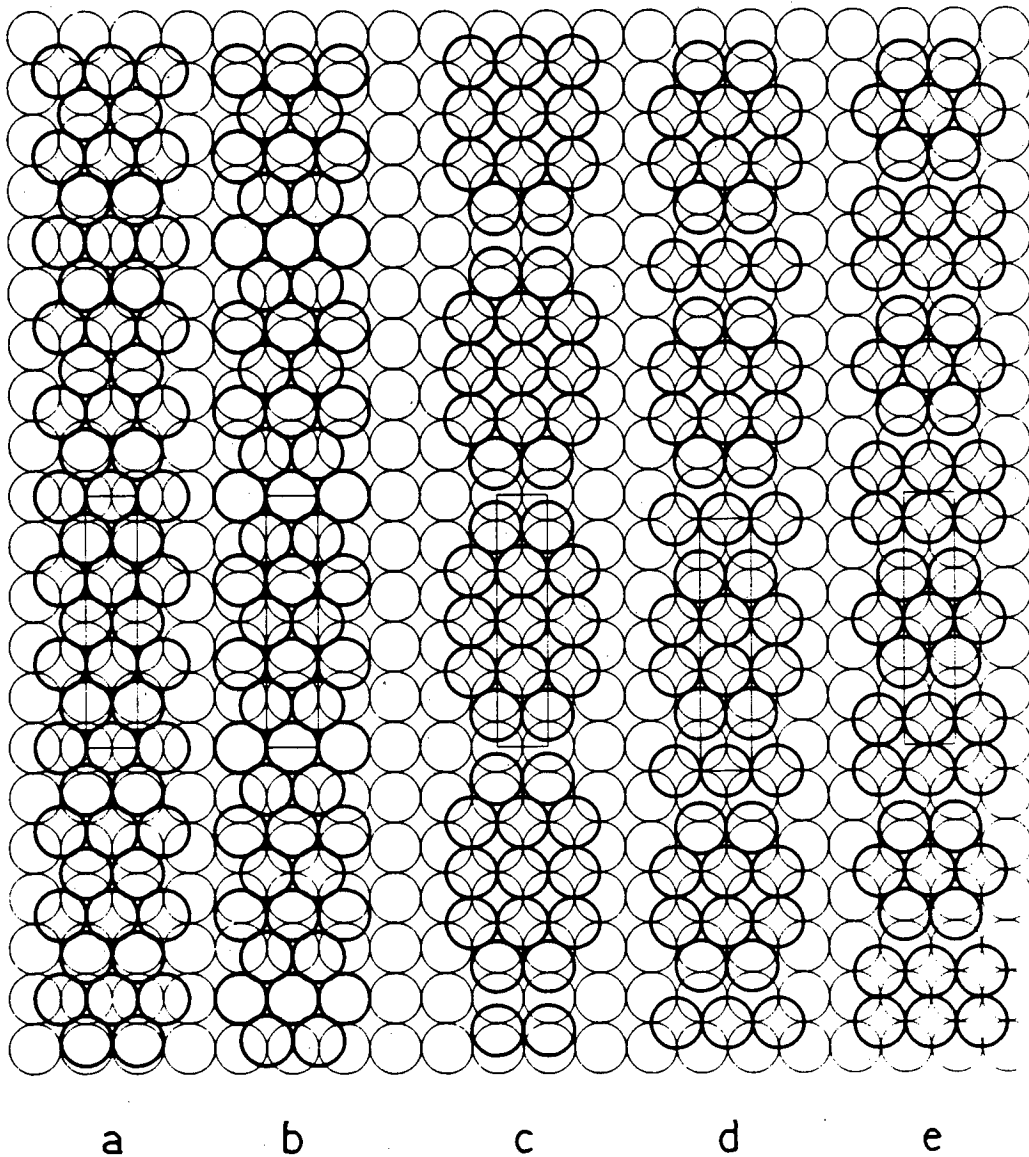
XBL 7912-13739

Fig. 9



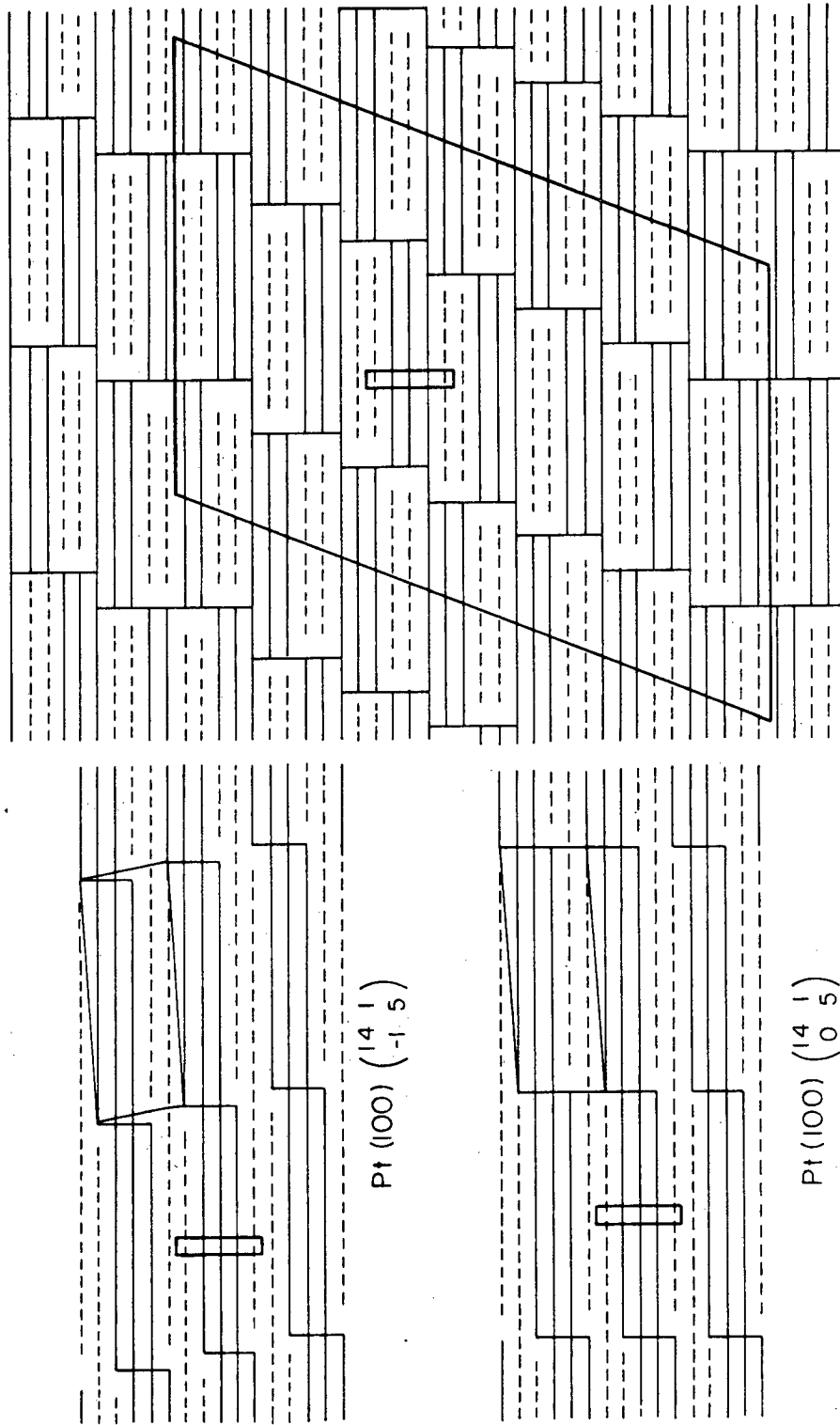
XBL763- 6631

Fig. 10



XBL 7912-13737

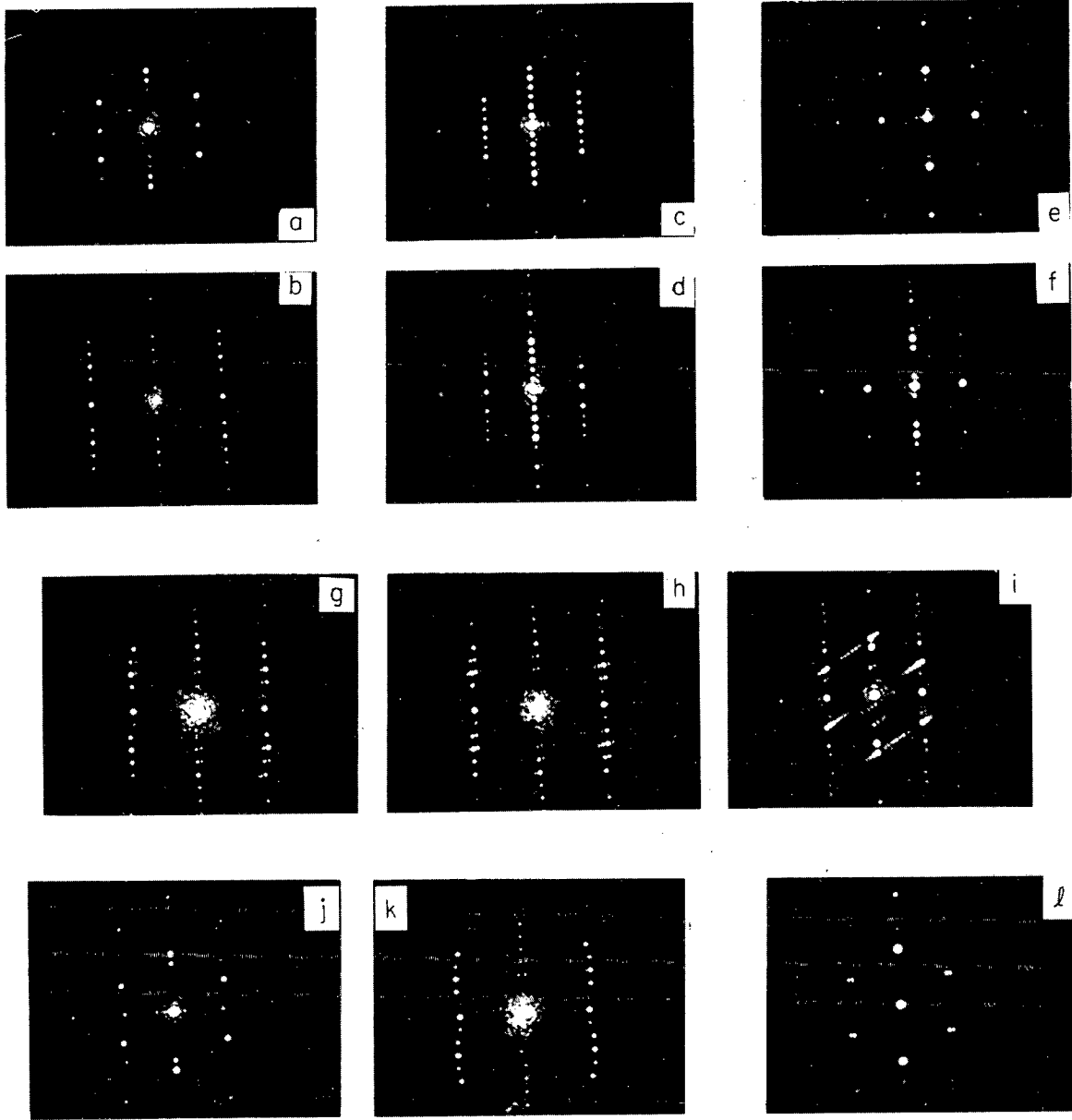
Fig. 11



$\text{Au (100) } c(26 \times 68)$

XBL80I-4535

Fig. 12



XBB 790-16402

Fig. 13

PART 2: STRUCTURE DETERMINATION OF THE Ir AND Pt(100) FACES

A. INTRODUCTION

In part 1, we analyzed the experimental information contained in the two-dimensional diffraction patterns of reconstructed Ir(100), Pt(100), Au(100) and Au(111). That analysis, together with the measurement of LEED intensity data for Ir(100)(1×5) and Pt(100) $\begin{pmatrix} 14 & 1 \\ -1 & 5 \end{pmatrix}$, prepared the way for a detailed structural investigation of these surfaces, which is described in this part of Chapter IV. The structural investigation is based on the analysis of measured LEED intensities with dynamical (multiple scattering) calculations.

Since Ir(100) has the surface reconstruction with the smallest unit cell and thereby is the most economical case for LEED calculations, we concentrate our efforts on this surface, analyzing many of the structures discussed in part 1. We also make calculations with a few structures for the Pt(100) $\begin{pmatrix} 14 & 1 \\ -1 & 5 \end{pmatrix}$ surface, using suitable approximations with minor consequences) to deal with the very large unit cell. The results will be discussed in terms of the mechanism of reconstruction and a comparison with other surface structures will be given.

B. DYNAMICAL LEED THEORY

i) Methods Used

The large unit cells of the models to be analyzed by dynamical LEED calculations present special computational problems for the existing theories. First, many beams occur, giving rise to high-dimensional

interlayer diffraction matrices. Second, many atoms fit in the unit cell, giving rise to high-dimensional intralayer multiple scattering matrices. We adopt the "combined space method,"¹ in which the spherical wave representation is used within each layer. The top reconstructed layer counts as one layer containing 5 or 6 atoms in the unit cell.

The plane wave representation is used between these layers. The Renormalized Forward Scattering (RFS) method² is used for the interlayer wave propagation. The intralayer multiple scattering is treated by the Matrix Inversion method^{1,2} for the strongly scattering platinum and by the Reverse Scattering Perturbation (RSP) method¹ for the less strongly scattering iridium (no calculations were made for gold). That iridium behaves relatively kinematically in LEED has been noticed before,³ but we have no explanation for it. Both RSP and RFS are allowed to converge to essentially the exact result and therefore involve the neglect of no important scattering events.

ii) Physical Parameters

The iridium atomic potential employed here, due to Arbman and Hoernfelt,⁴ has been used before in studies of Ir(111)³ and Ir(110)⁵ (the latter either reconstructed or overlayer-covered). The agreement between theory and experiment was often not as good as with many other metals, and this difficulty is thought to stem partly from the use of an inadequate potential: therefore we expect a corresponding measure of disagreement in the present case. A modification of this potential by Feder⁶ to include relativistic spin effects has also been applied in this work, but does not produce a noticeable improvement (as was already the case for Ir(110)(1×2)⁵). The platinum potential⁷

has also been used previously, namely in studies of Pt(111)⁸ and unreconstructed Pt(100).⁹ This potential appears to be better than the iridium potential, but is again not as good as in the case of a number of other metals. In this work, a relativistic spin correction to the potential is tried as well,⁶ with the same inconclusive result as for iridium. (The same result was also found in a study of Pt(111).^{8b})

The number of phase shifts used in our calculations is mostly 6 ($l_{\max} = 5$) for an energy range up to 120 eV for iridium and 100 eV for platinum. (Some platinum calculations were made with 5 phase shifts, but for platinum 5 phase shifts are not sufficient at the higher energies). The real part V_{OR} of the inner potential (muffin-tin constant) is set to 15 eV for iridium and 14.3 eV for platinum, based on results of previous work, and allowed to be fit a posteriori to experiment by shifting the zero point of energy. The imaginary part of the potential is set to a constant 5 eV for iridium and 4 eV for platinum and Debye temperatures of 236K and 193K, respectively, are used for all layers. These temperatures are reduced from bulk values to allow for enhanced atomic vibrations at the surface.

iii) Geometrical Aspects

Many of the (1×5) models discussed and illustrated in Section E of part 1 have structures with a pair of orthogonal mirror planes, e.g., the hexagonal models with two-bridge registry and with top/center registry (c.f. Fig. 9 of part 1), the missing row hexagonal model, the shifted row models (c.f. Fig. 11 of part 1) and the charge-density-wave model with an appropriate phase of the deformation wave. This symmetry

is then exploited at normal incidence in our calculations to considerably reduce the computational effort.¹ For the same reason, off-normal incidence calculations are performed for incidence directions retaining one mirror plane.

Among the large-unit-cell models, we chose to test the hexagonal model for the Pt(100) $\begin{pmatrix} 14 & 1 \\ -1 & 5 \end{pmatrix}$ structure since it is based on the most popular suggestion for the reconstruction. For this purpose it is necessary to make some simplifications since the top layer contains about 88 atoms in the unit cell and the number of beams is 71 times as large as with the unreconstructed surface. As one sees in Fig. 6 of part 1, the $\begin{pmatrix} 14 & 1 \\ -1 & 5 \end{pmatrix}$ unit cell can be regarded as being composed of 14 successive (1×5) units. The diffraction by the entire $\begin{pmatrix} 14 & 1 \\ -1 & 5 \end{pmatrix}$ unit cell is then simply the sum of the interfering diffraction amplitudes from each of those 14 (1×5) units. In the case of the abrupt dislocation model of the hexagonal top layer (cf. Fig. 10 of part 1) most of the 14 (1×5) units are identical with only a few different ones near the dislocations. This can then be simulated by a relatively simple (1×5) structure identical to that for Ir(100)(1×5) (thereby ignoring the effect of the few different (1×5) units containing the dislocation) and therefore an identical calculation is sufficient. We refer to the discussion below about the question of the correspondence of spots between the Ir and Pt structures.

On the other hand, in the rotated-hexagonal-layer model, each of the (1×5) units is slightly different from its immediate neighbors. The

difference is a small shift (of about 1/14th of the bond length, i.e., about 0.2Å) in the registry of the top layer. Since electron multiple scattering is not particularly sensitive to small geometric changes more than a few bond lengths away (because of damping) it should be adequate to assume that the diffraction by any one of these 14 (1×5) units is equal to the diffraction by a complete surface with this particular (1×5) unit as the repetitive unit cell. Therefore, we may simulate the overall diffraction by the sum of interfering beam amplitudes obtained from a series of relatively simple (1×5) structured surfaces, each with a slightly different registry of the top layer. Of course, different registries imply different bucklings perpendicular to the surface, and this is included in the calculation. Because of symmetry and structural-sensitivity considerations, it was found that four different registries would reasonably sample the 14 different registries of the (1×5) units. This small number of four comes about because all 14 registries, when mapped in a single (1×5) unit cell, correspond to a cumulative shift by only about half a bond length. By symmetry, one half of the registries are identical to the other half, leaving a total relevant shift of about a quarter bond length, i.e., about 0.7Å. Four equidistant registries are then separated by $0.7/4 < 0.2\text{Å}$ which is a lateral shift that LEED does not strongly detect near normal incidence.

To keep the computational effort within acceptable limits, a further slight simplification has to be made. The top layer registry has to satisfy a mirror plane symmetry (with the mirror plane being parallel to the 14-fold direction). This restriction induces an error

in atomic positions of at most about 0.1\AA and so is thought not to affect the result too much.

Finally, it must be realized that with these simplifications one effectively calculates the intensities of beams in the 1/5th order positions rather than of the multiplets of beams actually observed [cf. the differences between the Ir(100)(1 \times 5) and the Pt(100) $\begin{pmatrix} 14 & 1 \\ -1 & 5 \end{pmatrix}$ patterns]. However, it was found experimentally that the different components of these multiplets have very similar IV-curves, implying that the error in using either of these components or a hypothetical 1/5th order beam should be small. The error is mainly due to the small difference of at most a few degrees between the emission angles of the multiplet components. (This difference is less influential than when the crystal sample is tilted by such angles, since in our present case the incidence direction is not changed at all.)

We do not carry out an R-factor analysis to compare theoretical and experimental LEED IV-curves. There are two reasons for this. First, the photographic technique produces IV-curves that in this case have relatively large gaps with no intensity measurements being made over certain energy ranges of weak intensities. No presently available R-factor treats such gaps in a fair manner and, in any case, such gaps could induce serious spurious effects in the R-factor when the inner potential is varied. Second, the experimental curves have not been smoothed, so that any R-factors using derivatives (i.e., most presently

used R-factors) become useless. Thus it would be difficult to compare R-factor values from this work with those in other work. However, an R-factor analysis was carried out recently on a larger set of intensity data for the Ir(100)(1x5) structure collected by Lang et al.³⁶

C. RESULTS

The surface structures that have been tried with dynamical LEED calculations are listed and detailed in Table 1. In this table, the registry of a hexagonal layer ("two-bridge" or "center/top") is designated as in Section E of part 1. The rotated hexagonal layer for Pt(100) can be "anchored" at the bridge sites or at the center/top sites, and these sites are then chosen to designate the registry of the complete layer. The buckling of a hexagonal layer is described as either "full buckling" or "2/3 buckling" or "1/2 buckling," the non-buckled case being called "planar." Full buckling is obtained by at first assuming bulk bond lengths between the top and the next layers and then allowing the top layer to rigidly shift up and down normal to the surface, so that the buckling is not made dependent on this shift. For 2/3 and 1/2 buckling the fully-buckled top layer is contracted uniformly to 2/3 or 1/2 of its thickness, respectively. (Thickness is defined as the maximum distance between nuclear planes of the buckled layer.) The atoms in the planar hexagonal layer are assumed equally contracted parallel to the surface. In the buckled geometries the interatomic distances parallel to the surface are not changed from those in the planar case, although some small ($< 0.1\text{\AA}$) differences might occur in reality because of the different perpendicular displacements of the various atoms above the next unreconstructed layer. A test of the

effect of relaxing this assumption was made with the somewhat extreme "uneven contraction" model, in which the contraction is confined to one atom in the (1×5) unit cell, while the other atoms have diameters equal to their bulk value.

The reconstructed top layer has a "d-spacing" to the next unreconstructed layer. In the (1×5) structures this spacing is defined as the smallest of the distances between each nuclear plane of the top layer and the nuclear plane of the square-net second layer. This definition of spacing applies not only to hexagonal layers, but also to the shifted-rows and charge-density-wave (CDW) models. In the $\begin{pmatrix} 14 & 1 \\ -1 & 5 \end{pmatrix}$ calculations using a series of different registries, the d-spacing is referred to the distance D, which is the distance one would obtain by assuming bulk bond lengths between top-and-next-layer atoms. In the shifted-rows models, the shifted atoms are given bulk bond lengths to their neighbors, assuming positions as shown in Fig. 11 of part 1, and then the entire 5-atom-per-unit-cell top layer is allowed to rigidly shift up and down. In the CDW model the wave-like atomic deviations are either in the direction perpendicular to the surface or "angled." In the latter case, deviations parallel to the surface (in the 5-fold direction) are chosen, but the atoms are allowed to displace at an angle over the underlying atoms, so as to conserve bond lengths, again followed by rigid shifts up and down.

The phase shifts used are described as AH for Arbman-Hoernfelt,⁴ AHF for the same with correction by Feder,⁶ A for Andersen⁷ and AF for those with a correction by Feder.⁶

The search procedure through the plausible structures was as follows. The Ir(100)(1×5) surface was extensively studied since it has a relatively simple diffraction pattern and less multiple scattering than Pt (cf. Section B), making any results more reliable and more economical to achieve. The largest number of calculations were performed at normal incidence ($\theta = 0^\circ$) to benefit from higher symmetry, using 7 independent beams in the comparison with experiment. Two off-normal angles of incidence ($\theta = 10^\circ$ and $\theta = 20^\circ$) were chosen to further check the hexagonal model, using 13 and 14 independent beams, respectively. This structure was also chosen in the Pt(100) $\begin{pmatrix} 14 & 1 \\ -1 & 5 \end{pmatrix}$ analysis, in which various calculations were performed to independently test some of the geometrical variables.

Before the discussion of the comparison between theoretical and experimental IV-curves, it should be remembered that the quality of agreement between theory and experiment is not expected to be as good as for some other structural determinations. In addition to the usual uncertainties of experiment and theory, the atomic potentials appear to be of somewhat poorer quality, and for Pt(100), various small approximations have had to be introduced (cf. Section B). Also, many more structural parameters could, in principle, be optimized than we have done (For example, with 6 atoms in the unit cell there are 18 unknown position parameters, not counting possible distortions of the underlying atoms of the substrate.)

i) The Reconstructed Ir(100) Surface

A selection of calculated IV-curves for Ir(100)(1×5) are compared with experiment in Figs. 1-4. This selection exhibits the level of agreement between experiment and calculation as well as various trends with varying parameters. Lack of space prohibits the inclusion of enough figures to provide a basis for selection of the optimum geometry.

In examining all calculated IV-curves, it emerges in case of the hexagonal model of Ir(100)(1×5) the theory and experiment clearly agree best if the two-bridge registry rather than the center/top registry is assumed (cf. Fig. 9 of part 1). Furthermore, a 1/2 or 2/3 buckling appears best, with a d-spacing of $2.2 \pm 0.1 \text{ \AA}$. So the bridge-positioned surface atoms have essentially the bulk bond length to the next-layer atoms and the reduced buckling implies that those atoms sticking out above the bridged ones are drawn in somewhat toward the bulk, smoothing the surface. As a consequence, the most protruding atoms have bond length contractions of 6 or 9%, depending on whether one chooses 2/3 or 1/2 buckling. The average contraction of the backbond lengths are then 3 or 4%, respectively, with an uncertainty of $\pm 0.1 \text{ \AA}$ in determining the d-spacing. (The backbonds are the bonds between atoms in the first and second layers.) A more recent LEED analysis³⁶ using a larger data base confirms the hexagonal model, but it gives a fully buckled top layer with a slightly larger interlayer contraction of 5% with a d-spacing of $2.0 \pm 0.1 \text{ \AA}$. The Zanazzi-Jona R-factor for this geometry is 0.34 and the Pendry R-factor is 0.45.

The off-normal incidence calculations for the hexagonal model (see Table 1) are found to slightly favor a d-spacing of 2.0-2.1 \AA over other

D. DISCUSSION

i) Summary of Results

We first summarize the results presented in the preceding Section. For Ir(100)(1×5) the hexagonal model with two-bridge registry (cf. Fig. 9 of part 1, left) with 2/3 or 1/2 buckling and a d-spacing of 2.2 ± 0.1 Å is the favored structure. However, a more extensive LEED analysis³⁶ of normal incidence intensity curves obtained from the Ir(100)(1×5) structure gives a two-bridge hexagonal model with full buckling and a d-spacing of 2.0 ± 0.1 Å. For Pt (100) $\begin{pmatrix} 14 & 1 \\ -1 & 5 \end{pmatrix}$ the hexagonal model described above with a rotation of about 0.7° gives reasonable agreement with experiment, cf. Fig. 6 of part 1. The shifted-rows model was not tested for Pt and no calculations were performed for the reconstructed Au(100) surface.

The reconstructions of Ir, Pt and Au(100), as well as Au(111), can all be rationalized with the simple idea of a hexagonal top layer (see Section D of part 1). The diffraction patterns can be understood with appropriate choices of the lattice parameters and of the orientation of the hexagonal layers.

ii) Other Reconstructions

At this point it is of interest to mention other metal surface reconstructions. On the cooled clean W(100) crystal face a c(2×2) pattern is observed. The IV-curves from this surface structure have

been analyzed,¹⁰ showing that zigzag chains of W surface atoms probably form by slight displacements from the ideal positions. This structure can be understood in terms of a charge density wave.¹¹ The cooled clean Mo(100) surface exhibits a split $c(2 \times 2)$ pattern¹² that may have a similar structure as W(100) $c(2 \times 2)$ and then also can be interpreted as being due to a charge density wave.

The clean Ir(110) and Au(110) surfaces have (1×2) structures. These have been determined^{5,13} to probably consist of alternately missing rows, producing a microfaceted structure, each microfacet having the close-packed atomic arrangement of a (111) face. This result is an argument in favor of a hexagonally close-packed top layer for Ir, Pt and Au (100). Furthermore, relatively large backbond length contractions of about 3% occur in this case. Pt(110) also can exhibit a (1×2) structure, but several attempts at determining this structure have not yet led to conclusive results.

Finally, clean Au (111) has a reconstruction¹⁴ that may consist of a 4.55% uniaxially contracted top hexagonal layer (although a charge-density-wave structure is also possible), as discussed in Section D of part 1.

iii) Bond Lengths

It appears that bond length changes are an important aspect of the reconstructions. In the hexagonal models of reconstruction, we find that bond lengths in the Ir, Pt and Au exhibit contractions within the

hexagonal layer of 1%, 3% and 4.2%, respectively. (These numbers are averages over different directions parallel to the surface and take the buckling into account). Backbonds are reduced by, on the average, 3.5% and 6.3%, respectively for Ir and Pt, while the more recent Ir(100)(1x5) structure determination³⁶ indicates a 5% backbond contraction. Such values are compatible with bond length contractions observed at other, mostly unreconstructed, metal surfaces,¹ which range from 0 to 4%. However, so far contractions were only clearly observed on the less-densely-packed surfaces, such as fcc (110), fcc(311), bcc(100) and bcc (111). Diatomic molecules show rather larger contractions, such as 14% for Au₂ and 13% for Cu₂ as compared with bulk Au and Cu lengths, respectively.¹⁵

Bond length contractions have also been observed in small clusters of metal atoms. Platinum clusters of diameters 12Å and 20Å (containing about 60 and 280 atoms, respectively) have Pt-Pt bond length reductions of 7% and 5%, respectively.¹⁶ Slightly larger clusters have less contraction: 0.5% for 38Å -diameter Pt clusters,¹⁷ 0.3% for 35Å-diameter Au clusters,¹⁸ 0.6% for 40Å-diameter Ag clusters¹⁹ and 0±0.1% for clusters of Cu with diameter of 38Å and more.¹⁷ Note that platinum and gold clusters contract significantly, but not the copper clusters. This fits the pattern of surface reconstructions on Pt and Au surfaces and their absence on Cu surfaces. However, silver appears to behave more like platinum and gold in clusters, unlike the behavior at surfaces, where silver does not reconstruct. As is well known,²⁰ bond lengths increase monotonically with the number of nearest neighbors, i.e. the coordination number, and thus a contraction is indeed expected

for surface atoms. In Fig. 6 we show the bond length contractions observed at surfaces¹ assuming a value of 0% for many fcc(100), fcc(111) and bcc(110) surfaces, since most results for these surfaces give the bulk value within the uncertainty of the LEED method. We shall discuss these in more detail below.

It is interesting to add observations made during epitaxy of overlayers of one metal on substrates of another. A simple monolayer of Au or Ag deposited on Cu(100) produces different superstructures,¹⁵ despite virtually identical bulk Au and Ag bond lengths. These structures can both be interpreted as hexagonal overlayers, but then the Au layer requires a 3.3% larger uniaxial contraction than does the Ag layer. Thus Au has a greater tendency to bond length reduction than Ag. In another comparison, we start with the fact that the bulk Au lattice constant is about 4.3% larger than that of Pt. A monolayer of Pt deposited on Au(100) produces a square-lattice Pt layer about 5% smaller than the (by now unreconstructed) Au(100) substrate lattice,²¹ showing a small contraction of this Pt monolayer by about 1%. On the other hand, a Au monolayer deposited on Pt(100) produces a square lattice with the Pt lattice constant²¹ indicating a 4.3% contraction of the Au-Au distance. Thus Au can contract also more than Pt when deposited by epitaxy, in agreement with the findings discussed above for the reconstructions of clean Pt and Au surfaces of (100) and (111) orientations (ignoring backbond lengths, which we cannot compare).

Note, among the above results, the formation of contracted square-lattice overlayers, also observed for Au on Pd(100).¹⁵ It

appears that hexagonal layers are not the universal form of reconstruction even in the case of misfits, but we cannot assess whether these square-lattice overlayers are possibly only metastable phases that could transform to more stable hexagonal (or other) overlayers. Note also the dependence of the overlayer contractions on the substrate lattice constant. There is an interplay between the substrate lattice and the overlayer that, for a given adsorbate species, produces overlayer lattices different both in symmetry (square vs. hexagonal) and in size, depending on the particular substrate.²²

Clearly then the Ir, Pt and Au(100) reconstructions involve bond length contractions and this may be the very reason for the reconstructions. Frank and van der Merwe²³ have proposed a theory of the competition between pseudomorphism (crystal growth with the substrate's lattice) and independent-lattice growth. This theory predicts that for typical metals up to a 9% difference in lattice constants can be accommodated by strain for one monolayer deposited on a substrate and that only a smaller difference can be accommodated for multilayers. This behavior is observed for some of the above-mentioned cases, such as for the pseudomorphism of a monolayer of Au on Pd(100) or on Pt(100), but apparently not for other cases, such as for the 5% smaller monolayer of Pt on Au(100) or for the clean reconstructed Pt(100) and Au(100) structures, although the actual surface lattice constants in these examples differ by less than 9%.

iv) Mechanisms of Reconstruction

Bond length contractions are not necessarily the only mechanism for reconstruction that is operative for the (100) crystal faces of Ir, Pt,

and Au (as noted in Ref. 15). It appears that other effects such as rehybridization of bonding orbitals may play an important role as well. In this respect, Palmberg and Rhodin¹⁵ already pointed out the unusual electronic characteristics of Pt and Au (and predicted, before its observation that Ir might have a similar reconstruction²⁴). For Pt and Au, there is a relatively small activation energy between the atomic ground state and a state in which a 5d electron is promoted to a 6s or 6p orbital. Thus a reconstruction may induce a sufficient gain in energy to offset that small promotion energy. Such a mechanism is often invoked to explain bulk phase transformations²⁵ and may very well operate in the present case as well. But it must be pointed out that the electronic properties of Cu are not very different from those of Au in this respect, and Cu(100) is not known to reconstruct. Furthermore, an investigation of the known difference in cohesive energy for different bulk phases of various elements,²⁶ either experimentally measured or theoretically calculated for non-existing phases, shows that from the point of view of phase transformations Pt and especially Au are in fact unlikely to reconstruct. Au has one of the largest differences in cohesive energy of all metals between bulk phases.¹ Furthermore, V, Cr, Mo and W, all of which exhibit surface reconstructions, also have relatively large differences in cohesive energies between different bulk phases.

v) Layer Rotation

The question of a rotation of hexagonal top layer in the Pt(100) reconstruction is of particular interest. An analogous rotation by a small angle has been observed for a close-packed layer of Ar whose

lattice almost, but not quite, fits into a $(\sqrt{3}\times\sqrt{3})$ R30° structure on a graphite basal plane.²⁷ Moreover, such a possibility had been predicted theoretically.²⁸ Although this situation of physisorption cannot be directly compared with the metal-on-metal case, there is no immediately obvious reason why an orientational reordering might not also take place in the latter case.

The analogy between the Ir, Pt and Au(100) surface reconstructions and the reconstructions on bcc surfaces (Cr, Mo, W) seems tenuous. The Cr, Mo, and W(100) surface reconstructions may be due to charge density waves, which from our calculations are a very unlikely cause for the Ir, Pt and Au(100) surface reconstructions.

vi) Correlations with Material Constants

One may explore the possibility that the observed bond length contractions at Ir, Pt and Au surfaces, as well as the tendency of these surfaces to reconstruct, correlate with any other physical properties of these metals. Obvious quantities to consider are those describing the stiffness of the lattice such as the Debye temperature, the melting point, the cohesion energy and elastic constants. First, a clear trend is found in the bond length contractions themselves (see Fig. 6). The bond length contractions tend to increase markedly (only identical crystallographic surface orientations must be compared), as one goes to the right in the Periodic Table among the fcc metals, for which the most data are available. These bond length contractions also correlate well with the mechanical softness of the elements. Figure 6 includes the compressibility χ as an example; χ also increases towards the right in the Periodic Table among the fcc metals. On the other hand, although

the 5d metals exhibit larger bond length contractions than 4d or 3d metals, their compressibility is not smaller; W and Ir are well known to be hard materials. In fact, it is interesting to note that throughout the Periodic Table (Fig. 6) the compressibility tends to be locally minimized near metals that reconstruct.

Among various other materials constants and constants and combinations thereof, we have only found a clear-cut trend for the ratio of bulk Debye temperature to melting point. This ratio is unusually small for those metals that reconstruct. Since, on the one hand, a low Debye temperature is related to weak restoring forces of vibrating atomic cores (where the mass is concentrated), while, on the other hand, a high melting point is related to strong chemical bonds, this unusual combination may be pictured as a relatively free vibration of the atomic cores within a set of bonding orbitals that are more rigidly held in place by the neighboring atoms. In more conventional terms, this would correspond to a relatively high polarizability of the 5d metal atoms, coupled with strong bonding. A related point of view is that of the soft-phonon theory of reconstructions. Abnormally low phonon frequencies (which we tentatively relate here to lower Debye temperatures) are taken as a sign of propensity to reconstruction.

vii) Reconstructions and Adsorbates

We now consider the effect of adsorbates on the reconstructions of Ir(100) and Pt(100) crystal surfaces, since this may be relevant to the mechanism of reconstruction. Little work has been done in this respect on Au(100) surfaces partly because few atoms or molecules adsorb on that chemically inert surface near 300 K. The experimental evidence is

summarized in Table 2 for Ir(100) and Table 3 for Pt(100), where the resulting unit cell is indicated upon adsorption on either the clean unreconstructed surface or the clean reconstructed surface.

Because the reconstructions are rather sensitive to impurities and methods of preparation, some caution is required in interpreting the observations. One must also allow for molecular decomposition on the surface. A large molecule that decomposes can affect the surface structure through its fragments while the intact molecule may not have an effect.

Some trends are clearly discernible in Tables 2 and 3. The Ir(100) surface reconstruction seems to be more resistant to adsorbates than the Pt(100) surface reconstruction. This probably is attributable to electronic effects rather than geometric effects, since it is not clear how the small geometric differences between the reconstructions could be responsible for this difference in structural resistance to adsorbates.

Another trend is that the reconstruction is more resistant to adsorbates at lower temperatures. This is not surprising, given the fact that the reconstruction can be removed merely by heating the clean surface to a sufficiently high temperature, as described in Section B of part 1. Also the adsorbate bonding may change its character and could become stronger with increasing temperature.

It appears that molecules that easily dissociate also destroy the reconstruction more easily. This often may be due to individual carbon and oxygen atoms in the fragments strongly bonded to the metal surface. If the molecules do not dissociate, direct carbon bonding may still be involved in destroying the reconstruction. Namely, if carbon-carbon double or triple bonds in unsaturated molecules reduce their bond order

by one (or two), the carbon atoms can bind strongly to the substrate and affect its structure. This empirical rule is seen to be followed in Table 3. However, the presence of methyl groups ($-\text{CH}_3$) seems to often inhibit the effect on the substrate, perhaps by sterically keeping the multiple C-C bonds away from the metal atoms.

An interesting parallel appears in the effect of hydrogen on small platinum clusters. As mentioned before, these clusters (of 12-20 Å diameter) contract by 7-5% when "clean" (in fact helium-covered). When these clusters are covered with hydrogen rather than helium, the contraction virtually disappears.⁷ Such a bond length increase (although smaller, namely of the order of 1-2%) has also been detected on hydrogen adsorption on the Pt(111) surface, both by LEED³¹ and by High Energy Ion Scattering.³²

viii) Prospects For Finding Other Metal Surface Reconstructions

Finally, let us consider which other metals besides those mentioned here might exhibit clean-surface reconstructions. Since many 5d metals have small ratios of Debye temperature to melting point, one might expect, for example, rhenium and osmium to reconstruct, even though their bulk has the hcp structure. Since several bcc(100) surfaces reconstruct it would be useful to investigate for example Nb(100) and Fe(100) at low temperature. (They do not reconstruct at room temperature.^{33, 34}) Metals which have bulk phase transitions might reconstruct at their surfaces. Mn, Co and Tc are good candidates (but the surface of Co(111) and Co(0001) are known to have their respective bulk structure³⁵ at room temperature and above). One may also expect non-close-packed surfaces to reconstruct more easily than close-packed

surfaces, since W(110), Ir(111) and Pt(111) apparently do not reconstruct, while W(100), Ir(100), Ir(110), Pt(100) and Pt(110) do.

E. SUMMARY

Our structural analysis of the clean reconstructed Ir and Pt(100) surfaces indicates that a close-packed hexagonal top monolayer can explain each of the observed reconstructions. For Ir and Pt, the preferred model for the hexagonal top layer has the "two-bridge" registry, 1/2 or 2/3 of full buckling and average contractions of backbonds (i.e., bonds between atoms in the first and second layers) of $3.5\pm 3\%$ and 6.3% , respectively (cf. Fig. 9 of part 1). Recently a LEED analysis³⁶ of the Ir(100)(1 \times 5) structure using a larger set of normal intensity curves confirms the hexagonal model, but indicates full buckling in the top layer and a shorter d-spacing of 2.0 ± 0.1 Å (that corresponds to a 5% backbond length reduction.) The Zanazzi-Jona and Pendry R-factors (0.34 and 0.45) for this structure are very reasonable. Bond length contractions parallel to the surface are on the average about 1% for Ir, 3% for Pt and 4.2% for Au (cf. Fig. 6 of part 1). The hexagonal layer has close-packed rows of atoms aligned with a (110) direction for Ir and Au, but rotated by about 0.7° for Pt. (The figures for Pt apply to the $\begin{pmatrix} 14 & 1 \\ -1 & 5 \end{pmatrix}$ structure; slightly different values would apply for the closely-related $\begin{pmatrix} 14 & 1 \\ 0 & 5 \end{pmatrix}$, $\begin{pmatrix} 14 & 1 \\ -3 & 10 \end{pmatrix}$ and other structures.)

Thus the most likely reconstructions of Ir, Pt and Au(100) involve the formation of contracted and sometimes rotated hexagonal monolayers with a surface density of atoms increased by 20%, 23.7% and 27.7%, respectively, relative to a bulk (100) layer. The reason for this reconstruction might be a reduced bond length between surface atoms, which induces too much strain in the unreconstructed geometry. It may also be due to a decreased surface energy as a result of the closer packing.

We find a correlation of the occurrence of surface reconstructions in several 5d metals with a relatively small bulk compressibility and with a relatively small ratio of Debye temperature to melting point for the 5d metals. Thus a connection with the soft-phonon theory of reconstruction may exist. It also follows that other 5d metals, such as Ta, Re and Os, may exhibit surface reconstructions. Bcc(100) surfaces may also reconstruct in general at low temperatures, as well as metals with bulk phase transitions.

It is not clear that other experiments with the existing surface analytical techniques, other than LEED, will be able to more closely determine the reconstruction geometries of Ir, Pt and Au(100). But in the near future, Low-Energy Ion Scattering Spectroscopy and Atomic Diffraction may be able to quantitatively determine the roughness (buckling) of the topmost atomic layer and thereby further support our hexagonal model. Also, Atomic Resolution Electron Microscopy may soon be able to provide further information about the relative atomic locations at surfaces.

References for Chapter IV, Part 2

1. M. A. Van Hove and S. Y. Tong, Surface Crystallography by LEED, Springer-Verlag, Heidelberg, 1979.
2. J. B. Pendry, Low Energy Electron Diffraction, Academic Press, London, 1974.
3. C.-M. Chan, S. L. Cunningham, M. A. Van Hove, W. H. Weinberg, and S. P. Withrow, *Surface Sci.* 66 (1977) 394.
4. G. O. Arman and S. Hoernfelt, *J. Phys.* F2 (1972) 1033.
5. C.-M. Chan, M. A. Van Hove, W. H. Weinberg and E. D. William, *Sol. St. Comm.* 30 (1979) 47; *Surface Sci.* 91 (1980) 440.
6. R. Feder, private communication.
7. O. K. Anderson, *Phys. Rev.* B2 (1970) 883.
8. a) L. L. Kesmodel and G. A. Somorjai, *Phys. Rev.* B11 (1975) 630; *Surface Sci. Lett.* 64 (1977) 342.
b) D. L. Adams, H. B. Nielsen and M. A. Van Hove, *Phys. Rev.* B(20) (1979) 4789.
9. R. Feder, *Surface Sci.* 68 (1977) 229.
10. R. A. Barker, P. J. Estrup, F. Jona, and P. M. Marcus, *Sol. St. Comm.* 25 (1978) 375.
11. a) J. E. Inglesfield, *J. Phys.* C11 (1978) L69.
b) E. Tosatti, *Sol. St. Comm.* 25 (1978) 637.
12. T. E. Felter, R. A. Barker, and P. J. Estrup, *Phys. Rev. Lett.* 38 (1977) 1138.
13. W. Moritz and D. Wolf, *Surface Sci.* 88 (1979) L29.
14. J. Perdureau, J. P. Biberian, and G. E. Rhead, *J. Phys.* F4 (1974) 798.

15. P. W. Palmberg and T. N. Rhodin, J. Chem. Phys. 49 (1972) 134.
16. B. Moraweck, C. Clugnet, and A. J. Renouprez, Surface Sci. 81 (1979) L631; and A. J. Renouprez, communication at Cocoyoc (Mexico) Surfaces Meeting, January 2-5, 1980.
17. H. J. Wasserman and J. S. Vermaak, Surface Sci. 32 (1972) 168.
18. C. W. Mays, J. S. Vermaak, and D. Kuhlmann-Wilsdorf, Surface Sci. 12 (1968) 134.
19. H. J. Wasserman and J. S. Vermaak, Surface Sci. 22 (1970) 164.
20. L. Pauling, The Nature of the Chemical Bond, Cornell University Press, 1973.
21. J. W. A. Sachtler, private communication.
22. A more complete review of the structure of metal monolayers on metal substrates is found in Ref. 45b of Part 1 and in: J. P. Biberian and G. A. Somorjai (to be published).
23. F. C. Frank and J. H. van der Merwe, Proc. Roy. Soc. A189 (1949) 205.
24. T. N. Rhodin, P. W. Palmberg, and E. W. Plummer, in Structure and Chemistry of Solid Surfaces, ed. G. A. Somorjai, John Wiley & Son, Inc., New York, 1969.
25. L. Brewer, Science 161 (1968) 115; and in Phase Stability in Metals and Alloys, P. Rudman, J. Stringer, and R. I. Jaffee, eds., McGraw-Hill, New York, 1967, p. 39.
26. L. Brewer, The Cohesive Energies of the Elements, Lawrence Berkeley Laboratory Report 3720, 1975.
27. C. G. Shaw, S. C. Fain Jr., and M. D. Chinn, Phys. Rev. Lett. 41 (1978) 955.

28. A. D. Novaco and J. P. McTague, Phys. Rev. Lett. 38 (1977) 1286.
29. P. W. Davies and R. M. Lambert, submitted to Surface Sci.
30. See, for example, S. E. Trullinger, S. L. Cunningham, and D. L. Mills, Sol. St. Commun. 13 (1973) 975.
31. K. Christmann, M. A. Van Hove, and G. Ertl, unpublished.
32. P. R. Norton, D. K. Creber, D. P. Jackson, and W. N. Unertl.
communication at 39th Conf. on Physical Electronics, University of Maryland, June 18-20, 1979.
33. D. Tabor and J. M. Wilson, Surface Sci. 20 (1970) 203.
34. K. O. Legg, F. Jona, D. W. Jepsen, and P. M. Marcus, J. Phys. C10
(1977) 937.
35. B. W. Lee, R. Alsenz, A. Ignatiev, and M. A. Van Hove, Phys. Rev. B17 (1978) 1510.
36. E. Lang, K. Muller, K. Heinz, M. A. Van Hove, R. J. Koestner, and G. A. Somorjai, submitted to Surf. Sci.

Table 1. Surface structure models for which dynamical LEED calculations have been made. Explanations are given in the text.

Models for Ir(100)(1x5), all with 6 phase shifts					
- $\theta=0^\circ$					
1. Hexagonal,	planar,	center/top	AH ph.sh.,	d = 1.82	(0.10) 2.72 A
2. Hexagonal,	planar,	two-bridge	AH ph.sh.,	d = 2.20	(0.10) 2.70 A
3. Hexagonal,	1/2 buckling	two-bridge	AH ph.sh.,	d = 2.20	(0.10) 2.70 A
4. Hexagonal,	2/3 buckling	two-bridge	AH ph.sh.,	d = 1.90	(0.10) 2.40 A
5. Hexagonal,	2/3 buckling	two-bridge	AHF, ph.sh.,	d = 2.20	(0.10) 2.70 A
6. Hexagonal,	full buckling	two-bridge	AHF, ph.sh.,	d = 1.90	(0.05) 2.15 A
7. Hexagonal,	full buckling	two-bridge	AHF, ph.sh.,	d = 1.90	(0.10) 2.40 A,
				uneven contraction	
8. Hexagonal,	full buckling	two-bridge	AH ph.sh.	d = 1.90	(0.10) 2.40 A,
				uneven contraction	
9. Hexagonal,	full buckling	center/top	AH ph.sh.	d = 1.82	(0.10) 2.72 A
10. Hex. missing row,	planar	center/top	AH ph.sh.	d = 1.82	(0.10) 2.72 A
11. Hex. missing row,	planar	two-bridge	AH ph.sh.	d = 2.20	(0.10) 2.70 A
12. Hex. missing row,	full buckling	center/top	AH ph.sh.	d = 2.20	(0.10) 2.72 A
13. Hex. missing row,	full buckling	two-bridge	AH ph.sh.	d = 1.62	(0.10) 2.12 A
14. Shifted rows,	5-cluster,		AH ph.sh.	d = 1.62	(0.10) 2.12 A
15. Shifted rows,	4-cluster,		AHF ph.sh.	d = 1.62	(0.10) 2.12 A
16. Shifted rows,	3-cluster,		AHF ph.sh.	d = 1.62	(0.10) 2.12 A
17. CDW,	0.1 A amplitude,	perpendicular,	AH ph.sh.	d = 1.62	(0.10) 2.12 A
18. CDW,	0.1 A amplitude,	angled,	AH ph.sh.	d = 1.62	(0.10) 2.12 A
- $\theta=10^\circ$					
19. Hexagonal,	1/2 buckled,	bridges,	AHF ph.sh.	d = 1.90	(0.10) 2.40 A
- $\theta=20^\circ$					
20. Hexagonal,	1/2 buckled,	bridges,	AHF ph.sh.	d = 1.90	(0.10) 2.40 A

(continued)

Table 1. (continued)

		Models for Pt(100) $\begin{pmatrix} 14 & 1 \\ -1 & 5 \end{pmatrix}$ all with $\theta=0^\circ$			
<u>- as one registry of (1x5)</u>					
21.	Hexagonal,	full buckling,	two-bridge,	5 A ph.sh.,	d = 1.85 (0.10) 2.35 Å
22.	Hexagonal,	full buckling,	center/top,	5 A ph.sh.,	d = 1.85 (0.10) 2.35 Å
23.	Hexagonal,	1/2 buckling	two-bridge	6 A ph.sh.,	d = 1.85 (0.10) 2.35 Å
24.	Hexagonal,	2/3 buckling	two-bridge	6 AF ph.sh.,	d = 1.85 (0.10) 2.35 Å
<u>- as 14 registries of (1x5)</u>					
25.	Hexagonal,	full buckling	two-bridge	5 A ph.sh.,	d = D+n x 0.1 Å (n=-2,-1,....,2)
26.	Hexagonal,	full buckling	center/top,	5 A ph.sh.,	d = D+n x 0.1 Å (n=-2,-1,....,2)
27.	Hexagonal,	full buckling	two-bridge	6 AF ph.sh.,	d = D+n x 0.1 Å (n=-2,-1,....,2)
28.	Hexagonal,	1/2 buckling	two-bridge	6 AF ph.sh.,	d = D+n x 0.1 Å (n=-3,-2,....,1)

Table 2. Surface structures resulting from the deposition of various adsorbates on the (1x1) unreconstructed Ir(100) or the (1x5) reconstructed Ir(100) surface.

Adsorbate	Clean Surface		Temp. [K]	Refs.
	Ir(100)(1x1)	Ir(100)(1x5)		
Acetylene C≡C	(1x1)	(1x5)	150,300	1
Benzene		(1x5)	150	1
Benzene	(1x1)	(1x1)	298	1
Carbon C		c(2x2)+graphitic	298	this work
Carbon monoxide CO	c(2x2)		298	2
Carbon monoxide CO		(1x1) or split (2x2)+weak (1x5)	298	2,3
Carbon dioxide CO ₂	c(2x2)+ (20x7)	split (2x2)+ weak (1x5)	298	2
Ethylene C=C	(1x1)	(1x5)	150,300	1
Hydrogen H ₂		weak (1x5)	298	4
Nitric oxide NO		(1x1)	150,300	5
Oxygen O ₂		weak (1x5)	298	6
Oxygen O ₂		(2x1)	900	4
Oxygen O ₂	(2x1)		high	2
Xenon Xe	(1x1)	(3x5)	55	7

References for Table 2

1. T. N. Rhodin, G. Broden and W. Capehart, Surface Sci. 61 (1976) 143.
2. J. T. Grant, Surface Sci. 18 (1969) 228.
3. G. Broden and T. N. Rhodin, Sol. St. Comm. 18 (1976) 105.
4. T. N. Rhodin and G. Broden, Surface Sci. 60 (1976) 466.
5. J. Kanski and T. N. Rhodin, Surface Sci. 65 (1977) 63.
6. G. Broden and T. N. Rhodin, Faraday Disc. Chem. Soc. 60 (1975) 42.
7. A. Ignatiev, A. V. Jones, and T. N. Rhodin, Surface Sci. 30 (1972) 573.

Table 3. Surface structures resulting from the deposition of various adsorbates on the (1x1) unreconstructed or the "(20x5)" reconstructed Pt(100)




Adsorbate	Clean Surface		Temp. [K]	Refs.
	Pt(100)(1x1)	Pt(100) Reconstructed		
Acetylene C≡C		c(2x2)	200	1
Acetylene C≡C		c(2x2)	293,423	2
Aniline φ-NH ₂		(1x1)	298	2
Benzene φ(= )		(1x1)+streaks	298	2
Biphenyl φ - φ		(1x1)	298	2
1,3-butadiene C=C-C=C		(1x1)	298	3
cis-2-butene 		(1x1)	298	3
trans-2-butene C-C=C-C 		(1x1)	298	3

Table 3. (continued)

Adsorbate	Clean Surface		Temp. [K]	Refs.
	Pt(100)(1x1)	Pt(100) Reconstructed		
n-butylbenzene	C-C-C-C-φ	(1x1)	298	2
t-butylbenzene	$\begin{array}{c} \text{C} \\ \\ \text{C}-\text{C}-\phi \\ \\ \text{C} \end{array}$	(1x1)	298	2
Carbon	C	graphitic	298	4
Carbon monoxide	CO	(1x1)+c(2x2)	298	5
Carbon monoxide	CO	various structures not related to that of reconstructed surface	298	6,7
Carbon dioxide	CO ₂	(4x2) and c(4x2)	298	3,7
Cyanobenzene	NC-φ	weak (1x5)	298	2
Cyanogen (CN ₂)		(1x1)	298	8

Table 3. (continued)



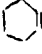

Adsorbate	Clean Surface		Temp. [K]	Refs.
	Pt(100)(1x1)	Pt(100) Reconstructed		
1,3-cyclohexadiene 		(1x1)+streaks	298	2
Cyclohexane 		"(20x5)" or diffuse (2x1)	298	2
Cyclohexane		streaked (2x1)	423	2
Cyclohexane		(1x1)	573	2
Cyclohexene 		diffuse (2x1)	298	2
Cyclohexene		streaked (2x1)	423	2
Cyclopentane 		(1x5) or diffuse (1x2)	298	2
Ethylene C=C	(1x1)	"(20x5)"	200	1
Ethylene	c(2x2)		298	1

Table 3. (continued)

Adsorbate	Clean Surface		Temp. [K]	Refs.
	Pt(100)(1x1)	Pt(100) Reconstructed		
Ethylene		c(2x2)	298	3
n-hexane		(1x1)	298, 523	2
Hydrogen	(1x1)	poor (2x2)	793-1493	5 7
Isobutylene		"(20x5)" + streaks	298	3
Mesitylene		"(20x5)" + streaks or (1x1)	298	2
2-methylnaphthalene		weak "(20x5)"	298	2
Naphthalene		(1x1)	298, 423	2
Nitric Oxide		(1x1)	298	9
Nitrobenzene		(1x1)	298	2

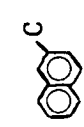
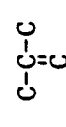
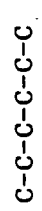


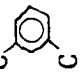


Table 3. (continued)

Adsorbate	Clean Surface		Temp. [K]	Refs.
	Pt(100)(1x1)	Pt(100) Reconstructed		
Oxygen	(1x1)	not adsorbed	298	5
Propylene C-C=C		(1x1)+streaks	298	2
Pyridine 		(1x1)	298	2
Pyridine		c(2x2)	523	2
Sulfur S (or H ₂ S)	c(2x2) or (2x2)	c(2x2) or (2x2)	298	1
Toluene 		"(20x5)" + streaks	298	2
Toluene		(1x1)	423	2
Vinyl Chloride C=C-Cl		c(2x2)	298	10
M-xylene 		"(20x5)" + streaks	298	2

References for Table 3

1. T.E. Fischer and S.R. Kelemen, Surface Sci. 69, (1977) 485.
2. J.L. Gland and G.A. Somorjai, Adv. in Colloid & Interface Sci. 5 (1976) 203.
3. A.E. Morgan and G.A. Somorjai, J. Chem. Phys. 51 (1969) 3309.
4. P.W. Palmberg, in Structure and Chemistry of Solid Surfaces, ed. G.A. Somorjai, Wiley & Son, New York, 1969.
5. C.R. Helms, H.P. Bonzel, and S. Kelemen, J. Chem. Phys. 65 (1976) 1773.
6. G. Kneringer and F.P. Netzer, Surface Sci. 49 (1975) 125.
7. A.E. Morgan and G.A. Somorjai, Surface Sci. 12 (1968) 465.
8. F.P. Netzer, Surface Sci. 52 (1975) 709.
9. H. Bonzel and G. Pirug, Surface Sci. 62 (1977) 45.
10. T.A. Clarke, R. Mason and M. Tescari, Proc. Roy. Soc. London A331 (1972) 321.

Figure Captions for Chapter IV Part 2

Figure 1. Experimental (dashed lines) and theoretical (solid lines) IV-curves for Ir(100) (1x5) with shifted-rows geometries. Curves labelled a: 5-atom clusters with d-spacing of 1.62Å. Curves labelled b: 3-atom clusters with d-spacing 2.12Å.

Figure 2. As Fig. 1, but comparing various hexagonal models, all with a d-spacing of 2.2Å. Curves labelled a: two-bridge registry, 1/2 buckling, Feder phase shifts; Curves labelled b: as 'a' without Feder correction. Curves labelled c: two-bridge registry, full buckling, no Feder correction; Curves labelled d: two-bridge registry, no buckling (planar), no Feder correction. Curves labelled e: center/top registry, full buckling, no Feder correction.

Figure 3. As Fig. 2, but for off-normal incidence ($\Theta=10^\circ$, $\phi=0^\circ$). The d-spacing is 2.1Å, with two-bridge registry, 1/2 buckling and Feder phase shifts.

Figure 4. As Fig. 3 for $\Theta=20^\circ$, $\phi=0^\circ$.

Figure 5. Experimental (dashed lines) and theoretical (solid lines) IV-curves for Pt(100) $\begin{pmatrix} 14 & 1 \\ -1 & 5 \end{pmatrix}$

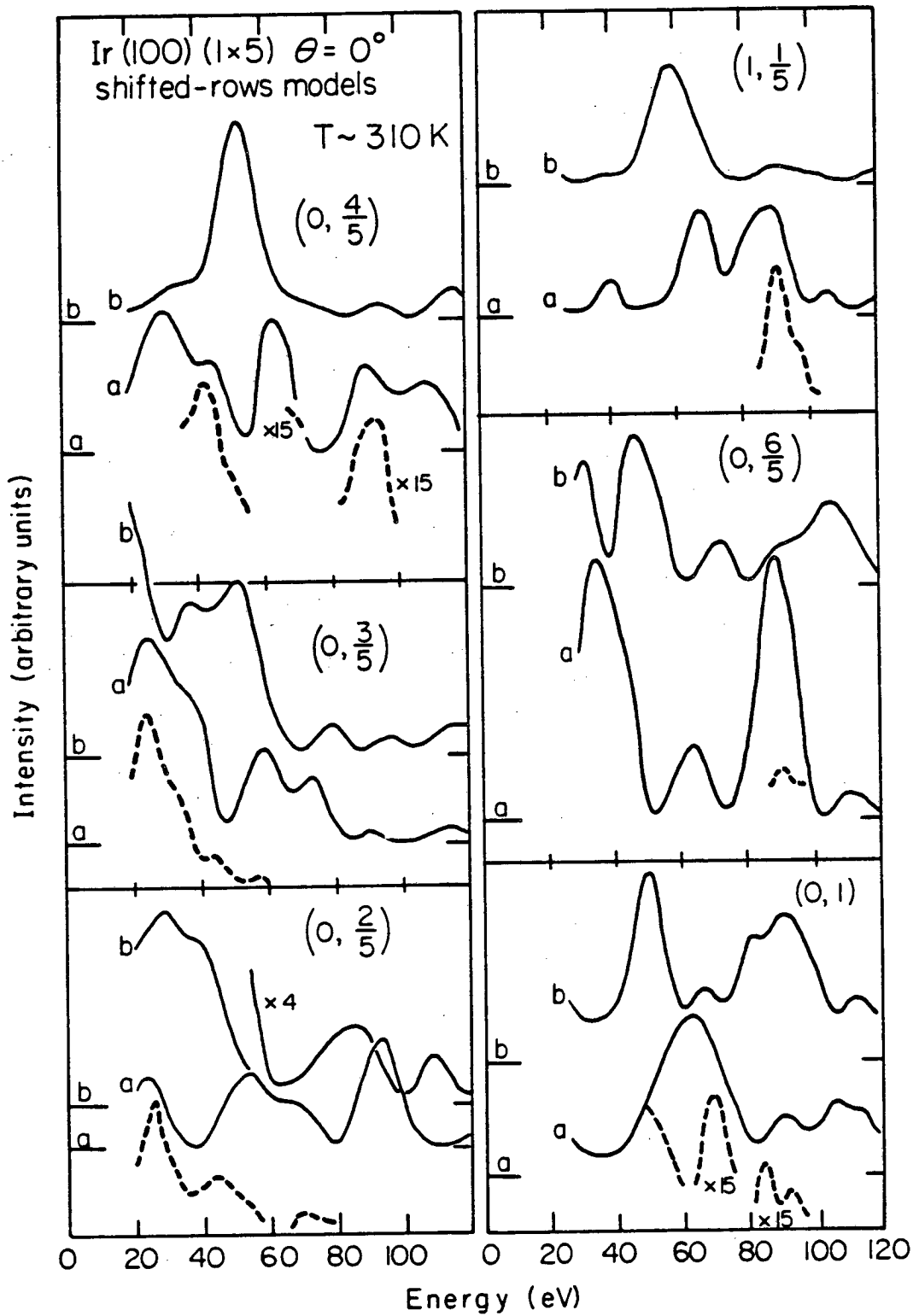
with a $1/2$ buckled hexagonal top layer in two-bridge registry, using Feder phase shifts. The d-spacing is $d=D-0.3\text{\AA}$ (curves b), and $d=D-0.1\text{\AA}$ (curves c), where D is defined in the text. The two dashed lines in each panel correspond to the two components of the split spots that are near the $1/5$ -order positions indicated. (Fig. 3 of part 1).

Figure 6. Part of the Periodic Table showing occurrences of clean-surface reconstructions, indicated by the Miller indices of the affected faces. For each element, bars at left have heights proportional to surface bond length contractions for different surface orientations, while other bars are proportional to selected bulk material constants (see key at top). A distinction is made between backbonds (between topmost and next atomic layers) and in-plane bonds parallel to the surface. The heights of the drawn bars can be compared directly from element to element. The plotted data, covering only the known results, are based mainly on the following references:

G. A. Somorjai and M. A. Van Hove, Structure and Bonding , Vol. 38, p. 1 (1979), Springer-Verlag, Heidelberg.

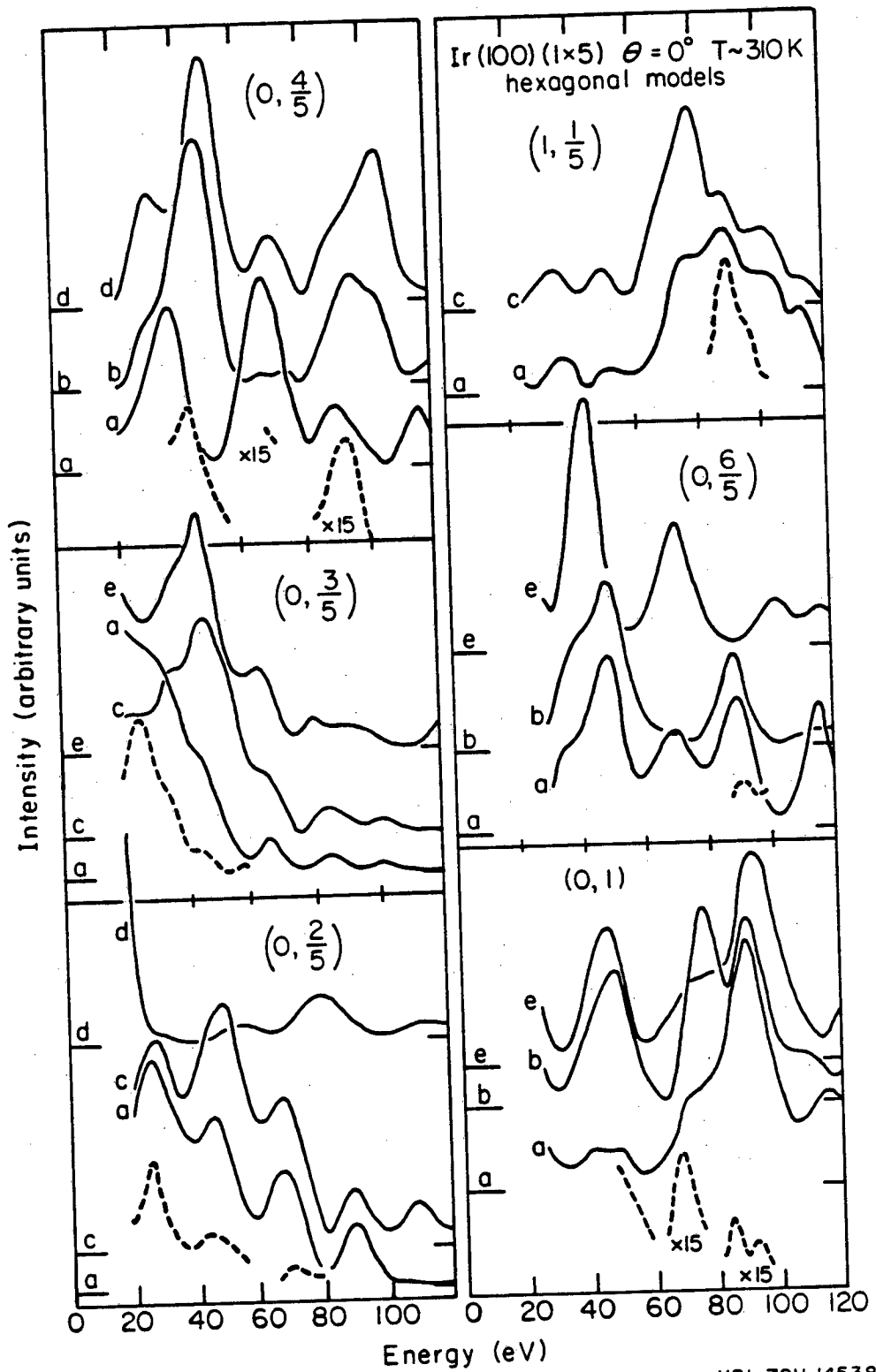
Handbook of the Physicochemical Properties of the Elements, G. V. Samsonov, ed, IFI/Plenum Press, New York (1968) pp. 397-8.

International Tables for X-ray Crystallography,
Vol. III, Kynoch Press, Birmingham, England (1962) pp.
233-41.



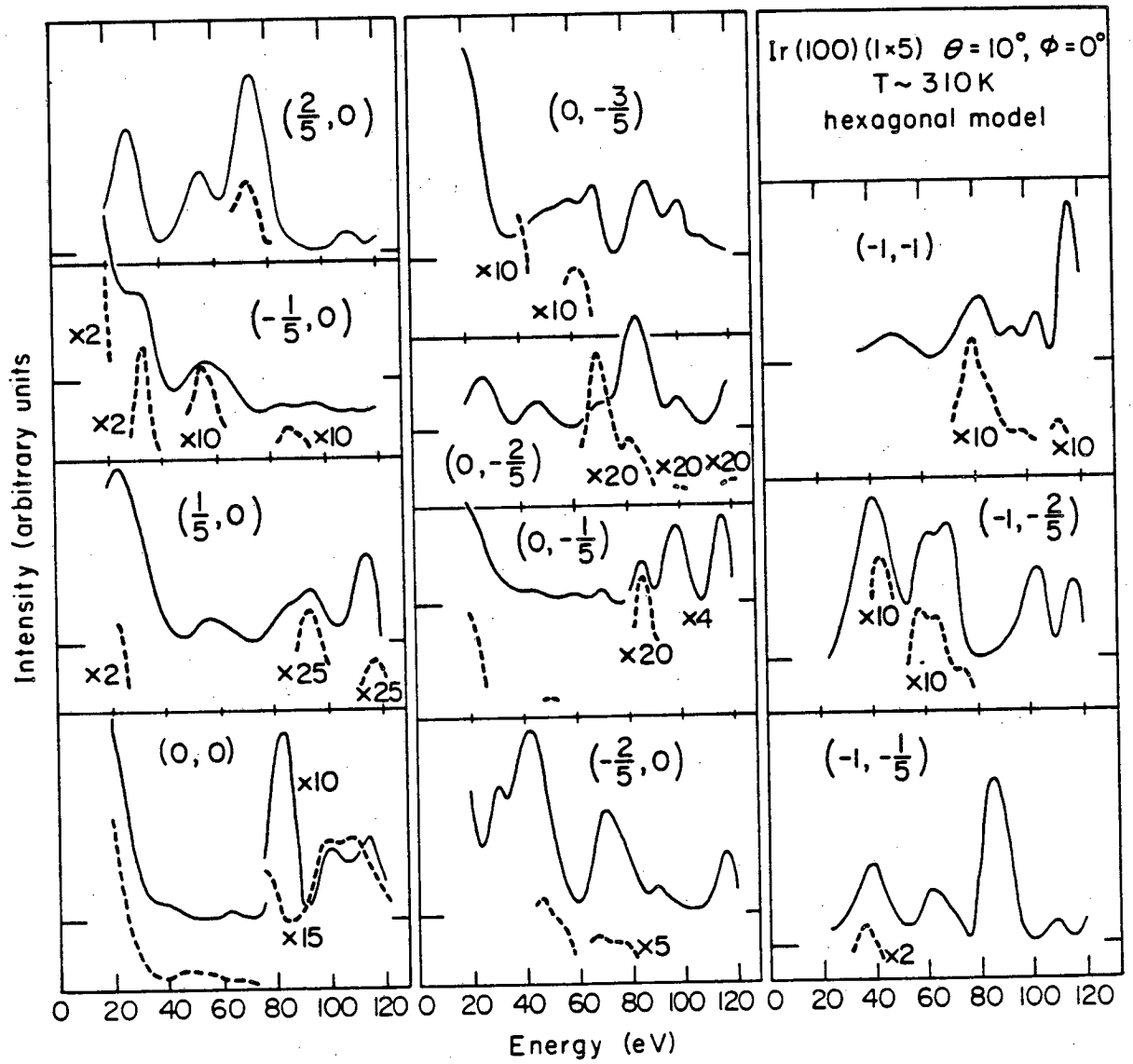
XBL7911-14537

Fig. 1



XBL 7911-14538

Fig. 2



XBL 7911-14539

Fig. 3

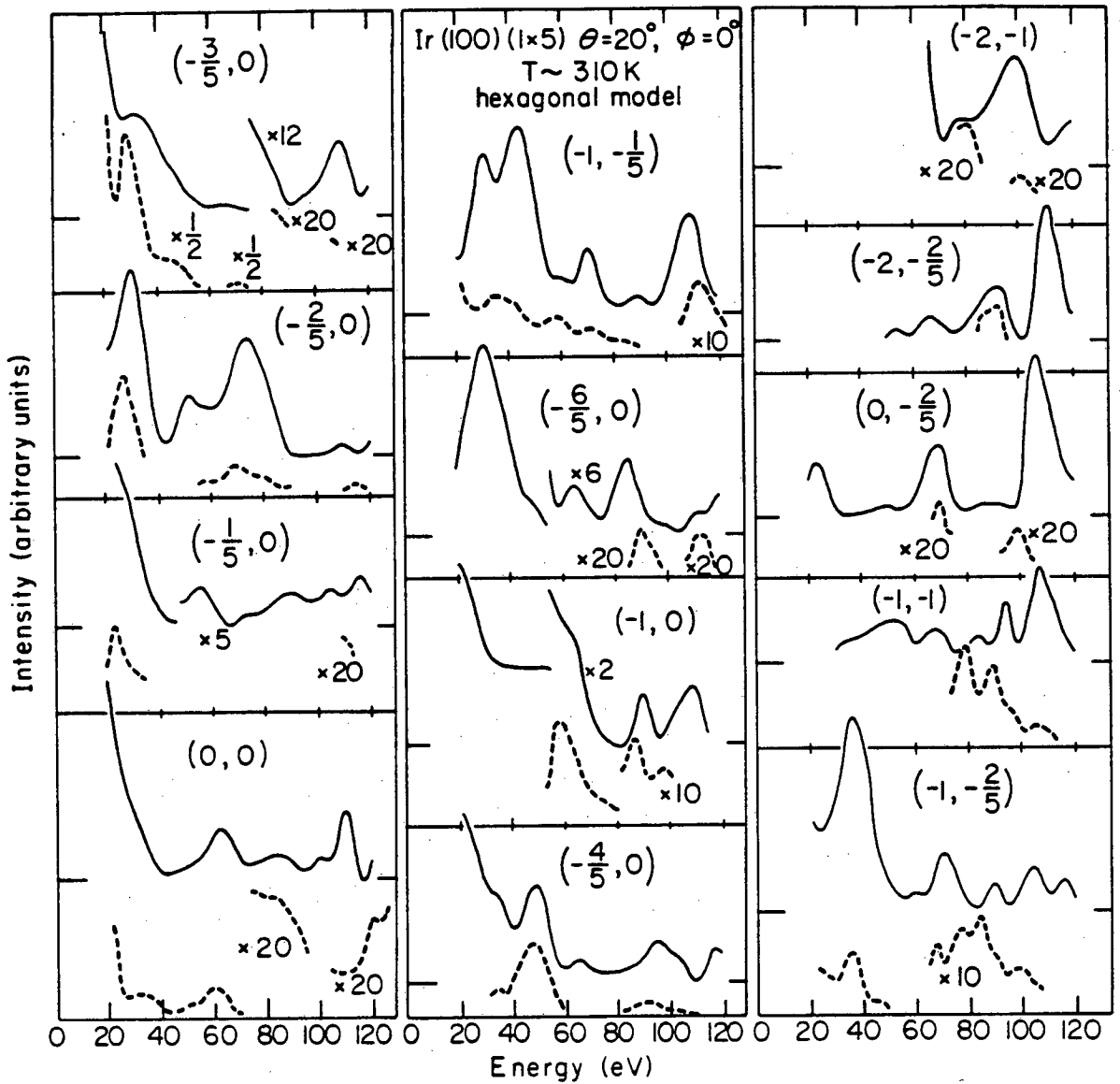
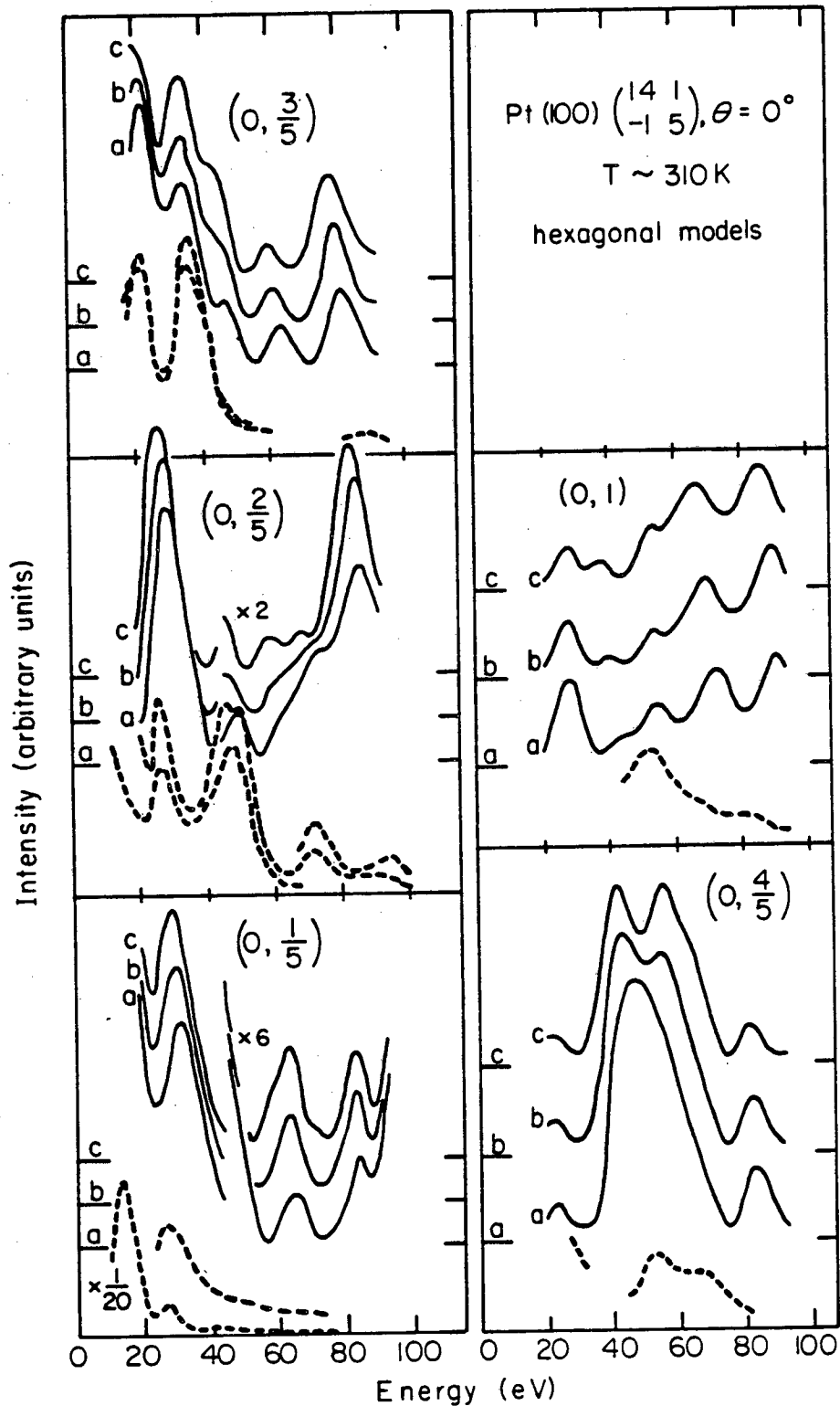
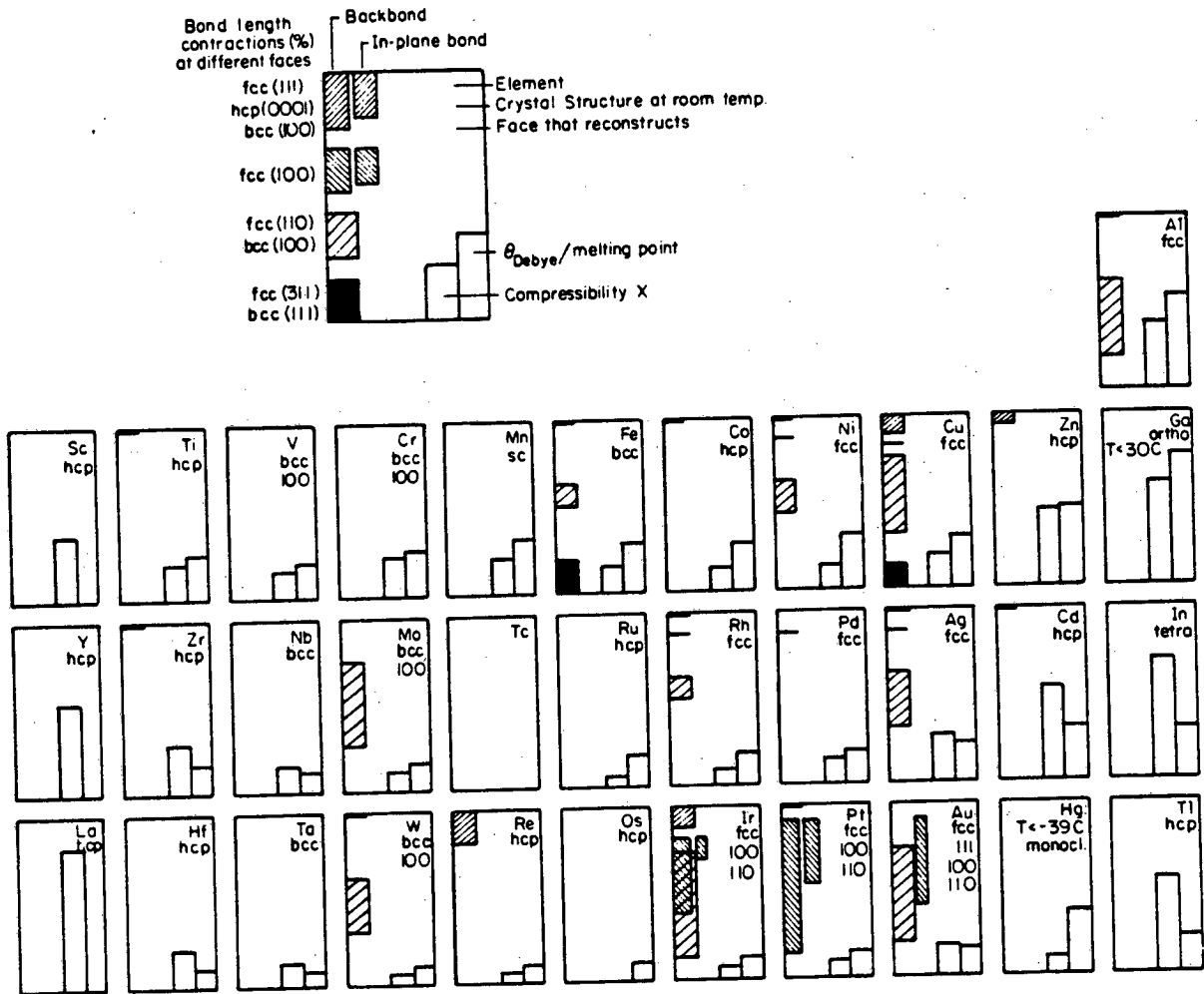


Fig. 4



XBL 7911-14536

Fig. 5



XBL 801-46 36

Fig. 6

V. CO AND CO₂ ADSORPTION ON RH(111)

PART 1: Rh(111)-($\sqrt{3}\times\sqrt{3}$)R30°-CO, CO₂ STRUCTURE DETERMINATION

A. INTRODUCTION

There have only been a few low energy electron diffraction (LEED) intensity analyses carried out to determine the structure of molecules adsorbed on metal surfaces; most surface crystallography studies have concentrated on the structure of adsorbed atoms on low Miller index faces of transition metals. The few molecular adsorption systems already investigated by dynamical LEED are CO on Ni(100),¹ Cu(100)^{1c,1d} and Pd(100)² as well as C₂H₂ and C₂H₄ on Pt(111).³

In this chapter we present a similar study on the Rh(111) ($\sqrt{3}\times\sqrt{3}$)R30° [Part 1] and (2×2) [Part 2] CO structures.

CO adsorption on Rh(111) has already been examined with a variety of surface sensitive techniques. Grant and Haas,⁴ using LEED and Auger electron spectroscopy (AES), were the first to investigate CO and CO₂ adsorbed on Rh(111); they saw a (2×2) LEED pattern for CO and a 'split' (2×2) for CO₂. Castner et al.⁵ observed a series of LEED patterns that appear with increasing CO coverage. The progression is a ($\sqrt{3}\times\sqrt{3}$)R30° at $\Theta=1/3$, a split (2×2) at $1/3<\Theta<3/4$, and a (2×2) pattern at $\Theta=3/4$. The patterns were interpreted as a continuous compression of a hexagonal overlayer of CO molecules in the coverage range $1/3<\Theta<3/4$. The order-order transition from the split (2×2) to the (2×2) structure was noted to be reversible with respect to CO pressure and temperature, while thermal desorption spectra (TDS) showed first-order desorption kinetics with only one CO peak detectable. CO₂, although requiring a

5-10 fold higher gas exposure, has an identical progression of LEED patterns and identical thermal desorption spectra as CO, suggesting dissociative chemisorption into an oxygen atom and a CO molecule. The fate of this oxygen atom was not further investigated.

Strong evidence that the oxygen atom, derived from dissociated CO₂, dissolves into the rhodium lattice was found by Thiel et al.⁶ At least 40% of the saturation coverage of O₂ on Rh(111) must be present before any O₂ desorption with increasing temperature can be measured; the large fraction of adsorbed oxygen that does not desorb dissolves into the crystal. However, the possibility that the oxygen could react with adsorbed CO and desorb as CO₂ cannot be ruled out. They also saw a residual oxygen peak in the Auger electron spectrum after a high temperature crystal heating of the Rh(111)-(2×2) O structure, indicating roughly a 1 atom% concentration near the surface; this residual oxygen peak had a very different line shape from chemisorbed oxygen, and the peak could not be reduced by extended heat treatments or H₂/CO adsorptions. More recently, Thiel and coworkers⁷ detected a low coverage ($\Theta=1/4$) (2×2) LEED pattern for CO adsorbed on Rh(111).

Dubois and Somorjai,⁸ using high resolution electron energy loss spectroscopy (HREELS) in combination with LEED, conclude that CO and CO₂ adsorb only at top sites ("terminal bonding") with the carbon end down at $\Theta=1/3$, begin populating the bridge-bonded positions in the $1/3 < \Theta < 3/4$ coverage range, and finally occupy about twice as many top as bridge sites at the saturation coverage of $\Theta=3/4$. In addition they studied CO chemisorption on pretreated Rh(111). H₂ pre- or post-adsorption at room temperature had no noticeable effect on the

vibrational or thermal desorption spectra, while O_2 and carbon preadsorption blocked possible CO adsorption sites as well as weakening the metal-CO bond and strengthening the CO bond. Interestingly, the O_2 pretreated surface inhibited the bridge-bonded species from appearing and the carbon pretreated surface inhibited the linear bonded species. Further evidence for the dissociation of chemisorbed CO_2 came from the observation that the adsorbed CO and CO_2 vibrational loss spectra were identical.

We report in the first part of this chapter a full dynamical LEED analysis with reliability factors for the $Rh(111)-(\sqrt{3}\times\sqrt{3})R30^\circ$ CO and CO_2 surfaces. The I-V curves for CO and CO_2 adsorption are found to be identical, which further indicates that CO_2 dissociates into CO on the $Rh(111)$ surface. Our determination of the $(\sqrt{3}\times\sqrt{3})R30^\circ$ CO structure provides a necessary check on the proposed correlation between adsorbed CO vibrational frequencies and its adsorption sites on fcc(111) metals (see Table 1); it also yields a calibration of the vibrational loss spectroscopies, which makes their predictions at different coverages, in different ordered states, and on different substrate faces more reliable.

B. EXPERIMENTAL

The crystal orientation ($\Theta=0^\circ$ and $\Theta\neq 0^\circ$, $\phi=0^\circ$) was determined by checking the degeneracy of beam I-V profiles; an engraved scale on the manipulator head would allow an accurate (within 0.1°) displacement of the polar angle (Θ) from normal incidence ($\Theta=0^\circ$). With the LEED beam at normal incidence, a 6-fold degeneracy should exist for the $(1/3,1/3)$

beams because of the mirror plane and rotational symmetry of the $(\sqrt{3}\times\sqrt{3})R30^\circ$ -CO, CO₂ unit cell on the Rh(111) surface. (Even if the basis of the $(\sqrt{3}\times\sqrt{3})R30^\circ$ unit cell had a lower symmetry, equivalent domains would regenerate the full symmetry in the diffraction pattern.) The $(2/3, -1/3)$, $(1/3, 1/3)$, and $(1/3, -2/3)$ beam profiles are indeed nearly degenerate at the assigned $\Theta=0^\circ$ orientation (Fig. 1). Similarly at $\Theta\neq 0^\circ$, $\Phi=0^\circ$ (that is, when the projection of the incident LEED beam on the crystal face is parallel to the $[112^-]$ direction), there should be a mirror symmetry about the plane containing the surface normal and this $[112^-]$ direction. Figure 2 shows that this symmetry is nearly realized in the experiment.

The I-V curves were collected using the photographic method previously described [Chapter IIIC and Ref. 9]. The Nikon F camera was adjusted to an aperture of f1.8 and a shutter time of 1/2 sec; a high speed Kodak film (pan 2484) was used. Four independent beam profiles, ranging from 44-224 eV were obtained for the clean Rh(111) surface at $\Theta=0^\circ$; these curves are identical to those published previously by others.¹⁰ The analysis of these experimental clean Rh(111) I-V curves will be published elsewhere.¹¹ A total of 27 independent profiles, ranging from 24-144 eV, were obtained for the Rh(111)+ $(\sqrt{3}\times\sqrt{3})R30^\circ$ CO, CO₂ system at three different incidence angles ($\Theta=0^\circ$; $\Theta=10^\circ$, $\Phi=0^\circ$; and $\Theta=20^\circ$, $\Phi=0^\circ$); most of these I-V curves for the clean and CO covered Rh surface are plotted in Appendix I. The I-V profiles for the CO overlayer were reproduced again with the Rh(111)+ $(\sqrt{3}\times\sqrt{3})R30^\circ$ CO₂ system (Figure 3). This not only supports the claim that CO₂ dissociates

into CO on this surface, as discussed in the Introduction, but also provides an independent check on the I-V curves for adsorbed CO.

The experience gained in the analysis of the Ni(100)-c(2x2)-CO structure by Andersson and Pendry^{1a} and by other authors^{1b-f} led us to take special precautions in this work. Three difficulties were encountered in the CO/Ni analysis. First, the ordering of CO on Ni(100) is very sensitive to surface perfection and cleanliness. Second, there was a considerable decrease of intensity (~30% for the (1/2,1/2) beam) in the extra diffraction spots during the time needed to collect the I-V curves with a telephotometer. Third, the c(2x2) pattern nucleates (island formation) quickly. The extra diffraction spots would reach near maximum intensity far before the optimal coverage of $\Theta=1/2$. In light of this Ni(100)-c(2x2)-CO work, we paid particular attention to the surface cleanliness of the Rh(111) crystal, the LEED beam induced damage of the CO overlayer, and the optimal exposure values for the $(\sqrt{3}\times\sqrt{3})R30^\circ$ structure.

An Auger electron spectrum of the crystal after only a few cleaning cycles showed substantial sulfur and boron as well as smaller chlorine and carbon peaks (Fig. 4). Boron (a 17 ppm bulk impurity) proved most troublesome to remove; only after weeks of continuous Ar⁺ bombardments (1-3 amps, 1.2 kV) with five minute annealing at 800°C and O₂ treatments (flowing 5×10^{-7} Torr O₂, 700°C) was it largely depleted from the near surface region. Auger electron spectra taken during the CO and CO₂ adsorptions still revealed small contaminant peaks (S, B, C, Cl (See Fig. 4b)); even months after this study was completed, with many additional cleaning cycles done, the amount of surface impurities had

not been further reduced. It should be noted that the residual probably subsurface oxygen seen by Thiel et al.⁶ treatments, is just below the detectability limit of our retarded-field Auger electron spectra; the expected residual oxygen peak ($O_{515}/Rh_{256}=1.5\%$) is comparable with the noise level near 515 eV in our spectra (see Fig. 4b,4c). It should be noted that although a substantial carbon peak is measured no oxygen peak is detected in the Auger electron spectra of $Rh(111)-(\sqrt{3}\times\sqrt{3})R30^\circ-CO$ surface (Fig. 4c); the expected O_{515}/Rh_{256} ratio is roughly 10%--a value significantly above the observed noise level of about 2-3%. This ratio is estimated from the Rh and oxygen peak height ratio measured for the $Rh(111)-(2\times 1)-O$ structure with coverage $\Theta=1/2$.¹² We believe that this discrepancy is due to the incident Auger electron beam (2.2 keV, 20 μ amps) induced fragmentation of the adsorbed CO and subsequent desorption of an oxygen ion. In fact, the higher coverage $Rh(111)-(2\times 2)-CO$ ($\Theta=3/4$) considered in the second part of this chapter shows the same effect even more dramatically.

The LEED beam would first slightly improve the ordering of the overlayer structure; then an exponential decay with electron exposure would start in the extra diffraction spots. Figure 5 shows this decay for the (1/3,1/3) beam intensity. There seems to be two distinct decay rates at different electron exposures, although this was not further investigated. In light of this, the electron beam damage was minimized by moving the electron beam across the crystal during photography,^{1b,1c} thus limiting the electron exposure of any given region of the surface to about 40 μ amp-secs. As a result, the LEED spots would actually increase somewhat in intensity (<5%), indicating that with this exposure

the exponential decay was not sufficient to offset the initial improvement in the ordering. A further check on our data is provided by the absence of detectable discontinuities in the I-V profiles at the energies where the electron beam was moved to a different region of the surface. In addition, the independent experiments to check for reproducibility had staggered energy intervals to insure that no false peaks would arise at the joining energies.

The gas exposure could not be accurately measured with the needle doser used, but a constant CO pressure burst would repeatedly produce a sharp, intense LEED pattern with low background. Thiel et al.⁷ found that the (1/3,1/3) beam intensity falls to a half-maximum value with a 15-20% over- or underexposure of CO, showing that the coverage can be fairly accurately determined by just checking the quality of the resulting LEED pattern. In addition, the CO₂ gas exposure was about 10-fold larger than the CO, but still produced identical I-V curves. If our overlayer coverage had been poorly controlled and if the I-V profiles were sensitive to CO coverage, we would not expect the CO and CO₂ beam profiles obtained in different gas exposure regimes to be identical. It should be mentioned that a small amount of ambient H₂ and CO were adsorbed on the crystal during cooling to -30°C (10 min) prior to CO or CO₂ exposure. After the adsorption of CO and CO₂, a crystal heating to 10-25°C would desorb H₂ and considerably sharpen the LEED spots.

C. LEED THEORY

We apply established dynamical LEED formalism in our theoretical analysis of the I-V curves.¹³ In particular, renormalized forward scattering is used between individual atomic layers, which include separate carbon and oxygen layers. The rhodium atoms are represented by a band structure muffin-tin potential,¹⁴ which has been used successfully in other work on Rh(111).^{10a,b} For the C and O atoms, X_{α} muffin-tin potentials calculated for a NiCO cluster have been chosen as these produced good LEED results on a nickel substrate.^{1e} We also tried the C and O atomic potentials used in other CO/Ni work with LEED^{1b} but found no material improvement in our results. The muffin-tin zero was initially set at -10 eV with respect to the vacuum level and then adjusted to -8 eV to best fit the clean Rh(111) I-V curves as described elsewhere.¹¹ This value is not further changed in the presence of the CO layer, since the work function change is negligible. Furthermore, the CO layer is given the same muffin-tin zero as the substrate, since a change was tested for CO on Ni(100)¹⁵ and on Pd(100)² but proved to have little effect at the energies under consideration. An imaginary part of the potential proportional to $E^{1/3}$ was chosen by observation of the peak widths in the experimental I-V curves. Rhodium thermal vibration amplitudes were increased by a factor of 1.4 relative to the bulk value for Rh, while the adatoms were given double the bulk rhodium vibration amplitudes. Variation of these amplitudes had a negligible effect on the structural determination.

Theory and experiment are compared through a set of R-factors and their average. These are:¹¹

ROS = fraction of energy range with slopes of opposite signs in the experimental and theoretical I-V curves; (1)

$$R1 = 0.75 \int |I_e - cI_t| dE / \int |I_e| dE ; \quad (2)$$

$$R2 = 0.5 \int (I_e - cI_t)^2 dE / \int I_e^2 dE ; \quad (3)$$

$$RRZJ = 0.5 \int \left\{ \frac{|I_e'' - cI_t''| |I_e' - cI_t'|}{(|I_e'| + \max |I_e'|)} \right\} dE / (0.027 \int |I_e| dE) ; \quad (4)$$

$$RPE = 0.5 \int (Y_e - Y_t)^2 / \int (Y_e^2 + Y_t^2), \quad Y(E) = L / (1 + v_{0i}^2 L^2), \quad L = I' / I \quad (5)$$

Here $c = \int |I_e| dE / \int |I_t| dE$; the apostrophe designates differentiation with respect to the energy. RRZJ is the reduced Zanazzi-Jona R-factor,¹⁶ while RPE is Pendry's R-factor,¹⁷ both renormalized with a factor 0.5 to match the scale of the other R-factors.

While the final R-factor value for a given surface structure is obtained by averaging over all available beams with weights proportional to each beam's energy range, we also exploit in the structural search the differences between R-factors for different beams. This is because different beams should simultaneously show minima when the correct surface structure is used, while it would be improbable to obtain this coincidence of minima with incorrect geometries. The justification for this is described in Ref. 11. In short, in the kinematic limit each beam is sensitive to the projection of the atomic positions onto the

direction of the particular momentum transfer vector corresponding to that beam. Therefore, it would be unlikely, even after multiple scattering is allowed for, that a particular incorrect surface geometry could have correct projections onto every available momentum transfer direction and produce R-factor minima in each beam.

Finally, the experimental curves were smoothed twice with a single three point smoothing formula. Both theory and experiment were also multiplied by an exponential function to give the high energy intensities weights equal to the low energy intensities and thus compensate for the intensity reduction due to thermal vibrations and the scattering amplitude.

D. RESULTS AND DISCUSSION

The clean Rh(111) surface was confirmed to have the ideal bulk structure, as described elsewhere,¹¹ with a Zanazzi-Jona R-factor value ($2 \times RRZJ$) of 0.14 and a Pendry R-factor value ($2 \times RPE$) of 0.20. For the Rh(111)-($\sqrt{3} \times \sqrt{3}$)R30°-CO structural determination, four adsorption sites were analyzed which may be labelled aaABC...(top site), bbABC...(hcp hollow site), ccABC...(fcc hollow site), and ddABC...(bridge site). The CO molecule was kept perpendicular to the surface. The hollow sites were easily ruled out by comparison of normal incidence I-V curves. Beam dependent R-factors for the top and bridge sites are plotted in Fig. 6 in the case of the $\Theta=10^\circ$ incidence direction. Variations in both the Rh-C and the C-O distances are included. It is easy to spot in Fig. 6 that coincidence of beam R-factor minima does not occur for any reasonable geometry of the bridge site; but coincidence is

easily recognized for the top site with interlayer spacings of $d_{\text{RhC}}=1.9\text{\AA}$ and $d_{\text{CO}}=1.1\text{\AA}$. This geometry is illustrated in Fig. 7.

More precise values for the interlayer spacings can be obtained as described in Ref. 18. Consider the two-dimensional space of the variables d_{RhC} and d_{CO} . For each d_{RhC} the value of d_{CO} giving the smallest average R-factor is plotted; lines of R-factor minima can then be produced. Two such lines intersect at the desired overall minimum. If the average R-factor near this minimum is taken to have a quadratic dependence on d_{RhC} and d_{CO} , the two lines in question are straight and a graphical determination of the position of the minimum is straight-forward, while points on the straight lines are easily determined by parabolic interpolations. In this fashion, the $\Theta=0^\circ$ data produce a minimum average R-factor (using ROS, R1, R2, RRZJ, and RPE) near $(d_{\text{RhC}}, d_{\text{CO}})=(2.01, 1.02)\text{\AA}$, while the $\Theta=10^\circ$ and $\Theta=20^\circ$ data produce minima at $(1.945, 1.075)\text{\AA}$ and $(1.945, 1.085)\text{\AA}$, respectively. Averaging with weights proportional to the amount of data at each angle of incidence produces values of $d_{\text{RhC}}=1.95\pm 0.1\text{\AA}$, and $d_{\text{CO}}=1.07\pm 0.1\text{\AA}$, where the conventional uncertainty of LEED analyses is quoted. We visually interpolate the average R-factor values at the minimum to 0.25 at $\Theta=0^\circ$, 0.20 at $\Theta=10^\circ$, and 0.26 at $\Theta=20^\circ$, averaging out at about 0.23. The corresponding Zanazzi-Jona R-factor is about 0.40 for this structure and the Pendry R-factor is about 0.50 which is to be compared with about 0.50 and 0.40 for CO on Ni and Cu(100).^{1d} Representative I-V curves are shown in Fig. 8.

It is interesting that the best Zanazzi-Jona R-factor for the bridge site is only slightly larger than that for the top site (about 0.42 to 0.40); whereas the other R-factors clearly favor the top site (on the average by about 0.30 to 0.23). Thus a conventional analysis using just the Zanazzi-Jona R-factor would not be considered decisive. This is a strong argument in favor of (1) using more than one R-factor, and (2) using the coincidence of beam R-factor minima for distinguishing between two local minima in the average R-factor.

An additional structural feature that was tested is the topmost Rh-Rh interlayer spacing, which was found to be indistinguishable from the clean surface case, i.e., essentially bulk-like.

We observe in the R-factor dependence on d_{RhC} and d_{CO} a feature already noted by Andersson and Pendry^{1d} for CO on Ni(100); an R-factor contour plot around the minimum can have an elongated elliptical shape with a major-to-minor axis ratio of up to 4:1. The elongation implies an uncertainty in the carbon position, but not in the oxygen position. This can also be seen by the constancy of the optimum Rh-O distances found at our three incidence directions (3.03, 3.02, and 3.03 Å at $\theta=0$, 10, and 20° respectively), while the C position varies by 0.07 Å. The idea of shadowing of the C atoms by the overlying O atoms put forward by Andersson and Pendry may be correct; however, our data sample shows more momentum transfer space farther away from the surface normal than theirs and should, therefore, be less susceptible to such shadowing.

The uncertainty in the carbon position may explain the slight discrepancy between our result ($d_{\text{RhC}}=1.95\text{Å}$, and $d_{\text{CO}}=1.07\text{Å}$) and known Rh-C and C-O bond lengths in rhodium carbonyls, which range from 1.82 to

1.91Å, and from 1.09 to 1.17Å, respectively, according to a tabulation for terminal bonding in 10 different such carbonyl cluster.¹⁹ In those clusters the Rh-O distance ranges from 2.96 to 3.04Å. Thus our determination puts the C atom somewhat far from the metal, but not the O atom.

The slightly too small C-O interlayer distance may also be explained^{1a} as due to the molecular axis bending away from the surface normal. However, it is difficult to understand an overestimated Rh-C distance with an argument of this kind.

The discrepancy in the case of CO on Rh(111) might also be ascribed to beam damage, as it was for the first CO/Ni(100) analysis. There a rather smaller CO interlayer spacing of 0.95Å was obtained. However, we have taken special precautions in this respect, as described in Section B. In addition, the CO/Pd(100) system suffered at least as much beam damage as the present one (as witnessed by clearly observable discontinuities between segments of I-V curves measured at different spots on the Pd sample), but produced very reasonable bond lengths, in particular 1.15Å for the C-O distance. Furthermore, that study did not use beams emerging at large polar angles. Thus it is not at all clear where the uncertainty in our carbon position comes from and whether it can be correlated with beam damage or with a lack of large polar-angle data.

Clearly the level of agreement that we obtain between theory and experiment is not of the best quality, but according to the Pendry R-factor it is essentially the same as Andersson and Pendry ultimately reached with CO on Ni(100). Probably improvements in either theory or

experiment for CO on Rh(111) would reduce the uncertainty in the carbon position. However, our various tests do not indicate where an improvement is required.

Our result of top site adsorption for Rh(111)- $(\sqrt{3}\times\sqrt{3})R30^\circ$ -CO serves as a confirmation of the postulated correspondence in vibrational loss work between adsorption site and frequency range for CO adsorbed on different metal surfaces. Our result extends this confirmation to other than the fcc(100) substrate face, for which it was established with CO on Ni, Cu, and Pd(100). A summary of these results is shown in Table 1. It is seen that the CO stretching frequency in the Rh(111)- $(\sqrt{3}\times\sqrt{3})R30^\circ$ structure is closer to the frequency range associated with a bridge-bonded CO molecule than that for CO on Ni or Cu(100). This determination provides an important calibration of the vibrational loss techniques in the sense that the knowledge of the CO adsorption site of one coverage or on one crystal face can be used to determine, without the help of further LEED intensity analyses, the adsorption site (but not necessarily the bond lengths and angles) at other coverages, in disordered states or on other substrate faces.

The identity, within experimental error, of the I-V curves measured for CO and CO₂ adsorption on Rh(111) provides a strong confirmation of the belief derived from TDS and HREELS work that CO₂ decomposes to CO and O, the CO taking the same structure as that described above for gaseous CO adsorption. The fate of the oxygen may be speculated upon in the light of the similarity in I-V curves. One has to account for 1/3 of a monolayer of oxygen. It is hard to image this oxygen settling in the immediate subsurface region of the rhodium without affecting the I-V

curves at least through a slight change in average Rh-Rh interlayer spacings, which we have tested. If the oxygen were interstitially located between the CO molecules on top of the substrate, the restricted available space would produce at least some degree of ordering of the oxygen atoms in a $(\sqrt{3}\times\sqrt{3})R30^\circ$ pattern and would thereby presumably affect the measured I-V curves. However, we found that the Rh(111)- $(\sqrt{3}\times\sqrt{3})R30^\circ$ -CO and CO₂ surfaces produce identical I-V profiles. Since TDS and HREELS do not detect this oxygen, it seems likely that it either diffuses deep into the substrate or desorbs as CO₂. The latter possibility actually requires that a substantial CO partial pressure is present during the CO₂ exposure.

E. SUMMARY

For the Rh(111)- $(\sqrt{3}\times\sqrt{3})R30^\circ$ CO system, CO was found to be terminally bonded with the carbon end down and perpendicular to the surface. The best fit interlayer spacings for the CO overlayer are $d_{\text{RhC}}=1.95\pm 0.1\text{\AA}$ and $d_{\text{CO}}=1.07\pm 0.1\text{\AA}$. The corresponding R-factors of this geometry are 0.40 for the Zanazzi-Jona factor (2 \times RRZJ) and 0.50 for the Pendry factor (2 \times RPE); these values are comparable with the Pendry R-factors 0.50 and 0.40 obtained for CO on Ni and Cu(100),^{1d} respectively.

The CO and CO₂ derived I-V curves are identical; this gives further evidence that the adsorbed CO₂ dissociates into a CO molecule and an oxygen atom. There is no identifiable trace of this oxygen in the I-V curves, supporting the claim that this oxygen dissolves into the substrate or desorbs as CO₂.

The Zanazzi-Jona R-factor did not adequately distinguish between the top (0.40) and the bridge (0.42) site adsorption models. However, the other R-factors clearly favor the top site (on the average by about 0.30 to 0.23), and the coincidence of the individual beam R-factor minima with only the top site geometry also provided a clear discrimination among the structural models tested.

The R-factor contours around the minimum in the $d_{\text{RhC}}-d_{\text{CO}}$ plane imply a larger uncertainty in the Rh-C spacing than for the Rh-O spacing. To further support this observation, the Rh-O distance obtained agrees well with organometallic cluster compound values and is well reproduced in the different polar-angle data, while the Rh-C distance appears slightly too large when compared to the organometallic compounds and is not as well reproduced in the different polar-angle data.

Our result of the top site adsorption for $\text{Rh}(111)-(\sqrt{3}\times\sqrt{3})\text{R}30^\circ\text{-CO}$ extends the postulated correlation in vibrational loss spectroscopies between the adsorption site and the adsorbed CO vibration frequency range to fcc(111) metal surfaces.

References for Chapter V, Part 1

1. a) S. Andersson and J. B. Pendry, Surface Sci. 71 (1978) 75.
b) M. Passler, A. Ignatiev, F. Jona, D. W. Jepsen, and P. M. Marcus, Phys. Rev. Lett. 43 (1979) 360.
c) S. Andersson and J. B. Pendry, Phys. Rev. Lett. 43 (1979) 363.
d) S. Andersson and J. P. Pendry, J. Phys. C (in press).
e) S. Y. Tong, A. Maldonado, C. H. Li, and M. A. Van Hove, Surface Sci. 94 (1980) 73.
f) K. Muller, E. Lang, P. Heilmann, and K. Heinz, to be published.
2. R. J. Behm, K. Christmann, G. Ertl, M. A. Van Hove, P. A. Thiel, and W. H. Weinberg, Surface Sci. 88 (1979) L59.
3. a) (for the metastable species) L. L. Kesmodel, R. C. Baetzold, and G. A. Somorjai, Surface Sci. 66 (1977) 299.
b) (for the stable species) L. L. Kesmodel, L. H. Dubois, and G. A. Somorjai, J. Chem. Phys. 70 (1979) 2180.
4. J. T. Grant and T. W. Haas, Surface Sci. 21 (1970) 76.
5. D. G. Castner, B. A. Sexton, and G. A. Somorjai, Surface Sci. 71 (1978) 519.
6. P. A. Thiel, J. T. Yates, Jr., and W. H. Weinberg, Surface Sci. 82 (1979) 22.
7. P. A. Thiel, E. D. Williams, J. T. Yates, Jr., and W. H. Weinberg, Surface Sci. 84 (1979) 59.
8. L. H. Dubois and G. A. Somorjai, Surface Sci. 91 (1980) 514.
9. a) P. C. Stair, T. J. Kaminska, L. L. Kesmodel, and G. A. Somorjai, Phys. Rev. B11 (1975) 623.

- b) M. A. Van Hove, R. J. Koestner, P. C. Stair, J. P. Biberian, L. L. Kesmodel, I. Bartos and G. A. Somorjai, *Surface Sci.*, 103 (1981) 189.
10. a) D. C. Frost, K. A. R. Mitchell, F. R. Sheperd, and P. R. Watson, *Proc. 7th IVC and 3rd ICSS, Vienna, (1977)* 2725.
b) K. A. R. Mitchell, F. R. Shepherd, P. R. Watson, D. C. Frost, *Surface Sci.* 64 (1977) 737.
c) C. Chan, P. A. Thiel, J. T. Yates, Jr., and W. H. Weinberg, *Surface Sci.* 76 (1978) 296.
11. M. A. Van Hove and R. J. Koestner, *Proc. Conf. on Determination of Surface Structure by LEED, Plenum Press (New York) 1982.*
12. D. G. Castner and G. A. Somorjai, *Surface Sci.*
13. M. A. Van Hove and S. Y. Tong, *Surface Crystallography by LEED*, Springer-Verlag, Heidelberg, 1979.
14. V. L. Moruzzi, A. R. Williams, and J. F. Janak, *Calculated Electronic Properties of Metals*, Pergamon (New York) 1978.
15. M. A. Van Hove, unpublished.
16. E. Zanazzi and F. Jona, *Surface Sci.* 62 (1977) 61.
17. J. B. Pendry, *J. Phys.* C13 (1980) 937.
18. D. L. Adams, H. B. Nielsen, and M. A. Van Hove, *Phys. Rev.* B20 (1979) 4789.
19. P. Chini, V. Longoni, and V. G. Albano, *Adv. Organomet. Chem.* 14 (1976) 285.
20. a) See, N. Sheppard and T. T. Nguyen, in *Infrared and Raman Spectroscopy*, Vol. 5 (R. J. H. Clark and R. E. Hestner, eds.) Heyden and Son, London, 1978, 67.

- b) R. P. Eischens and W. A. Pliskin, *Advan. Catalysis* 10 (1958) 1.
21. S. Andersson, *Solid State Commun.* 27 (1977) 75.
22. C. Andersson, in *Proc. 2nd European Conf. Surface Sci.*, Cambridge, 1977.

Table 1. Summary of LEED and HREELS results for CO adsorption.

Substrate	Pd(100) ²	Ni(100) ^{1,21}	Cu(100) ^{1,22}	Rh(111) ⁸
Adsorption site	bridge	atop	atop	atop
Interlayer spacings	$d_{PdC} = 1.93 \text{ \AA}$	$d_{NiC} = 1.71 \text{ \AA}$	$d_{CuC} = 1.90 \text{ \AA}$	$d_{RhC} = 1.95 \text{ \AA}$
LEED pattern	$(2\sqrt{2} \times \sqrt{2})R45^\circ$	$c(2 \times 2)$	$c(2 \times 2)$	$(\sqrt{3} \times \sqrt{3})R30^\circ$
CO, RhC stretching frequency	236, 42 meV	256.5, 50.5 meV	256, 59.5 meV	248, 57 meV
	1905, 340 cm^{-1}	2010, 405 cm^{-1}	2069, 480 cm^{-1}	2000, 460 cm^{-1}
Temperature	330-340 K	295 K	295 K	300 K

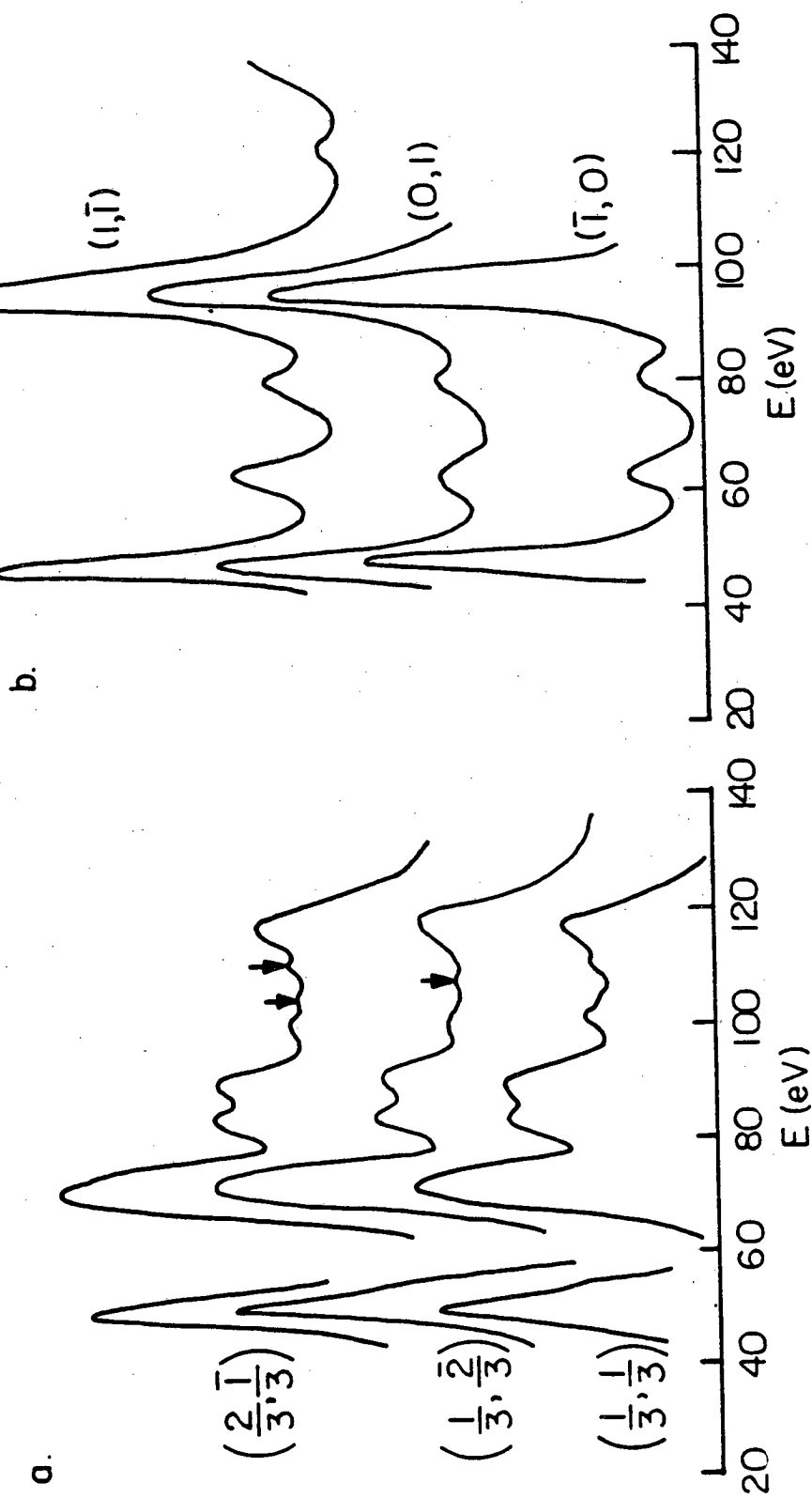
Note: proposed rule²⁰

1. $\nu_{CO} < 230 \text{ meV}$ (1855 cm^{-1}), 3-fold hollow site
2. 230 meV (1855 cm^{-1}) $< \nu_{CO} < 248 \text{ meV}$ (2000 cm^{-1}), 2-fold bridge site
3. $\nu_{CO} > 248 \text{ meV}$ (2000 cm^{-1}), atop site.

Figure Captions for Chapter V, Part 1

- Fig. 1. Nearly degenerate beams at assigned $\theta=0^\circ$ orientation. (Minor discrepancies pointed out by arrow head.)
- Fig. 2. Nearly degenerate beams at assigned $\phi=0^\circ$ orientation.
- Fig. 3. Identity of CO and CO₂ derived I-V curves.
- Fig. 4. Auger electron spectra.
- Fig. 5. (1/3, 1/3) Beam intensity decay with electron exposure.
- Fig. 6. Plot of individual beam R-factor minima with respect to d_{RhC} and d_{CO} .
- Fig. 7. Structure of Rh(100)-($\sqrt{3}\times\sqrt{3}$)R30°-CO.
- Fig. 8. Comparison between experimental (dark) and theoretical (light) I-V curves for (a) $\theta=0^\circ$, (b) $\theta=10^\circ$, $\phi=0^\circ$, and (c) $\theta=20^\circ$, $\phi=0^\circ$.

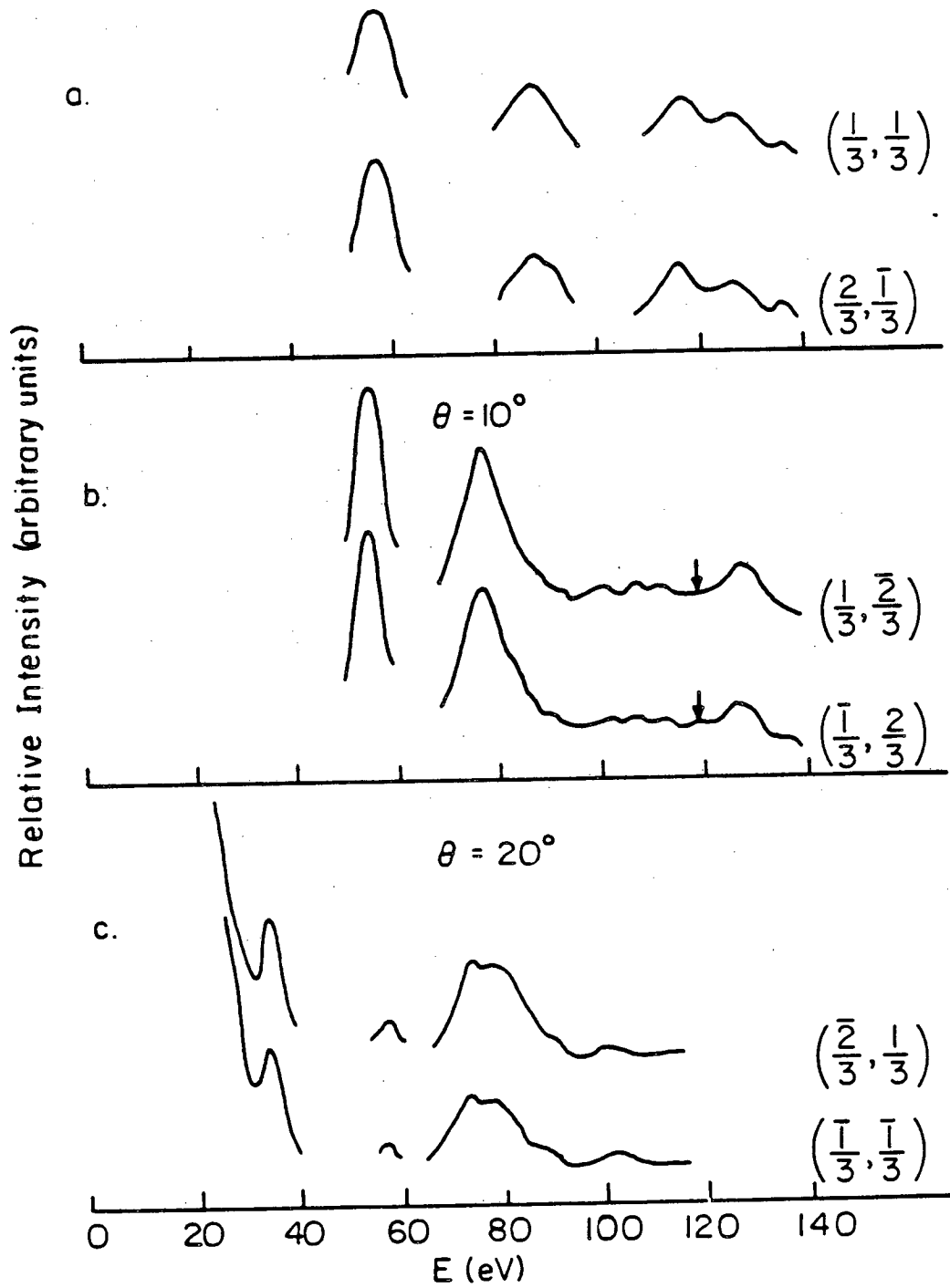
Rh(III) - $(\sqrt{3} \times \sqrt{3}) R30^\circ - CO$ T ~ 240K
 $\theta = 0^\circ$



XBL808-5664

Fig. 1

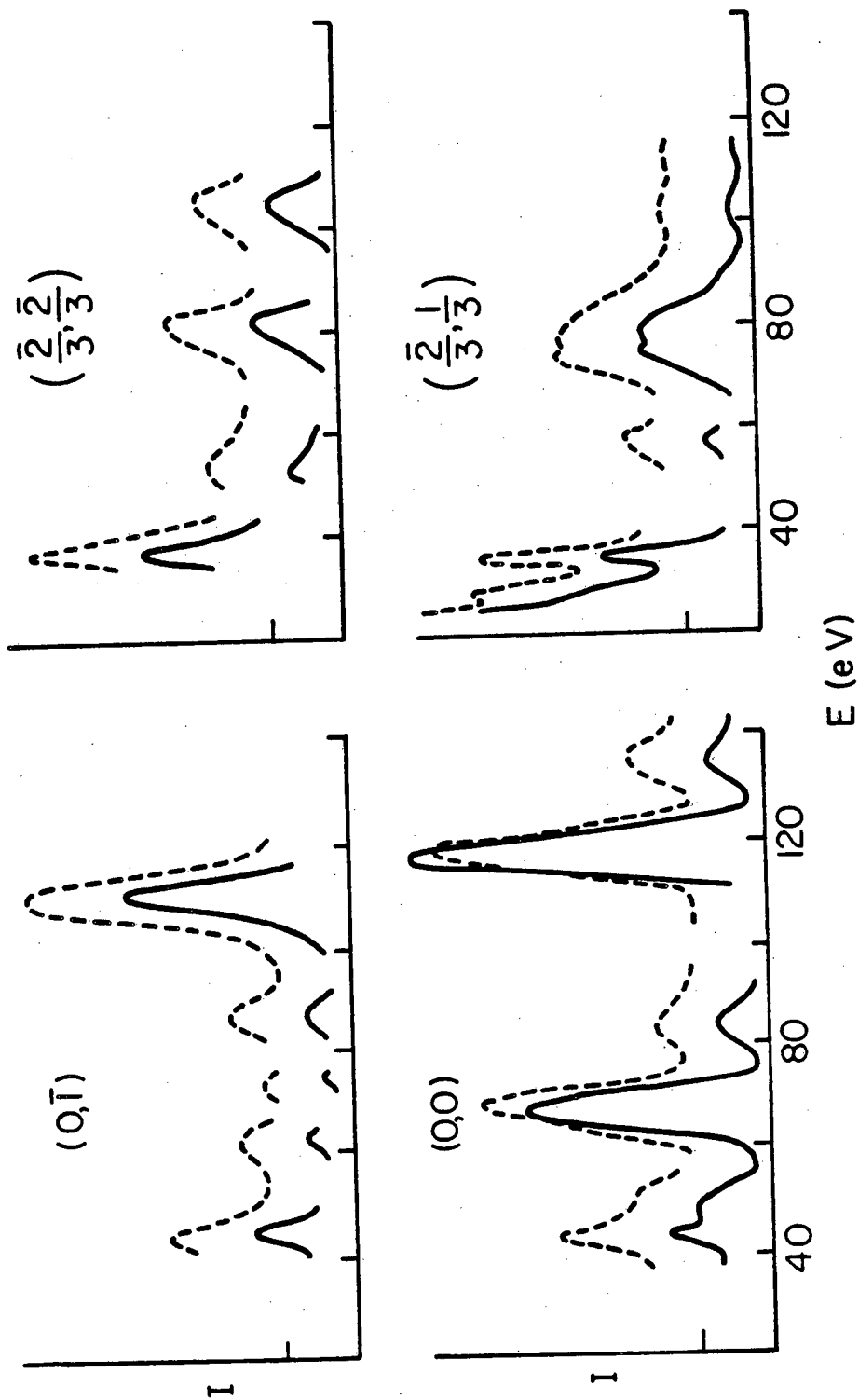
Rh (III) - $(\sqrt{3} \times \sqrt{3})R30^\circ$ - CO T~240K $\phi = 0^\circ$
 $\theta = 10^\circ$



XBL 808-5662

Fig. 2

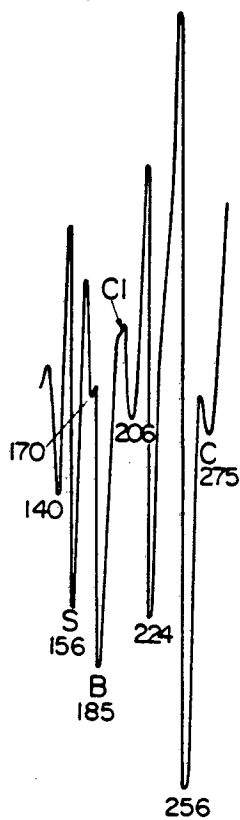
Rh (111) + $(\sqrt{3} \times \sqrt{3}) R30^\circ$ CO_2 --- $\theta = 20^\circ, \phi = 0^\circ$ $T \sim 240 \text{ K}$
 CO —



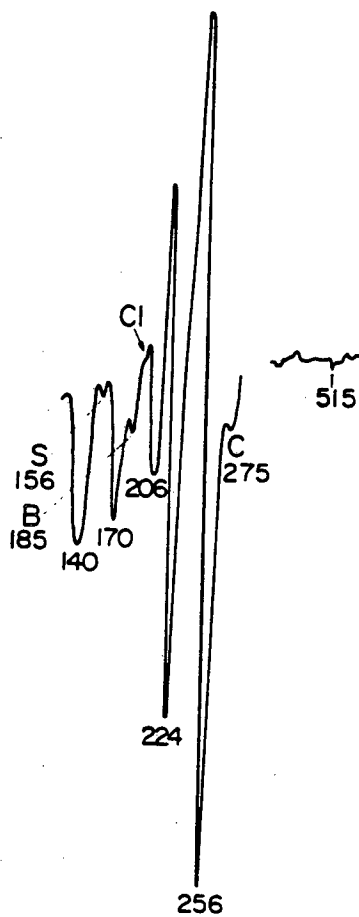
XBL 808-5661

Fig. 3

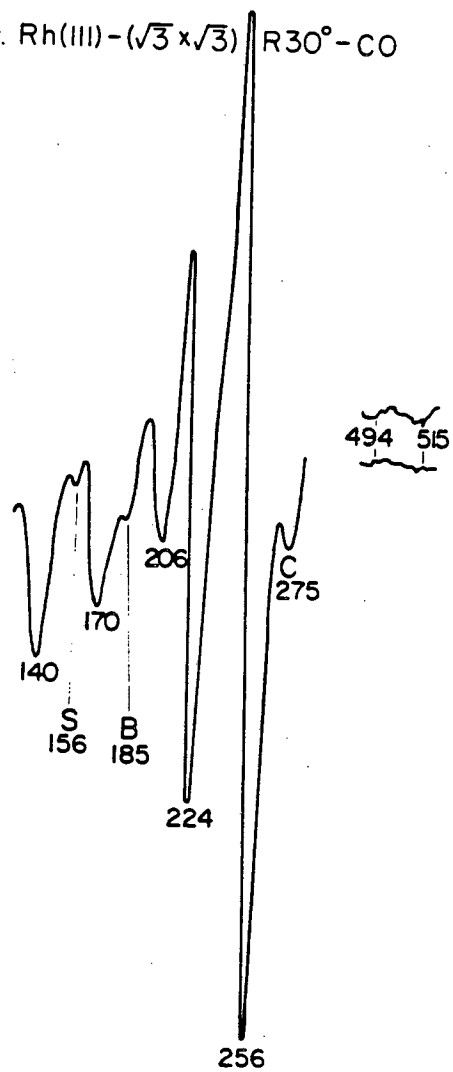
a. Contaminated Rh(III)



b. Clean Rh(III)

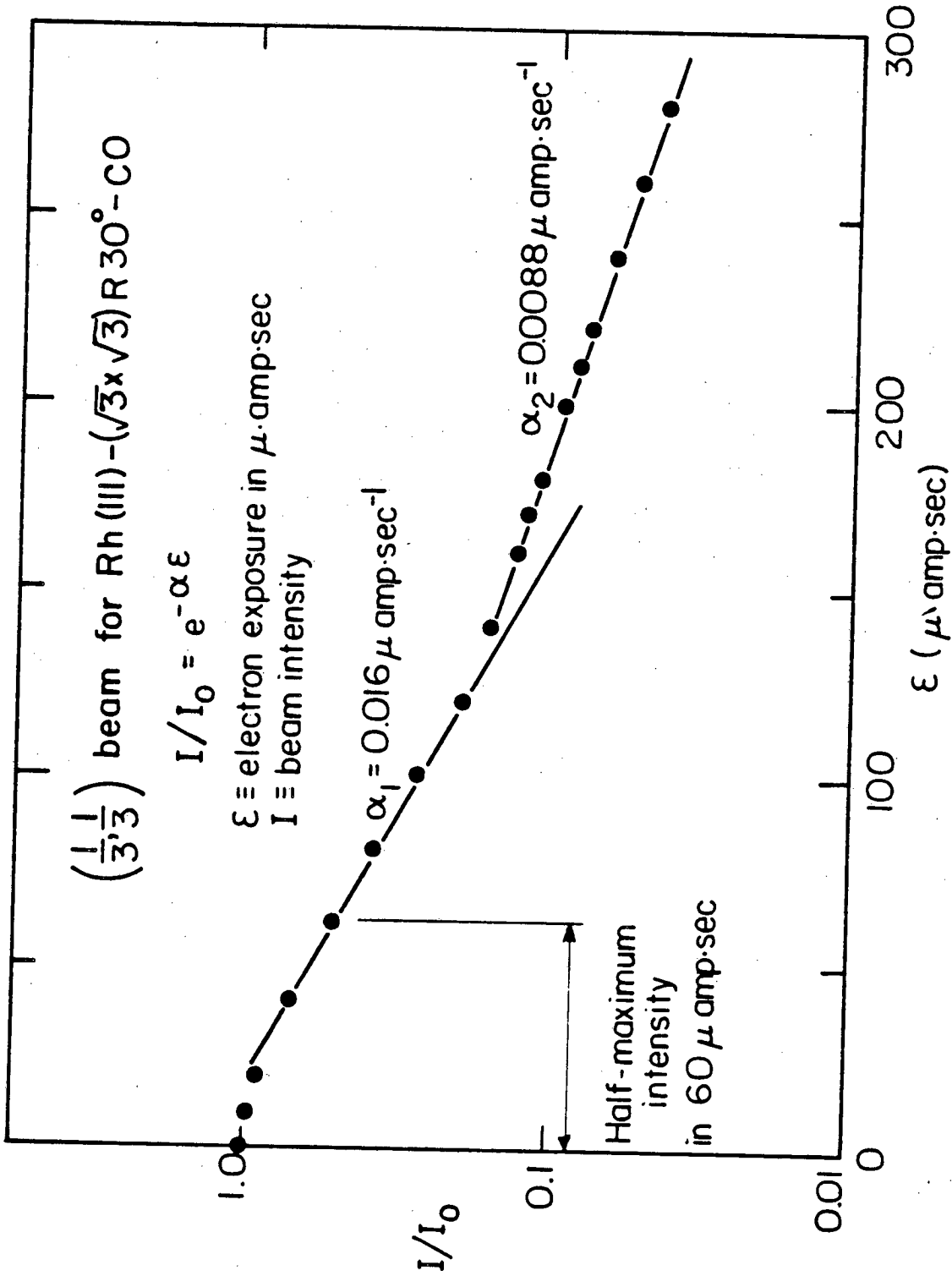


c. Rh(III) - ($\sqrt{3} \times \sqrt{3}$) R30° - CO



XBL808-5665

Fig. 4



XBL808-5663

Fig. 5

Rh(111) + ($\sqrt{3} \times \sqrt{3}$)R30° CO
 $\theta = 10^\circ$, $\phi = 0^\circ$, 240K

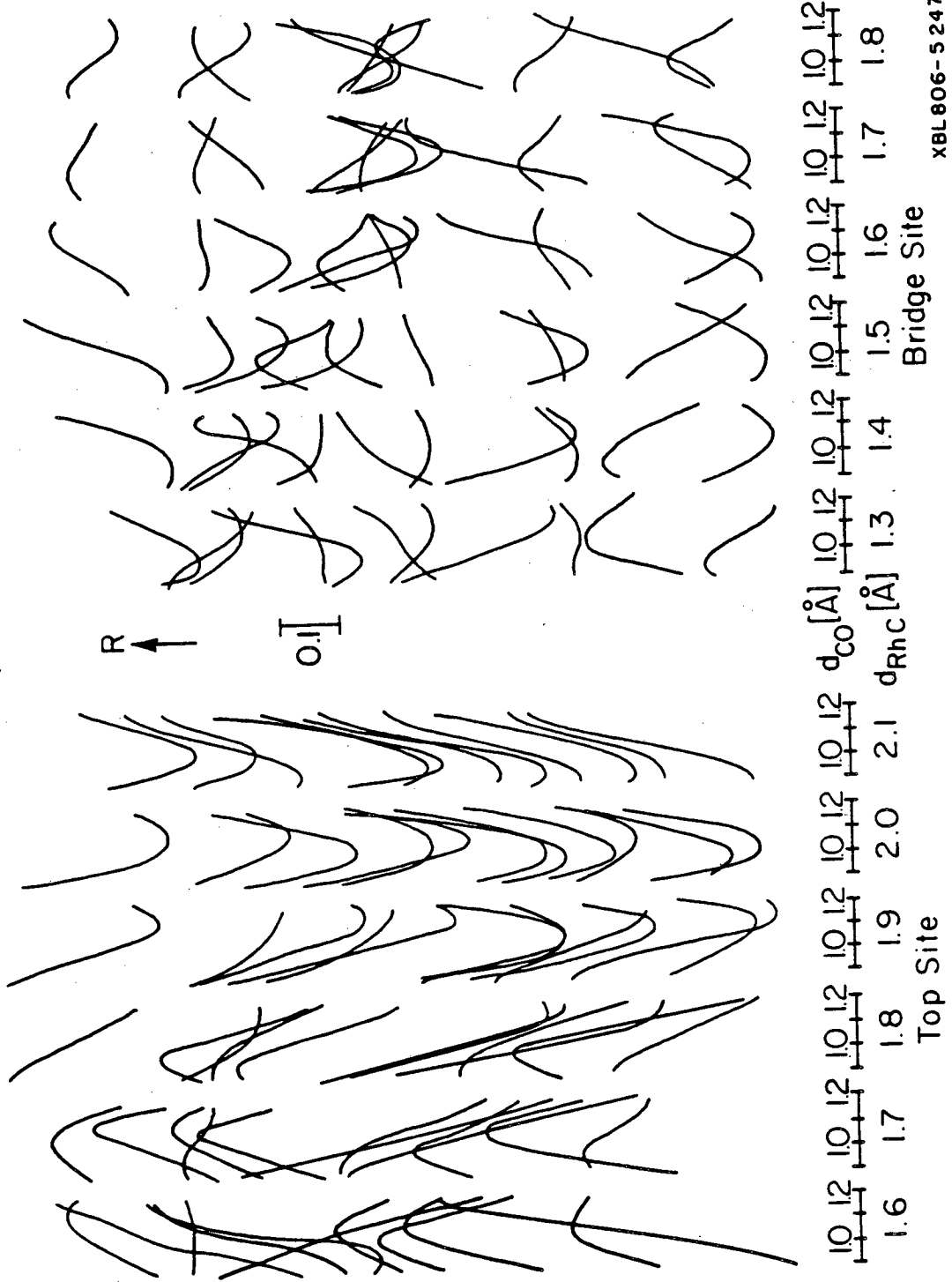
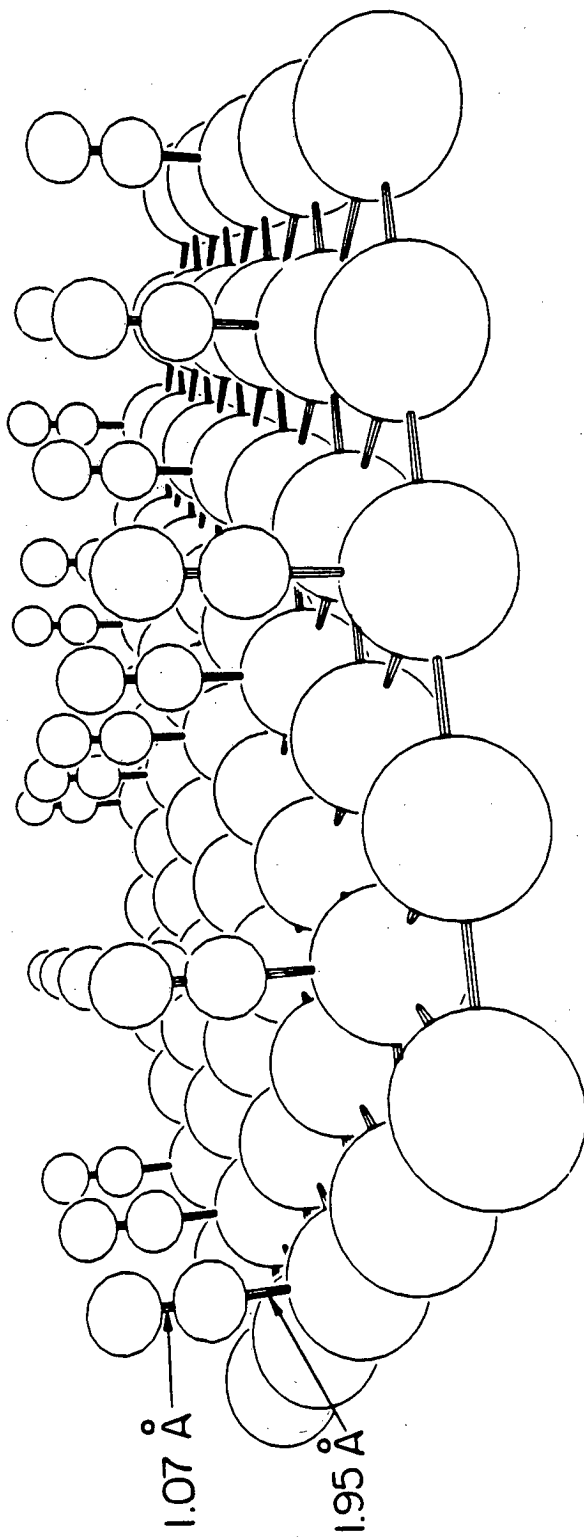


Fig. 6



XBL 807-5494A

Fig. 7

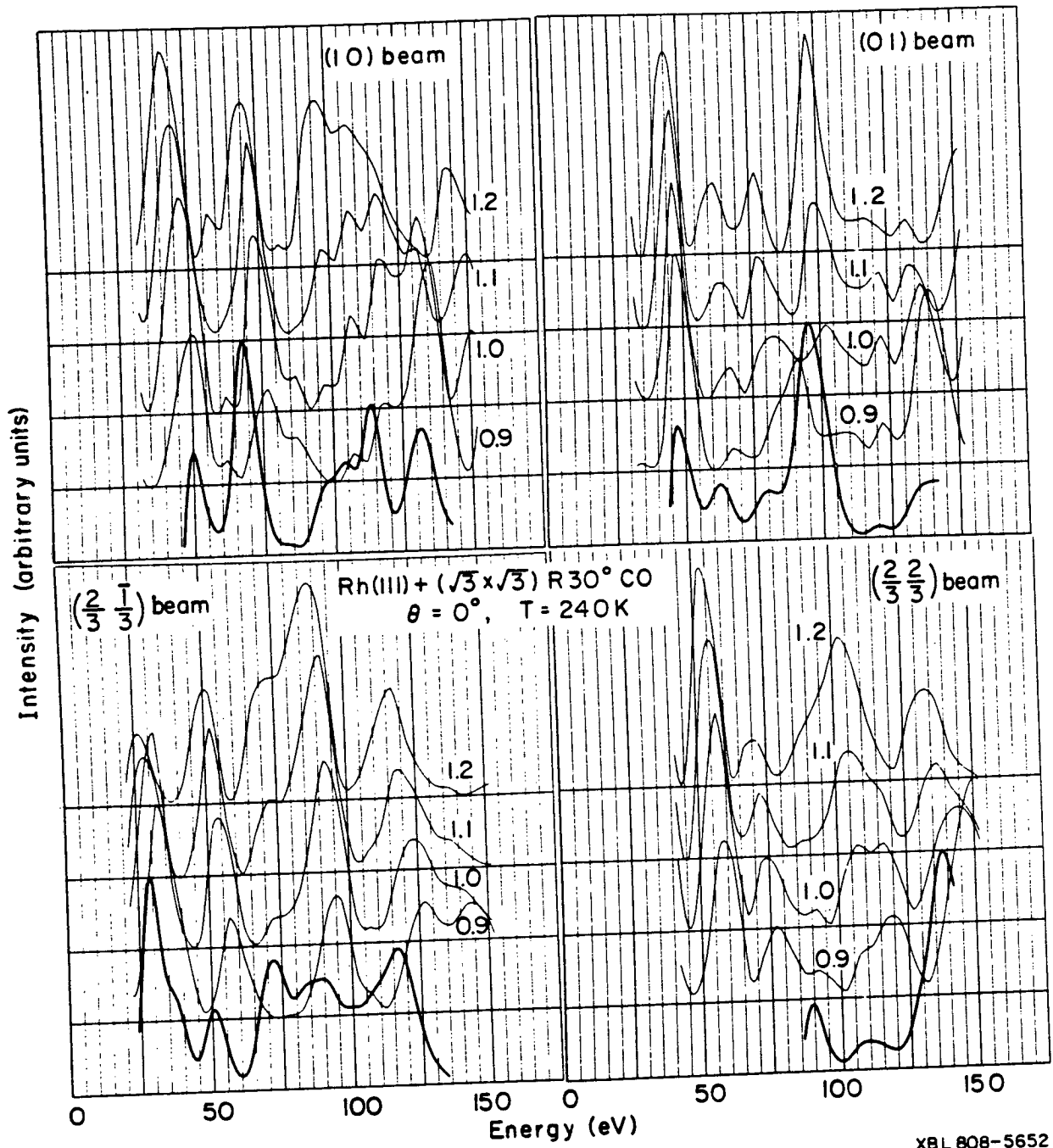
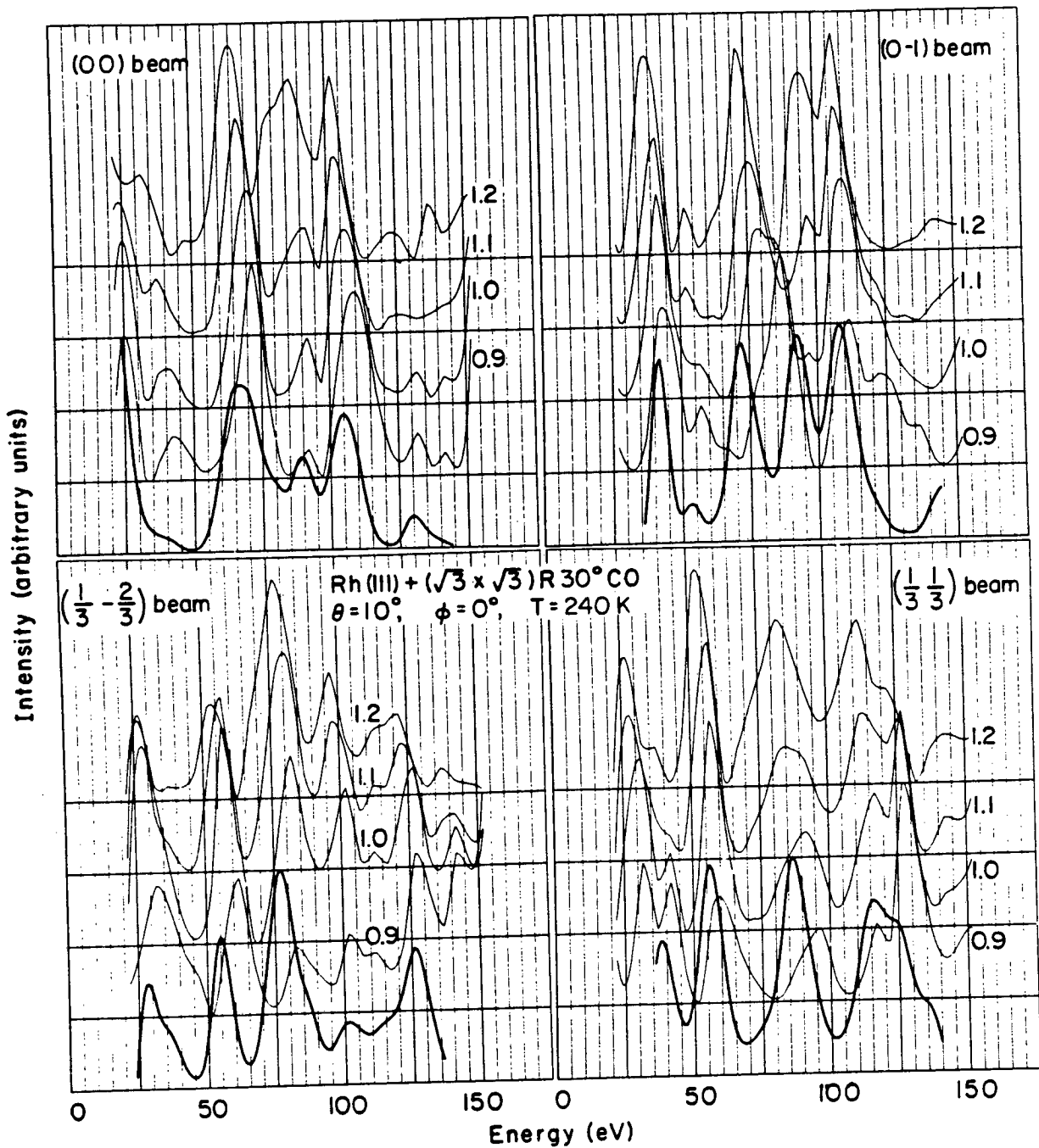
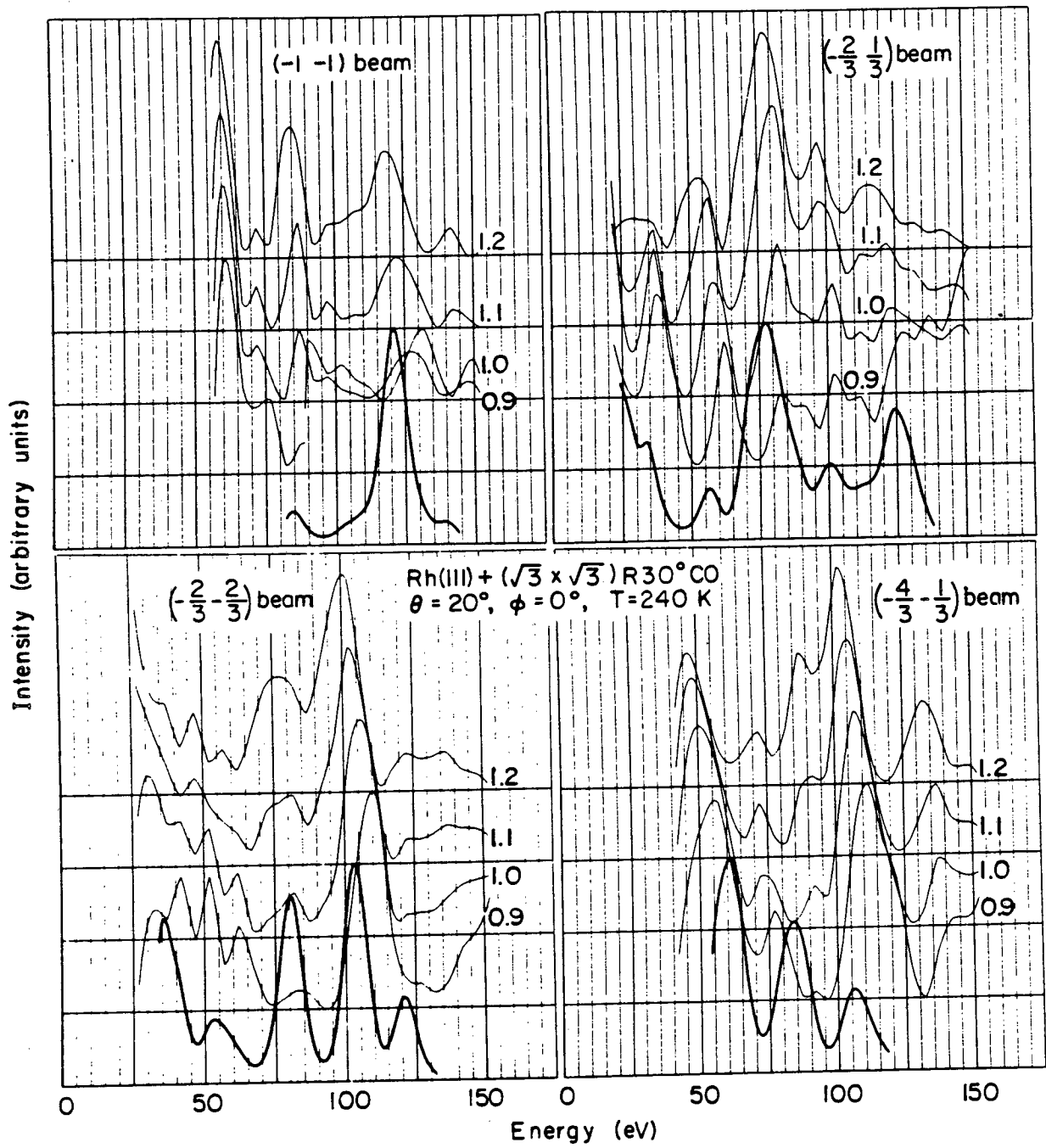


Fig. 8a



XBL 808-5651

Fig. 8b



XBL808-5650

Fig. 8c

PART 2: Rh(111)-(2x2)-3CO STRUCTURE DETERMINATION

A. INTRODUCTION

The adsorption of carbon dioxide on single crystalline transition metal surfaces has received considerable attention¹ over many years. This is readily understood since the chemisorption of CO on a metal surface can be regarded as a model adsorption system and since the industrial importance of CO hydrogenation² (in the Fischer Tropsch Synthesis) and oxidation³ (in controlling auto exhaust emission) using metal catalysts is well-recognized. Recent Low Energy Electron Diffraction (LEED),⁴ Thermal Desorption Spectroscopy (TDS),⁵ and Ultraviolet Photoemission Spectroscopy¹ studies suggest very similar bonding of CO to the (111) faces of noble metals, despite their varying electronic configuration and metal-metal distances. Yet vibrational spectroscopy results^{1,6} indicate substantial differences in the bonding of CO to these metals. The CO species is found to occupy atop, bridge, or possibly even hollow sites at low coverages (less than one half of a monolayer) while multiple site adsorption often occurs as the CO overlayer compresses towards saturation coverage. (The form that this compression takes is under debate: a compound hexagonal CO lattice has been proposed for many cases, but ordered domain structures are generally in better agreement with all observations.)

In the hope of obtaining a more detailed picture of the bonding of CO to metal surfaces, we have been studying ordered CO overlayer structures that form on Rh(111) system with LEED crystallography. In Part 1 of this chapter we found that CO stands above the atop sites

in the low-coverage $(\Theta=1/3)(\sqrt{3}\times\sqrt{3})R30^\circ$ structure in agreement with an earlier High Resolution Electron Energy Loss Spectroscopy investigation.⁶ In this part we report the determination of the high-coverage $(\Theta=3/4)(2\times 2)-3CO$ structure; there are four salient points in this LEED analysis that we should mention here.

(1) Our determination provides a necessary check and also a calibration on the rule originally proposed by Eischens and Pliskin⁷ that relates the measured C-O stretching frequency to either atop, bridging, or hollow site adsorption. The need for a calibration of this rule is indicated best by way of example. The C-O stretching frequency ranges between $1820 - 1840 \text{ cm}^{-1}$ at low coverage ($\Theta < 1/3$) on Pd(111); this frequency is probably related to hollow site adsorption since coexisting bands at 1936 cm^{-1} and 2092 cm^{-1} are assigned to bridging and terminal CO, respectively.⁸ On the Ni(111) surface the CO stretching frequency shifts from 1810 to 1910 cm^{-1} as the coverage increases⁹; this band falls into the bridge-bonding range (Table 1 in part 1). However it may also be related to hollow site adsorption that has a large frequency shift with coverage which could be caused by adsorbate-adsorbate repulsion, vibrational coupling, dipole-dipole interactions, and decreased metal-carbon back bonding effects. From these earlier studies then, we can only conclude that the 1860 and 2070 cm^{-1} stretching frequencies measured for the Rh(111)- $(2\times 2)-3CO$ overlayer by HREELS⁶ can be assigned to either hollow/top or bridge/top site adsorption.

(2) The relative importance of adsorbate-adsorbate and metal-adsorbate interactions can be examined in this structure analysis. If metal-adsorbate interactions dominate, CO should stand directly above high symmetry sites; yet if adsorbate-adsorbate interactions are significant, the CO overlayer may relax into a more hexagonal arrangement above the metal surface.

(3) Until now, LEED crystallography has been applied to only a few molecular overlayers which usually had two scattering atoms in the unit cell. (See Introduction to Part 1.) However in this study we demonstrate that LEED can be successfully applied to a molecular overlayer which contains six atoms in the overlayer unit cell.

(4) Since a larger computational effort is required, we calculated the diffraction beam intensity curves by including increasing amounts of multiple scattering in the overlayer. We found that the kinematic approximation (single scattering) is sufficiently accurate to select a few probable structures which can then be tested and refined with a full dynamical calculation. An intermediate approximation that considers multiple scattering only within each CO molecule gave intensity spectra that are very similar to the curves obtained with the full dynamical treatment.

B. EXPERIMENTAL

The rhodium sample was prepared as described in Part 1 of this chapter. Here we are concerned with the high coverage end in the progression of ordered structures that form on the Rh(111) surface with

increasing CO exposures. The order-order transition from the "split" $(2 \times 2)[1/3 < \theta < 3/4]$ to the (2×2) structure $[\theta = 3/4]$ is reversible with respect to the ambient CO pressure and crystal temperature. Near 300K a background pressure of $10^{-6} - 10^{-5}$ torr CO is necessary to produce the (2×2) overlayer; however if the crystal temperature is raised to 325K, even an ambient CO presence of 10^{-5} torr is not sufficient to produce the (2×2) structure. In our experiment the (2×2) layer was formed by cooling the sample to 240 K and exposing it to a constant pressure of $2 - 4 \times 10^{-6}$ torr CO. This steady state pressure was maintained by using a small leak rate and throttling the ion pump.

The intensity vs. voltage (I-V) profiles for a number of diffraction beams were collected using a photographic technique described in Chapter III C. The intensity data was measured at three angles of incidence and a second independent experiment was done in each case to check for reproducibility. The data set contains 5 independent beams at normal incidence ($\theta = 0^\circ$), 8 beams at $\theta = 10^\circ$, $\phi = 0^\circ$, and 8 beams at $\theta = 20^\circ$, $\phi = 0^\circ$. Electron beam damage to the (2×2) overlayer was minimized by moving the sample during the course of photography, in this way, the electron exposure at any given region of the surface was always less than 40 μ ampsec.

The decay rate of the $(0, 1/2)$ beam intensity with electron exposure is about one tenth as large as that measured for the $(1/3, 1/3)$ beam in the Rh(111)- $(\sqrt{3} \times \sqrt{3})$ -CO overlayer. If electron beam induced desorption of CO is more probable than decomposition, the background presence of CO needed to produce the (2×2) structure may fill any vacancies that are

due to desorption. This could be the reason why we measured a significantly lower decay rate in the diffraction beam intensity from the (2×2) overlayer. Alternatively, the dense crowding of CO molecules in the (2×2) cell may inhibit CO tilting; and the tilting motion may be required in the decomposition mechanism.

C. RESULTS AND DISCUSSION

i) Structural Models

The left hand side of Fig. 1 describes the model geometry that we tested in the LEED analysis along with the adjustable bond lengths and angles. The upper illustration presents a side view and the lower one gives an atop view of the CO layers. Three CO molecules need to be positioned in the (2×2) unit cell above the Rh(111) surface. One CO molecule is placed directly above a bridge site, while the two other CO molecules stand along the long diagonal of the (2×2) cell near the atop sites. Two mirror line symmetries were maintained in the model along the large and short diagonals of the (2×2) overlayer cell to minimize the computational effort in the structural search. (Only one of these mirror line symmetries has a corresponding mirror plane symmetry in the metal lattice.) Registries other than the bridge/near atop geometry were not tested since the agreement between calculated and measured intensity curves for this geometry was found to be very satisfactory. The Zanazzi-Jona and Pendry R-factors were 0.25 and 0.47, respectively.

The CO bond length (d_{CO}) was assumed to be the same for all the admolecules. The carbon atom in the bridge-bonded CO species is a distance, d_{RhC} , above the first metal layer, while the other carbon atoms located near the atop site were raised by an additional distance,

$d_{\perp CC}$, from the Rh lattice. The two near-atop CO molecules which were symmetrically disposed to each other, were moved a distance, $d_{\parallel CO-CO}$, from the bridged CO molecules and were allowed to tilt by an angle, θ , towards the bridged molecules along the diagonal.

So five separate parameters ($d_{\perp CO}$, $d_{\perp RhC}$, $d_{\perp CC}$, $d_{\parallel CO-CO}$ and θ) were considered in determining the structure of the (2×2) -3CO overlayer. Among the model geometries tested, we find the fully relaxed hexagonal layer of CO (see dotted small circles in Fig. 1) that would result if adsorbate-adsorbate interactions are dominant as well as the bridge/atop site geometry that would result if only the metal-adsorbate interactions are most important.

ii) LEED Theory

The muffin-tin potentials used for the Rh, C, and O atoms are the same on those in Part 1 of this chapter and will not be reported here. The Renormalized Forward Scattering (RFS) approximation¹⁰ [see Chapter IIc] was used to calculate the interlayer multiple scattering for the metal and CO lattices. The in-plane multiple scattering of the metal was treated fully, but three different approximation schemes were tried for the CO layer.

- (1) In the poorest approximation, no multiple scattering between carbon and oxygen atoms was considered (kinematic limit).
- (2) For a better approximation, only multiple scattering within each molecule was properly treated.
- (3) Finally, a calculation including full multiple scattering was done for the CO overlayer.

This approach was taken to examine how important different multiple scattering events are in the CO overlayer. If only reasonable agreement between theoretical and experimental intensity curves can be achieved with the kinematic or even partial multiple scattering scheme, the savings in computational costs would allow many more models to be tested in a preliminary structural search. The complete multiple scattering calculations would then be used in the refinement stage of the LEED analysis to choose among the more probable geometries.

iii) Structure Determination with Dynamical LEED

Let's first discuss the geometry of the CO unit cell predicted by the full dynamical calculation. The structural result is illustrated on the right-hand side of Fig. 1; and the degree of agreement between theory and experiment is shown in Fig. 2 using reliability factors. The agreement is significantly better for the (2x2) structure (average R-factor = 0.19) than that we obtained for the ($\sqrt{3}\times\sqrt{3}$)R30° overlayer (average R-factor = 0.23). Both the Zanazzi-Jona (0.25 to 0.40) and Pendry (0.47 to 0.50) R-factors favored the (2x2) structure determination. We find the two CO molecules within the (2x2) unit cell move 0.53Å off the atop site towards each other. This is still 0.25Å short of the displacement necessary to produce an hexagonal lattice of CO. The closest bridge to near-atop and near-atop to near-atop CO distances are fairly small, 2.85 or 2.88Å, respectively (see Fig. 1); these distances are well below the Van der Waals radius for CO (3.1 or 3.2Å) which suggests a strong repulsive interaction between these CO species.¹¹ The next larger CO separations are 3.23 and 3.60Å.

The CO-CO distance that we find to be significantly shorter than the Van der Waals distance (2.8 or $2.9 < 3.2\text{\AA}$) must be balanced with the cost in energy for moving the CO molecule away from the high-symmetry atop site. In our model, the CO species must move along the diagonal by a distance of 0.78\AA from the atop site to produce an hexagonal lattice. We measure that the CO molecules are in fact displaced by most of that distance (0.53 out of 0.78\AA) in the actual structure.

The other interesting parameter in this structure determination is the tilt angle (θ) of the near-atop CO molecules. We find that these CO molecules stand perpendicular to the metal layer which gives an OCRh bond angle of about 16° . A strain energy is undoubtedly present in this "bent" bond where the overlap between the CO (5σ , $2\pi^*$) and metal ($4d$) orbitals is reduced.

Both the near CO-CO distance (2.85\AA) and the bent CO-metal bonds suggest a much weaker adsorption energy than that found at lower coverages. Since the (2×2) -3CO unit cell will transform to the lower coverage split (2×2) structure at 300K in the absence of a background CO pressure, we know that the adsorption energy is less than 15 kcal/mol (which should be compared to 30 kcal/mol at low coverages). (This is calculated via $\Delta H_{\text{ad}} = RT \ln P_{\text{vap}}$ where $RT = .6$ kcal/mol and $P_{\text{vap}} = 10^{-9}$ atm.) A more accurate isosteric (differential) heat of adsorption could be obtained by measuring the pressure versus temperature dependence at saturation coverage, but we did not have a reliable method to measure the coverage (work function change, for example).

The other distances ($d_{\perp\text{CC}}$, $d_{\perp\text{RhC}}$, and $d_{\perp\text{CO}}$) we determine are expected from organometallic analogues.¹² The CO bond length is

1.15Å, while the metal-carbon bond distances are 1.94 and 2.03Å for the near-atop and bridged species, respectively. The relative uncertainty for the five structural parameters can be estimated in the R-factor contour plots. The distance, $d_{\parallel\text{CO-CO}}$, appears the most uncertain in Fig. 2; the elongated contours are narrow in the $d_{\perp\text{RhC}}$ direction (0.1Å), but quite wide in the $d_{\parallel\text{CO-CO}}$ direction (.2 - .3Å). The large error associated with the displacement of the CO molecules parallel to the metal surface (as reflected in $d_{\parallel\text{CO-CO}}$) is probably caused by our diffraction experiment being most sensitive to the projection of bond distances onto the momentum transfer vector, Δk . At normal incidence, the electron beam with a typical energy of 100 eV has a momentum transfer component of 8Å^{-1} perpendicular to the surface and only one of 1Å^{-1} in the parallel direction. We are presently analyzing the off-normal incidence data where a greater sensitivity to the $d_{\parallel\text{CO-CO}}$ distance is anticipated.

The $d_{\perp\text{CO}}$ vs. $d_{\perp\text{RhC}}$ plot implies that the Rh-O distance in the bridge-bonded CO molecule is fairly precise, but the carbon position is determined with less certainty. This can clearly be seen since the oval-shaped contour in the R-factor plot has a minor axis along the $(d_{\perp\text{CO}} + d_{\perp\text{RhC}})$ direction and a major axis along the $(d_{\perp\text{CO}} - d_{\perp\text{RhC}})$ direction. As pointed out in part 1 of this chapter, shadowing of the carbon atom by the overlying oxygen atom may be responsible for the uncertainty in the carbon atom position. If the incident LEED beam is not normal to the metal surface, we may expect less shadowing of the carbon atoms. In fact we found in the $(\sqrt{3}\times\sqrt{3})\text{R}30^\circ$ - CO structure that

the C-O distance approached the expected value (1.15Å) with the larger polar angle data (1.02Å for $\Theta=0^\circ$, 1.07Å for $\Theta=10^\circ$, and 1.09Å for $\Theta=20^\circ$).

The $d_{\perp CC}$ vs. $d_{\perp RhC}$ plot in Fig. 2 also suggests an uncertainty in the carbon position of the near-atop CO but not in the oxygen position. The sum ($d_{\perp CC} + d_{\perp RhC}$) indirectly gives the height of the oxygen atom above the surface (since the C-O bond length is kept constant) while the difference ($d_{\perp CC} - d_{\perp RhC}$) depends on the carbon atom position as well. The contour shapes in the θ vs. $d_{\perp RhC}$ plots do not have any special meaning because of the different units used for the x- and y- axis. However, an uncertainty of 10° in θ is suggested.

iv) Comparison between Kinematic and Multiple Scattering

Calculations

The search for the best structural model can be facilitated with the use of R-factors and more importantly by reducing the cost of the preliminary indicate how the relevant bond distances and angles should be varied to achieve a local minimum. Even if the actual minimum is not included in the plot, the shape of the contours surrounding the minimum will suggest in what direction the plot should be extended. However, these R-factor plots can only be used to search for a local and not a global minimum.¹³

In order to sample a large number of preliminary structures, we have used a less accurate and less expensive calculation of the intensity curves for the (2x2)-3CO overlayer. Figure 3 gives the R-factor plots obtained with the intensity curves that were calculated assuming only kinematic scattering in the CO layer. There are three major differences in the R-factor plots given in Figs. 2 and 3.

(1) The R-factor minima are significantly lower for the full-dynamical calculation. (2) The R-factor contours are slightly wider in the kinematic approximation indicating a larger uncertainty in the position of the minima; and finally, (3) the optimal bond distances ($d_{\perp\text{CO}}$, $d_{\perp\text{CC}}$, $d_{\perp\text{RhC}}$, and $d_{\parallel\text{CO-CO}}$) are slightly different ($\pm 0.1\text{\AA}$).

This comparison does however demonstrate the usefulness of the kinematic approximation in the early stages of the structural search. Well-defined minima do occur for all four R-factor plots illustrated in Fig. 3 and they represent bond distances and angles which are very consistent with those in the full-dynamical treatment. This approximation probably works as well as it does because the neighboring CO molecules in the overlayer are fairly well separated and are weaker scatterers than the Rh metal atoms.

Figure 4 shows similar R-factor plots obtained with the intermediate case of partial multiple scattering in the overlayer. Here we allowed full dynamical scattering between the carbon and oxygen in each molecule, but did not include intermolecular multiple scattering. This approximation gave substantially lower R-factor minima than the pure kinematic limit. This result is very reasonable since the carbon and oxygen atoms in the same molecule are fairly close to one another and should be more likely to multiply scatter the incident electrons.

D. SUMMARY

(1) We find that the structure of the CO layer that forms on the Rh(111) surface at 240 K and at saturation coverage is a compromise between adsorbate-adsorbate and metal-adsorbate interactions. One CO molecule stands above the bridge site, and two others lie near atop sites. On the one hand, repulsive adsorbate-adsorbate interactions displace the near-atop CO by 0.53 Å from the direct atop position; and on the other, the attractive metal-adsorbate interactions force the adsorbed CO fairly close to one another (2.8-2.9 Å) when compared to its Van der Waals diameter (3.1-3.2 Å).

(2) The carbon-metal and carbon-oxygen bond distances that we determine are consistent with similar organometallic clusters; and the three CO molecules in the (2x2) overlayer unit cell do not appear to be tilted.

(3) The average R-factor that we obtained in the (2x2)-3CO structure analysis (0.19) is significantly better than that in the $(\sqrt{3}\times\sqrt{3})\times R30^\circ$ -CO study (0.23) presented in the first part of this chapter. Both the Zanazzi-Jona (0.25 to 0.40) and Pendry (0.45 to 0.47) R-factors are also significantly better in the (2x2) structure determination. The uncertainty in three of the bond distances in the (2x2) layer ($d_{\perp CO}$, $d_{\perp RhC}$, and $d_{\perp CC}$) is estimated to be $\pm 0.05\text{Å}$ by looking at the R-factor contour plots. The fourth bond distance, $d_{\parallel CO-CO}$, has a greater uncertainty ($\pm 0.1-0.15\text{Å}$) because our diffraction experiments is more sensitive

to perpendicular rather than parallel displacements at the surface. The uncertainty in the tilt angle (θ) of the near-atop CO molecules is about $\pm 10^\circ$.

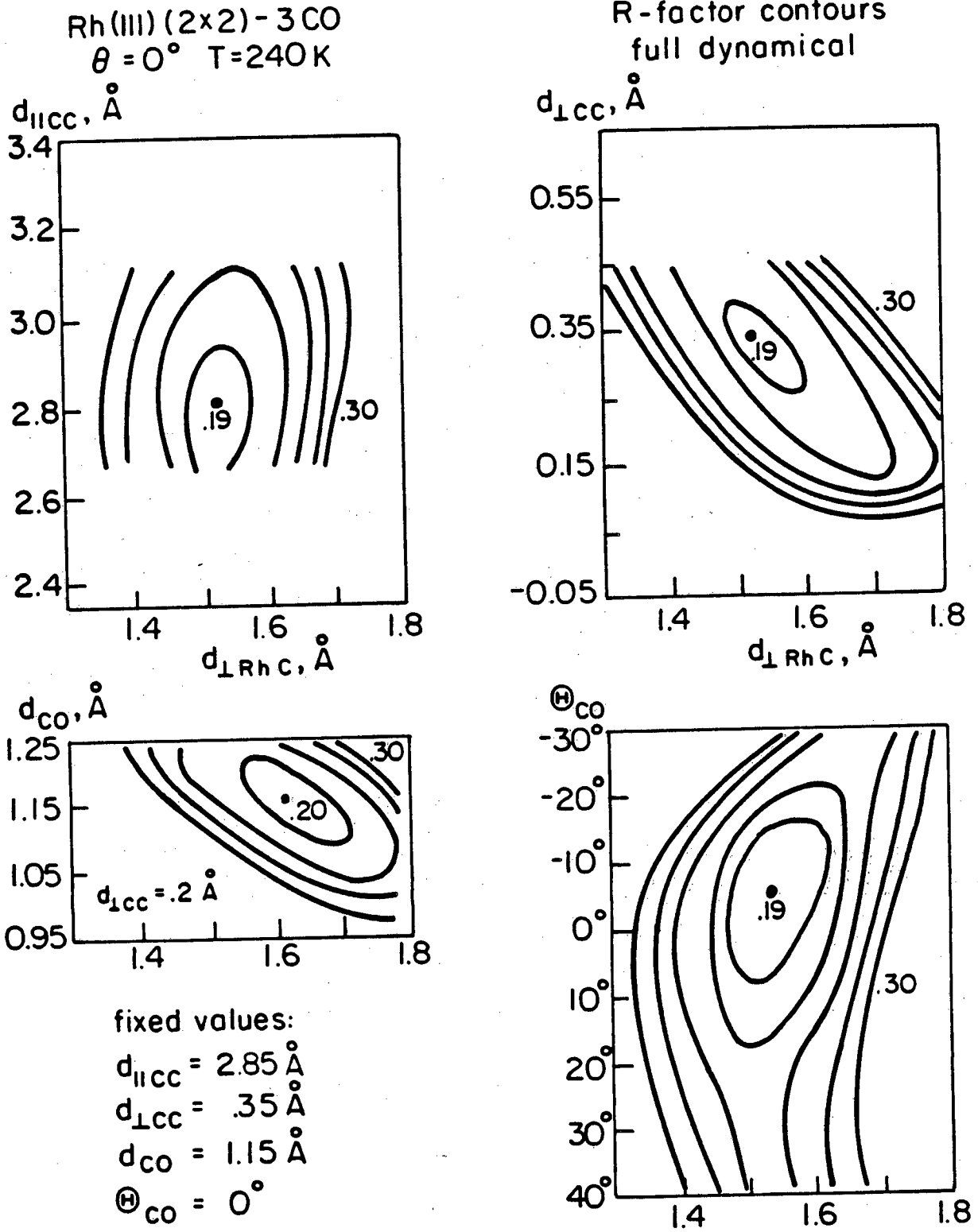
(4) We found that a kinematic approximation for the electron scattering in the CO layer was quite useful in the preliminary stage of our structural determination; the resulting bond distances and angles obtained from the less expensive calculation are consistent with those obtained from the full dynamical treatment.

References for Chapter V, Part 2

1. A. M. Bradshaw, Surface Sci. 80 215 (1979).
2. H. H. Storck, N. Golumbic and R. B. Anderson, in "The Fischer Tropsch and Related Reactions (Wiley, New York, 1951).
3. F. G. Dwyer, Catalysis Rev. 6 261 (1972).
4. G. A. Somorjai, "Chemistry in Two Dimensions: Surfaces," (Cornell University Press, Ithaca, 1981), p. 196.
5. D. G. Castner, B. A. Sexton and G. A. Somorjai, Surf. Sci. 71 (1978) 519.
6. L. H. Dubois and G. A. Somorjai, Surf. Sci. 91 (1980) 514.
7. R. P. Eischens and W. A. Pliskin, Advan. Catalysis 10 (1958) 1.
8. A. M. Bradshaw and F. M. Hoffmann, Surf. Sci. 72 (1978) 513.
9. W. Erley, H. Wagner and H. Ibach, Surf. Sci. 80 (1979) 612.
10. M. A. Van Hove and S. Y. Tong, Surface Crystallography by LEED, (Springer-Verlag, Heidelberg, 1979).
11. T. B. MacRury, W. A. Steele and B. J. Berne, J. Chem. Phys. 64 (1976) 1288.
12. P. Chini, V. Longoni and V. G. Albano, Adv. Organomet. Chem. 14 (1976) 285.
13. M. A. Van Hove and R. J. Koestner, Proc. Conf. on Determination of Surface Structure by LEED, Plenum Press (New York) 1981.

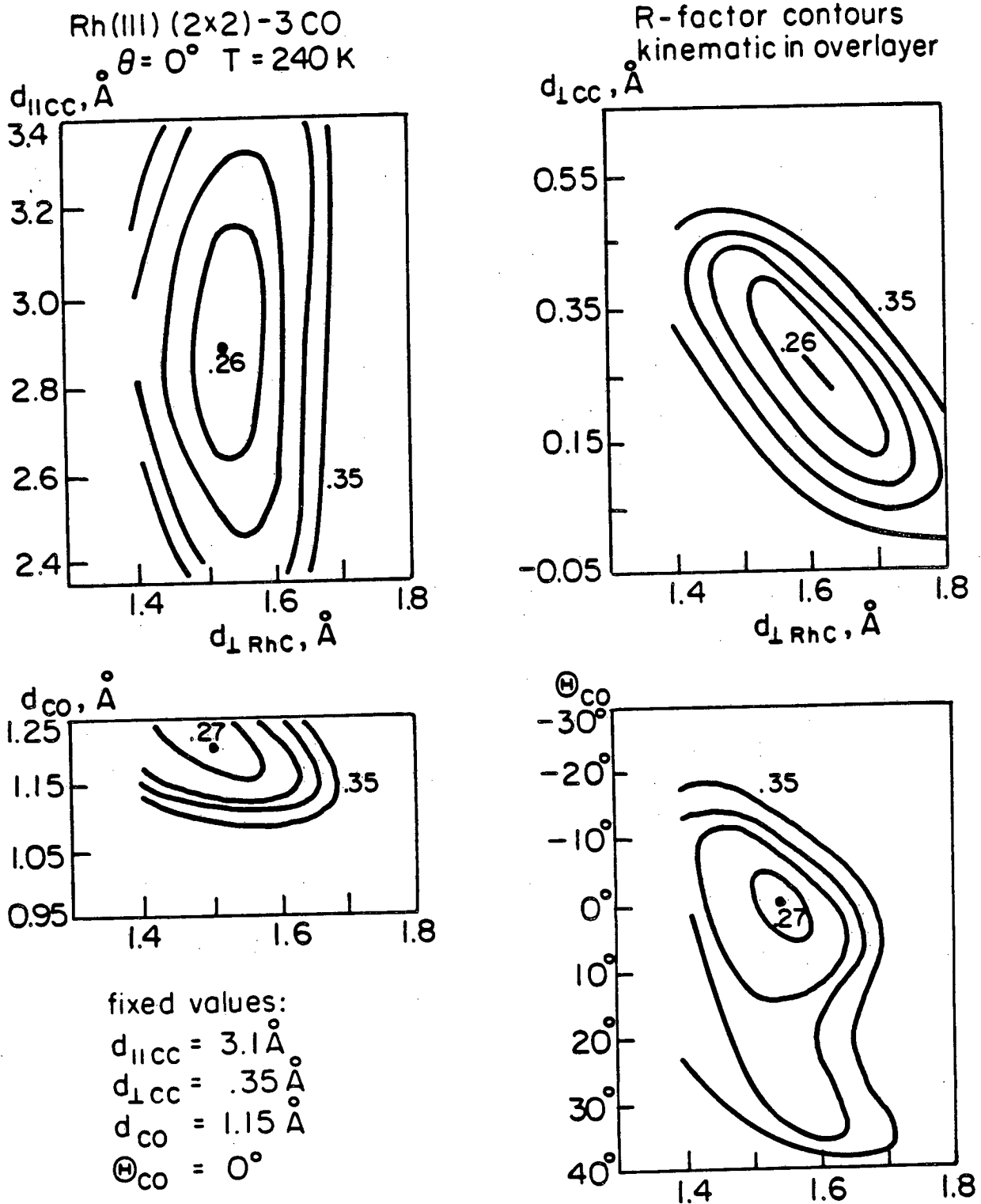
Figure Captions for Chapter V, Part 2

- Fig. 1. The structure of the (2×2) -3CO layer is shown. The upper figure presents a side-view of the surface and the lower figure gives an atop-view. The large circles represent Rh atoms (dotted--out of plane, full--in plane); and the small circles are either carbon or oxygen atoms (dotted--hexagonal mesh, full--measured positions). The five structural parameters that were varied in the LEED analysis are illustrated on the left side.
- Fig. 2. Reliability factor contour plots for the normal incidence data are shown. The calculated intensity curves in this R-factor analysis included full dynamical scattering for the overlayer.
- Fig. 3. R-factor plots obtained with only kinematic (single) scattering in the overlayer are illustrated.
- Fig. 4. R-factor plots for partial multiple scattering in the CO layer.



XBL828-6275

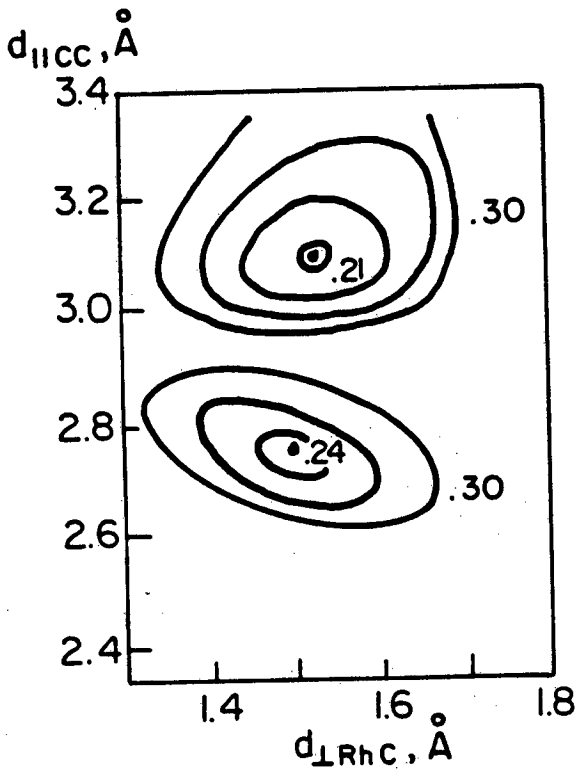
Fig. 2



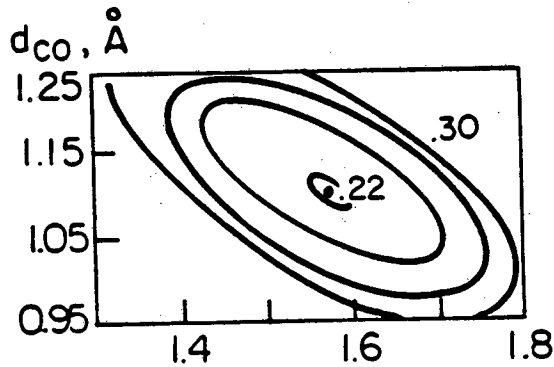
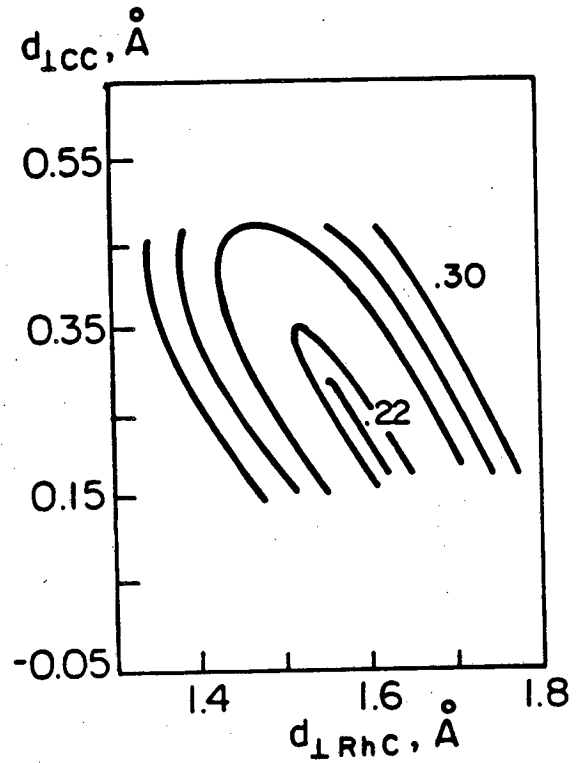
XBL 828-6274

Fig. 3

Rh(III) (2x2) - 3 CO
 $\theta = 0^\circ$ T = 240 K



R-factor contours
dynamical in molecules



fixed values:

- $d_{\parallel \text{CC}} = 3.1 \text{\AA}$
- $d_{\perp \text{CC}} = .35 \text{\AA}$
- $d_{\text{CO}} = 1.15 \text{\AA}$
- $\theta_{\text{CO}} = 0^\circ$

XBL828-6273

Fig. 4

VI. THE ADSORPTION OF C_3H_4 , C_3H_6 , AND CIS- OR TRANS-2- C_4H_8

ON Pt(111)

A. INTRODUCTION

The structure of adsorbed monolayers of unsaturated hydrocarbons on platinum single crystal surfaces has been the subject of intense investigation with a variety of techniques over the last several years. For the most part, these studies concentrated on the structure of acetylene and ethylene adsorbed on the Pt(111) face as a function of temperature. A clear picture is now emerging on the bonding of these simple hydrocarbons to the Pt(111) surface. Below room temperature, both acetylene and ethylene have been proposed to be di- σ bonded to two Pt atoms and have their carbon-carbon bond parallel to the surface; however, only acetylene forms an ordered overlayer (with a diffraction pattern corresponding to a (2×2) surface structure). Figure 1 shows the model proposed for this metastable, low temperature acetylene phase on the basis of high resolution electron energy loss spectroscopy (HREELS)^{1,2} and ultraviolet photoemission spectroscopy (UPS)^{3,4} studies; acetylene is thought to be roughly sp^2 hybridized and may have some additional π bonding to a third metal atom that tilts the molecular plane away from the surface normal. The metastable, low temperature ethylene species is probably di- σ bonded to two Pt atoms and sp^3 hybridized.^{1,3,4}

In the temperature range of about 350-450 K, the low temperature acetylene phase transforms irreversibly into vinylidene ($=C=CH_2$) in the absence of coadsorbed hydrogen and into ethylidyne ($\equiv C-CH_3$) in the presence of coadsorbed hydrogen. Evidence for the vinylidene transition comes from UPS⁵ and HREELS¹ studies, and from the existence of similar reactions in organometallic chemistry;⁶ the transition to ethylidyne was first proposed by a dynamical low energy electron diffraction (LEED) analysis.⁷ This transition to ethylidyne is an order-order transformation of $(2 \times 2) \rightarrow (2 \times 2)$ surface structures, while it is not known whether the transition to vinylidene gives an ordered surface structure. In addition to the ethylidyne model, early HREELS work¹ suggested an ethylidene ($=CHCH_3$) species and UPS studies⁵ indicated a vinyl-like ($=CH-CH_2^-$) species (better named 1-ethanyl-2-ylidene). Recently, however, the ethylidyne species (see Fig. 2) has gained acceptance over the competing models partly as a consequence of a normal mode analysis⁸ of the IR spectrum for an organometallic analogue, $Co_3(CCH_3)(CO)_9$, that shows excellent agreement with the ethylidyne model's vibrational peak assignment for the original HREELS spectrum.¹ Further, the C_2H_3 stoichiometry of ethylidyne was measured for the ethylene overlayer from a combined UPS and thermal desorption spectroscopy (TDS) study,⁵ while an angle-resolved UPS study⁹ indicated the presence of an ethylidyne species.

The low temperature ethylene phase was similarly observed to make an irreversible transition to an ethylidyne species at 280 K since the resulting LEED pattern,¹⁰ I-V profiles,¹⁰ HREELS spectra,¹ and

UPS spectra¹¹ are identical to those obtained from the stable, hydrogen-treated acetylene overlayer. Finally, both acetylene and ethylene above 450 K have been seen by HREELS¹² to fragment into smaller hydrocarbon species ($\equiv\text{CH}, =\text{CH}_2$).

These studies reveal the rich diversity and temperature dependent character of the surface chemical bond of organic molecules. It is our aim, by systematic studies of the structure of small hydrocarbon molecules on transition metal surfaces, to uncover the dominant bonding characteristics common to this family of adsorbed molecules. For this reason we have studied and report in this chapter the structure of ordered monolayers of propylene, methylacetylene, and the cis- and trans-2-butenes adsorbed on the Pt(111) face. We present interpretations of both the observed LEED patterns and the large set of intensity vs. energy (I-V) curves obtained for these molecules. In this way we aim to demonstrate that these larger, unsaturated hydrocarbons bond to the Pt(111) face in a way very similar to acetylene and ethylene by forming alkylidyne ($\equiv\text{C}-(\text{CH}_2)_n-\text{CH}_3$) species at room temperature. Specifically, the C_3 and C_4 structures can be obtained by substituting methyl groups for single hydrogens of the C_2 and C_3 alkylidyne species, respectively. Table 1 summarizes our models for C_2 , C_3 , and C_4 hydrocarbon adsorption on the Pt(111) surface; this table is included to aid in following the discussion below by exhibiting the relationship among various structures.

Convincing additional evidence for our proposed alkylidyne structure on the Pt(111) comes from similar HREELS¹³ and LEED (Chapter VIII and Ref. 14) experiments being performed for the same

hydrocarbon molecules adsorbed on a different metal surface, Rh(111), where a very similar sequence of LEED patterns and I-V curves occurs.

B. EXPERIMENTAL

The C₃ and C₄ hydrocarbon adsorption experiments were carried out in two different vacuum chambers; each was equipped with retarding-field Auger electron spectroscopy, a Varian ion sputtering gun, a Varian off-axis LEED gun, a UTI quadrupole mass spectrometer, and a modified Varian manipulator allowing azimuthal and polar rotations. The base pressure of both chambers was maintained at 1×10^{-9} torr with H₂ and CO as the major background gases. The I-V curves were measured using a photographic technique already described in Ref. 15 and Chapter III.C. The photographs of the LEED spot pattern, taken at 2 eV intervals, were digitized with a scanning microdensitometer; the resulting density map at successive energies was translated with a new computer program into the desired intensity-energy (I-V) profiles.

The Pt sample was cleaned of calcium, phosphorus, and carbon by a combination of oxygen treatments (5×10^{-7} torr O₂, 10 minutes, 700°C with a subsequent flash to 1000°C) and Ar ion bombardments (with subsequent 800°C annealing for 5 minutes). Ar ion bombardments would not leave any contaminating carbon on the surface after a series of 1-2 L hydrocarbon exposures; however, after the 100-1000 L exposures, oxygen treatments were necessary to effectively remove the carbon. The sample was flashed just before the hydrocarbon exposures to remove any pre-adsorbed carbon monoxide and hydrogen; yet about 0.05 monolayers of carbon monoxide (as determined by Thermal Desorption Yield Spectroscopy)

would co-adsorb with each hydrocarbon exposure due to the displacement of the carbon monoxide from the chamber wall.

C. RESULTS

i) LEED Patterns

The clean platinum (111) crystal face was held at 300 K while it was exposed to the different hydrocarbons. A 1-2 L exposure (1 L = 10^6 torr sec) of methylacetylene or propylene was sufficient to produce a well ordered (2x2) surface structure with sharp diffraction beams. (Our gas exposures are uncorrected for ion-gauge sensitivity and for any pressure difference between the ion-gauge and crystal.) It was found that overexposure to either organic vapor would not reduce the quality of the LEED pattern, whereas only a 10% overexposure to acetylene in previous studies would cause a noticeable disordering of the adsorbed layer.¹⁰ Both C₃ hydrocarbons ordered spontaneously upon adsorption, unlike ethylene that ordered well only when exposed to the electron beam.¹⁰ The C₃ adsorbates showed about a 50% higher carbon coverage than the C₂ overlayers by Auger Electron Spectroscopy (AES).

Only one ordered phase of propylene was found by the inspection of the I-V curves from its (2x2) surface structure in the temperature range of 280-400 K. Below 280 K a poor (1x1) LEED pattern is obtained that is indicative of disordered propylene adsorption. The methylacetylene that also adsorbs in a (2x2) surface structure at room temperature makes an order-order transition [(2x2)metastable+(2x2)stable] in the presence of a background hydrogen after one hour at 350-400 K or after 24 hours at 300 K as determined by monitoring the

I-V curves. The (2×2) surface structures of both C₃ hydrocarbons would disorder at around 400 K similar to the behavior of the C₂ hydrocarbons adsorbed on Pt(111).

The cis- and trans-2-butenes were admitted into the chamber at low (~10 L), intermediate (~100 L), and high (~1000 L) exposures. For even the lowest exposures (~1/4 L), a $(2\sqrt{3}\times 2\sqrt{3})R30^\circ$ surface structure was observed. The half-order spots of this very low exposure pattern, i.e., those already present in the diffraction pattern of a (2×2) unit cell, had gained substantial intensity and were fairly well focused, while the remaining spots (those in addition to the half-order and integral-order spots) were very diffuse and weak in intensity. Upon increasing the exposure to ~10 L, the half-order spots would reach near-maximum intensity, though the remaining sixth-order spots did not become comparably strong and sharp until an exposure of ~1000 L had been reached. At intermediate exposures of ~100 L, a well-ordered LEED pattern corresponding to an (8×8) surface structure would sometimes form, while at other times the $(2\sqrt{3}\times 2\sqrt{3})R30^\circ$ structure would continue to appear with the sixth-order beams becoming gradually more intense and better focused as the hydrocarbon exposure approached 1000 L. When the (8×8) phase did form, it could easily transform into the $(2\sqrt{3}\times 2\sqrt{3})R30^\circ$ structure with increasing exposure. Figure 3 shows the LEED patterns associated with (a) the stable propylene (2×2) structure, (b) the (2×2) structure of the 2-butenes formed at ~10 L, (c) the $(2\sqrt{3}\times 2\sqrt{3})R30^\circ$ -2-butene overlayer at ~1000 L, and (d) the (8×8)-2-butene structure seen at ~100 L.

The cis- and trans-2-butenes did not give an ordered LEED pattern below about 280 K, while the ordered, room temperature phases $[(2\sqrt{3}\times 2\sqrt{3})R30^\circ$ and $(8\times 8)]$ would disorder at 325 K. Interestingly, the intensity of the half- and integral-order spot intensities would not fade as quickly as that from the other spots in the $(2\sqrt{3}\times 2\sqrt{3})R30^\circ$ and (8×8) overlayers when the temperature or the electron beam exposure is increased. Thus the gradual emergence of a well-ordered $(2\sqrt{3}\times 2\sqrt{3})R30^\circ$ surface structure with increasing hydrocarbon exposure as well as the delicate nature of the sixth- or eight-order spots with increasing temperature or LEED beam exposure suggests the presence of a $(2\sqrt{3}\times 2\sqrt{3})R30^\circ$ superlattice imposed on the usual (2×2) lattice of hydrocarbon adsorption sites.

ii) Comparison of I-V Curves

The I-V spectra for metastable methylacetylene (28 independent beams), stable methylacetylene (28 independent beams), and propylene (26 independent beams) at five angles of incidence ($\theta=0,4,8,10,16^\circ$; $\phi=0^\circ$) were obtained. A smaller data base of only normal incidence curves ($\theta=0^\circ$, 4-7 independent beams) was obtained for the $(2\sqrt{3}\times 2\sqrt{3})R30^\circ$ cis- and trans-2-butene, and (8×8) trans-2-butene structures; these C_4 spectra are shown in Appendix I. In this chapter we show several I-V curves that may be taken as representative of the available much larger data base.

There are many identities and similarities to be found in the diffraction data obtained for the different hydrocarbons studied. We would like to call attention to four important findings: (1) Figure 4

illustrates the similarity between I-V curves obtained for the metastable methylacetylene and acetylene structures. (2) Figures 5 and 6 show that the stable phases of acetylene, ethylene, methylacetylene, and propylene have nearly identical I-V curves except for a few systematic and reproducible differences which occur between the curves for C_2 hydrocarbons and C_3 hydrocarbons. (3) We compare in Fig. 7 the low exposure (~ 10 L) (2×2) cis-2-butene I-V curves to both the high exposure (~ 1000 L) $(2\sqrt{3} \times 2\sqrt{3})R30^\circ$ cis- or trans-2-butene and the (2×2) propylene curves. The spectra for the (2×2) cis-2-butene structure are intermediate between those for (2×2) propylene and those for $(2\sqrt{3} \times 2\sqrt{3})R30^\circ$ cis- or trans-2-butene. This comparison of I-V curves indicates that when the extra diffraction beams from the $(2\sqrt{3} \times 2\sqrt{3})R30^\circ$ structures of the C_4 hydrocarbon overlayer are very weak in intensity and diffuse, the half-order intensity spectra are very similar for all the C_2 , C_3 , and C_4 hydrocarbon overlayers. But once the $(2\sqrt{3} \times 2\sqrt{3})R30^\circ$ surface pattern is fully developed, the half-order intensity curves for the C_2 or C_3 hydrocarbons and the C_4 hydrocarbon diverge. (4) We compare in Fig. 8 some common I-V profiles for the high exposure $(2\sqrt{3} \times 2\sqrt{3})R30^\circ$ cis- or trans-2-butene as well as the intermediate exposure (8×8) trans-2-butene structures. The three sets of common I-V spectra are seen to be identical within experimental error, indicating the cis- and trans-isomers probably form the same overlayer structure, as well as showing that the (8×8) trans-2-butene overlayer geometry must be very similar to that of the $(2\sqrt{3} \times 2\sqrt{3})R30^\circ$ surface structure.

D. DISCUSSION

The similarity or virtual identity of the C₂, C₃, and C₄ hydrocarbon I-V spectra indicate the structural similarity in the adsorbed species. The geometric location, bond distances, and orientation of that part of the carbon skeleton in each molecule ($\equiv\text{C}-\text{CH}_2\text{R}$ or $\text{H}_2\text{C}=\text{CHR}$) that is responsible for anchoring it to the platinum surface in an ordered structure is the same from adsorbate to adsorbate. The very similar progression of LEED patterns for these adsorbed species with increasing temperature further indicates the similarity in both their structure and their intramolecular rearrangement during the metastable to stable phase transition.

The similarity of the temperature dependent structural reorganization is also demonstrated in a recent thermal desorption study (TDS)¹⁶ of these molecules as can be seen in Fig. 9. The desorption of hydrogen is monitored from the adsorbed monolayers of the alkenes on the Pt(111) crystal face. The peaks indicate the maximum rates of desorption. The adsorbed layers dehydrogenate sequentially with increasing temperature in a very similar manner. Peaks A and C are found in all the desorption traces for ethylene, propylene, and the 2-butenes, while peak B shifts to lower temperature with the longer chain hydrocarbons. Peak A is assigned to partial dehydrogenation of the alkene by removal of one hydrogen in the conversion from a parallel bonded, metastable species to a stable species. Peak B corresponds to C-C bond scission and fragmentation of the hydrocarbons, and peaks C probably represent the final dehydrogenation of the small hydrocarbon fragments left on the platinum surface. It is important to note the

adsorbed hydrocarbons do not (at peak A) decompose into the species that the smaller hydrocarbons adopt; this indicates that the larger adsorbed hydrocarbons retain their gas-phase carbon skeleton at room temperature.

Let us now address the question why certain diffraction beam intensities from the ordered overlayers of the C_2 , C_3 , and C_4 hydrocarbons remain unaltered. A perfectly disordered layer is diffuse in space. If that layer gradually orders into a certain lattice, the contribution by that layer to beams defined by its reciprocal lattice grows. As a result, existing I-V curves can be strongly affected if the scattering strength of the newly ordered atoms is significant. Thus our observations of a $(2\sqrt{3}\times 2\sqrt{3})R30^\circ$ surface structure developing from a (2×2) structure with gradual changes in the I-V curves from the (2×2) structure indicate that atoms which were disordered, are ordering into a $(2\sqrt{3}\times 2\sqrt{3})R30^\circ$ lattice; at the same time the other atoms responsible for the ordered (2×2) structure are very little affected by this new ordering process.

We shall now discuss the proposed structures for each adsorbate (methylacetylene, propylene, and the 2-butenes). These surface structures are also summarized in Table 1.

i) Metastable Methylacetylene ($H_3C-C\equiv CH$)

We interpret the virtual identity of the metastable acetylene and methylacetylene I-V spectra shown in Fig. 4 as follows: Replacing a hydrogen atom of the adsorbed C_2H_2 species by a methyl group produces the structure of adsorbed methylacetylene, if one assumes a

randomness in the choice of the hydrogen atom or a randomness in the orientation of the methyl group. The probable sp^2 rehybridization of methylacetylene twists the methyl group away from the surface, thereby giving it the necessary space to rotate more freely. Figure 10 illustrates our proposed geometry for the metastable methylacetylene species.

ii) Stable Propylene ($CH_3-CH=CH$)

Between 280 K and the decomposition temperature of 400 K, the I-V spectra for propylene and ethylene are nearly identical, as can be seen in Figs. 5 and 6. This can be interpreted to imply that the room temperature propylene species has a structure like that of the room temperature ethylene except that one of the ethylidene hydrogens is replaced by a methyl group that is rotationally disordered. This model, consisting of a propylidene species, is illustrated in Fig. 11. Using standard Van der Waals atomic radii, we find that neighboring molecules nearly touch in this structure. In fact, some relative orientations of neighboring methyl groups are sterically not possible, but enough rotational freedom is left to explain the virtual identity of I-V curves mentioned above. These steric considerations are also consistent with the observed spontaneous ordering of the stable propylene molecules, contrasting with the non-spontaneous ordering of the smaller stable ethylene molecules that require exposure to the electron beam. Furthermore, a 50% overexposure of propylene or methylacetylene does not disorder the (2x2) LEED pattern, whereas it does

with ethylene or acetylene; this should be expected since there would be less interstitial adsorption due to the C₃ hydrocarbons' larger size.

iii) Stable Methylacetylene (CH₃-C≡CH)

Methylacetylene like acetylene shows a hydrogen assisted order-order transformation to form a stable (2×2) overlayer at 300-350 K. The stable structure I-V curves (Figs. 5, 6) are nearly identical to those for the room temperature ethylene, acetylene, and propylene phases. This, together with the intactness of the carbon skeleton, demonstrates that the parallel bonded sp² hybridized methylacetylene transforms in the presence of additional hydrogen into the same propylidyne species that propylene does (Fig. 11).

iv) Low (~10 L) and High (~1000 L) Exposure 2-Butenes
(CH₃-CH=CH-CH₃)

The cis- and trans-2-butenes gave identical (2√3×2√3)R30° I-V profiles in Fig. 8 and have been shown to yield identical TDS spectra.¹⁶ This indicates that both isomers form the same surface structure so that we can ignore their different molecular origin in the following discussion.

At even the lowest 2-butene exposures (~1/4 L) tried, a LEED pattern corresponding to a (2√3×2√3)R30° unit cell was observed with poorly developed extra spots, i.e., those in addition to the half-order and integral-order ones. In Fig. 7 we saw that the half-order I-V profiles for the low exposure 2-butene phase seem intermediate between the stable propylene spectra and the 2-butene curves from the well developed (2√3×2√3)R30° structure. This suggests that the low exposure

structure consists of a butylidyne species ($\equiv\text{C}-\text{CH}_2-\text{CH}_2-\text{CH}_3$) with a partially disordered ethyl group ($-\text{CH}_2-\text{CH}_3$), while the high exposure structure consists of a butylidyne species with the ethyl group ordered into a $(2\sqrt{3}\times 2\sqrt{3})R30^\circ$ unit cell.

From a parallel study,¹⁴ propylene adsorbed on the Rh(111) surface is shown to behave very much like the 2-butenes on Pt(111) by forming a low exposure (2×2) and, at higher exposures, a $(2\sqrt{3}\times 2\sqrt{3})R30^\circ$ surface structure. In fact, the half-order diffraction beam I-V curves from the low exposure propylene phase on Rh(111) are even more similar to the I-V spectra obtained from the (2×2) ethylene structure than for the corresponding low exposure 2-butene intensity spectra on Pt(111). This observation is to be expected since the partially ordered ethyl group ($-\text{CH}_2-\text{CH}_3$) of butylidyne ($\equiv\text{C}-(\text{CH}_2)_2-\text{CH}_3$) has a larger scattering strength than the methyl group ($-\text{CH}_3$) of propylidyne ($\equiv\text{C}-\text{CH}_2-\text{CH}_3$) and thus should alter the resulting I-V spectra more dramatically.

The appearance of a $(2\sqrt{3}\times 2\sqrt{3})R30^\circ$ unit cell is presumably due to the interaction between neighboring ethyl groups in the butylidyne overlayer. A possible structural model is illustrated in Fig. 12. Few other models are compatible with the available experimental evidence. Three butylidyne molecules fit in the unit cell, but are restricted in the orientation of the ethyl groups by mutual steric hindrance. The upper part of Fig. 12 shows hydrogen atoms with their Van der Waals radii, while the lower part emphasizes the hydrocarbon skeleton in the same structure. The neighboring hydrocarbon arms are rotated as far as possible from each other, while the well-known planar zig-zag

conformation of the carbon skeleton within each butylidyne species leads to a minimum in the repulsion of non-bonding carbon atoms in the chain. Note that this model places the upper methyl groups in a vertical direction, thus minimizing overlap between these groups on neighboring molecules. We have assumed in Figs. 11 and 12 a "staggered" rather than "eclipsed" bonding arrangement about the two carbon atoms closest to the metal surface, paralleling the lowest energy conformation of ethane. The exact bond lengths and angles in the ethyl groups can only be determined by a detailed analysis of the I-V curves which would also test the correctness of our structural model. Such an analysis is planned.

Finally, we note that the butylidene [$=\text{CH}-(\text{CH}_2)_2-\text{CH}_3$] or 1-butanyl-2-ylidene [$=\text{CH}-\text{CH}(\text{CH}_2\text{CH}_3)-$] species cannot be as easily packed into the $(2\sqrt{3}\times 2\sqrt{3})R30^\circ$ unit cell; this, then, provides further support for ethylidyne ($\equiv\text{C}-\text{CH}_3$) over ethylidene ($=\text{CH}-\text{CH}_3$) or 1-ethanyl-2-ylidene ($=\text{CH}-\text{CH}_2-$).

Interestingly, a 100-fold higher exposure is needed to adequately order the sixth-order spots in the diffraction pattern for the $(2\sqrt{3}\times 2\sqrt{3})R30^\circ$ structure. It may be that the large hydrocarbons can block neighboring adsorption sites so that only after a period of time would any given butylidyne species conform in such a way to open a neighboring, unoccupied site to an approaching molecule. In this way the saturation coverage is reached only after a fairly long time and only then could the C_4 molecules be crowded enough to adequately order into the $(2\sqrt{3}\times 2\sqrt{3})R30^\circ$ unit cell. Yet it should be emphasized

that we believe a near-saturation coverage is already achieved at 10 L since the half-order spots are very well focused and near maximum intensity.

v) Intermediate Exposure (~100 L) 2-Butenes

The (8×8) trans-2-butene pattern formed after ~100 L exposure at 300 K on the Pt(111) surface; Fig. 8 shows that the common beam profiles between the (8×8) and $(2\sqrt{3}\times 2\sqrt{3})R30^\circ$ structures are identical. This indicates that the two phases must have very similar structures, yet we cannot suggest a reasonable model for the (8×8) structure at present.

E. SUMMARY

Within the range of molecules considered in this paper (ethylene, acetylene, propylene, methylacetylene, and the 2-butenes), the alkenes and alkynes have closely related LEED patterns and I-V spectra. Two phases exist for each of these molecules adsorbed on Pt(111); for each molecule, a low temperature, "metastable" species is parallel bonded to the surface. Upon warming to about room temperature, and in the presence of hydrogen for the alkynes, a conversion takes place to an alkylidyne species that is bound to three platinum atoms and has its C-C bond nearest to the metal substrate oriented perpendicularly to the surface. Table 1 summarizes the different surface structures proposed for the C₂, C₃, and C₄ hydrocarbons considered.

Though a LEED analysis should be undertaken to confirm our proposed butylidyne structure, convincing evidence is already contained in the similarity of the I-V spectra, in the Van der Waals models of these large close-packed hydrocarbons, in the gradual development of a

$(2\sqrt{3}\times 2\sqrt{3})R30^\circ$ LEED pattern with increasing exposure, and in the correlations among C_2 , C_3 , C_4 hydrocarbon TDS spectra. We show that the LEED pattern comes about by having the ethyl group of the butylidyne species begin to order into a $(2\sqrt{3}\times 2\sqrt{3})R30^\circ$ unit cell, while two carbon atoms of the C_4 molecule that are nearest the metal remain in positions that are identical to those occupied in the ethylidyne species with (2×2) unit cell. We further show that the model of the alkylidyne surface species agrees with the experimental evidence much better than other models such as alkylidene or 1-alkanyl-2-ylidene. Of interest also is a parallel sequence of very similar structures found for C_2 and C_3 hydrocarbons on Rh(111).

Finally, we suggest that the intermediate exposure (8×8) 2-butene structure may also consist of a butylidyne species. Yet more experiments are needed to elucidate this structure.

References for Chapter VI

1. H. Ibach and S. Lebwald, J. Vac. Sci. & Technol. 15 407 (1978).
2. H. Ibach, H. Hopster and B. Sexton, Appl. Phys. 14 21 (1977).
3. J. E. Demuth, Surface Sci. 84 315 (1979).
4. T. E. Felter and W. H. Weinberg, Surface Sci. 103 265 (1981).
5. J. E. Demuth, Surface Sci. 80 367 (1979).
6. a) A. J. Deeming and M. Underhill, J. C. S. Dalton, 1415 (1974).
b) A. J. Deeming and M. Underhill, J. C. S. Dalton, 1614 (1975).
7. L. L. Kesmodel, L. H. Dubois and G. A. Somorjai, J. Chem. Phys. 70 2180 (1979).
8. P. Skinner, M. W. Howard, I. A. Oxton, S. F. A. Kettle,
D. B. Powell and N. Sheppard, J. Chem. Soc. Faraday Trans. 77
1203 (1981).
9. M. R. Albert, L. G. Sneddon, T. Gustafsson and E. W. Plummer,
Surface Sci. 120 (1982).
10. P. C. Stair and G. A. Somorjai, J. Chem. Phys. 66 2036 (1977).
11. W.-J. Lo, Y.-W. Chung, L. L. Kesmodel, P. C. Stair and G. A.
Somorjai, Solid State Comm. 22 335 (1977).
12. A. M. Baro and H. Ibach, J. Chem. Phys. 74 4194 (1981).
13. L. H. Dubois, D. G. Castner and G. A. Somorjai, J. Chem. Phys. 72
5234 (1980).
14. R. J. Koestner, M. A. Van Hove and G. A. Somorjai (to be
published).

15. P. C. Stair, T. J. Kaminska, L. L. Kesmodel, and G. A. Somorjai, Phys. Rev. B11 623 (1975).
16. M. Salmeron and G. A. Somorjai, J. Phys. Chem. 86 341 (1982).

Table 1. Summary of Structural Models for C₂, C₃, and C₄ Hydrocarbons Adsorbed on Pt(111)

	C ₂ H ₂ (acetylene)	C ₂ H ₄ (ethylene)	C ₃ H ₄ (methylacetylene)	C ₃ H ₆ (propylene)	low exposure (10 L)	cis- or trans- 2-C ₄ H ₆ high exposure (1000 L)	intermediate exposure (100 L)
<u>METASTABLE SPECIES</u>							
LEED pattern	(2x2)	disordered	(2x2)	disordered	disordered	--	--
proposed structure	parallel bonded	parallel bonded	parallel bonded	possibly parallel bonded	possible parallel bonded	--	--
	di-o, (~sp ²)	di-o, (~sp ³)	di-o, (~sp ²)	di-o, (~sp ²)	di-o, (~sp ³)	--	--
techniques used	ELS, UPS	ELS, UPS	LEED (this work)	TDS	TDS	--	--
<u>CONVERSION TO STABLE SPECIES</u>							
temperature	350 K	280 K	350 K	280 K	280 K	--	--
hydrogen needed?	Yes	No	Yes	No	No	--	--
<u>STABLE SPECIES</u>							
LEED pattern	(2x2)	(2x2) (with e ⁻ beam)	(2x2)	(2x2)	diffuse (2√3x2√3)R30°	(2x√3x2√3)R30°	(8x8)
proposed structure	ethylidyne	ethylidyne	propylidyne extra methyl randomly oriented	butylidyne extra ethyl randomly oriented	butylidyne extra ethyl randomly oriented	butylidyne extra ethyl locked in position	butylidyne
techniques used	LEED, ELS, TDS	LEED, ELS, TDS	LEED (this work)	LEED (this work)	LEED (this work), TDS	LEED (this work)	LEED (this work)
ALKYLIDYNE DECOMPOSITION TEMPERATURE	450 K	450 K	400 K	400 K	325 K	325 K	325 K

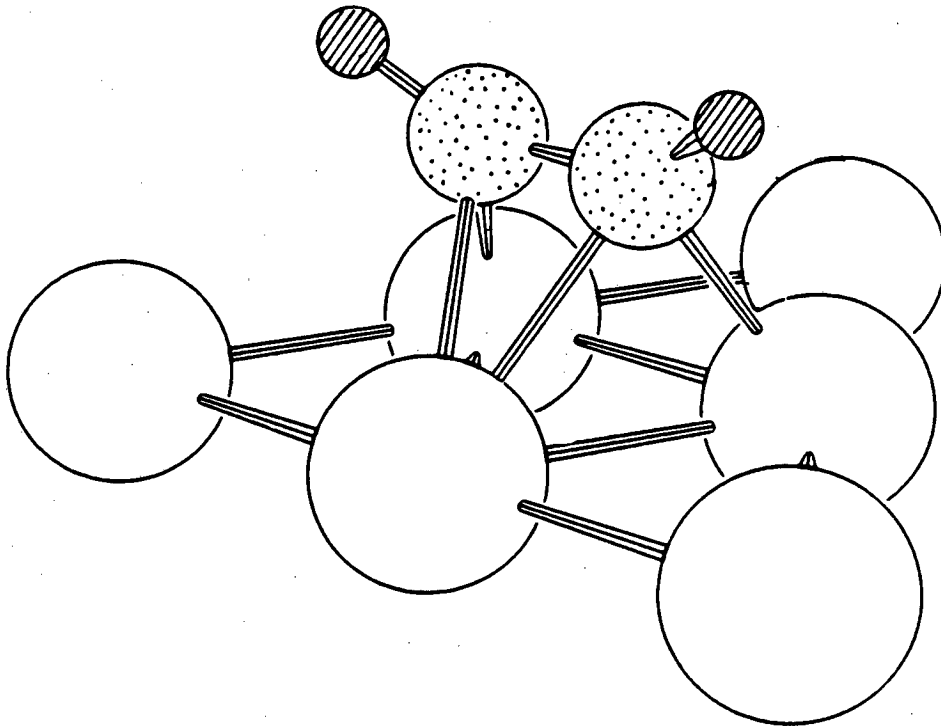
Figure Captions for Chapter VI

- Fig. 1. The metastable acetylene species is shown di- σ bonded to two Pt atoms with some additional π bonding to a third Pt atom.
- Fig. 2. The stable acetylene or ethylene phase forms an ethylidyne species.
- Fig. 3. Progression of LEED patterns for the room temperature structures of the C_2 , C_3 , and C_4 hydrocarbons.
- Fig. 4. Comparison of the I-V curves obtained from the metastable acetylene and methylacetylene structures.
- Fig. 5. Comparison of the I-V curves obtained from the stable acetylene, ethylene, methylacetylene, and propylene phases.
- Fig. 6. Comparison of the I-V curves obtained from the stable acetylene, ethylene, methylacetylene, and propylene phases.
- Fig. 7. Comparison of the I-V curves obtained from the (2×2) propylene, the low exposure (~ 10 L) $(2\sqrt{3} \times 2\sqrt{3})R30^\circ$ 2-butene, and the high exposure (~ 1000 L) $(2\sqrt{3} \times 2\sqrt{3})R30^\circ$ cis-2-butene structures.
- Fig. 8. Comparison of the I-V curves obtained from the high exposure (~ 1000 L) $(2\sqrt{3} \times 2\sqrt{3})R30^\circ$ cis-2-butene, the high exposure (~ 1000 L) $(2\sqrt{3} \times 2\sqrt{3})R30^\circ$ trans-2-butene, and the intermediate exposure (~ 100 L) (8×8) trans-2-butene structures.
- Fig. 9. TDS spectra of ethylene (C_2H_4), propylene (C_3H_6), and the 2-butenes (C_4H_8) adsorbed on Pt(111). (This figure is taken from Ref. 16).

Fig. 10. The metastable methylacetylene species is di- σ bonded to two Pt atoms with some additional π -bonding to the third Pt atom. The methyl groups is presumed randomly attached to either of the two lower carbon atoms.

Fig. 11. The stable methylacetylene or propylene phase forms a propylidyne species, shown here with various methyl orientations.

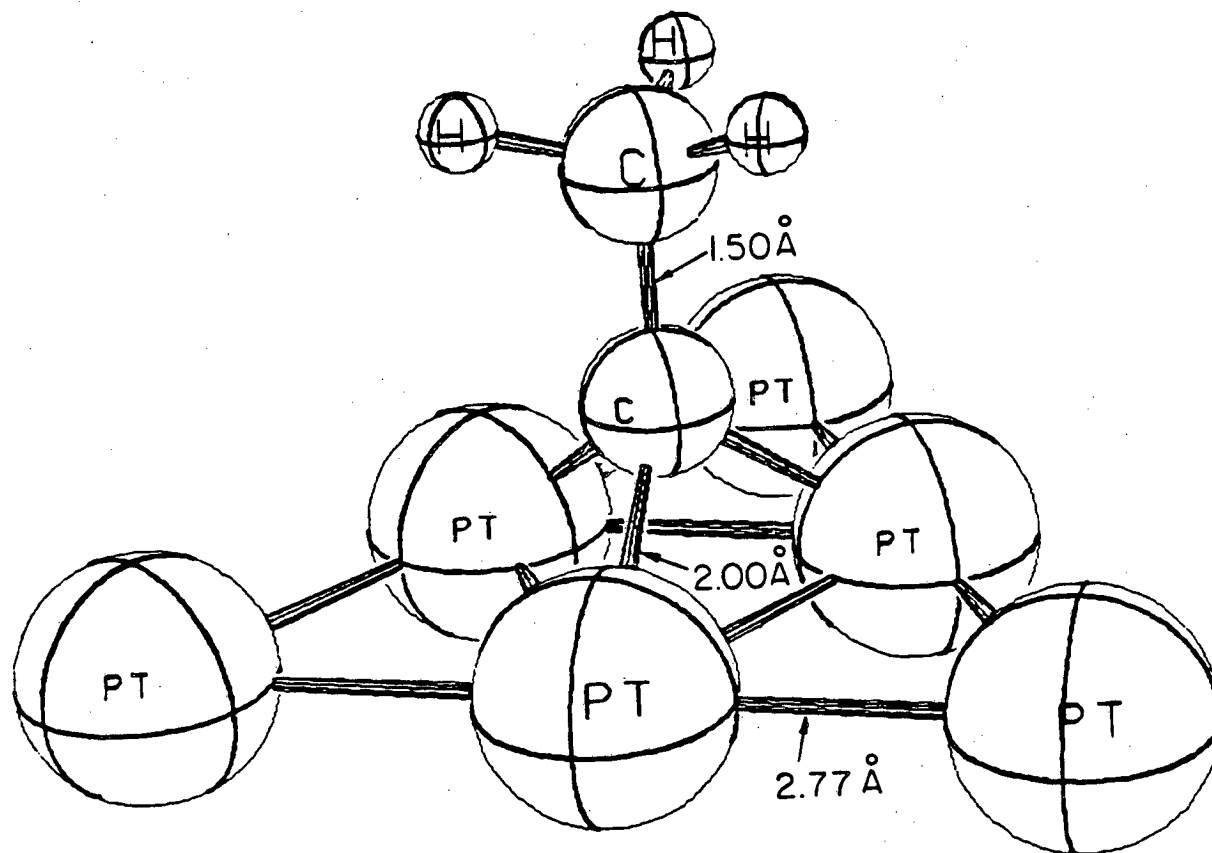
Fig. 12. The 2-butenes form a butylidyne complex on Pt(111), seen here perpendicular to the surface. The upper sketch shows the Van der Waals radii of the adsorbed hydrocarbon, while the lower sketch emphasizes the carbon skeleton. The $(2\sqrt{3}\times 2\sqrt{3})R30^\circ$ unit cell containing three butylidynes is drawn.



Metastable acetylene on Pt(III)

XBL817-6066

Fig. 1



Pt (III) + ethynidyne

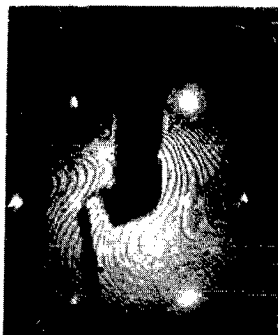
XBL794-6167

Fig. 2

T = 300 K,

$\theta = 0^\circ$,

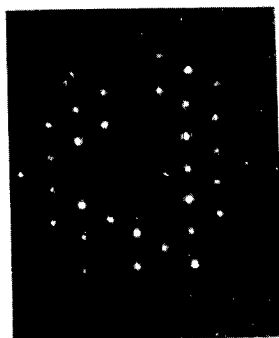
52 eV



Pt(III) - C₂H₄ - (2×2)
" - C₂H₂+H- "
" - C₃H₆- "
" - C₃H₄+ H- "



Pt(III)-cis-2-C₄H₈- (2×2) + diffuse (2√3×2√3) R30°



Pt(III) - cis-2- C₄H₈- (2×2) + (2√3×2√3) R30°
" - trans-2- C₄H₈- " "



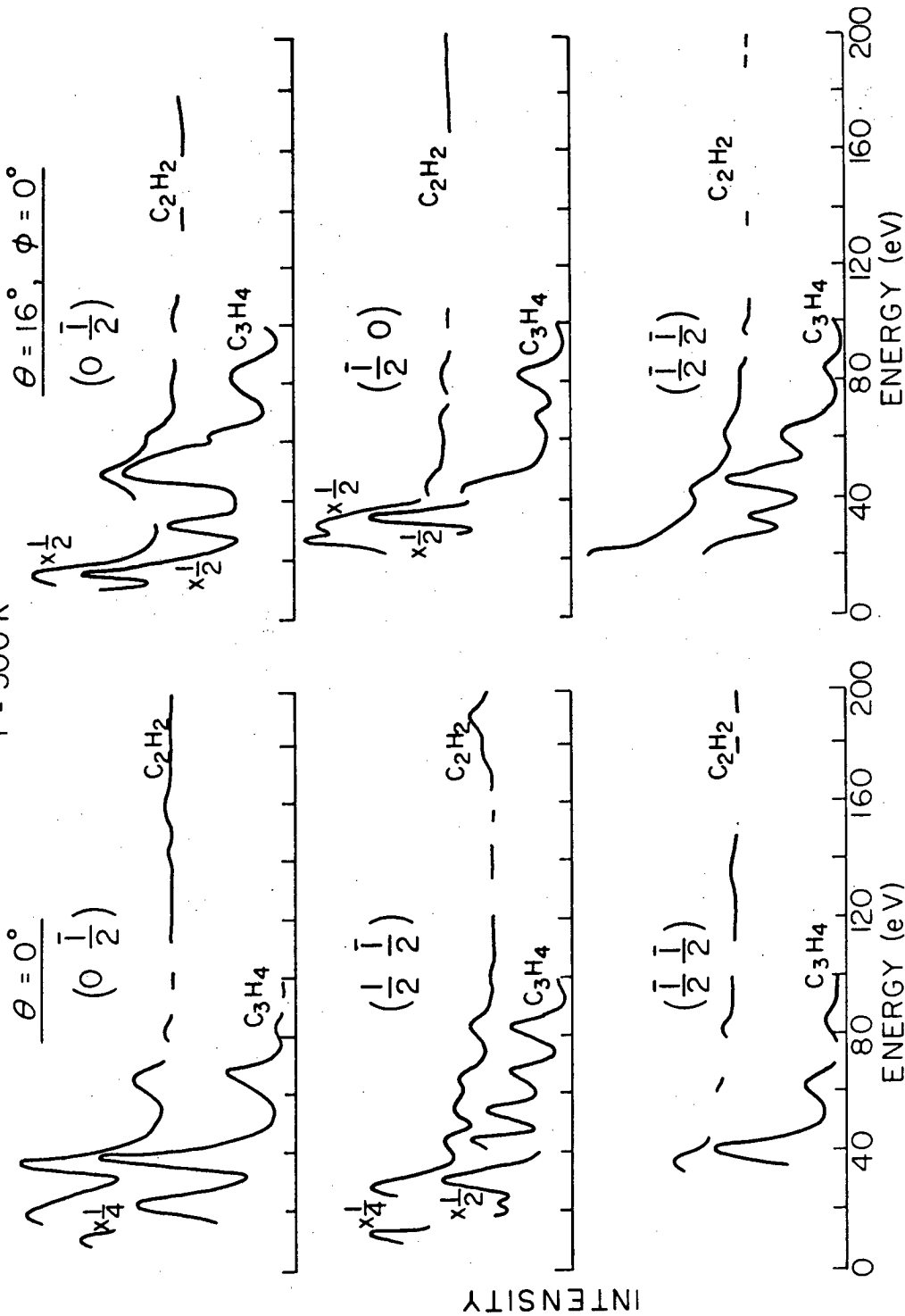
XBB 813-2590

Pt(III) - trans-2- C₄H₈- (8×8)

Fig. 3

METASTABLE STRUCTURE

T = 300 K



XBL 817-6050

Fig. 4

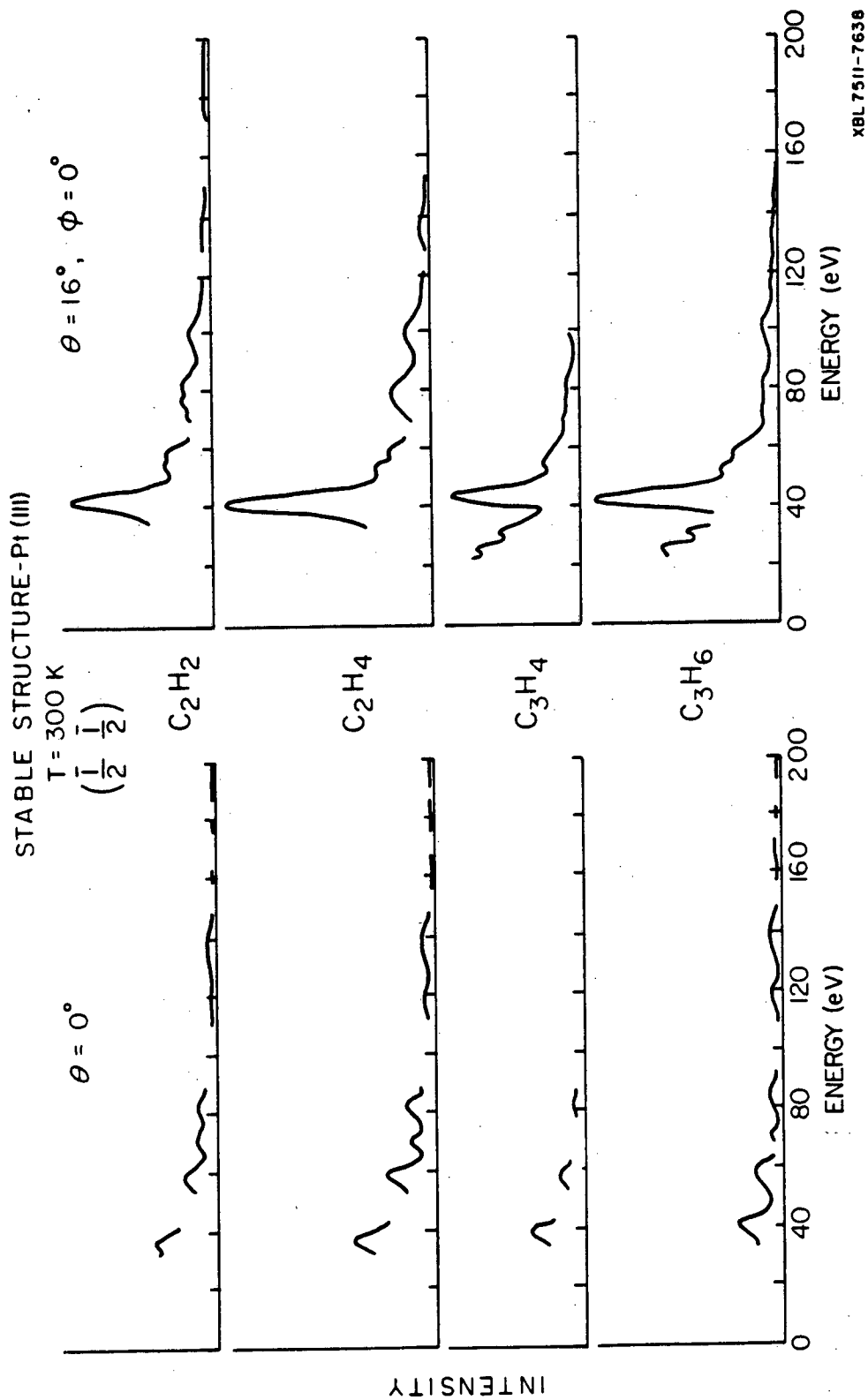
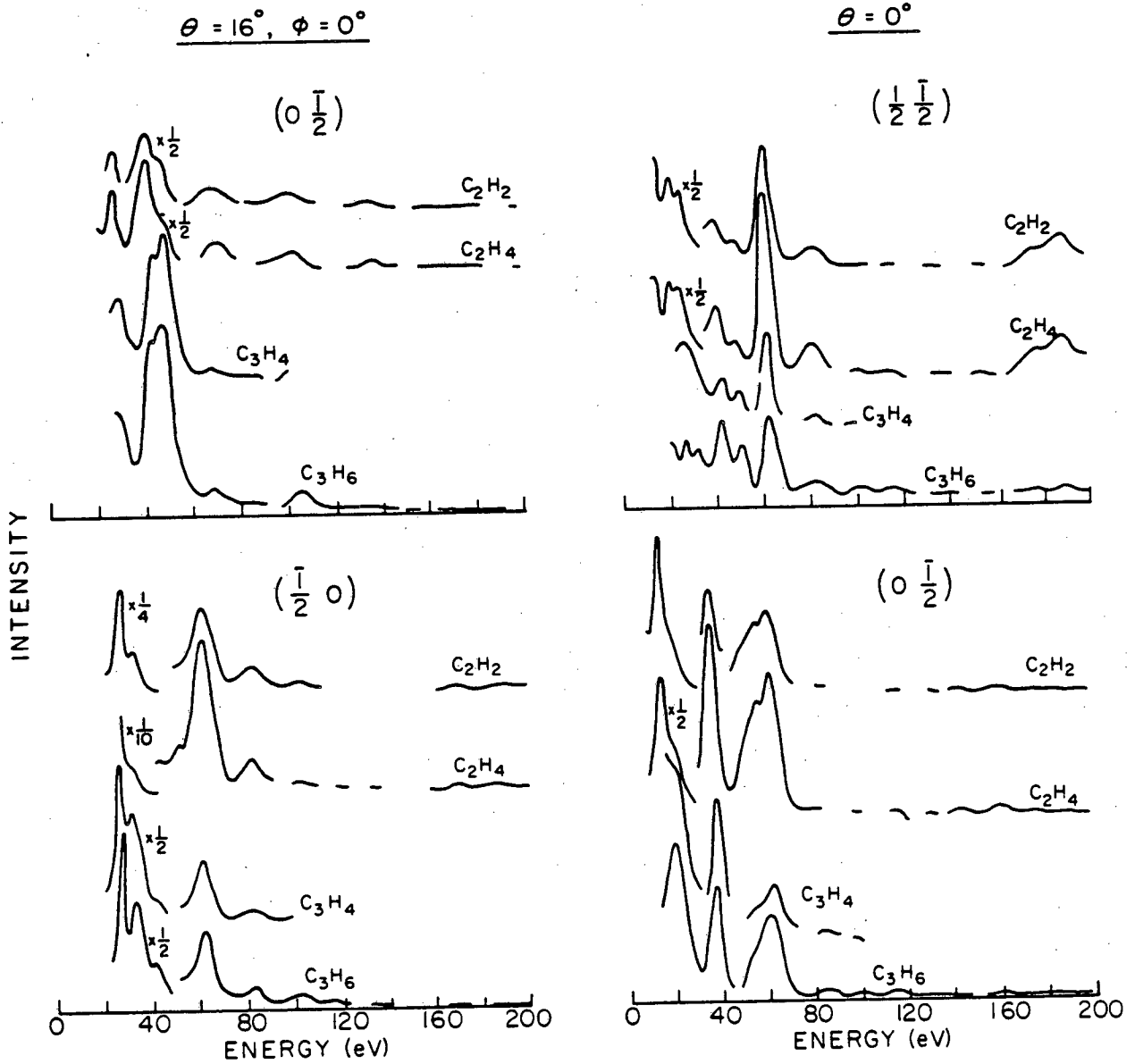


Fig. 5

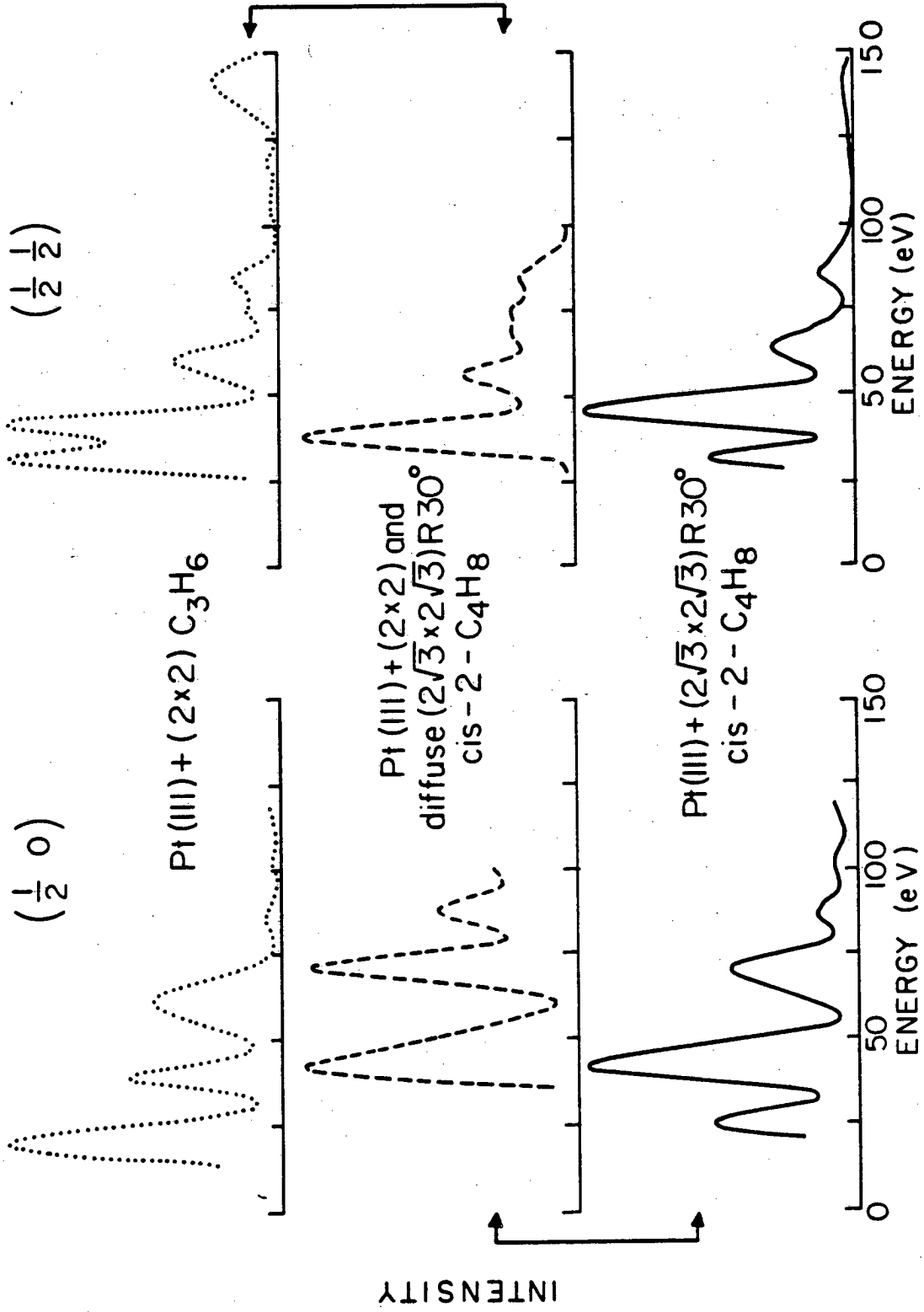
STABLE STRUCTURE - Pt(III)
T = 300 K



XBL 817-6064

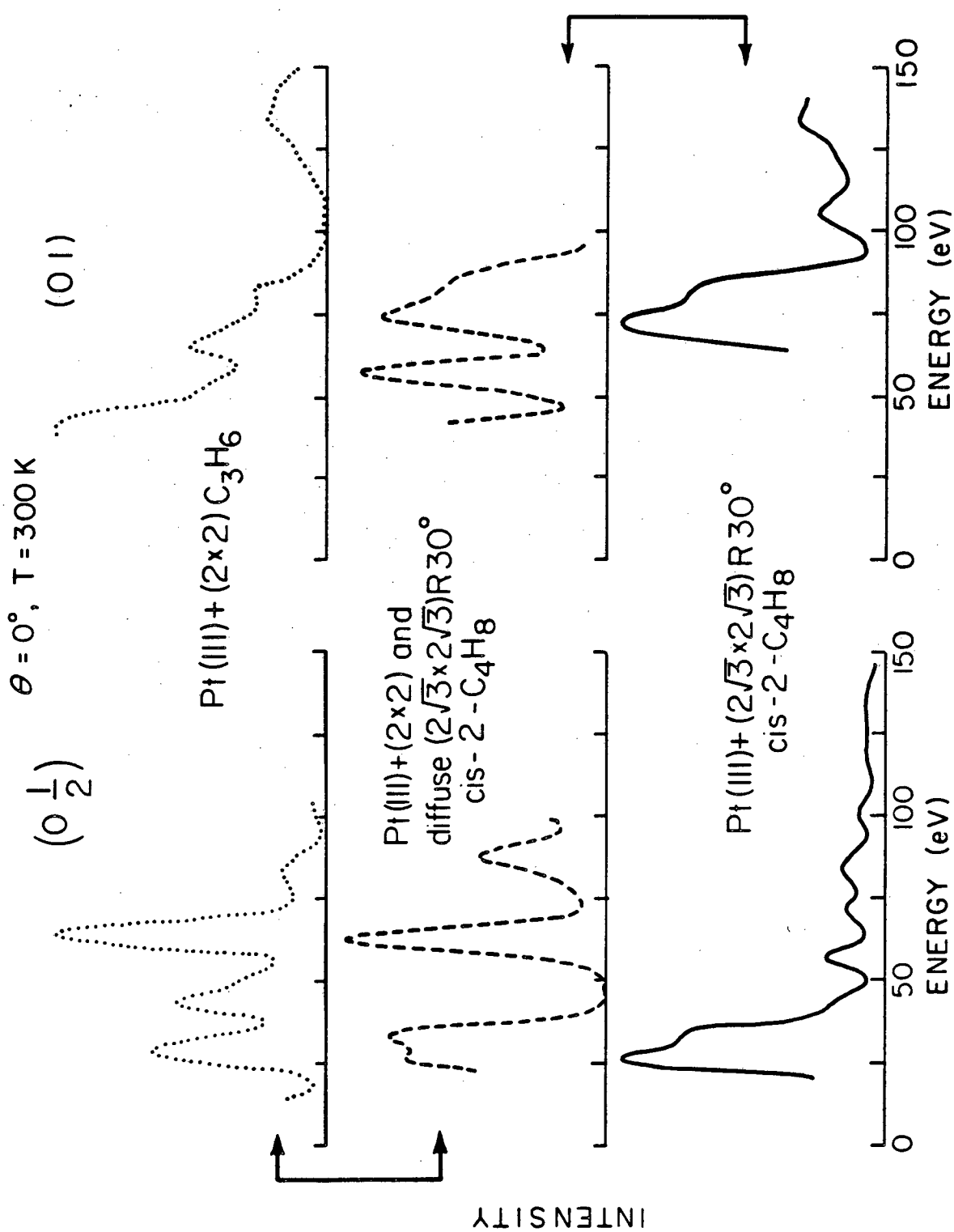
Fig. 6

$\theta = 0^\circ$, $T = 300$ K



XBL 813 - 5396

Fig. 7a

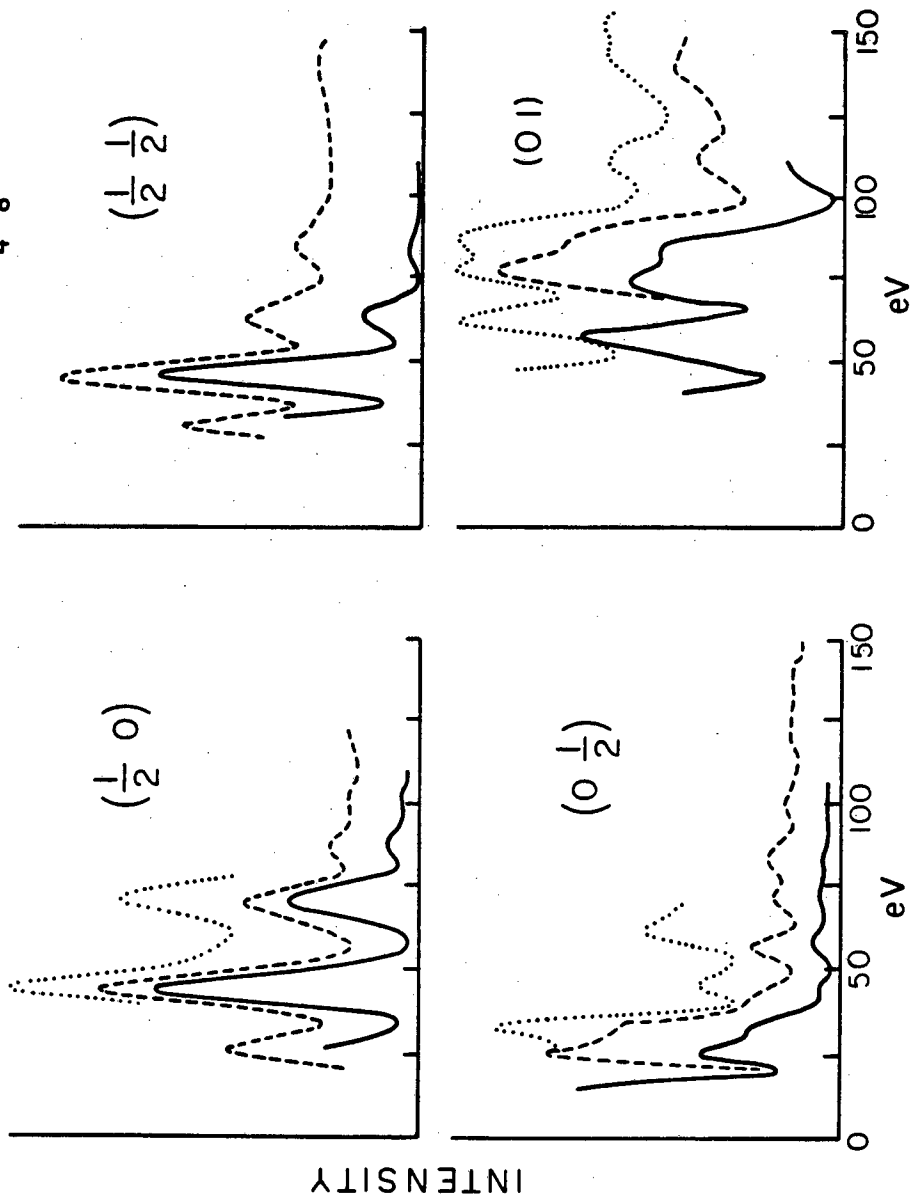


XBL813-5395

Fig. 7b

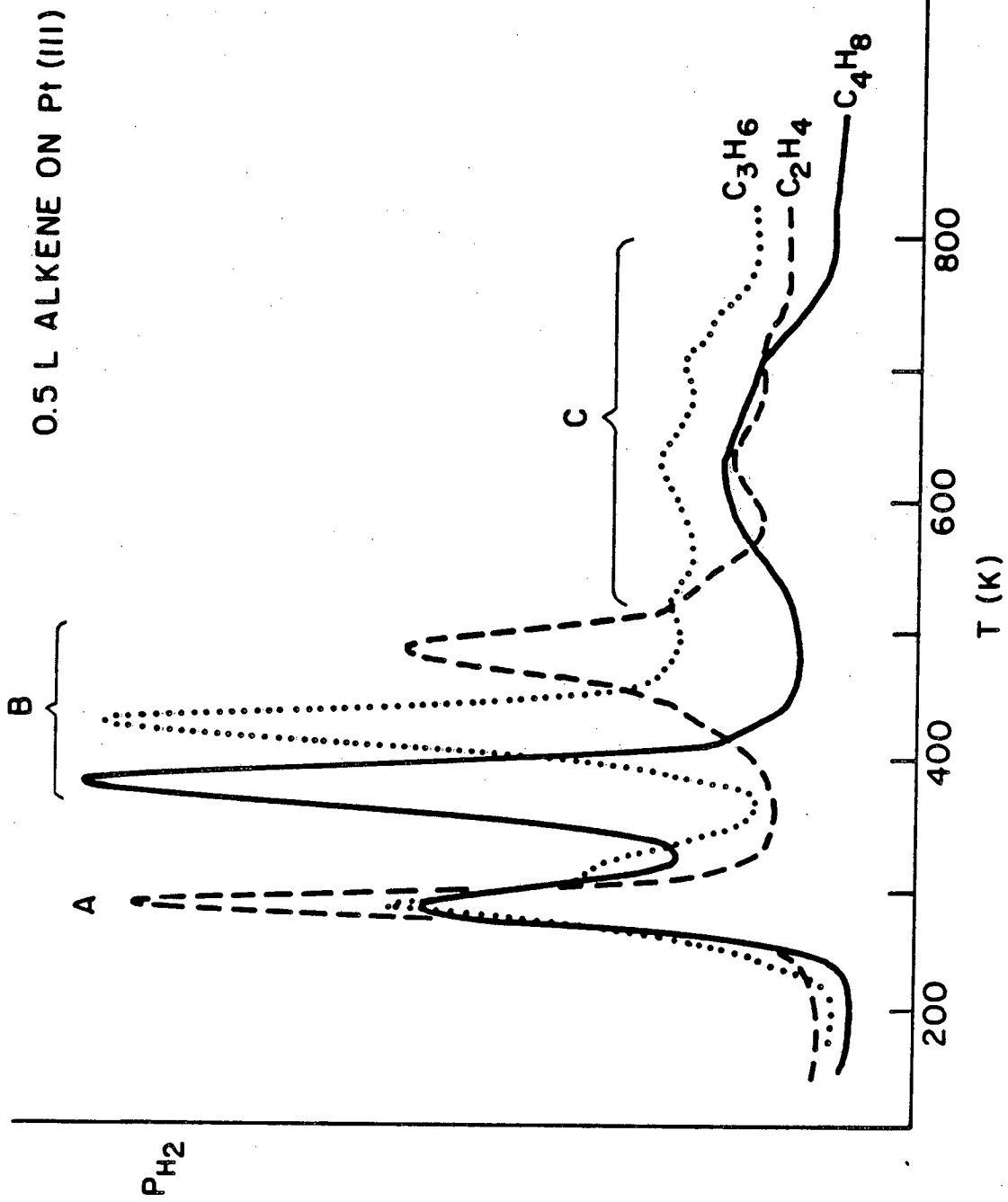
$\theta = 0^\circ$, $T = 300\text{ K}$

- Pt (III) + p (8x8) trans-2-C₄H₈
- Pt (III) + (2√3 x 2√3) R 30° trans-2-C₄H₈
- Pt (III) + (2√3 x 2√3) R 30° cis-2-C₄H₈



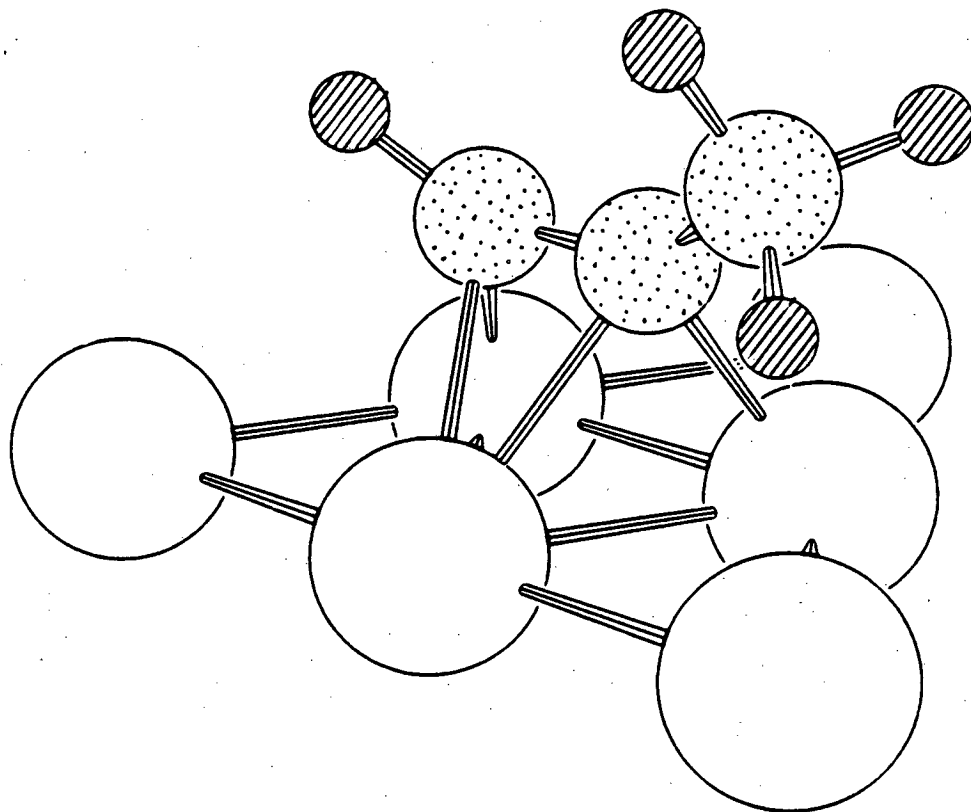
XBL 813-5394

Fig. 8



XBL 814-5475

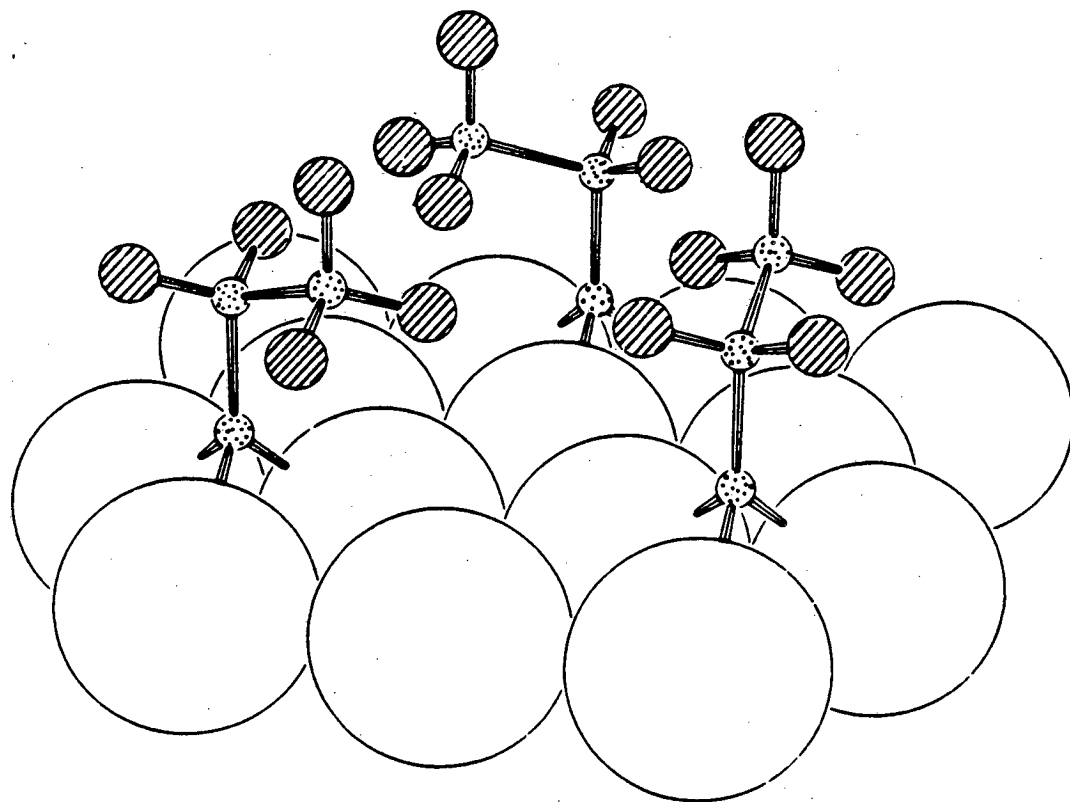
Fig. 9



Metastable methylacetylene

XBL 817-6067

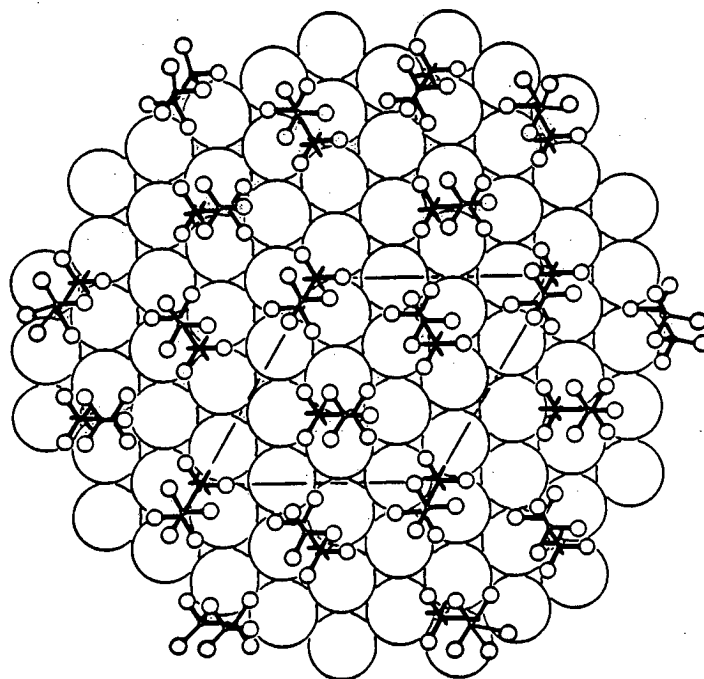
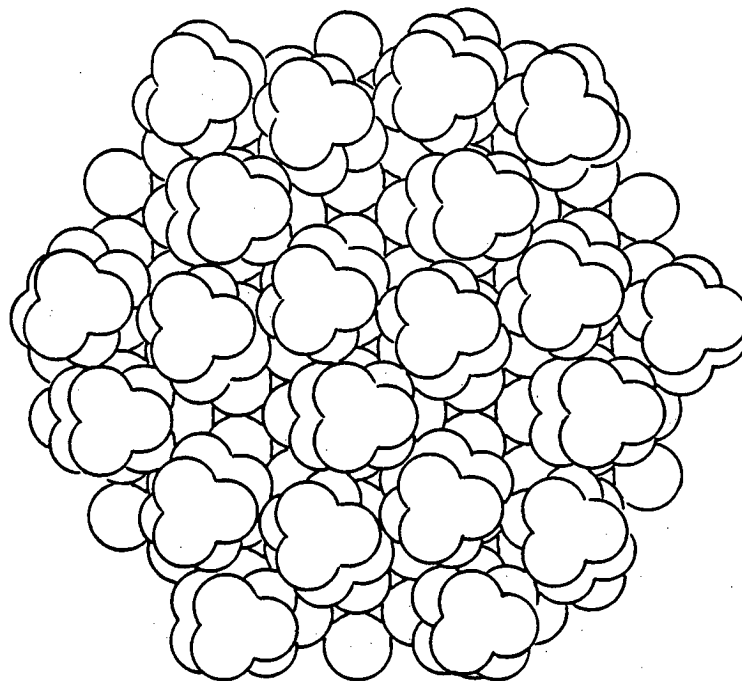
Fig. 10



fcc (III) + C₃H₅ (propylidyne)

XBL817-6065

Fig. 11



fcc(111) + $(2\sqrt{3} \times 2\sqrt{3}) R 30^\circ C_4H_7$ (butylidyne)

XBL 813-541

Fig. 12

VII. ETHYLENE ADSORPTION ON THE Rh(111) SURFACE

A. INTRODUCTION

In the past several years the structure of acetylene and ethylene adsorbed on the Pt(111) face has been investigated with a number of techniques including dynamical low energy electron diffraction (DLEED), high resolution electron energy loss spectroscopy (HREELS), ultraviolet photoemission spectroscopy (UPS), and thermal desorption spectroscopy (TDS). A progression of different surface phases is believed to form with increasing temperature. Below room temperature, HREELS^{1,2} and UPS^{3,4} indicate a di- σ , π bonded acetylene and a di- σ bonded ethylene species; yet an early DLEED investigation⁵ proposed a purely π bonded acetylene complex. In the temperature range 300-450 K, the same "stable" phase structure forms with either ethylene or acetylene plus hydrogen adsorption.^{2,6,7} This room temperature phase has been fairly controversial, and three very different structures have been proposed: ethylidyne ($\equiv\text{C}-\text{CH}_3$) based on DLEED,⁸ ethylidene ($=\text{CH}-\text{CH}_3$) based on HREELS,² and a vinyl-like species ($=\text{CH}-\text{CH}_2^-$), better named 1-ethanyl-ylidene, based on UPS.⁹

Recently though, the ethylidyne model has gained a clear preference over the ethylidene and 1-ethanyl-2-ylidyne due to a reinterpretation of the HREELS spectrum.¹⁰ A normal mode analysis¹¹ was done on the IR spectrum of an organometallic analogue, $\text{Co}_3(\text{CO})\text{CCH}_3$, to surface ethylidyne; the vibrational peaks observed in the IR and HREEL spectra have a one-to-one correspondence except for two additional peaks in the surface case. These additional peaks however are removed

by a thorough hydrogen treatment of the surface¹⁰ and can be assigned to the presence of some coadsorbed vinylidene ($=C=CH_2$) by comparison with a vinylidene HREEL spectrum² and by similar reactions on small metal clusters.¹²

Interestingly, Rh(111),¹³ Pd(111),¹⁴ and Pt(100)¹⁵ have an ethylene overlayer with nearly identical HREEL spectra to the ethylidyne structure on Pt(111). The vibrational study on the Rh(111) surface indicated that two different ethylidyne phases form as a function of temperature. At <230-270 K, a (2x2) lattice of ethylidyne appears at a 1/4 monolayer coverage; while heating to 270-420 K produces a c(4x2) lattice of ethylidyne. Above 420 K, the carbon-carbon bond breaks to leave a C-H species present on the surface to 700 K.

In this chapter, we will present our structural determination of the Rh(111)-(2x2)-C₂H_n layer using a LEED intensity analysis. Our study confirms the ethylidyne model found by HREELS and also provides additional bonding information. First, ethylidyne is clearly shown to stand above an hcp hollow site rather than the fcc hollow found for ethylidyne in Pt(111).⁸ We believe that this shift is probably caused by the presence of coadsorbed hydrogen on Rh(111) and by its absence on Pt(111). Second, the measured carbon-carbon (1.45 Å) and metal-carbon (2.03 Å) bond distances for ethylidyne on Rh(111) can be neatly explained by σ - π hyperconjugation. That is, the lower (or apical) carbon atom in ethylidyne is probably carbynic (sp -hybridized) permitting effective delocalization of the C-H group's σ -bond electrons into the metal valence band. The bonding of ethylidyne to the surface

can then be represented by a non-directional triple bond rather than three separate sp^3 orbitals pointed toward different Rh atoms.

Substantial evidence for this unusual bonding arrangement is also present in similar organometallic clusters, such as $Co_3(CO)_9CCH_3$.

However, our LEED analysis of the $c(4 \times 2)-C_2H_n$ layer could not confirm the ethynidyne structure predicted by HREELS. Possible reasons for this discrepancy will be discussed in Chapter VIII where we include the $c(4 \times 2)-C_3H_n$ layer obtained after C_3H_6 or $C_3H_4+H_2$ adsorption.

B. EXPERIMENTAL

The apparatus and sample cleaning are described in Chapters III and V so we will only discuss the preparation of the $(2 \times 2)-C_2H_n$ overlayer and the subsequent collection of the intensity data. Before the ethylene exposure, the crystal was routinely flashed to $400^\circ C$ to remove pre-adsorbed carbon monoxide and hydrogen; the crystal would then cool to $-30^\circ C$ in less than 10 minutes. A measured exposure of 0.5 L was used to produce a well-ordered (2×2) lattice. (The exposure value is not corrected for the ion gauge sensitivity or for the pressure difference between the pump and the gauge.) With this procedure, some carbon monoxide would be displaced from the chamber walls and would then coadsorb to give 0.05 monolayer coverage, as determined by thermal desorption yield experiments.

An over- or under-exposure of ethylene would cause the ethylene layer to disorder. Upon heating the crystal gently to room temperature over the course of several hours, the LEED pattern indicated the overlayer first disordered and then reordered into a $c(4 \times 2)$ structure.

Figure 1 shows the LEED patterns for the clean Rh(111), Rh(111)-(2x2)-C₂H_n and Rh(111)-c(4x2)-C₂H_n surfaces. If however coadsorbed hydrogen is present on the Rh(111) surface, both (2x2) and c(4x2) structures can form simultaneously at 230 K. To show this, we deliberately predosed the surface with atomic hydrogen; the ethylene that was then adsorbed at 230 K produced weak but well-focused quarter-order LEED spots corresponding to domains with a c(4x2) lattice as well as much more intense and similarly well-focused spots corresponding to domains with a (2x2) lattice. So it appears the order-order transition [(2x2) → c(4x2)] of adsorbed ethylene can be forced at lower temperatures by the presence of coadsorbed hydrogen.

The intensity vs. voltage (I-V) curves for the various diffraction beams were collected by a photographic method already described in Chapters II and III. The intensity curves were checked for a 3-fold symmetry at normal incidence ($\theta=0^\circ$) and a remaining mirror-plane symmetry off normal incidence ($\theta \neq 0$, $\phi=0$); in addition, each IV profile was reproduced in a second, independent experiment. For use in the reliability factor analysis, the I-V spectra were then averaged over degenerate beams and independent runs, normalized to a 1 μ amp incident beam current, and smoothed twice with a three-point formula.

Similar to our finding in an earlier study of the Rh(111)-($\sqrt{3} \times \sqrt{3}$)R30-CO system [Chapter V], the LEED beam would first slightly improve the ordering of the (2x2)-C₂H_n layer, and then an exponential decay with electron exposure would begin in the extra order diffraction spot

intensities. Figure 2 shows the change in the (0,1/2) beam intensity for the $(2 \times 2)\text{-C}_2\text{H}_n$ overlayer as a function of electron beam exposure. There is a slight increase in the beam intensity during the first 15 μ amp-sec and then an exponential decay that reached half-maximum intensity in another 36 μ amp-sec. The extent of enhanced ordering by the electron beam depended on the amount of coadsorbed background hydrogen on the surface; as the coadsorbed hydrogen coverage increased, a longer electron beam exposure was necessary to reach the maximum spot intensity. In yet another similarity with the earlier CO/Rh(111) study, a semilog plot of the (0,1/2) beam intensity vs. electron exposure (see Fig. 3) for the $(2 \times 2)\text{-C}_2\text{H}_n$ phase again shows two rather different decay constants. Although the initial decay rate for the ethylene overlayer ($\alpha_1 = 0.029 \mu$ amp-sec) is about twice as fast for the carbon monoxide overlayer ($\alpha_1 = .016 \mu$ amp-sec⁻¹), the second decay rates are essentially identical ($\alpha_2 = .0086 \mu$ amp-sec⁻¹ for ethylene, $\alpha_2 = .0088 \mu$ amp sec⁻¹ for carbon monoxide).

In light of this sensitivity, the electron beam damage was minimized by moving the beam across the crystal during photography,¹⁶ thus limiting the electron beam exposure of any given region of the surface to less than 25 μ amp-sec. As a result, the LEED spots associated with the ethylene overlayer would stay within 5-10% of the maximum intensity during photography.

C. LEED THEORY

The LEED calculations for the Rh(111)-(2x2)-C₂H_n structure were performed with convergent multiple scattering through renormalized forward scattering.¹⁷ The rhodium atoms are represented by a band structure muffin-tin potential,¹⁸ used in previous LEED calculations for rhodium surfaces [Chapter V and Ref. 19]. For the adsorbed molecular species we used the approach indicated by Kesmodel et al.^{8,20} for a similar molecular species on Pt(111). The hydrogen atoms are ignored, being weak electron scatterers. The spherically symmetrical potential inside the carbon muffin-tin spheres was obtained from molecular-orbital wave functions given by Palke and Lipscomb²¹ in a self-consistent field treatment for acetylene. The potential consists of an electrostatic term and a Slater exchange term, and some overlap with nearby platinum atoms is included. An imaginary part of the potential proportional to $E^{1/3}$ was chosen. Rhodium thermal vibration amplitudes were increased by a factor of 1.4 relative to the bulk value for Rh, while the adatoms were given double the bulk vibration amplitudes.

Theory and experiment are compared through a set of R-factors (reliability factors) and their average. These are an R-factor measuring the fraction of the energy range with slopes of opposite signs in the experimental and theoretical I-V curves, two R-factors based on intensity differences (both in absolute value and squared) as well as Zanazzi-Jona and Pendry R-factors (called ROS, R1, R2, RRZJ, and RPE, respectively, in Chapter V and Ref. 19.f). We not only average R-factors over all available beams but also contrast the R-factors for

different beams, looking for coincidence in the structural predictions by the different beams.

D. RESULTS

Four different adsorption sites were tested for the Rh(111)-(2x2)-C₂H_n determination; they are the atop (aaABC...), the hcp hollow (bbABC..., xbABC...), the fcc hollow (ccABC...), and the bridge (ddABC...) sites. At each site, the carbon-carbon axis was kept perpendicular to the surface except for the hcp hollow (xbABC...) where the axis was also tilted by 28-40° from the normal along the [011] direction; the carbon-carbon and carbon-metal distances were then varied in 0.10 Å increments. Table 1 summarizes the set of all 220 structural models tried.

The comparison between theoretical and experimental I-V curves at normal incidence (nine independent beams) eliminated the atop (aaABC...) and fcc hollow (ccABC...) sites as well as the models with a tilted carbon-carbon axis (xbABC...) and with a quarter monolayer of atomic carbon (bABC...). Figure 4 shows the average R-factor contour plots for the hcp hollow (bbABC...) and bridge (ddABC...) sites. We see that the minimum R-factor reached in both plots, when varying the metal-carbon and carbon-carbon distances, is about the same (0.29 for the hcp hollow, 0.30 for the bridge). Yet the contours for the hcp hollow site are much steeper than those for the bridge site.

To confidently distinguish between those two models, we considered the intensity curves (39 independent beams) taken at three off-normal incidence angles. Figure 5 shows the R-factor contour plots for the hcp hollow and bridge sites at each of the three off-normal incidence

angles. The R-factor minima for the hcp hollow sites are significantly lower than those for the bridge site at $\theta=21^\circ$ and $\theta=31^\circ$; while we again notice that the contours are much steeper for the hcp hollow than for the bridge site. Also, the metal-carbon and carbon-carbon distances are much more consistent for the hcp hollow site at the different polar angles. Figure 6 gives a representative comparison between theoretical and experimental intensity curves for our best structure.

The R-factor contours obtained in this determination are comparable both in shape and magnitude to those available in two other molecular structure determinations using dynamical LEED. For the Rh(111)-($\sqrt{3}\times\sqrt{3}$)R30°-CO system [Chapter V], a Zanazzi-Jona reliability factor of 0.40 and a Pendry factor of 0.50 were obtained, while Pendry R-factors of 0.50 and 0.40 were found for CO on Ni and Cu(100),²² respectively. We obtain a Zanazzi-Jona R-factor of 0.49 and a Pendry R-factor of 0.52 for the Rh(111)-(2x2)-C₂H₃ determination. It is interesting that the R-factor contour plots around the minimum have, in this work and in the CO investigations, an elongated elliptical shape that becomes less pronounced at polar angles further off normal incidence, thus implying a greater uncertainty in the position of the underlying carbon atom. This feature has already been discussed in Chapter V and Ref. 22.

Our analysis gives the projected metal-carbon ($d_{\perp\text{RhC}}$) and carbon-carbon ($d_{\perp\text{CC}}$) distances to be 1.31 and 1.45 Å, respectively. These values represent a weighted average over the polar angle data that accounts for the different number of beam profiles at each angle. The individual metal-carbon ($d_{\perp\text{RhC}}$) and carbon-carbon ($d_{\perp\text{CC}}$)

distances for each angle can be found in the R-factor plots (Figs. 4 and 5) or Table 4. An ethylidyne species ($\equiv\text{C}-\text{CH}_3$) is strongly implied by these distances in agreement with earlier HREELS work. Figure 7 illustrates the $(2\times 2)-\text{C}_2\text{H}_3$ structure we find by dynamical LEED as well as the $c(4\times 2)-\text{C}_2\text{H}_n$ geometry predicted by HREELS.¹³ Our result for the (2×2) -ethylidyne layer should be contrasted with a similar study⁸ of the $\text{Pt}(111)-(2\times 2)-\text{C}_2\text{H}_3$ system which indicated an ethylidyne group standing above a fcc rather than an hcp hollow site. This change could not be detected with HREELS, but is clearly seen in our LEED determination. Table 2 summarizes the bond distances determined for these two overlayers.

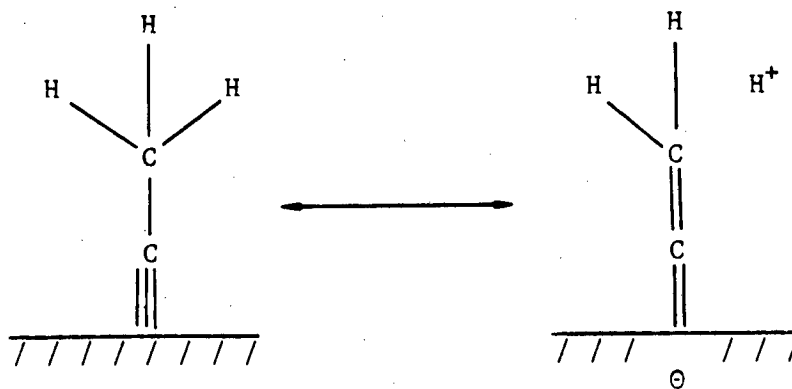
A possible explanation why ethylidyne would select different hollow sites on the Pt and Rh(111) surfaces involves the role of coadsorbed hydrogen. Thermal desorption spectra (TDS) of the Rh(111)- and Pt(111)- $(2\times 2)-\text{C}_2\text{H}_3$ surfaces^{13,23} indicate that the extra hydrogen released to form ethylidyne from ethylene remains on the Rh surface (240 K), but mostly desorbs from Pt (300 K). The hydrogen that is then present on the Rh surface may block a fcc hollow site but still permit adsorption above the hcp hollow near it. However, it should be mentioned that the adsorbed ethylene probably has only a quarter monolayer coverage so there are other fcc hollow sites present on the surface for ethylidyne to occupy if it were sufficiently mobile.

E. DISCUSSION

The objective of most structural studies is to gain more information on the bonding of the molecule or complex being investigated. In this section, we will interpret our structural results in the context

of similar organometallic compounds that have been extensively studied to date. The carbon-carbon bond distance (1.45 Å) for the Rh(111)-(2x2)-C₂H₃ structure is significantly smaller than the single bond distances (1.53-1.54 Å) found in saturated hydrocarbons and also substantially larger than the double (1.34 Å) or triple (1.20 Å) bond lengths found in unsaturated hydrocarbons. Though our LEED study cannot determine the hydrogen positions, HREELS and TDS work¹³ indicate that an ethylidyne species does exist on the surface.

After considering similar organometallic species, we can arrive at a consistent explanation of the slight double bond character in the carbon-carbon distance for the surface ethylidyne species. The apical carbon does not make classical sp³ hybridized bonds to the surface, but rather becomes sp-hybridized and then π bonds to the surface in a way very similar to the metallocenes. This rehybridization of the apical carbon permits the energetically favorable delocalization of electrons from the alkyl group into the metal valence band; the delocalization is due to σ-π hyperconjugation of the CH groups and the π orbitals of the M₃C group, as illustrated below:



The carbon-carbon distance acquires some double bond character in the resonance structures. Some charge is also transferred to the electron withdrawing metal at the expense of the CH orbitals; and the apical carbon-metal surface bond strength is decreased.

Let's now consider the available structural evidence for the carbon-carbon and metal-carbon distances of organometallic and surface ethylidyne complexes; we will find that the bond lengths fit our simple hyperconjugation model very neatly. In Table 3, we group carbon-carbon single bond distances for organic, organometallic, and surface ethylidyne complexes according to their assigned hybridizations. The single bond in diacetylene ($\text{HC}\equiv\text{C}-\text{C}\equiv\text{CH}$) is shortened by electron delocalization to practically a double bond distance (1.37 Å). While we observe the $(\text{CO})_9\text{Co}_3\text{C}-\text{CCo}_3(\text{CO})_9$ cluster has the same shortened carbon-carbon distance although there are no explicit double or triple bonds on the carbon atoms. This suggests that there is substantial π bonding between the carbon atoms in $(\text{CO})_9\text{Co}_3\text{C}-\text{CCo}_3(\text{CO})_9$ and requires that the apical carbon become nearly sp -hybridized.

Turning now to the M_3CCH_3 clusters in Table 3, the ethylidyne carbon-carbon distance falls into the same hybridization category ($\text{C}_{\text{sp}^2}-\text{C}_{\text{sp}^3}$) as the single bond length in propylene; this would give the apical carbon in the M_3CCH_3 clusters close to a sp^2 -hybridization. Yet the carbon-carbon distance of the surface ethylidyne falls into the $\text{C}_{\text{sp}}-\text{C}_{\text{sp}^3}$ hybridization category along with the single bond length of propyne. This difference in hybridization for the surface and cluster ethylidyne group is to be expected since a balance must be met

between the energetically favorable delocalization of electrons from the alkyl group into the metal and the energetically unfavorable sp-hybridization of the apical carbon that reduces the overlap with the metal d-orbitals. The metal surface can produce a more extensive delocalization of the alkyl group's electron density to offset the rehybridization energy than the M_3C-R cluster can since more metal atoms are present on the surface than in the M_3C-CH_3 cluster.

This ability for the metal surface to better delocalize the alkyl group's electrons is suggested in the IR spectra²⁸ for CH_3COCH_3 , $PhCOPh$, and $[Co_3(CO)_9C]_2CO$. These spectra show a progressive weakening of the CO bond strength [$\nu_{CO} = 1719, 1667, \text{ and } 1385 \text{ cm}^{-1}$, respectively] since the CO π -electrons are most delocalized in the $[Co_3(CO)_9C]_2CO$ cluster. The very low CO stretch frequency for this cluster indicates how much more effectively the $Co_3(CO)_9C$ can delocalize the CO valence electrons than the phenyl group can. This should be anticipated since the $Co_3(CO)_9C$ cluster has 121 valence electrons while the phenyl group has only 29. The valence band of the Rh surface should produce an even more extensive delocalization of the alkyl group's electron density than the $Co_3(CO)_9C$ cluster and thus be able to offset the considerable energy needed to sp-hybridize the apical carbon.

In Table 4, we list the apical carbon covalent radii (r_c) for three different alkylidyne groups; the radius is defined as the metal atom to apical carbon bond distance minus the metal-metal distance. The covalent radii in the first group of M_3CCH_3 , $M_3C-C \equiv$, and M_3C-O- clusters are all 0.66-0.67 Å, even though different ligands

are attached to the trinuclear cluster and different metal atoms are used. The surface ethylidyne with an apical carbon covalent radius of 0.69 Å comprises the second group. While the $\text{Co}_3\text{C}-\text{C}-\text{Co}_3$ dimer of the third group gives a carbon covalent radius of 0.73 Å. This trend in covalent radii indicates that the α -carbon (or apical carbon) to metal bond strength decreases as the α -carbon to β -carbon single bond strength increases; in other words when the α -carbon in $\text{M}_3\text{C}-\text{R}$ allows a greater electron delocalization from the alkyl group (R) into the metal cluster (M_3), the overlap of the α -carbon orbitals with the metal d_{xz} , d_{yz} orbitals is reduced.

Thus, the structural evidence from the organometallic compounds $\text{M}_3(\text{CO})_9\text{CCH}_3$ as well as our $\text{Rh}(111)-(2 \times 2)-\text{C}_2\text{H}_3$ determination indicates a sp^2 - or sp -hybridized α -carbon and significant σ - π hyperconjugation in the ethylidyne group. Table 5 now summarizes the complementary electronic evidence available on the organometallic compound, $\text{Co}_3(\text{CO})_9\text{CCH}_3$, for sp^2 -hybridization and hyperconjugation. Unfortunately, the determination of the $\text{Pt}(111)-(2 \times 2)-\text{C}_2\text{H}_3$ structure does not fit snugly into this picture (Table 2); the carbon-carbon distance for ethylidyne is slightly too large (1.50 rather than 1.45 Å) and the apical carbon covalent radius is much too small (0.61 rather than 0.69 Å). A likely explanation for this departure is that no R-factor analysis was used in the $\text{Pt}(111)$ study to interpolate between the tested bond distances. That is, the $\text{Pt}(111)$ study considered only some carbon-carbon distances that occur at regular intervals (1.20, 1.30, 1.40, and 1.50 Å); while an R-factor

analysis could interpolate between these values to yield our bond length of 1.45 Å.

Another less likely explanation can account for this departure. We recall that ethylidyne stands above an hcp hollow site on Rh(111) and above a fcc hollow site on Pt(111). This change could pull the apical carbon of ethylidyne into the hollow site on Pt and may strengthen the overlap between the metal d-orbitals and the apical carbon's sp^3 orbitals. Hyperconjugation should then be reduced because it requires a more strongly bound sp^3 -hybridized apical carbon to be replaced by sp -hybridized apical carbon.

F. SUMMARY

Ethylidyne forms on the Rh(111) surface at <230-270K after ethylene adsorption; it orders into a (2×2) lattice with one molecule per unit cell. The CCH_3 fragment stands above an hcp site rather than the fcc hollow site found for ethylidyne on Pt(111). This change in adsorption sites for Pt and Rh may be due to the coadsorbed hydrogen present only on the Rh surface; this hydrogen could occupy a fcc hollow site that may block ethylidyne adsorption if the CCH_3 group is not very mobile.

The carbon-carbon (1.45 Å) and metal-carbon (2.03 Å) distances determined in this study have a Pendry R-factor of 0.52 and a Zanazzi-Jona R-factor of 0.49. The distances suggest that the carbon atom bound to the surface is carbynic (sp -hybridized) and that the electron density in the C-H bond is delocalized into the metal valence band.

References for Chapter VII

1. H. Ibach, H. Hopster and B. Sexton, Appl. Phys. 14 21 (1977).
2. H. Ibach and S. Lehwald, J. Vac. Sci. & Technol. 15 407 (1978).
3. T. E. Felter and W. H. Weinberg, Surf. Sci. 103 265 (1981).
4. J. E. Demuth, Surf. Sci. 84 315 (1979).
5. L. L. Kesmodel, R. C. Baetzold and G. A. Somorjai, Surf. Sci. 66 299 (1977).
6. P. C. Stair and G. A. Somorjai, J. Chem. Phys. 66 2036 (1977).
7. W.-J. Lo, Y. W. Chung, L. L. Kesmodel, P. C. Stair and G. A. Somorjai, Solid State Commun. 22 335 (1977).
8. L. L. Kesmodel, L. H. Dubois and G. A. Somorjai, J. Chem. Phys. 70 2180 (1979).
9. J. E. Demuth, Surf. Sci. 80 367 (1979).
10. H. Ibach and D. L. Mills, Electron Energy Loss Spectroscopy and Surface Vibrations (Academic Press, N.Y., 1982), p. 326ff.
11. M. H. Howard, S. F. A. Kettle, I. A. Oxton, D. B. Powell, N. Sheppard and P. Skinner, J. Chem. Soc. Faraday Trans. 77 1203 (1981).
12. a) A. J. Deeming and M. Underhill, J. Chem. Soc. Dalton 1415 (1974).
b) A. J. Deeming, S. Hasso and M. Underhill, J. Chem. Soc. Dalton 1614 (1975).
13. L. H. Dubois, D. G. Castner, and G. A. Somorjai, J. Chem. Phys. 72 5234 (1980).
14. L. L. Kesmodel and J. A. Gates, Surf. Sci. 111 (1981).

15. A. M. Baro and H. Ibach, Proc. Conf. on Vibrations in Adsorbed Layers (Julich, West Germany, 1978).
16. M. Passler, A. Ignatiev, F. Jona, D. W. Jepsen and P. M. Marcus, Phys. Rev. Lett. 43 360 (1979).
17. a) J. B. Pendry, Low Energy Electron Diffraction, Academic Press, London, 1974.
b) M. A. Van Hove and S. Y. Tong, Surface Crystallography by LEED, Springer-Verlag, Heidelberg, 1979.
18. V. L. Moruzzi, A. B. Williams and J. F. Janak, Calculated Electronic Properties of Metals, Pergamon Press, New York, 1978.
19. a) D. C. Frost, K. A. R. Mitchell, F. R. Shepherd and P. R. Watson, in Proc. 7th IVC and 3rd ICSS, Vienna (1977) p. 2725.
b) K. A. R. Mitchell, F. R. Shepherd, P. R. Watson, and D. C. Frost, Surf. Sci. 64 737 (1977).
c) P. R. Watson, F. R. Shepherd, D. C. Frost and K. A. R. Mitchell, Surf. Sci. 72 562 (1978).
d) C.-M. Chan, P. A. Thiel, J. T. Yates, Jr. and W. H. Weinberg, Surf. Sci. 76 296 (1978).
e) F. R. Shepherd, P. R. Watson, D. C. Frost, and K. A. R. Mitchell, J. Phys. C11 4591 (1978).
f) M. A. Van Hove and R. J. Koestner, Proc. Conf. on Determination of Surface by LEED, Plenum, New York (1981).
20. a) L. L. Kesmodel, R. C. Baetzold and G. A. Somorjai, Surface Sci. 66 299 (1977).
b) L. L. Kesmodel, L. H. Dubois and G. A. Somorjai, Chem. Phys. Lett. 56 267 (1978).

21. W. E. Palke and W. N. Lipscomb, *J. Am. Chem. Soc.* 88 2384 (1966).
22. a) S. Andersson and J. P. Pendry, *Phys. Rev. Lett.* 43 363 (1979).
b) S. Andersson and J. P. Pendry, *J. Phys. C.* (in press).
23. M. Salmeron and G. A. Somorjai, *J. Phys. Chem.* 86 341 (1982).
24. Tables of Interatomic Distances and Configurations in Molecules and Ions, L. E. Sutton, ed., Chemical Society Special Publication, Vol. 11, 18.
25. M. D. Brice and B. R. Penfold, *Inorg. Chem.* 11 1381 (1972).
26. R. J. Dellaca, B. R. Penfold, B. H. Robinson, W. T. Robinson and J. L. Spencer, *Inorg. Chem.* 9 2204 (1970).
27. R. J. Dellaca and B. R. Penfold, *Inorgan. Chem.* 10 1269 (1971).
28. P. W. Sutton and L. F. Dahl, *J. Amer. Chem. Soc.* 89 261 (1967).
29. G. M. Sheldrick and J. P. Yesinowski, *J. Chem. Soc. Dalton*, p. 873 (1975).
30. J. P. Yesinowski and D. Bailey, *J. Organometallic Chem.* 65 627 (1974).
31. M. D. Brice, B. R. Penfold, W. T. Robinson and S. R. Taylor, *Inorg. Chem.* 9 362 (1970).
32. M. D. Brice, R. T. Dellaca, B. R. Penfold and J. L. Spencer, *Chem. Commun.*, p. 72 (1971).
33. G. Palyi and F. Piacenti, L. Mavko, *Inorg. Chim. Acta Rev.* p. 109 (1970).
34. F. Klanberg, W. B. Askew and L. J. Guggenberger, *Inorg. Chem.* 7 2265 (1968).
35. V. Batzel, V. Muller and R. Allmann, *J. Organomet. Chem.* 102 109 (1975).

36. M. D. Brice, B. R. Penfold, W. T. Robinson and S. R. Taylor,
Inorgan. Chem. 9 362 (1970).
37. D. Seyferth, Adv. Organomet. Chem. 14 97 (1976).
38. D. C. Miller and T. B. Brill, Inorgan. Chem. 17 240 (1978).

Table 1. Summary of the 220 different structural models tested in the LEED determination of Rh(111)-(2x2)-C₂H₃.

Site	d _{⊥RhC} [Å]	d _{⊥CC} [Å]	d _{∥CC} [Å]	Remarks
ccABC...	1.1(.1)1.4	1.1(.1)1.6	0	
bbABC...	1.1(.1)1.8	1.1(.1)1.6	0	
xbABC...	1.1(.1)1.4	1.1(.1)1.6	.74	gives tilt angle θ _{CC} = 42.3, 30, 27.5° at d _{⊥CC} = 1.1, 1.5, 1.6 Å, respectively
aaABC...	1.1(.1)2.2	1.1(.1)1.6	0	
ddABC...	1.1(.1)1.8	1.1(.1)1.6	0	
bABC...	1.1(.1)1.4	-	-	no 2nd C; 1/4 monolayer C coverage

Table 2. Comparison of ethynidyne bond distances on Pt(111) and Rh(111). (c = carbon-carbon distance, m = metal-carbon distance, r_M = measured metallic radius, r_C = carbon covalent radius).

	c (Å)	m (Å)	r_M (Å)	r_C (Å) = m - r_M
Rh(111)-(2×2)-C ₂ H ₃	1.45	2.03	1.34	0.69
Pt(111)-(2×2)-C ₂ H ₃	1.50	2.00	1.39	0.61

Table 3. Variation of carbon-carbon bond lengths for organometallic clusters and surface species: evidence for sp and sp² hybridization of the apical carbon for YCo₃(CO)₉.

$C_{sp} - C_{sp}$		$C_{sp^2} - C_{sp^2}$	
HC≡C--C≡CH ²⁴	1.37 Å	H ₂ C=HC--CH=CH ₂ ²⁴	1.48 Å
(CO) ₉ Co ₃ C--CCo ₃ (CO) ₉ ²⁵	1.37	(π-C ₆ H ₃ Me ₃)(CO) ₆ Co ₃ C--C ₆ H ₅ ³²	1.48 Å
(CO) ₉ Co ₃ C--C≡C--CCo ₃ (CO) ₃ ²⁶	1.37	(π-C ₈ H ₈)(CO) ₆ Co ₃ C--C ₆ H ₅ ³²	1.47
$C_{sp^2} - C_{sp^3}$		$C_{sp} - C_{sp^3}$	
H ₂ C=CH--CH ₃ ²⁴	1.51 Å	HC≡C--CH ₃ ²⁴	1.46 Å
(CO) ₉ Co ₃ C--CH ₃ ²⁸	1.53	Rh(111)-(2×2)C--CH ₃	probably 1.45
(CO) ₉ H ₃ Ru ₃ C--CH ₃ ²⁹	1.51		
(CO) ₉ H ₃ Os ₃ C--CH ₃ ³⁰	1.51		
[P(C ₆ H ₅) ₃](CO) ₉ Co ₃ C--CH ₃ ³¹	1.50		

Table 4. Comparison of apical carbon covalent radii for alkylidyne clusters and ethylidyne on Rh(111). (c = carbon-carbon distance, m = metal-carbon distance, r_M = measured metallic radius, r_C = carbon covalent radius)

	c(Å)	m(Å)	r_M (Å)	r_C (Å)=m- r_M
I. M_3CCH_3 , $M_3C-C \equiv$, or M_3C-O-				
1) $Co_3(CO)_9CCH_3$ ²⁸	1.53(3)	1.90(2)	1.24	0.66
2) $H_3Ru_3(CO)_9CCH_3$ ²⁹	1.51(2)	2.08(1)	1.42	0.66
3) $H_3Os_3(CO)_9CCH_3$ ³⁰	1.51	2.08	1.42	0.66
4) $(CO)_9Co_3COBH_2N(C_2H_5)_3$ ³⁴	--	1.92(1)	1.25	0.67
5) $(CO)_9Co_3COBCl_2N(C_2H_5)_3$ ³⁵	--	1.89(2)	1.24	0.67
6) $(CO)_8[P(C_6H_5)_3]Co_3CCH_3$ ³⁶	1.50(2)	1.91(2)	1.25	0.66
7) $(CO)_6(\pi-C_6H_5Me_3)Co_3CPh$ ³²	1.48(2)	1.89(2)	1.23	0.66
8) $(CO)_6(\pi-C_8H_8)Co_3CPh$ ³²	1.48(2)	1.89(2)	1.23	0.66
II. Rh(111)-(2x2)- C_2H_3				
9) average	1.45	2.03	1.34	0.69
10) $\theta = 0^\circ$	1.41	2.03	1.34	0.69
11) 11°	1.44	2.03	1.34	0.69
12) 21°	1.49	2.01	1.34	0.67
13) 31°	1.46	2.03	1.34	0.69
III. Co_3C-CCo_3 ²⁵				
	1.37(1)	1.96(1)	1.23	0.73

Table 5. Complementary electronic evidence for sp - or sp^2 -hybridization and hyperconjugation in $Co_3(CO)_3CCH_3$.

Technique	Result	Implication
1) H^1 NMR ²⁵	$\delta_H = 6.5$ ppm for $Co_3(CO)_9CCH_3$ -- deshielded to C_2H_6 ($\delta_H = 9.1$ ppm) --midway between C_2H_4 ($\delta_H = 8.2$ ppm) and C_2H_2 ($\delta_H = 4.7$)	C-H bond weakening; hyperconjugation
2) H^1 NMR ³⁷	$\Delta\delta_{H^*} = 0.6$ ppm for $Co_3(CO)_9CCH_2^*$ and $Co_3(CO)_9CCH_2^*OH$ -- $\Delta\delta_{H^*} =$ 8.5 ppm for $Me_2CH_2^*$ and Me_2CH^*OH	positive charge on cluster carbonium ion very delocalized
3) ^{13}C NMR ³⁷	$\Delta\delta_{C^*} = 13.5$ ppm for $Co_3(CO)_9CC^*H_2$ and $Co_3(CO)_9CC^*H_2OH$ -- $\Delta\delta_{C^*} = 255.3$ ppm for $Me_2C^*H_2$ and $Me_2C^*H_2OH$ -- $\Delta\delta_{C^*} = 26.2$ ppm for $(C_6H_6)Fe(C_6H_5C^*H_2OH)$ and $(C_6H_6)Fe(C_6H_5C^*H_2)$	positive charge on cluster carbonium ion very delocalized

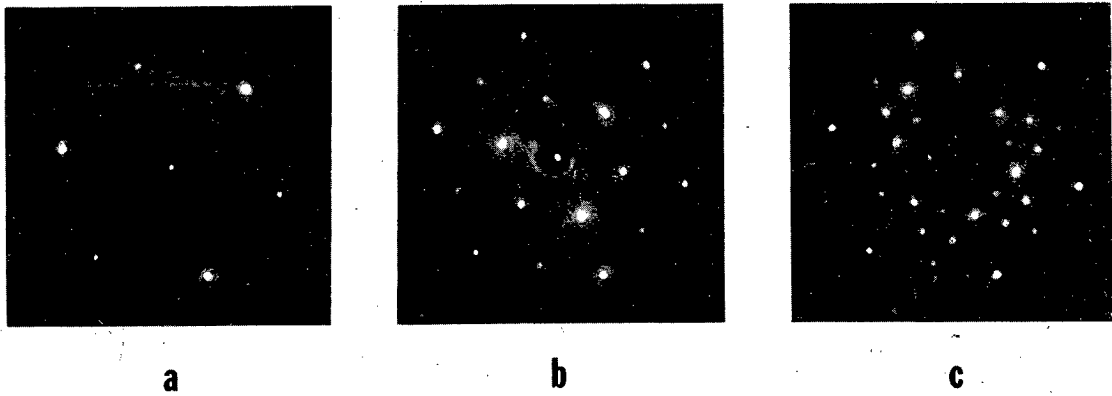
(continued)

Table 5. Complementary electronic evidence for sp- or sp²-hybridization and hyperconjugation in Co₃(CO)₃CCH₃. (continued)

Technique	Result	Implication
4) ¹³ C NMR ³⁷	δ _{C*} =258.4 ppm for Co ₃ (CO) ₉ - CCO ₂ Et--only close to carbyne complexes RC*≡M(CO) ₄ X	sp- or sp ² - hybridization of apical carbon
5) ⁵⁹ Co Nuclear Quadrupole Resonance ³⁸	electron donation or withdrawal from R to Co ₃ group in Co ₃ (CO) ₉ CR occurs via π- resonance expected for sp- or sp ² -hybridized apical carbon	sp- or sp ² - hybridization of apical carbon

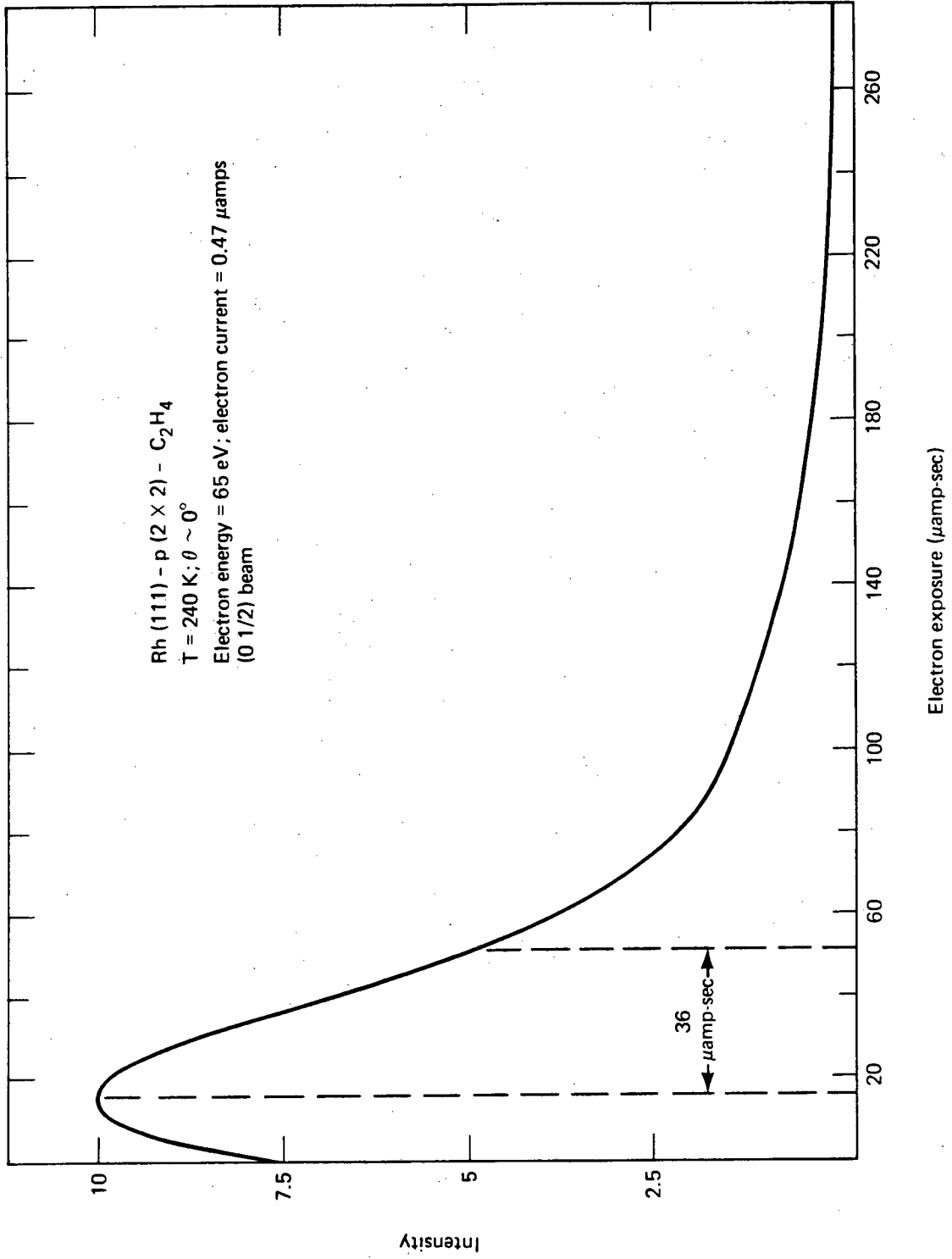
Figure Captions for Chapter VII

- Fig. 1. LEED patterns from surface structures produced by C_2H_4 adsorption on Rh(111). (a) clean Rh(111) at 93 eV, (b) $(2 \times 2)-C_2H_3$ at 74 eV, and (c) $c(4 \times 2)-C_2H_3$ at 68 eV.
- Fig. 2. Plot of $(0 \ 1/2)$ beam intensity vs. electron beam exposure.
- Fig. 3. Semilog plot of $(0 \ 1/2)$ beam intensity vs. electron beam exposure.
- Fig. 4. R-factor contour plot for bridge and hollow sites at $\theta = 0^\circ$. (Contour levels occur at 0.025 intervals.)
- Fig. 5. R-factor contour plot for bridge and hollow sites at $\theta \neq 0^\circ$, $\phi = 0^\circ$. (Contour levels occur at 0.025 intervals.)
- Fig. 6. Representative set of I-V curves for Rh(111)- $(2 \times 2)-C_2H_3$. Experimental curves, taken at $T = 240$ K, are drawn with thick lines. Corresponding theoretical curves, drawn with thin lines and shifted upward for clarity, refer to the bbABC... structure (hcp-type hollow site) with $d_{\perp RhC} = 1.3$ Å, $d_{\perp CC} = 1.5$ Å and C-C axis perpendicular to the surface, which is close to the "best" structure ($d_{\perp RhC} = 1.31$ Å, $d_{\perp CC} = 1.45$ Å).
- Fig. 7. Schematic of the ethylidyne lattices that appear on the Rh(111) surface. Our LEED analysis confirms the (2×2) -ethylidyne but not the $c(4 \times 2)$ -ethylidyne structure proposed in a HREELS study.¹³



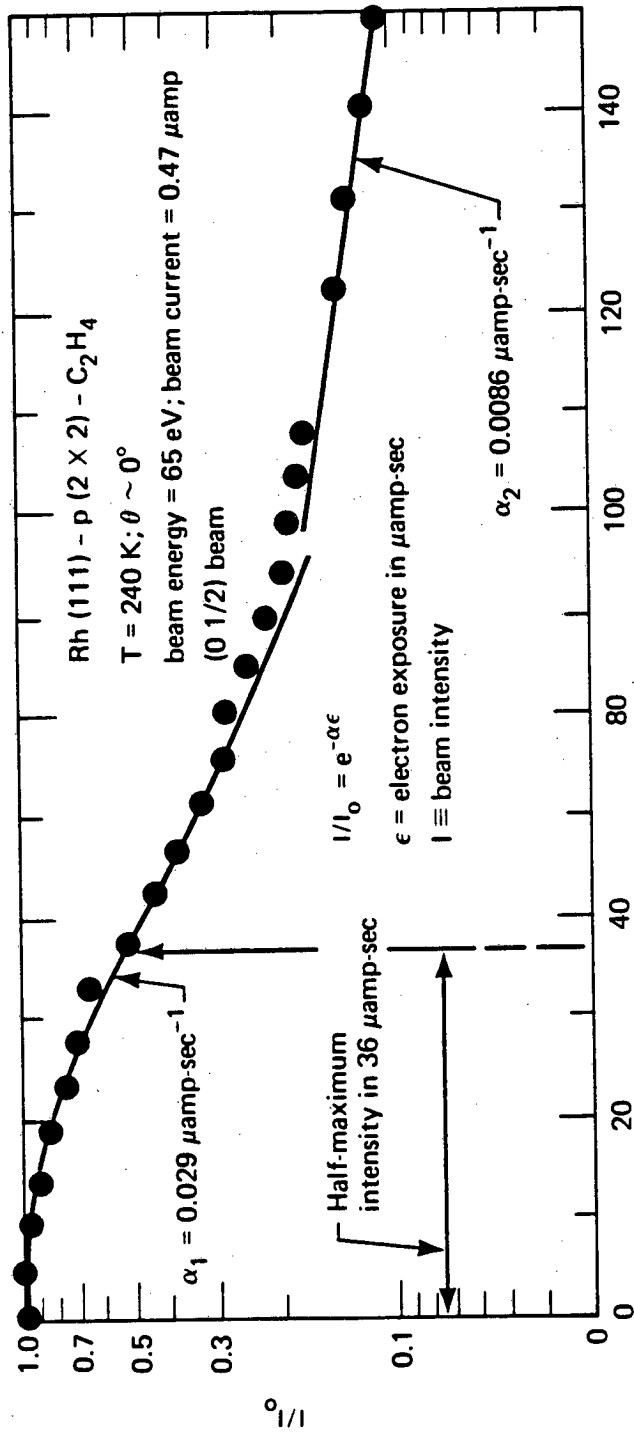
XBB 788-10161

Fig. 1



XBL 818:1092

Fig. 2

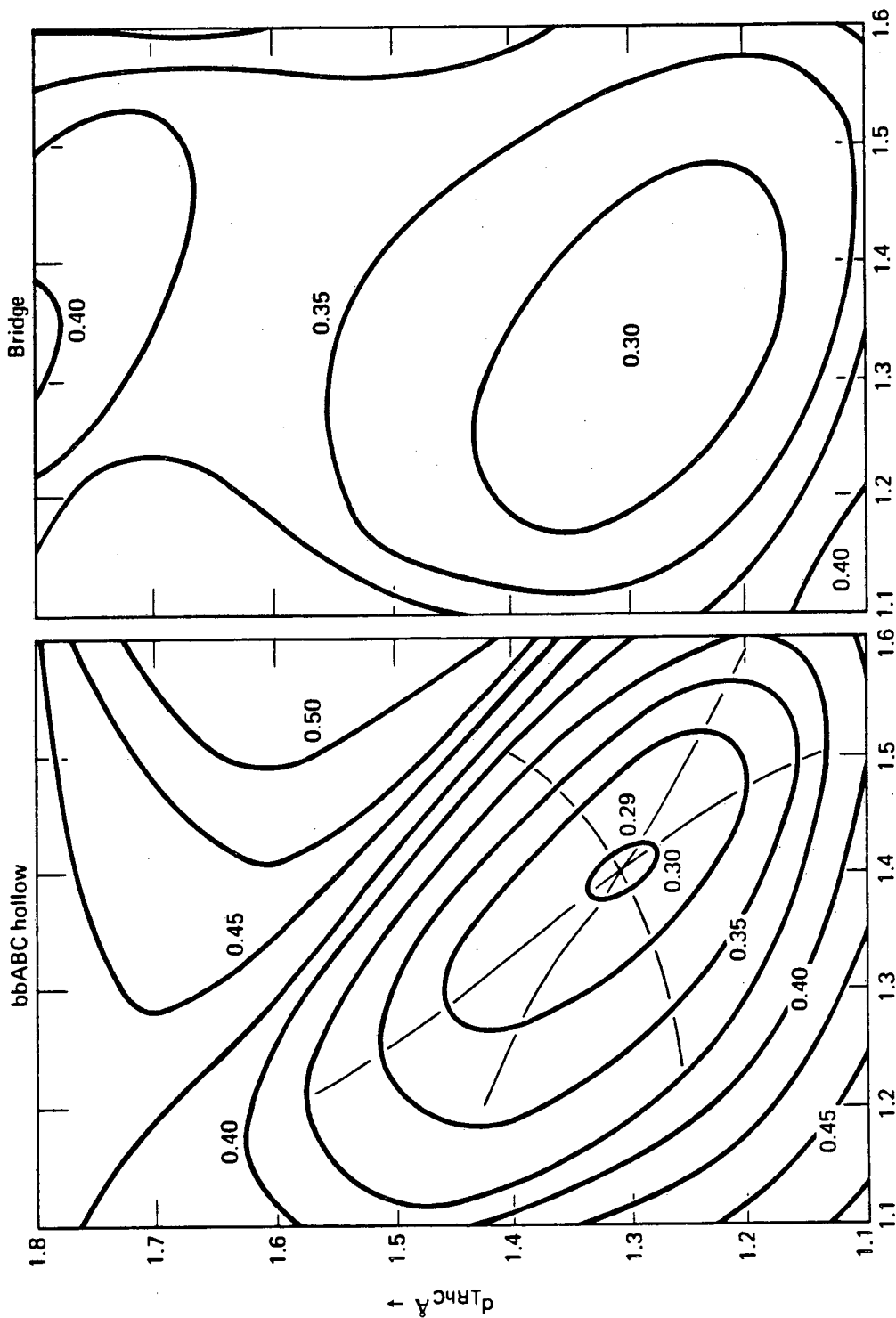


ϵ ($\mu\text{amp-sec}$)

XBL 818-11195

Fig. 3

Rh (111) + (2 X 2) C₃ (H₃)
Average over 5 R-factor
 $\theta = 0^\circ$

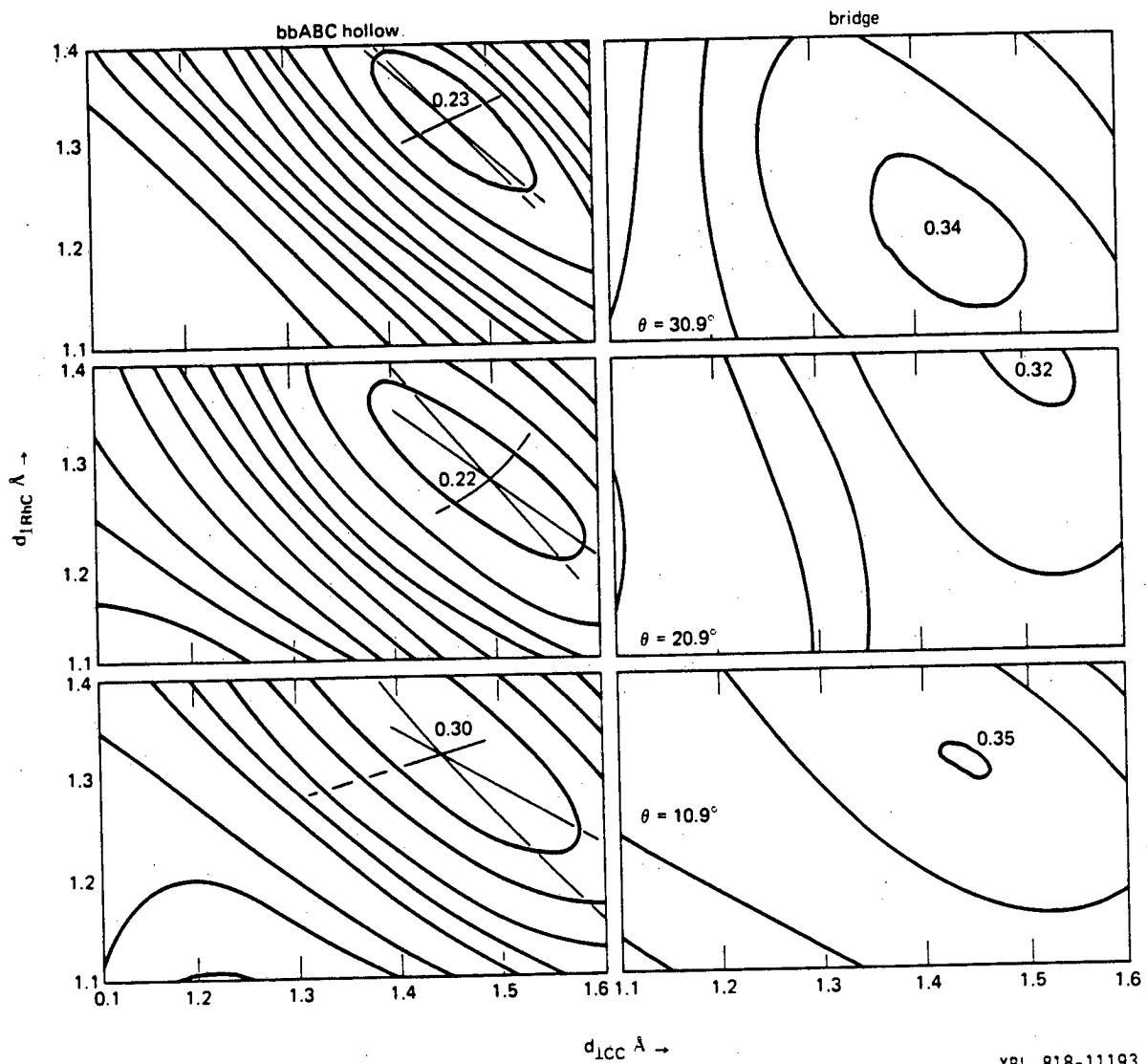


$d_{LCC} \text{ \AA} \rightarrow$

XBL 818-11192

Fig. 4

Rh (111) + (2 × 2) C₂ (H₃)
average over 5 R-factors



XBL 818-11193

Fig. 5

Rh(III) + (2x2) C₂H₃, T = 240 K, $\phi = 0^\circ$

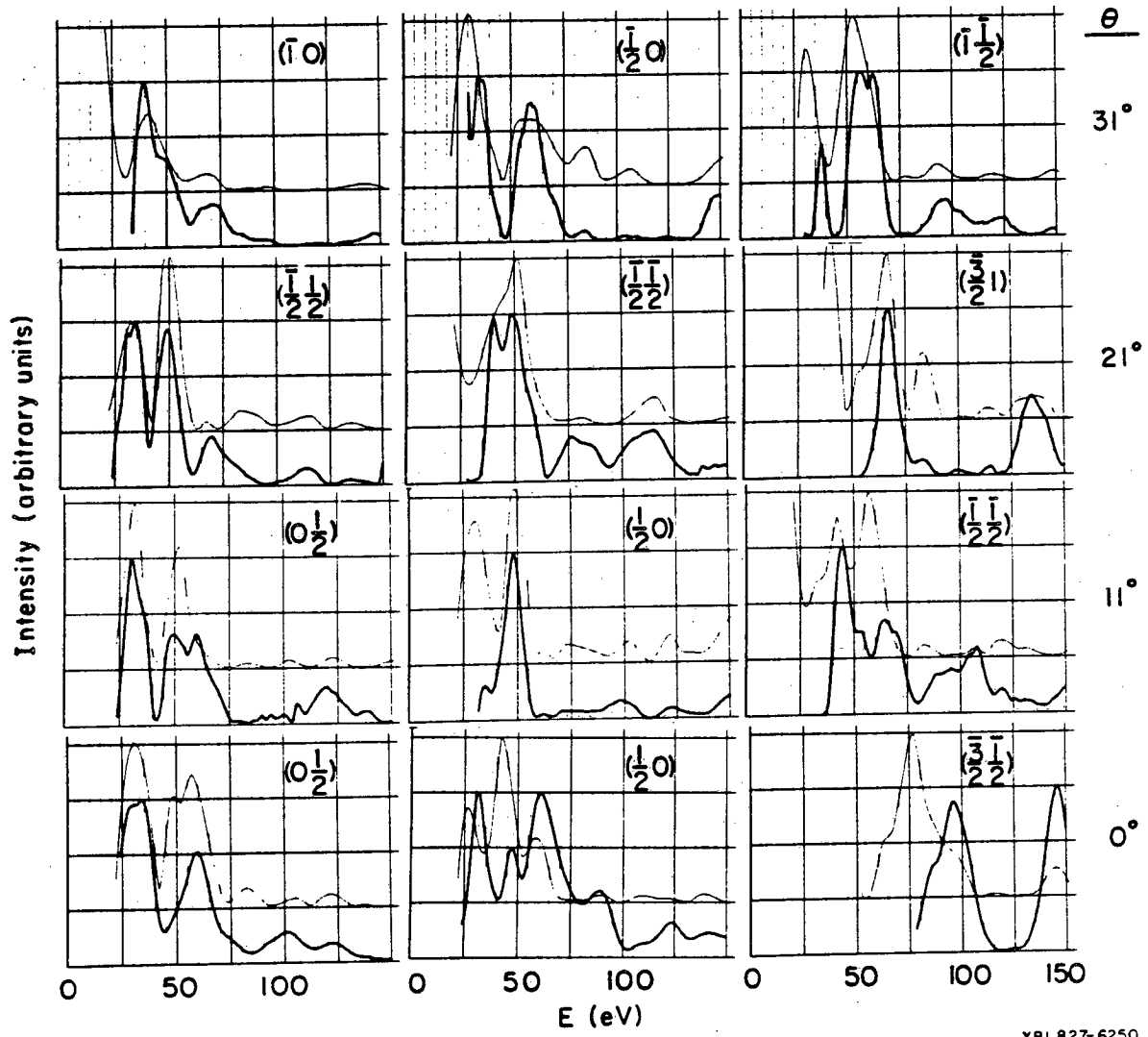
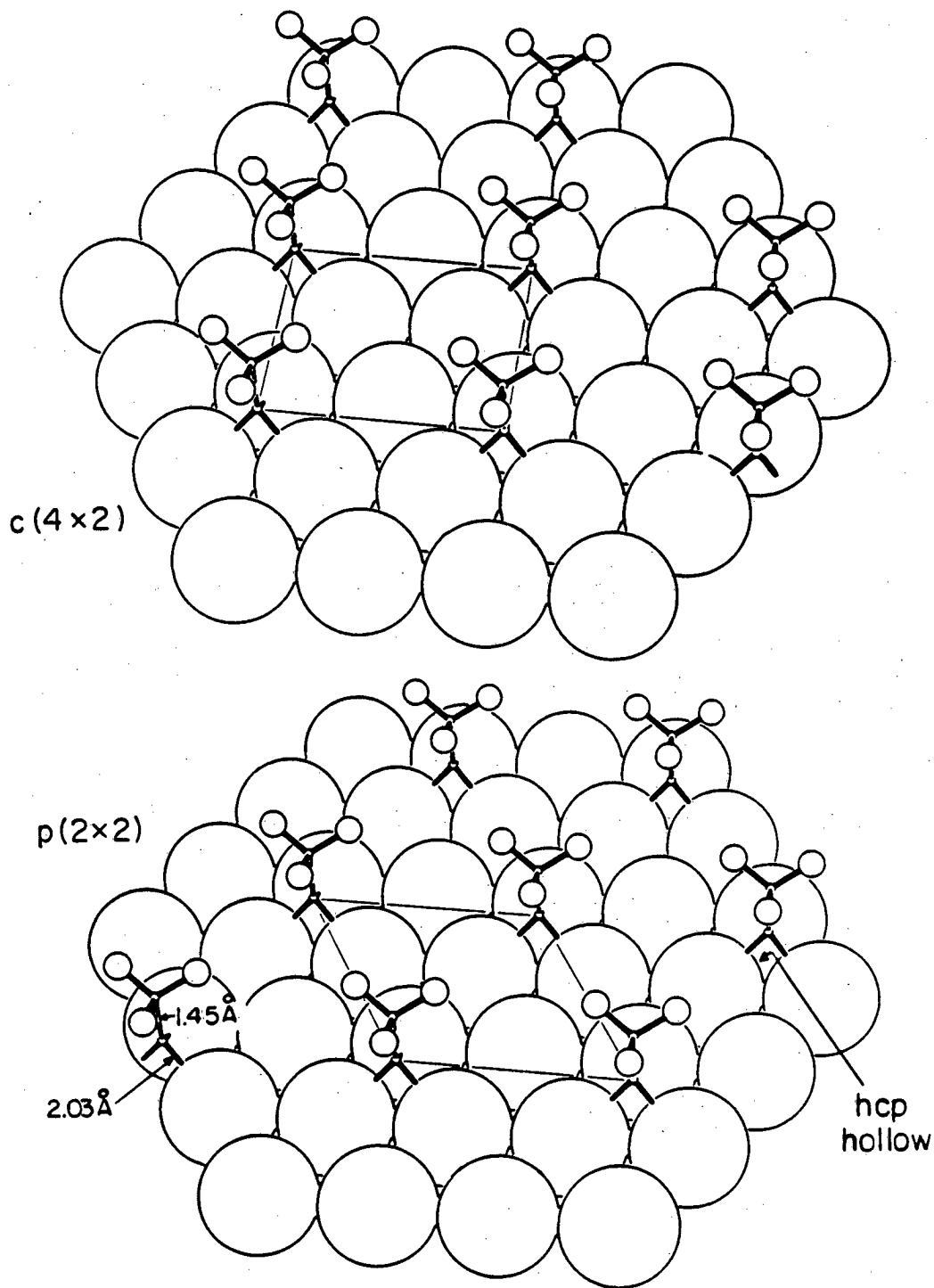


Fig. 6



fcc (111) + C_2H_3 (ethynylidyne)

XBL813-5407A

Fig. 7

VIII. C_2H_2 , C_3H_4 , AND C_3H_6 ADSORPTION ON THE Rh(111) SURFACE

A. INTRODUCTION

In this chapter we will consider three different hydrocarbon structures that occur on the Rh(111) surface.

(1) A $c(4 \times 2)$ overlayer lattice forms above 270 K if ethylene, propylene, acetylene plus hydrogen or methylacetylene plus hydrogen is adsorbed. Intensity vs. voltage (I-V) profiles for all the $c(4 \times 2)$ layers are found to be identical within experimental uncertainty which implies that their structure should also be the same or very similar. High Resolution Electron Energy Loss Spectroscopy (HREELS) results¹ suggest that the $c(4 \times 2)$ layer obtained with ethylene or acetylene plus hydrogen contains an ethylidyne species. Our LEED analysis cannot at present confirm this claim, and we will examine possible reasons for the discrepancy.

(2) Propylene adsorption on the Rh(111) surface at <240-270 K produces a (2×2) lattice of propylidyne; the overlayer structure is analogous to the (2×2) - C_2H_3 layer we considered in Chapter VII with one important difference. The extra carbon atom in the propylidyne group can produce a $(2\sqrt{3} \times 2\sqrt{3})R30^\circ$ superlattice. The formation of the superlattice is probably driven by the Van der Waals forces acting between the neighboring methyl groups. This structure is found by a preliminary LEED analysis (which assumes kinematic scattering in the hydrocarbon layer) and by a direct comparison of intensity curves that were measured after propylene and ethylene adsorption at 240 K.

Quite interestingly, low propylene exposures (1-2 L) will generate a well-ordered (2x2) adsorption lattice, while much higher gas exposures (~1000 L) are necessary to order the γ -carbon superlattice in the propylidyne overlayer. (Our gas exposures are uncorrected for ion-gauge sensitivity and for the different gas pressures at the ion-gauge and crystal.) Our Auger Electron Spectroscopy (AES) and diffraction beam intensity measurements indicate the carbon coverage of the low and high exposure phases is nearly the same. We believe the disorder-order transition that is observed with increasing gas exposure may be caused by the kinetics of propylene adsorption near saturation coverage. The kinetics is probably controlled by a repulsive Van der Waals interaction between the adsorbing propylene and the propylidyne already present on the metal surface.

(3) A (2x2) lattice also forms during methylacetylene adsorption on the Rh(111) surface at <240-270 K; as in the (2x2) propylidyne layer, a $(2\sqrt{3}\times 2\sqrt{3})R30^\circ$ superlattice appears with increasing gas exposure and becomes well-ordered only near ~1000 L. We have collected intensity data for this system and they bear little resemblance to the intensity curves for the $(2\sqrt{3}\times 2\sqrt{3})R30^\circ$ - $3C_3H_5$ layer. (I should mention that Frank Ogletree is most responsible for generating this set of intensity spectra from the data on film.) Although we have not yet begun a LEED analysis of these curves, the structure of this overlayer is probably analogous to other alkyne layers formed on the Rh¹ and Pt(111) surface (Chapter VI).

B. EXPERIMENTAL

i) Apparatus and Intensity Measurement

The cleaning of the Rh(111) crystal and the apparatus that was used for these experiments have been described in earlier Chapters III and V; so we will only add a few more experimental details here. The base pressure of our UHV chamber was typically $5-10 \times 10^{-10}$ torr during these adsorption experiments; and the measured H_2/CO ratio in the ambient gas was ~ 4 . This translates as a partial pressure ratio of ~ 2 after correcting for the sensitivity of the mass spectrometer.

The UTI 100C mass spectrometer was also used in the thermal desorption experiments; the mass numbers were detected with only a 2-3 amu resolution to improve the signal-to-noise ratio. So we did not distinguish between C_3H_6 and C_3H_8 or C_3H_4 desorption. The linear temperature ramp was ~ 6 K/sec.

The intensity vs. voltage profiles for all the adsorption systems to be discussed were collected using the photographic technique. The overlayers were sufficiently sensitive to electron beam damage that the incident LEED beam was moved across the crystal during the course of photography. In this way, the electron dose at any given region of the crystal was limited to about 25 $\mu\text{amp-sec}$; and the resulting intensity loss due to electron beam damage was less than 5%. The half-order beams for these overlayers decayed to half their maximum intensity in 100-200 $\mu\text{amp-sec}$.

Interestingly, the intensity of the half-order spots were observed to increase initially with electron exposure for all the low temperature (240 K) structures (see also Chapter VIIIB). This effect (also observed

for the ethylidyne and CO layers at 240 K on Rh(111)) is probably caused by the electron beam-induced desorption of coadsorbed hydrogen. In agreement with this explanation, we did not find an initial increase in the spot intensity with increasing electron exposure for the $c(4 \times 2)$ overlayers that were formed at 300 K since a quarter monolayer of coadsorbed hydrogen should have a significant desorption rate at this temperature.

ii) Preparation of the $c(4 \times 2)$ Overlayer

When the (2×2) lattice of ethylidyne (Chapter VII) that we formed at ($<240-270$ K) was slowly warmed to room temperature over the course of 2-3 hours, a well-ordered $c(4 \times 2)$ overlayer would develop.¹ The LEED patterns for both the (2×2) and $c(4 \times 2)-C_2H_n$ structures are shown in the upper part of Fig. 1. The (2×2) layer would quickly disorder if heated to ~ 270 K, but the $c(4 \times 2)$ lattice would then take several hours to fully order. The $c(4 \times 2)$ layer ordered best if a high background of hydrogen was present. This was achieved by flowing 10^{-7} torr H_2 through the UHV chamber for 1/2 hr with the mass spectrometer filaments on; the crystal was then flashed to 400 K to desorb the hydrogen prior to the ethylene exposure. In some cases, a $c(4 \times 2)$ layer was obtained at 240 K together with the (2×2) phase when a hydrogen treatment preceded the ethylene exposure; however, both layers disordered and only the $c(4 \times 2)$ lattice re-emerged when the crystal was slowly warmed to room temperature.

Propylene adsorption behaved very much like ethylene. Adsorbed acetylene and methylacetylene on the other hand would produce a very poorly ordered $c(4 \times 2)$ lattice unless a hydrogen treatment preceded the

hydrocarbon exposure. An atomic hydrogen treatment done after alkyne adsorption would still not yield a well-ordered $c(4 \times 2)$ lattice even though the crystal was kept at 240 K and allowed to warm slowly to room temperature.

iii) Preparation of the (2×2) Layer of Adsorbed Propylene

As shown in the lower left panel of Fig. 1, the propylene layer that appears after a 1-2 \underline{L} gas exposure (which is uncorrected for ion gauge sensitivity and the pressure difference between gauge and sample) with the crystal at $<240-270$ K has a well-ordered (2×2) lattice but also a coexisting $(2\sqrt{3} \times 2\sqrt{3})R30^\circ$ lattice which is fairly disordered. With increasing exposure ($\sim 1000 \underline{L}$), the $(2\sqrt{3} \times 2\sqrt{3})R30^\circ$ lattice becomes well-ordered as illustrated in the lower right section of Fig. 1. Using a telephotometer, we measured that the half-order diffraction beam intensity would reach a near-maximum level after only a 2 \underline{L} exposure, while the intensity of the sixth order reflections (that arise from the $(2\sqrt{3} \times 2\sqrt{3})R30^\circ$ lattice) would increase steadily until an exposure of $\sim 1000 \underline{L}$ was reached. However, we did not observe any improvement in the ordering of the $(2\sqrt{3} \times 2\sqrt{3})R30^\circ$ lattice if a high exposure ($\sim 1000 \underline{L}$) of n-butane ($n-C_4H_{10}$) followed the adsorption of 1-2 \underline{L} propylene.

iv) Preparation of the (2×2) Layer of Adsorbed Methylacetylene

Methylacetylene adsorption at 240 K gives the same progression of LEED patterns with increasing exposure as propylene (see Fig. 1). A well-ordered (2×2) coexists with a fairly disordered $(2\sqrt{3} \times 2\sqrt{3})R30^\circ$ lattice at low exposures (1-2 \underline{L}), while higher exposures ($\sim 1000 \underline{L}$) produce a well-ordered $(2\sqrt{3} \times 2\sqrt{3})R30^\circ$ periodicity. The ordering of the $(2\sqrt{3} \times 2\sqrt{3})R30^\circ$ lattice was fairly sensitive to the amount of background

H₂ in the chamber. In fact, we only did about three adsorption experiments (each using ~1000 L exposures) before another bakeout was found necessary. Already during the third adsorption experiment, ordering of the (2√3×2√3)R30° lattice was noticeably poorer than that obtained after the first experiment. To insure that the slight disordering did not affect our measured intensity curves, we made certain that one set of intensity data at each polar-angle was collected during the first or second adsorption experiment in every bakeout cycle.

Acetylene adsorption was more sensitive to our background H₂ pressure than methylacetylene. Operating at a lower base pressure (~1×10⁻¹⁰ torr), L. H. Dubois et al.¹ produced a sharply focused (2×2) LEED pattern after a low acetylene exposure (1-2 L) at a low temperature (240 K). We were only able to produce a fairly disordered (2×2) pattern just after an extended bakeout of our UHV chamber. After a few adsorption experiments the (2×2)-C₂H₂ pattern became even more disordered.

v) Coadsorption of Background H₂ and CO

The major background gases in the UHV chamber (H₂ and CO) did influence our hydrocarbon adsorption experiments. H₂ desorption occurs near 300 K on the clean Rh(111) surface; but a substantial amount of H₂ can remain adsorbed with the hydrocarbon layer at 240 K where the desorption rate is quite small. This coadsorbed hydrogen is probably responsible for the poor ordering of the acetylene and methylacetylene overlayers on the Rh(111) surface at 240 K. We believe the hydrogen reacts with the adsorbed alkyne to produce a mixed phase of alkylidyne and alkyne.

To a lesser extent, coadsorbed hydrogen can also disorder molecular overlayers which do not react with it. This was observed in plots of the intensity of the overlayer diffraction beams vs. the electron exposure. For both CO and hydrocarbon adsorption at 240 K, the intensity for the overlayer reflections would show a slight increase at first (20 μ amp sec for (2×2) - C_2H_3 as shown in Fig. 2 of Chapter VII) and then an exponential decay with electron exposure. As the background H_2 pressure rose, we needed larger electron exposures (~ 100 μ amp-sec for (2×2) - C_2H_3) to reach the maximum intensity in the overlayer reflection. (Yet the resulting intensity curves were found to be the same for both preparations of the (2×2) - C_2H_3 layer.) On the other hand, CO and hydrocarbon adsorption at 300 K, where the H_2 desorption rate is significant, did not show any electron-beam induced ordering of the overlayer lattice. In another experiment described in Chapter V, the $(\sqrt{3} \times \sqrt{3})R30^\circ$ -CO layer obtained at 240 K was slightly disordered, but could become very well-ordered by flashing the sample to 325 K whereupon some H_2 desorption was detected with the mass spectrometer.

CO coadsorption was also observed during our hydrocarbon exposures. Thermal Desorption Yield Spectroscopy indicates that very little CO adsorbs prior to the hydrocarbon exposure. However, during the hydrocarbon exposure about 0.05-0.10 monolayers of CO adsorb on the Rh(111) surface. This coverage is estimated by comparing the peak areas of thermal desorption spectra obtained from the $(\sqrt{3} \times \sqrt{3})R30^\circ$ -CO structure at $\theta=1/3$ and from the coadsorption phases. These coadsorption phases include the ethylene, propylene, methylacetylene, and acetylene layers

that order into (2×2) or $c(4 \times 2)$ lattices; it also includes the (2×2) and $c(4 \times 2)$ ethylene overlayers that were post-exposed to a few langmuirs of CO.

We should point out however that the post-adsorption of CO can be important under more severe conditions; we found that an ordered $c(4 \times 2)$ ethylene layer can be disordered with a ~ 10 L CO exposure. As shown in Fig. 2, the disorder is directed only along the long edge of the primitive rectangular unit cell. The estimated coverage of CO after this treatment is still near 0.10 monolayers as measured by Thermal Desorption Yield Spectroscopy. This suggests that only a small amount of CO can be post-adsorbed into the $c(4 \times 2)$ ethylene overlayer and that this amount will cause a disordering in the $c(4 \times 2)$ lattice.

Other evidence also implies that post-adsorption of CO into the $c(4 \times 2)$ lattice is not significant. As we'll see in the Results section, the intensity spectra for the ethylene and propylene-derived $c(4 \times 2)$ overlayers are identical within experimental error. Since the propylene layer is more crowded than ethylene, we would expect the propylene and ethylene intensity spectra to be different if CO post-adsorption were significant. That is, the more crowded propylene layer should allow less CO to post-adsorb than the ethylene $c(4 \times 2)$ lattice.

C. RESULTS

i) $c(4 \times 2)$ Layer

a) Domain Preference

The LEED pattern for the $c(4 \times 2)$ layer has many diffraction beams which arise from only one of the three possible rotational domains. If we look at Fig. 1, we see that the intensity for equivalent diffraction

beams from separate domains can be dramatically different. Two domains give nearly the same intensity to equivalent LEED spots, while the third domain has much weaker diffraction intensities. We can see this quite easily by looking at the equivalent spots about the mirror planes in the (10) and (01) directions in the $c(4 \times 2)$ pattern given in Fig. 1. (We should not forget however that the intensity vs. voltage spectra for all the equivalent spots are proportional to each other even though their absolute intensities are found to be different.)

Since one domain has a corresponding set of diffraction beams that are fairly weak in intensity, it should have a lower coverage on the surface. The probable reason for this domain preference is the presence of a fairly large step density on the metal surface. Two of the rotational domains would then remain nearly equivalent with respect to the step edge and their orientation would be favored over the third domain.

The orientation of the step edge must lie in only a few possible directions to give the observed domain preference in the $c(4 \times 2)$ structure. There are six mirror lines in the ethylene overlayer (three of which are also mirror planes in the metal substrate). Since two rotational domains are nearly equivalent with respect to the step edge, this edge must lie along one of two possible mirror planes. Now the step edge may also be rotated by as much as 3° away from these mirror planes since this small perturbation should not strongly affect the apparent symmetry between the two near equivalent domains. This simple argument implies that the step edge lies in a 12° sector out of a possible 180° .

Next we can ask what probability is there that the step edge would lie in a direction that makes two rotational domains nearly equivalent. Here again we will assume that the step edge may be rotated about 3° away from the mirror plane without appreciably affecting the measured intensities in the near-equivalent domains. The probability we calculate is $1/5$.

b) Comparison of Intensity Curves

We collected a full set of intensity curves for the $c(4 \times 2)$ ethylene and propylene overlayers that are being used in the LEED analysis. The intensity data includes four angles of incidence ($\theta=0^\circ$, 11° , 21° and 31° with $\phi = 0^\circ$) and has an energy range of 24-150 eV. We also measured I-V spectra for the acetylene plus hydrogen and methylacetylene plus hydrogen overlayers at two angles of incidence ($\theta=0^\circ$ and 31° with $\phi=0^\circ$). Figures 3-5 show 12 independent diffraction beam intensity curves for each of the $c(4 \times 2)$ overlayers. We see that within experimental uncertainty these curves are identical.

ii) $(2\sqrt{3} \times 2\sqrt{3})R30^\circ$ Propylene Layer

a) Comparison of Half-Order Intensity Curves
for Ethylene and Propylene Structures

At low exposures (1-2 L) with the crystal at $<240-270$ K, the propylene layer forms a well-ordered (2×2) lattice but also a fairly disordered $(2\sqrt{3} \times 2\sqrt{3})R30^\circ$ lattice appears. Only normal incidence intensity curves were collected for the half and integral order reflections in the low exposure propylene phase, while a full set of spectra including the sixth order diffraction beams was obtained for the high

exposure propylene phase at four angles of incidence ($\theta = 0, 11, 21$ and 31 at $\phi=0^\circ$). The high exposure propylene curves were checked for reproducibility by a second, independent experiment.

Figures 6-8 show a comparison of corresponding intensity curves for six different diffraction beams from the $(2 \times 2)\text{-C}_2\text{H}_3$, the low exposure propylene, and the high exposure propylene structures. We see that the intensity spectra from the $(2 \times 2)\text{-C}_2\text{H}_3$ and low exposure propylene phases are very similar, but they depart significantly from those for the high exposure propylene layer.

b) $(2\sqrt{3} \times 2\sqrt{3})R30^\circ$ Structure Determination by LEED

We did a preliminary structure determination of the high exposure propylidyne lattice using only the normal incidence intensity curves. The LEED theory has already been described in Chapter VII.C for the similar $(2 \times 2)\text{-C}_2\text{H}_3$ structure determination. In this preliminary analysis, the electron scattering in the overlayer was assumed to be fully kinematic.

The model geometries that were tested in the LEED analysis assumed the α and β carbon atoms of adsorbed propylene occupy the same positions as those measured for adsorbed ethylene in the $(2 \times 2)\text{-C}_2\text{H}_3$ structure determination. Only the distance of the α -carbon atom above the hollow site ($d_{\perp\text{RhC}}$) was varied. This approach is based on the strong similarity in the intensity curves measured for the ethylene and low exposure propylene phases.

The γ -carbon atom position in the $(2\sqrt{3} \times 2\sqrt{3})R30^\circ$ structure was varied over a fairly large range of possible bond distances and angles. The β -carbon to γ -carbon distance, d_{CC} , was set at either 1.50 \AA (for

a single bond) or 1.33 Å (for a double bond), while the $c(\alpha)-c(\beta)-c(\gamma)$ bond angle (θ_{CC}) was varied from 105-130°. The γ -carbon was also allowed to rotate (ϕ_{CC}) about the $c(\alpha)-c(\beta)$ bond; however we always kept the three γ -carbon atoms in the $(2\sqrt{3}\times 2\sqrt{3})R30^\circ$ unit cell rotated by 120° relative to each other.

The reliability factors for this model geometry are plotted in Fig. 9. We first notice the well-behaved minima that appear in each plot and also the values of the R-factor minima are of the right magnitude. The best agreement between theory and experiment is obtained for $d_{\perp RhC} = 1.40$ Å, $d_{CC} = 1.50$ Å, $\theta_{CC} = 106^\circ$, and most importantly $\phi_{CC} = 30^\circ$. The distance between the top Rh layer and the α carbon ($d_{\perp RhC}$) is only slightly greater than that obtained in our earlier $(2\times 2)-C_2H_3$ determination ($d_{\perp RhC} = 1.31$ Å); and the values for d_{CC} and θ_{CC} are consistent with a propylidyne species above the Rh surface (where $d_{CC} = 1.54$ Å and $\theta_{CC} = 109^\circ$). The small scatter in these distances and angles from expected values can be due to the fairly crude approximation (kinematic) used to model the electron diffraction in the hydrocarbon overlayer. (See Chapter V, Part II).

An atop view of the $(2\sqrt{3}\times 2\sqrt{3})R30^\circ$ lattice is shown in Fig. 10. The γ -(or methyl) carbon atoms are rotated about the $C(\alpha)-C(\beta)$ bond by an angle $\phi_{CC} = 30^\circ$; the significance of this orientation will be fully considered in the Discussion section. To our knowledge, the propylidyne layer illustrated in Fig. 10 is the first example of an adsorbate exhibiting two separate periodicities. That is, the α and β carbon atoms occupy a (2×2) lattice, while the γ -carbon atom orders into a $(2\sqrt{3}\times 2\sqrt{3})R30^\circ$ superlattice.

iii) $(2\sqrt{3}\times 2\sqrt{3})R30^\circ$ Methylacetylene Layer

Intensity data for the low and high exposure methylacetylene phases has been collected. (Frank Ogletree is most responsible for generating the I-V spectra from the intensity data on film.) The low exposure (1-2 L) methylacetylene layer has a well-ordered (2x2) but a fairly disordered $(2\sqrt{3}\times 2\sqrt{3})R30^\circ$ periodicity. The $(2\sqrt{3}\times 2\sqrt{3})R30^\circ$ lattice also becomes well-ordered after a high exposure (~1000 L) of methylacetylene. The data for each methylacetylene overlayer contains four angles of incidence ($\theta = 0, 1l, 2l$ and $3l$ at $\phi=0^\circ$) that spans an energy range of 24-150 eV.

Unfortunately we could not examine the series of intensity curves for the acetylene, low exposure methylacetylene and high exposure methylacetylene phases as we did for the C_2 and C_3 alkenes on Rh(111). The acetylene layer could not be ordered well enough to take intensity measurements. As mentioned in the experimental section, we believe the relatively high H_2 background pressure is responsible for this disordering of the acetylene overlayer. Since an HREELS study¹ of the (2x2)- C_2H_2 layer has already been done, the comparison of intensity spectra from the (2x2)- C_2H_2 and low exposure methylacetylene layer could have provided valuable structural information. Nonetheless, a structural determination of the well-ordered $(2\sqrt{3}\times 2\sqrt{3})R30^\circ$ -methylacetylene overlayer using dynamical LEED is planned.

D. DISCUSSION

Throughout this section, we will compare intensity spectra from different adsorption systems which will give us valuable structural information directly without any LEED calculations. To do this, it will

be important to realize that our diffraction experiments are not sensitive to atoms that are disordered above the metal surface. These atoms do not scatter the incident plane wave of electrons coherently and thereby cannot influence the resulting intensity curves. On the other hand, if these atoms begin to order into an overlayer lattice, we should expect to find changes in the resulting I-V spectra.

i) c(4x2) Layer

a) Comparison of Intensity Curves

Our intensity curves for the c(4x2) lattices of adsorbed ethylene and acetylene plus hydrogen are very similar; this indicates the structures of these C₂ overlayers should be nearly identical. A HREELS study¹ of the ethylene and acetylene plus hydrogen overlayers predicts that an ethylidyne species occupies the c(4x2) unit cell. Figure 11 shows the HREELS spectra measured for the (2x2) and c(4x2) ethylene overlayers; these spectra are nearly identical to each other. In Chapter VII, we found that the (2x2)-ethylene layer consisted of an ethylidyne species adsorbed above an hcp hollow site. The near identity in the (2x2) and c(4x2) HREELS spectra implies that an ethylidyne group probably also exists within the c(4x2) unit cell. Figure 12 illustrates the c(4x2) ethylidyne structure, which is predicted by HREELS, along with the (2x2) lattice determined by our earlier LEED intensity analysis.

We can now consider the near identity in the measured intensity curves for the C₂ and C₃ unsaturated hydrocarbon overlayers with a c(4x2) lattice. This identity implies that the C₃ hydrocarbons produce a propylidyne layer with randomly oriented γ-(or methyl)

carbon atoms. Since the randomly oriented γ -carbon appears disordered in our diffraction experiment, the intensity spectra for the C_2 and C_3 layers should be the same.

We can rule out the possibility that the adsorbed propylene or methylacetylene molecules fragment to form a $c(4 \times 2)$ lattice of ethylidyne plus a disordered carbon residue by our Thermal Desorption Spectroscopy experiments. These measurements strongly suggest that carbon skeleton of the C_3 hydrocarbons remains intact up to temperatures near 380 K. Figure 13 shows the $c(4 \times 2)$ lattice of propylidyne with the methyl group randomly oriented above the metal surface.

b) LEED Analysis

Our intensity analysis for the $c(4 \times 2)$ overlayer cannot confirm the ethylidyne structure predicted by HREELS,¹ even though we have tested over 900 possible geometries. There are a number of possible reasons for this disturbing discrepancy. (1) The HREEL spectrum may be misleading because the $c(4 \times 2)$ lattice was not well-ordered during the measurement.³ The overlayer was prepared with a very low background pressure of H_2 in the HREELS study since the total pressure in the UHV chamber during the adsorption experiment was $\sim 1 \times 10^{-10}$ torr.³

We found during our LEED study that the ordering of the $c(4 \times 2)$ lattice is promoted by a fairly large background H_2 pressure. So it is possible that a substantial amount of the (2×2) ethylidyne phase was still present on the surface when the HREELS spectrum was measured. On the other hand, the HREEL spectra for the $c(4 \times 2)$ layer obtained from either ethylene or acetylene plus hydrogen adsorption were very similar

which suggests that sufficient hydrogen was available to make a nearly complete transition from the (2x2) phase.

(2) Another possible explanation for the discrepancy between LEED and HREELS concerns the coadsorption of CO in the c(4x2) hydrocarbon layers. We measured with Thermal Desorption Yield Spectroscopy that very little CO pre-adsorbs on the Rh(111) surface, but about 0.05-0.10 monolayers of CO coadsorbs during the hydrocarbon exposure. In our preparation, the (2x2) and c(4x2) ethylene structures must have the same amount of coadsorbed CO and we have already done a LEED intensity analysis on the (2x2)-C₂H₃ layer that produced very satisfactory agreement between calculated and experimental spectra. So we do not believe that coadsorption of CO is the cause of the discrepancy.

(3) We should also consider the post-adsorption of CO into the c(4x2) ethylene or propylene overlayer. The c(4x2) ethylene layer was kept in vacuo for 5-10 hours prior to measurement of the diffraction intensities, while the intensity data from the low temperature (240 K) (2x2) phases of ethylene and propylene was collected immediately after adsorption.

Our Thermal Desorption Yield measurements indicate however that the c(4x2) ethylene layer also has a CO coverage of about 0.05-0.10 monolayers. We would expect to measure a higher coverage in the c(4x2) layer if CO post-adsorption were significant. In addition, we do not find a noticeable increase in the CO coverage for the c(4x2) ethylene layer after a 10 L CO exposure, even though the LEED pattern shows a disordering along the longer edge in the rectangular overlayer unit

cell. This suggests that CO does not post-adsorb easily into the $c(4 \times 2)$ ethylene layer, while the small amounts of CO that can post-adsorb under fairly severe conditions will disorder the $c(4 \times 2)$ lattice.

To further support our claim that post-adsorption is negligible for the $c(4 \times 2)$ hydrocarbon phases, we remember that the intensity spectra for the propylene and ethylene $c(4 \times 2)$ lattices are nearly identical. If post-adsorption of CO was indeed a significant problem, we would expect the more crowded propylene layer to be less affected than the ethylene overlayer and to give noticeably different intensity curves.

The relative crowding of the propylene and ethylene overlayers has been illustrated in earlier experiments. We found that overexposing the Rh(111) (Chapter VII) or Pt(111) (Chapter VI) surfaces to ethylene will disorder the hydrocarbon overlayer; yet high exposures of propylene will not disorder the C_3 overlayer. We believe this occurs because additional ethylene molecules can adsorb at interstitial sites after the (2×2) layer is fully developed, but interstitial adsorption is much more difficult in the more crowded propylene phase.

It is not apparent which of the above-mentioned possibilities is the actual cause for the discrepancy between LEED and HREELS. We believe further HREELS experiments are necessary to rule out some or possibly all the suggested problems. This would mean studying more closely the effect of H_2 and CO on the $c(4 \times 2)$ overlayer. Another HREEL Spectrum should be measured for an ethylene layer that has been thoroughly pretreated with H_2 to insure a complete conversion to the $c(4 \times 2)$ structure. Also HREEL spectra should be obtained for the $c(4 \times 2)$ -ethylene layers after post-exposures of CO in order to be

certain that our LEED intensity measurements were not carried out on a $c(4 \times 2)$ lattice which had significant amounts of post-adsorbed CO. If both the LEED and HREELS experiments were done correctly, we plan to test even more ethylidyne structures in the LEED intensity analysis for the $c(4 \times 2)$ overlayer.

ii) $(2\sqrt{3} \times 2\sqrt{3})R30^\circ$ Propylene Layer

a) Comparison in Intensity Curves

Figures 6-8 showed the comparison of corresponding half- and integral-order diffraction beam intensity curves for the (2×2) -ethylidyne, low exposure propylene, and high exposure propylene phases. The ethylene and low-exposure propylene curves are nearly identical. This similarity could arise from a (2×2) -propylidyne lattice that is identical to (2×2) -ethylidyne except for the presence of an extra carbon atom. The γ -carbon atoms that are present only in the propylidyne layer would then be disordered and essentially not detected by our LEED experiment.

Our TD spectra show a large H_2 desorption at 390 K that strongly suggests the propylene carbon skeleton is kept intact during the formation of the (2×2) overlayer.² This evidence speaks against the possibility that ethylidyne plus a disordered carbon fragment forms after propylene adsorption on Rh(111) at <240-270 K.

The high exposure intensity spectra in Figs. 6-8 look very different from the low exposure curves. We interpret this as an ordering of the γ -carbon atoms. When these extra carbon atoms do become ordered, they can scatter the incident electrons coherently and begin

to change the resulting intensity curves. The $(2\sqrt{3}\times 2\sqrt{3})R30^\circ$ unit cell seen in the LEED pattern would then correspond to the ordering of those γ -carbon atoms.

b) $(2\sqrt{3}\times 2\sqrt{3})R30^\circ$ Propylene Structure Determination

The interpretation of the TD and intensity spectra given in the previous section is supported by our preliminary LEED analysis of the $(2\sqrt{3}\times 2\sqrt{3})R30^\circ$ propylene structure that assumes only kinematic scattering in the overlayer. Figure 10 shows the result of this determination with an atop view of the propylidyne lattice. The α - and β - carbon atoms have a (2×2) periodicity, while the γ -carbon orders into a $(2\sqrt{3}\times 2\sqrt{3})R30^\circ$ unit cell which is drawn. The α, β -carbons occupy the same positions in the (2×2) adsorption lattice as they did in the (2×2) -CCH₃ layer. However, the most interesting feature of this overlayer is the configuration of methyl groups (or γ -carbon atoms). Figure 14 suggests why the γ -carbons assume their measured positions. The neighboring hydrogen atoms in a triplet of propylidyne groups are blown up to their Van der Waals radii; we see that these Van der Waals spheres just touch one another when the γ -carbon atoms are rotated to their measured positions. This implies that Van der Waals forces between neighboring propylidyne species are probably driving the superlattice formation.

Force field calculations⁴ that consider standard Van der Waals potentials also suggest that the γ -carbon superlattice is driven by only Van der Waals forces. The methyl groups shown in Fig. 10 are allowed in these calculations to rotate in phase about the α -carbon to β -carbon bond. If no intramolecular rotational barrier is assumed for

the methyl carbon, the predicted positions of the γ -carbons coincide with those measured by our LEED analysis.

c) The Disorder-Order Transition

The half-order diffraction beams were found to reach near maximum intensity with only a 1-2 L exposure of propylene, while the sixth order beams (which arise from the $(2\sqrt{3}\times 2\sqrt{3})R30^\circ$ superlattice) do not reach near-maximum intensity until exposures of about 1000 L. Why should the (2×2) cell order at much lower propylene exposures than the $(2\sqrt{3}\times 2\sqrt{3})R30^\circ$ superlattice? There are two likely explanations.

(1) The low exposure of propylene already saturates the metal surface with propylidyne, but larger exposures are needed to anneal the methyl superlattice by energy transfer from the impinging molecules. A recent molecular beam experiment⁵ observed that adsorption of NO in a second layer above the Pt(111) surface occurs with complete energy accommodation; or in other words, the NO molecules that strike a saturated overlayer of adsorbed NO on Pt(111) at 290 K can effectively transfer energy to the ad molecules even though the residence time of the second layer NO is only about 0.1 msec.

2) An alternative explanation considers the kinetics of propylene adsorption near saturation coverage after a 1-2 L exposure of propylene, the hydrocarbon layer is nearly saturated as evidenced by the near maximum intensity measured for the half-order diffraction beams in the LEED pattern. However, a number of residual vacancies could exist; and they may require a much higher gas exposure to be completely filled. A likely reason for the low sticking coefficient

near saturation coverage is that neighboring propylidyne groups can block adsorption of propylene at the vacancy site. This is illustrated in the top part of Fig. 15 where the hydrogen atoms attached to the propylene group are blown up to their full Van der Waals radii. We see that neighboring propylidyne species could easily rotate their methyl groups above the vacancy sites thus blocking adsorption of an incoming propylene molecule. A very similar process was shown to dominate the adsorption kinetics of ethylene on Pt(100)⁶ using Auger Electron and Ultra Violet Photoemission Spectroscopies (AES and UPS). Upon adsorption ethylene is thought to form a c(2x2) lattice of acetylene. (See Chapter IX). The probability of ethylene adsorption decreases significantly if a nearest neighboring site in the c(2x2) lattice is occupied by acetylene. The probability of acetylene adsorption however is not influenced by the occupation of nearest neighboring sites. So an incoming ethylene molecule probably experiences much stronger Van der Waals repulsive forces than acetylene; and these forces significantly affect the adsorption kinetics of ethylene but not acetylene.

Unfortunately, our retarding field Auger Electron Spectrometer can not resolve the small changes in total carbon coverages to see if the residual vacancies are removed with increasing gas exposure. Instead we tried a simple experiment where a ~1000 L butane (C₄H₁₀) exposure followed the adsorption of 1-2 L propylene. Butane will not adsorb on the Rh surface at 240 K, but can transfer energy to the γ -carbon in propylidyne to help order the superlattice. We should recall that gas phase NO (which has a lower heat of vaporization than

butane) was able to fully transfer its energy to the adsorbed layer present on the Pt(111) face. Since the $(2\sqrt{3}\times 2\sqrt{3})R30^\circ$ lattice did not become better ordered after the ~ 1000 L butane exposure, we believe the residual vacancy model is probably the correct one.

In Chapter VI we found that adsorbed propylene on the Pt(111) surface produces a propylidyne group with a randomly oriented γ or methyl carbon atom. This layer was prepared at 300 K but no change was observed when it was cooled to 240 K. (In fact, Frank Ogletree has recently cooled the Pt sample to 140 K, but the expected superlattice still did not form.) Why should the γ -carbon in propylidyne order into a superlattice on Rh(111) and not Pt(111)? We believe the 4% larger lattice spacing of Pt moves the methyl groups of neighboring propylidyne species sufficiently far away from one another to reduce their Van der Waals interactions. On the Rh(111) at 240 K, we believe the enthalpy term (ΔH) in the Gibbs free energy governs to produce an ordered superlattice, but on Pt(111) at 240 K the entropy term (TDS) is more important which leaves the γ -carbon atoms disordered.

It should be interesting to cool the propylidyne layer on Pt below 140 K to see at what temperature the enthalpy term becomes more important than the entropy. This transition may very well be first order since the entropy ($S = \partial G / \partial T \Big|_P$) should be different for the disordered and ordered γ -carbon atoms. Similar transitions are observed in many bulk crystal (such as CO, NO, and some hydrocarbons). At a certain temperature, the molecules change from a cubic lattice where no rotation is possible to an hexagonal one where they can rotate freely about their center of mass.

Quickly heating above the transition temperature could also yield information on the kinetics of this transition. One may wonder why we didn't try heating the propylidyne on Rh layer to see the order-disorder transition of the γ -carbons. Unfortunately for this system, the propylidyne groups rearrange into a completely different structure (probably a $c(4 \times 2)$ lattice of propylidyne) before the order-disorder transition can occur.

iii) $(2\sqrt{3} \times 2\sqrt{3})R30^\circ$ Methylacetylene Layer

The methylacetylene overlayer on Rh(111) produces a well-ordered (2×2) unit cell and a fairly disordered $(2\sqrt{3} \times 2\sqrt{3})R30^\circ$ superlattice at low exposures (1-2 \underline{L}) and low temperature ($<240-270$ K). With higher exposures (~ 1000 L), the $(2\sqrt{3} \times 2\sqrt{3})R30^\circ$ superlattice also becomes well-ordered; this disorder-order transition with increasing gas exposure parallels that for the propylidyne overlayer on Rh(111). Figure 16 shows a likely structure for this methylacetylene species predicted by a number of HREELS studies.^{1,7,8} The unsaturated carbon atoms are sp^2 -hybridized and di- σ bonded to two metal atoms. The carbon-carbon double bond probably also π -bonds to a third metal atom on the Rh surface. The unsaturated carbon-carbon bond is parallel to the metal surface and centered nearly above the hollow site.

HREEL spectra for acetylene on Rh(111)¹ at 240 K, Pt(111)⁷ at 140 K, and Pd(111)⁸ at 150 K predict a geometry similar to that shown in Fig. 16; however a LEED analysis has not been done to confirm any of these structures. (Actually an early dynamical LEED study of acetylene on Pt(111) was done,⁹ but the results are questionable at this time.)

In Chapter VI, we found that the "metastable" acetylene and methylacetylene layers on Pt have intensity curves that are nearly identical and thereby concluded that adsorbed methylacetylene may also di- σ , π bond to the metal surface. The extra carbon atom in the methylacetylene species was not detected in the diffraction experiment because it is randomly oriented due to tumbling about the unsaturated carbon-carbon bond and possibly the arbitrary attachment of the methyl group to either unsaturated carbon atom. Similarly, methylacetylene may adsorb like acetylene on the Rh(111) surface at 240 K and give the structure illustrated in Fig. 16. Unfortunately, we could not compare the intensity curves for acetylene and methylacetylene adsorbed on Rh(111) because the acetylene overlayer did not order well with our high H_2 background pressure. We believe the comparison however would indicate that the intensity spectra are nearly identical and that the methylacetylene does in fact di- σ , π bond to the metal. A LEED analysis of our experimental intensity curves is planned that will hopefully confirm our proposed geometry.

The $(2\sqrt{3} \times 2\sqrt{3})R30^\circ$ superlattice that is observed in the methylacetylene layer on Rh(111), but not on Pt(111), is probably caused by the ordering of the methyl carbons; the driving force for the superlattice formation should again be Van der Waals interactions. We remember that the propylidyne superlattice formed on the Rh(111) surface but not on Pt(111) due to the 4% larger lattice spacing for Pt(111). Probably for the same reason, methylacetylene produces a superlattice on Rh but not Pt. If we cool the Pt substrate

below 300 K, we should hope once more to observe a disorder-order transition in the position of the methyl carbons.

We can again ask ourselves what causes the ordering of the superlattice at higher gas exposures. We believe the residual vacancy explanation should be favored over annealing of the methylacetylene layer after larger gas exposures.

E. SUMMARY

Three different hydrocarbon structures that form on Rh(111) were considered in this Chapter. (1) Ethylene, propylene, acetylene plus hydrogen, and methylacetylene plus hydrogen all produce a $c(4 \times 2)$ lattice at 300 K. The nearly identical intensity spectra for these separate overlayers indicate that the same or nearly the same hydrocarbon structure exists. By Thermal Desorption Spectroscopy (TDS), we determine that the C_2 and C_3 hydrocarbon chain is kept intact under our experimental conditions and that the extra carbon atom in the C_3 overlayers is randomly oriented. A HREELS study of ethylene and acetylene plus hydrogen on Rh(111) predicts an alkylidene species forms in the $c(4 \times 2)$ lattice. However, our LEED analysis has not been able to confirm this at present; this discrepancy may be due to CO post-adsorption into the hydrocarbon lattice before the LEED intensity measurements were made or may be due to the partial transition from the $(2 \times 2) \rightarrow c(4 \times 2)$ phases during the HREELS experiment. It is also possible that more model geometries should be tested in the LEED analysis.

(2) Propylene produces a (2×2) lattice of propylidyne at $<240-270$ K; with high gas exposures (~ 1000 L), the γ -carbon atoms further order into a superlattice. To our knowledge, this is the first example of an

admolecule that exhibits two different surface periodicities. The α, β carbons have a (2×2) periodicity, while the γ -carbon atoms order into a $(2\sqrt{3} \times 2\sqrt{3})R30^\circ$ superlattice. The α, β carbons occupy the same positions as we found for ethylidyne in Chapter VII; the methyl groups of the neighboring propylidyne species rotate towards each other due to their Van der Waals interaction. This result is consistent with force-field calculations that assume standard Van der Waals parameter and predict the same γ -carbon position which we measure by LEED.

Our preliminary LEED analysis of the high exposure propylene phase assumed only kinematic scattering in the overlayer. A more refined calculation that considers full multiple scattering in the hydrocarbon layer is presently underway and should confirm our early result. (See Chapter V, Part 2). At low exposures ($1-2 \underline{L}$), the propylidyne species has a randomly oriented γ - (or methyl) carbon atom; this is shown by a direct comparison of intensity curves for the ethylene and low exposure propylene layers.

(3) HREELS studies indicate that adsorbed acetylene bonds to the Rh, Pt, and Pd(111) in the same way. The molecule is thought to di- σ , π -bond to three top layer metal atoms with the carbon-carbon bond parallel to the surface and its center near as hollow site. Methylacetylene on Pt(111) gave very similar LEED intensity curves to the acetylene overlayer investigated with HREELS (Chapter VI); this implies that methylacetylene also di- σ , π bonds to the metal but the extra carbon atom is randomly oriented.

Although we couldn't collect intensity spectra for the acetylene layer on Rh(111), we believe they would again be similar to the low exposure methylacetylene curves. The high exposure methylacetylene layer produces a $(2\sqrt{3}\times 2\sqrt{3})R30^\circ$ superlattice in addition to the (2×2) adsorption lattice seen at lower exposures. We plan to do a LEED analysis of this high exposure methylacetylene structure.

References for Chapter VIII

1. L. H. Dubois, D. G. Castner and G. A. Somorjai, J. Chem. Phys. 72 5234 (1980).
2. M. Salmeron and G. A. Somorjai, J. Phys. Chem., 86 341 (1982).
3. L. H. Dubois, private communication.
4. A. Gavezzotti, M. Simonetta, M. A. Van Hove, and G. A. Somorjai, submitted to Surf. Sci.
5. F. Frenkel, J. Hager, W. Krieger, H. Walther, C. T. Campbell, G. Ertl, H. Kuipers and J. Segner, Phys. Rev. Lett. 46 152 (1981).
6. T. E. Fischer, S. R. Kelemen, and H. P. Bonzel, Surf. Sci. 64 157 (1977).
7. H. Ibach and S. Lehwald, J. Vac. Sci. Tech. 15 407 (1978).
8. J. A. Gates and L. L. Kesmodel, to be published.
9. L. L. Kesmodel, R. C. Baetzold and G. A. Somorjai, Surf. Sci. 66 299 (1977).
10. A. M. Baro and H. Ibach, "Proc. Conf. on Vibrations in Adsorbed Layers," Julich, Germany (1978).

Figure Captions for Chapter VIII

- Fig. 1. LEED patterns obtained at 84 eV and normal incidence are shown for the C_2H_4 , C_3H_4 , and C_3H_6 derived overlayers.
- Fig. 2. The $c(4 \times 2)$ ethylene overlayer can disorder after a 10 L CO exposure. This post-exposure of CO changes the $c(4 \times 2)$ LEED pattern shown in Fig. 1 into the pattern illustrated here. The elongation in the LEED spots represents a disordering along the longer edge in the $c(4 \times 2)$ rectangular unit cell.
- Figs. 3-5. Intensity spectra for the $c(4 \times 2)$ lattice of ethylene, propylene, acetylene plus hydrogen, and methylacetylene plus hydrogen overlayers are plotted. The curves from the different hydrocarbon layers are identical within our experimental uncertainty.
- Figs. 6-8. Intensity curves are shown for the ethylene, the low exposure (1-2 L) propylene, and the high exposure (~1000 L) propylene layers. The (2×2) -ethylidyne lattice has intensity curves that are very similar to the low exposure propylene spectra.
- Fig. 9. Reliability factor contour plots indicate the degree of agreement between theoretical and experimental intensity curves. The calculated curves that were used in this R-factor analysis did not consider any multiple scattering in the overlayer.

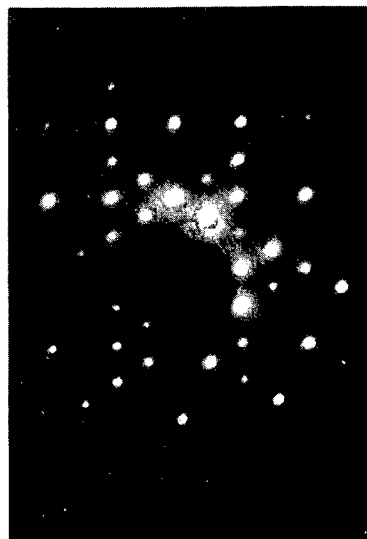
- Fig. 10. An atop view of the propylene structure that is suggested by our preliminary LEED analysis is illustrated. The large circles are top layer Rh atoms and the slashed circles represent hydrogen atoms. The unit cell drawn indicates the $(2\sqrt{3}\times 2\sqrt{3})R30^\circ$ superlattice that the γ -carbon atoms occupy.
- Fig. 11. High Resolution Electron Energy Loss Spectra are given for ethylene adsorbed on the Pd(111),⁸ Rh(111),¹ and Pt(111)⁷ surfaces. The similarity in the vibrational spectra suggest that ethylidyne exists in each of the overlayers.
- Fig. 12. Real space models for the $c(4\times 2)$ (top) and (2×2) (bottom) ethylidyne structures are illustrated.
- Fig. 13. A real space model for the $c(4\times 2)$ propylene or methylacetylene plus hydrogen overlayer is drawn.
- Fig. 14. A glancing view of three propylidyne groups adsorbed on Rh(111) in a (2×2) lattice. The γ -carbon atoms are rotated to their measured position as determined by our LEED analysis; and the nearest neighboring hydrogen atoms are blown up to their Van der Waals radii.
- Fig. 15. Another atop view of the $(2\sqrt{3}\times 2\sqrt{3})R30^\circ$ lattice of propylidyne is shown. The crowding of this overlayer can be appreciated when all the hydrogen atoms in the propylidyne group are blown up to their Van der Waals radii.

Fig. 16. A possible structure for the $(2\sqrt{3}\times 2\sqrt{3})R30^\circ$ methylacetylene overlayer is drawn. The methyl carbon atom could be disordered by a tumbling about the unsaturated carbon-carbon bond or by attaching it randomly to either of the two unsaturated carbon atoms.

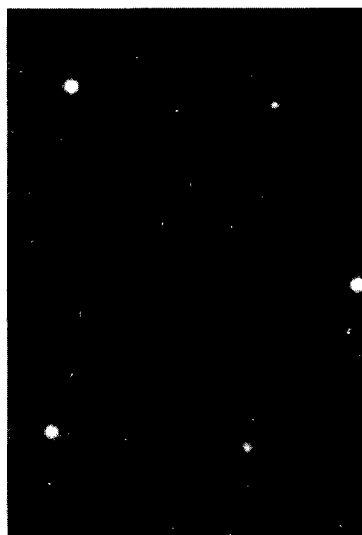
-285-
Leed patterns
84 eV; $\theta = 0^\circ$



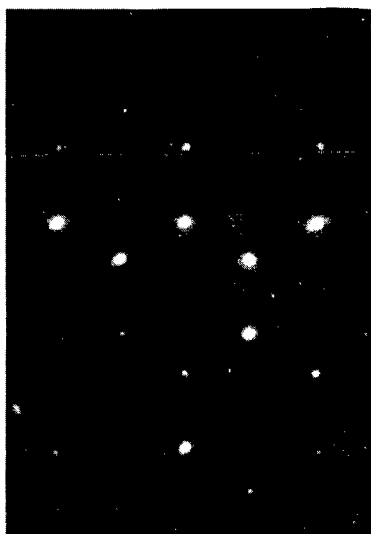
Rh (111) - (2 x 2) - C₂H₄



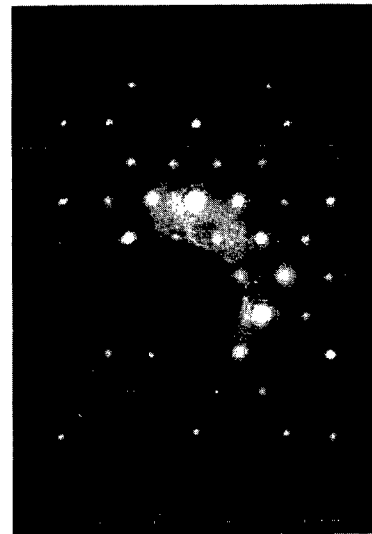
Rh (111) - c (4 x 2) - C₂H₄



Clean Rh (111)



Rh (111) - (2 x 2) + diffuse



Rh (111) - (2/3 x 2/3)

XBB 818-7425

Fig. 1

Rh(III)-c(4x2) - C₂H_n + 10 L CO

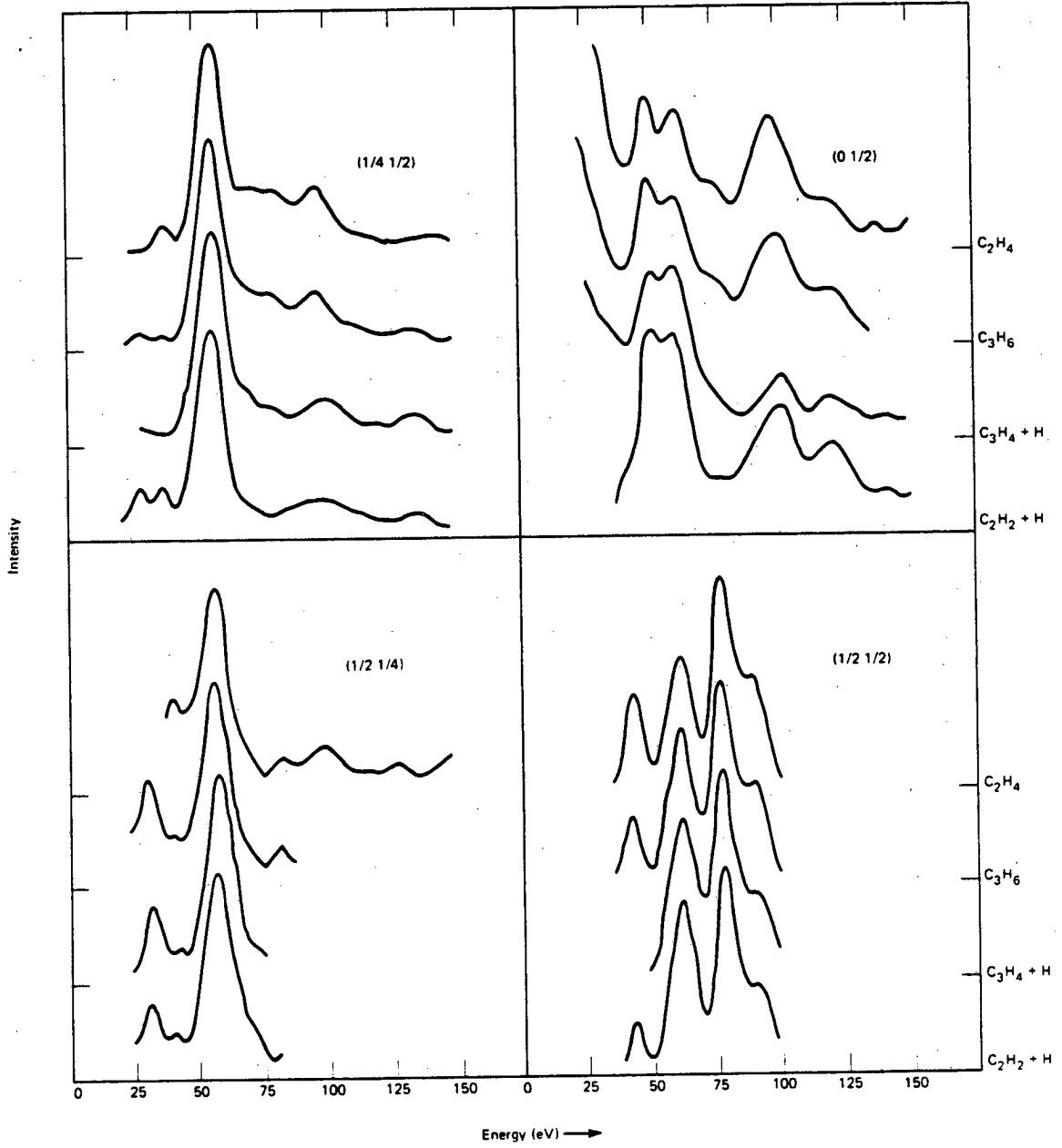
T = 300K, E ~ 80 eV



Fig. 2

XBB 828-6780

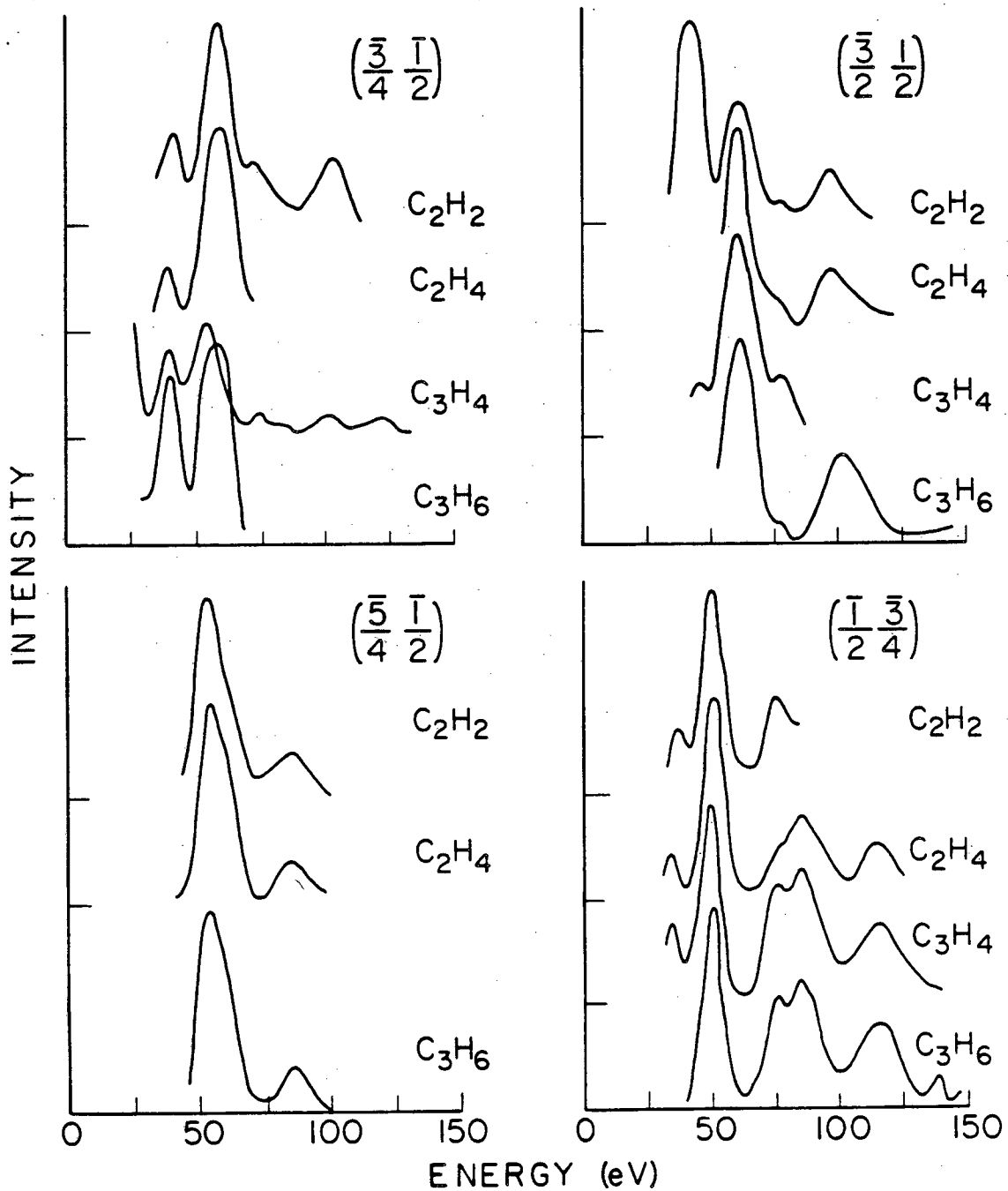
S Table Structure
Rh (111) - C (4 × 2)
T = 300 K; $\theta = 0^\circ$



XBL 818-1090

Fig. 3

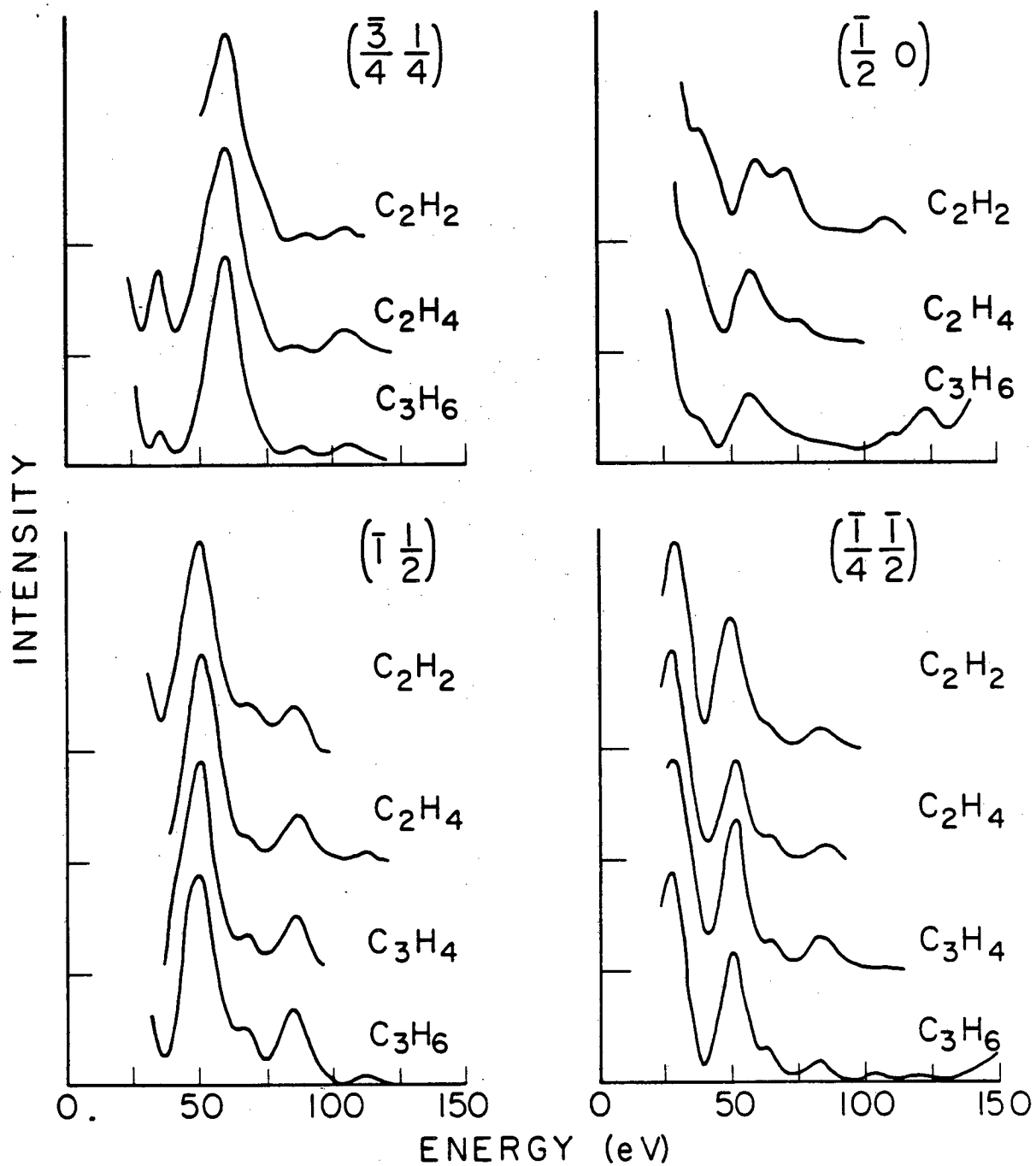
Rh(III) - c(4x2)
T=300 K, $\theta=31^\circ$, $\phi=0^\circ$
Stable Structure



XBL 818-6220

Fig. 4

Rh(III) - c(4x2)
T = 300 K, $\theta = 31^\circ$, $\phi = 0^\circ$
Stable Structure



XBL 818-6221

Fig. 5

$\theta = 0^\circ$ T = 240 K

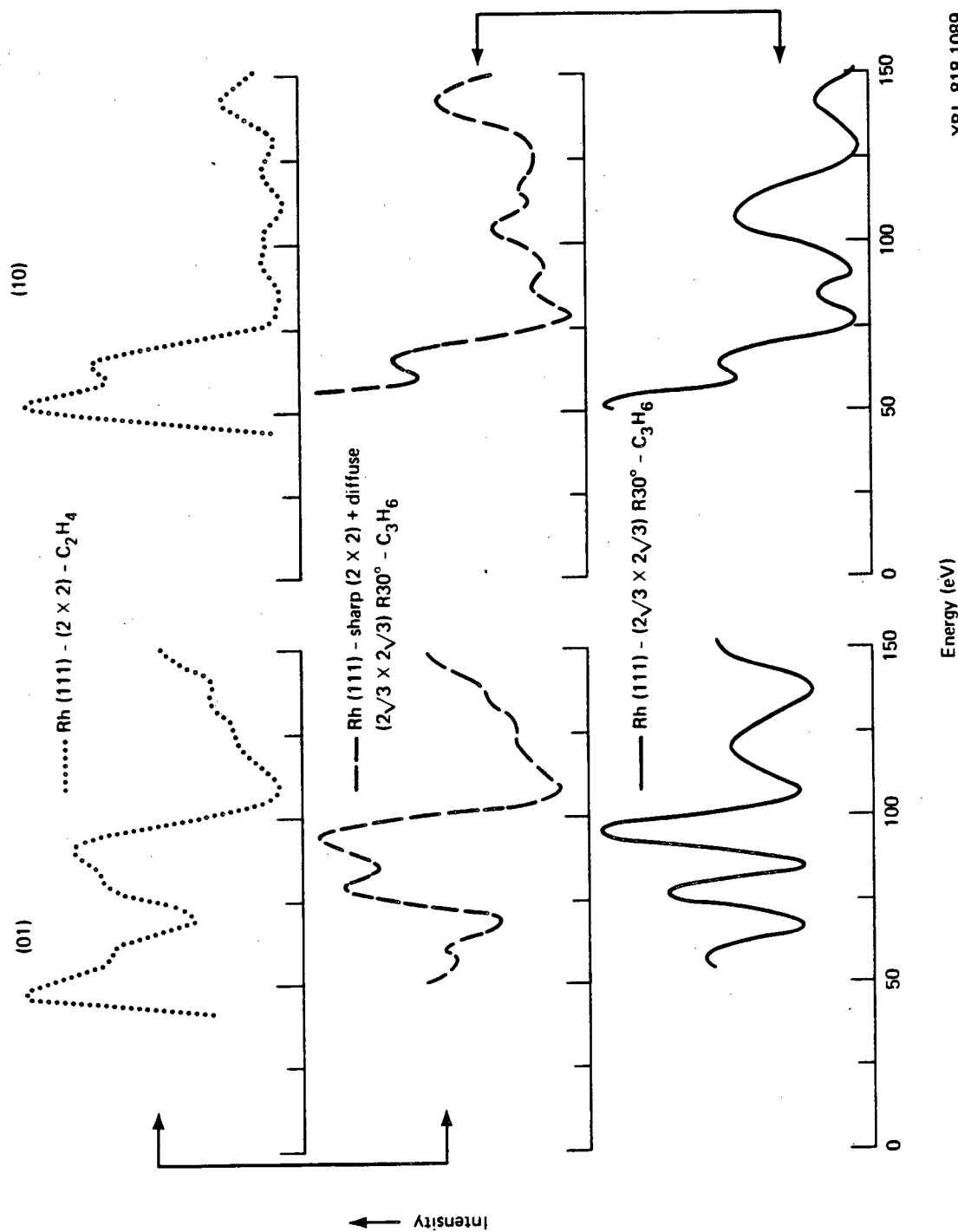
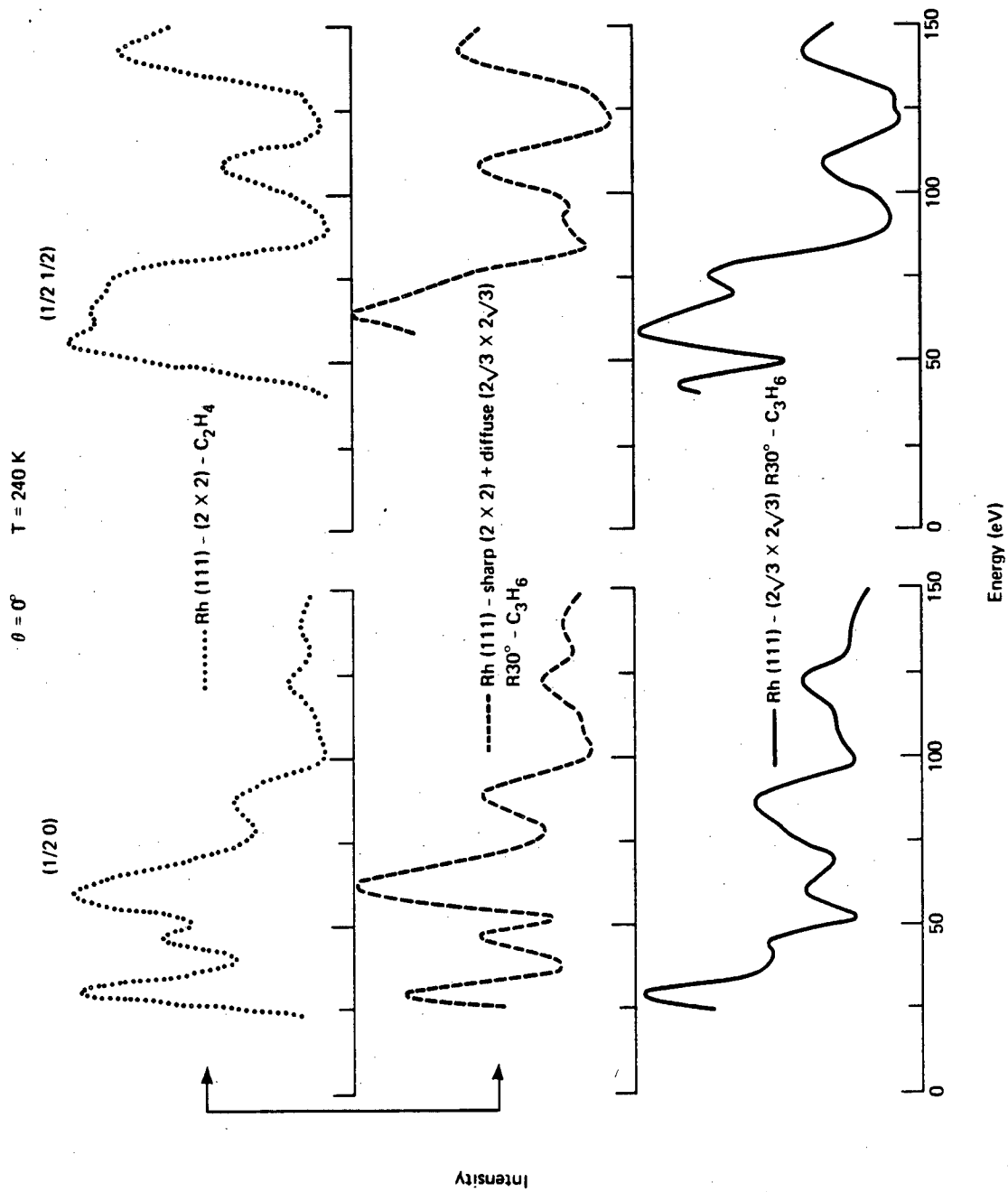
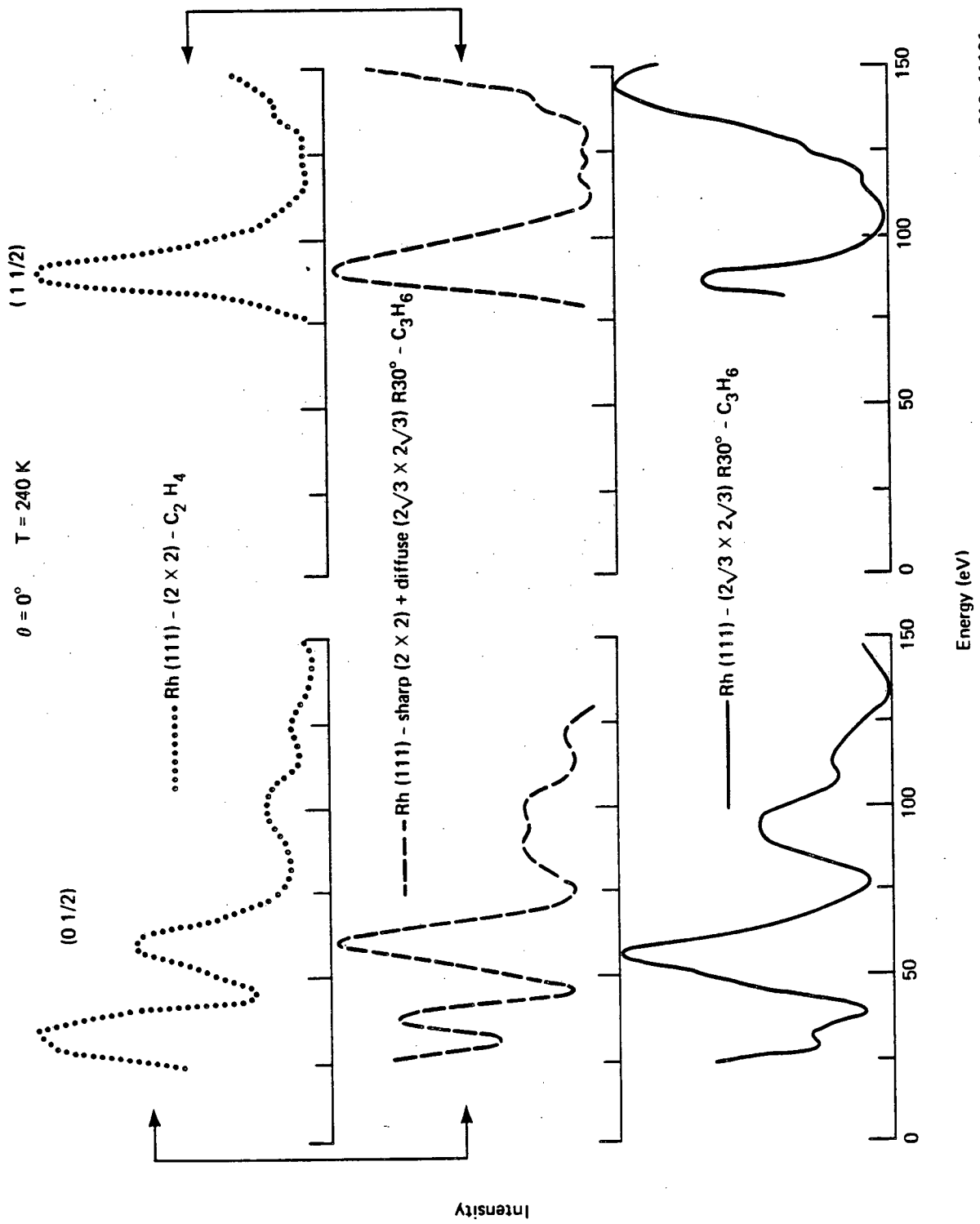


Fig. 6



XBL 818-1091

Fig. 7

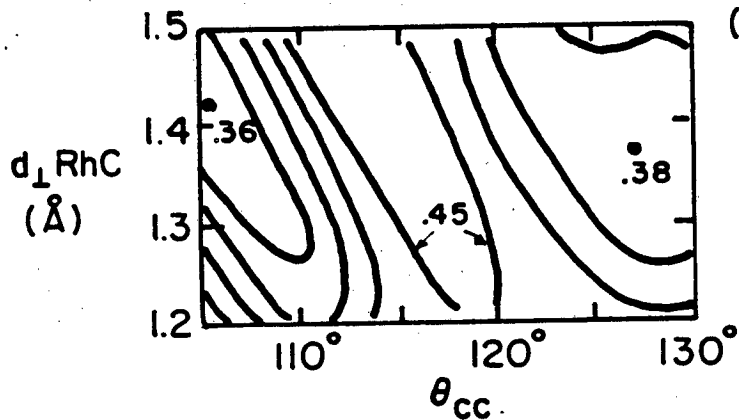


XBL 818-11191

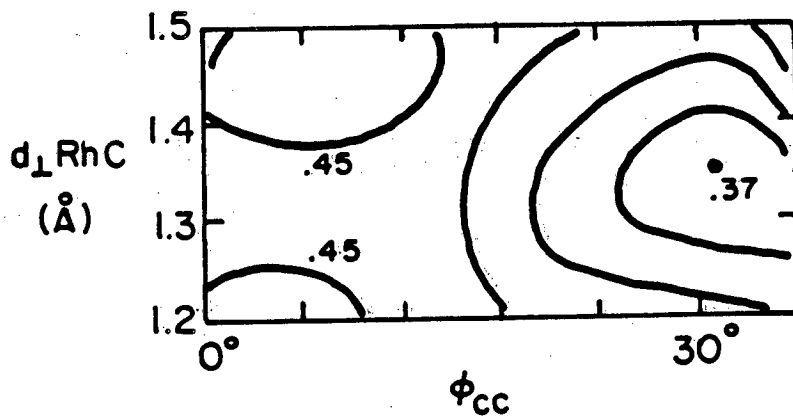
Fig. 8

Rh(III) + $(2\sqrt{3} \times 2\sqrt{3}) R 30^\circ$ $(C_3H_n)_3$ propylidyne
 $\theta = 0^\circ$, $T = 240\text{K}$

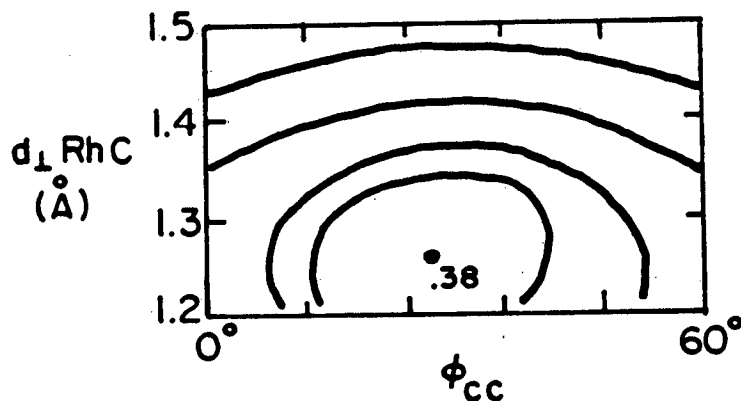
R-factor contours
(average over 5 R-factors)



$d_{cc} = 1.50 \text{ \AA}$
 $\phi_{cc} = 35^\circ$



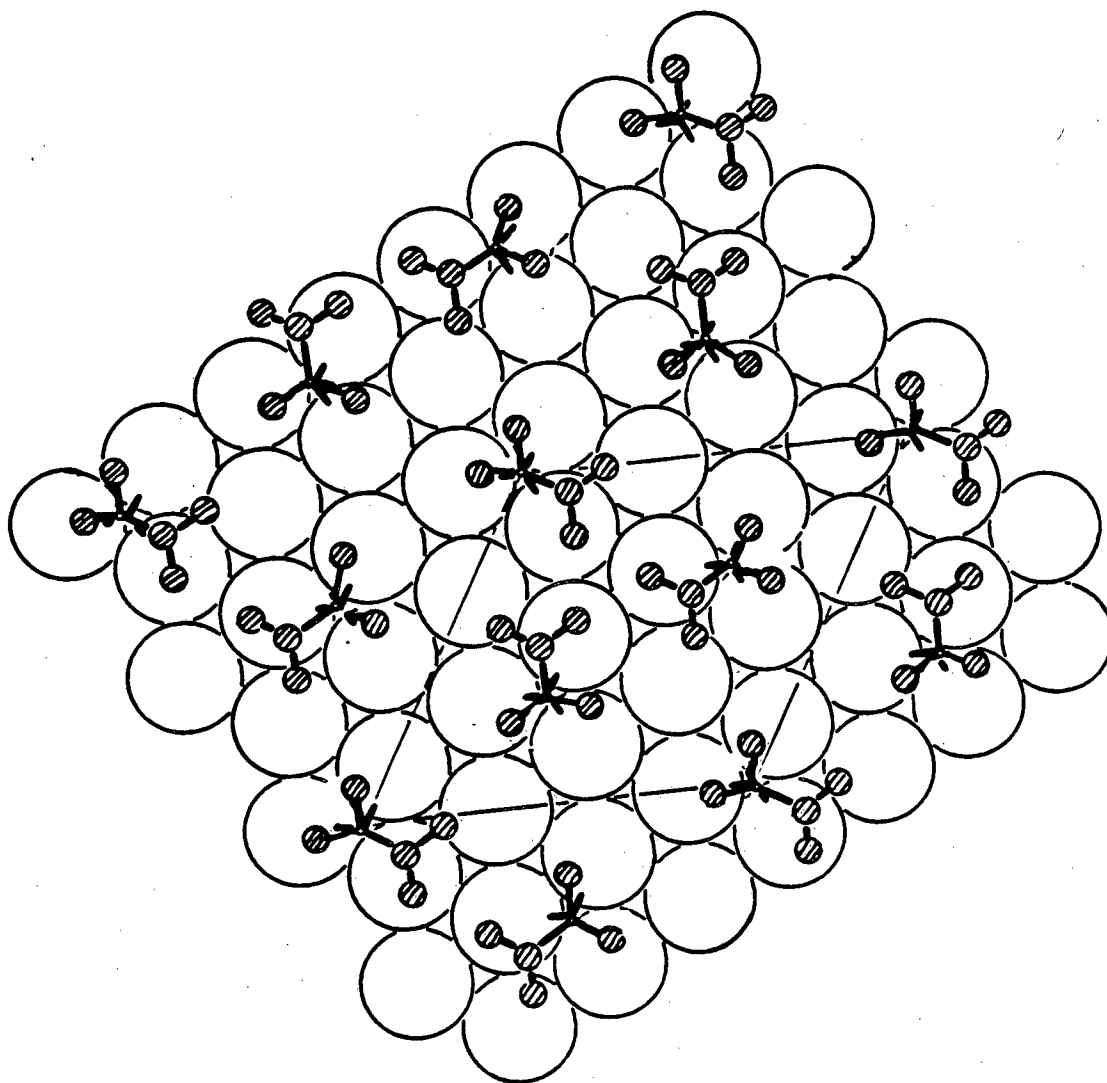
$d_{cc} = 1.50 \text{ \AA}$
 $\theta_{cc} = 109.5^\circ$



$d_{cc} = 1.33 \text{ \AA}$
 $\theta_{cc} = 122^\circ$

XBL 827-6249

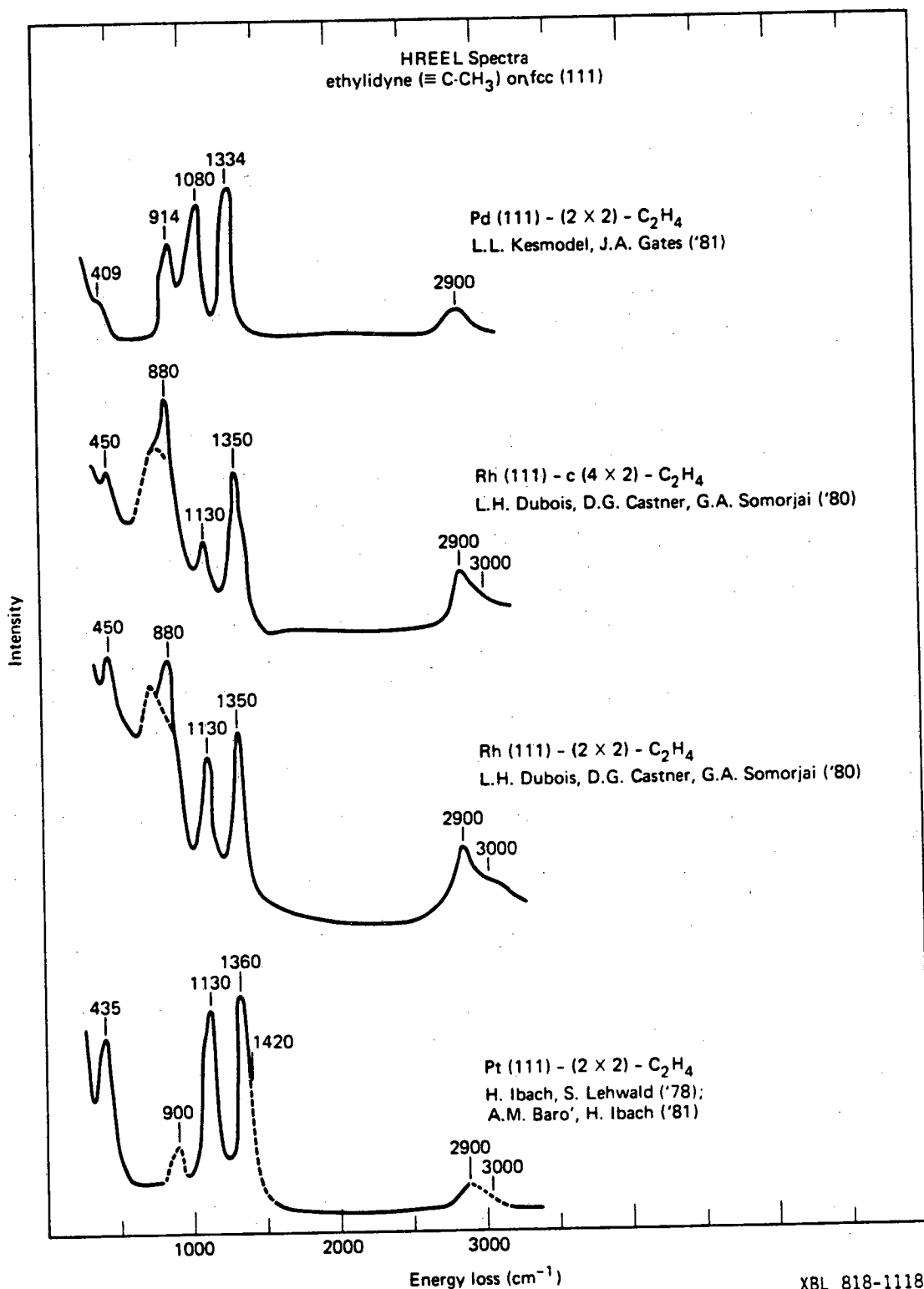
Fig. 9



$\text{Rh(III)} + (2\sqrt{3} \times 2\sqrt{3})\text{R}30^\circ$ (propylidyne)

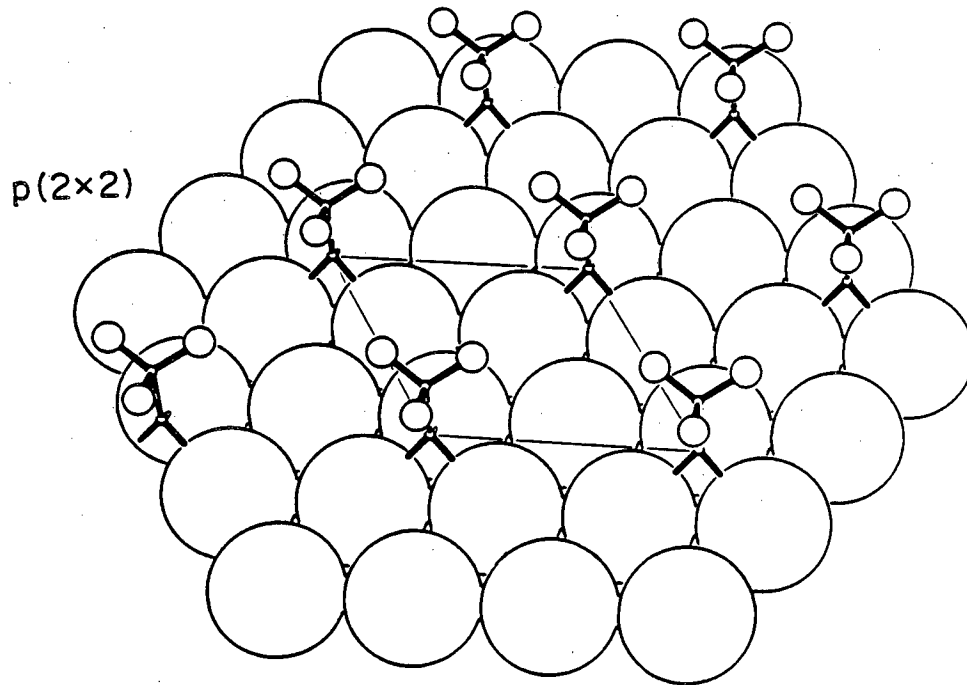
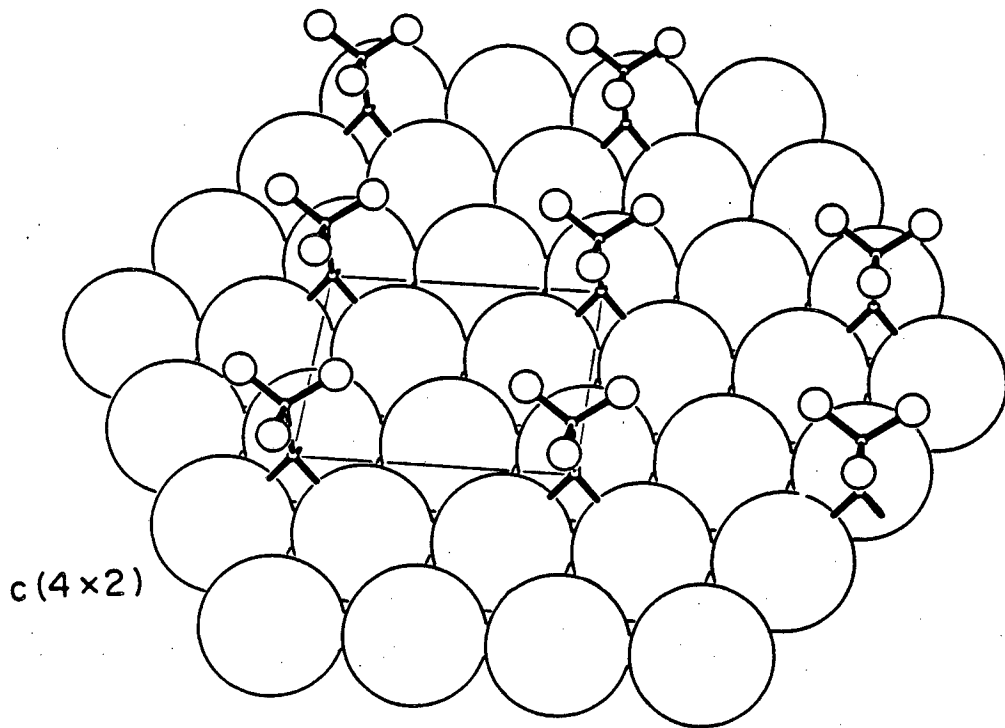
XBL 821-5101

Fig. 10



XBL 818-11189

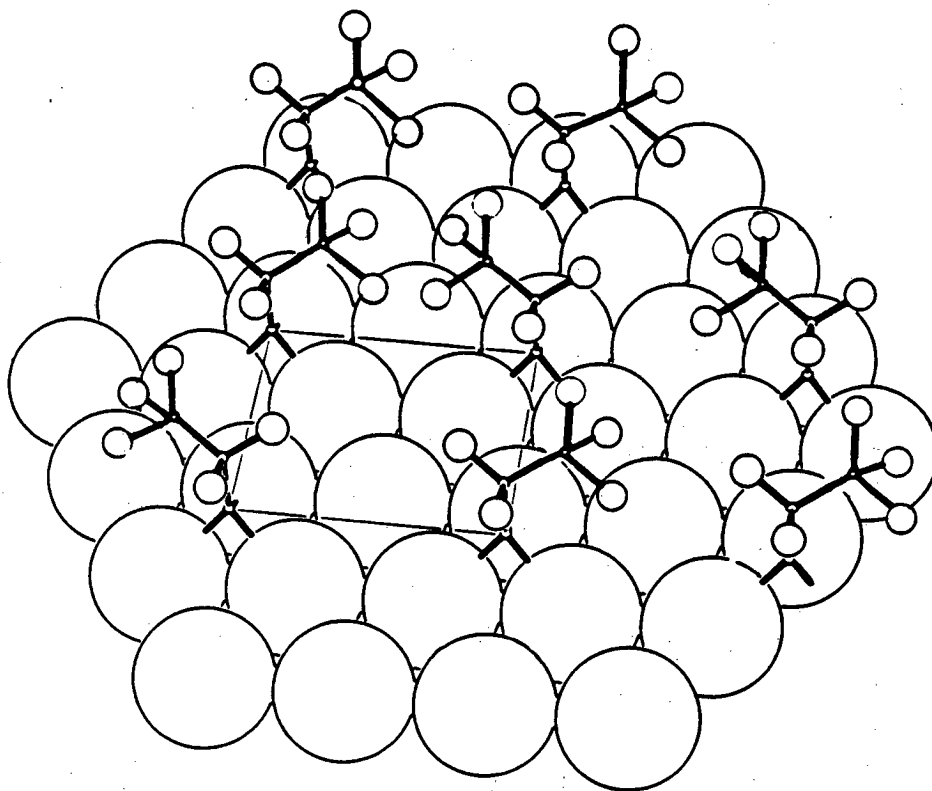
Fig. 11



fcc (111) + C_2H_3 (ethynidyne)

XBL813-5407

Fig. 12

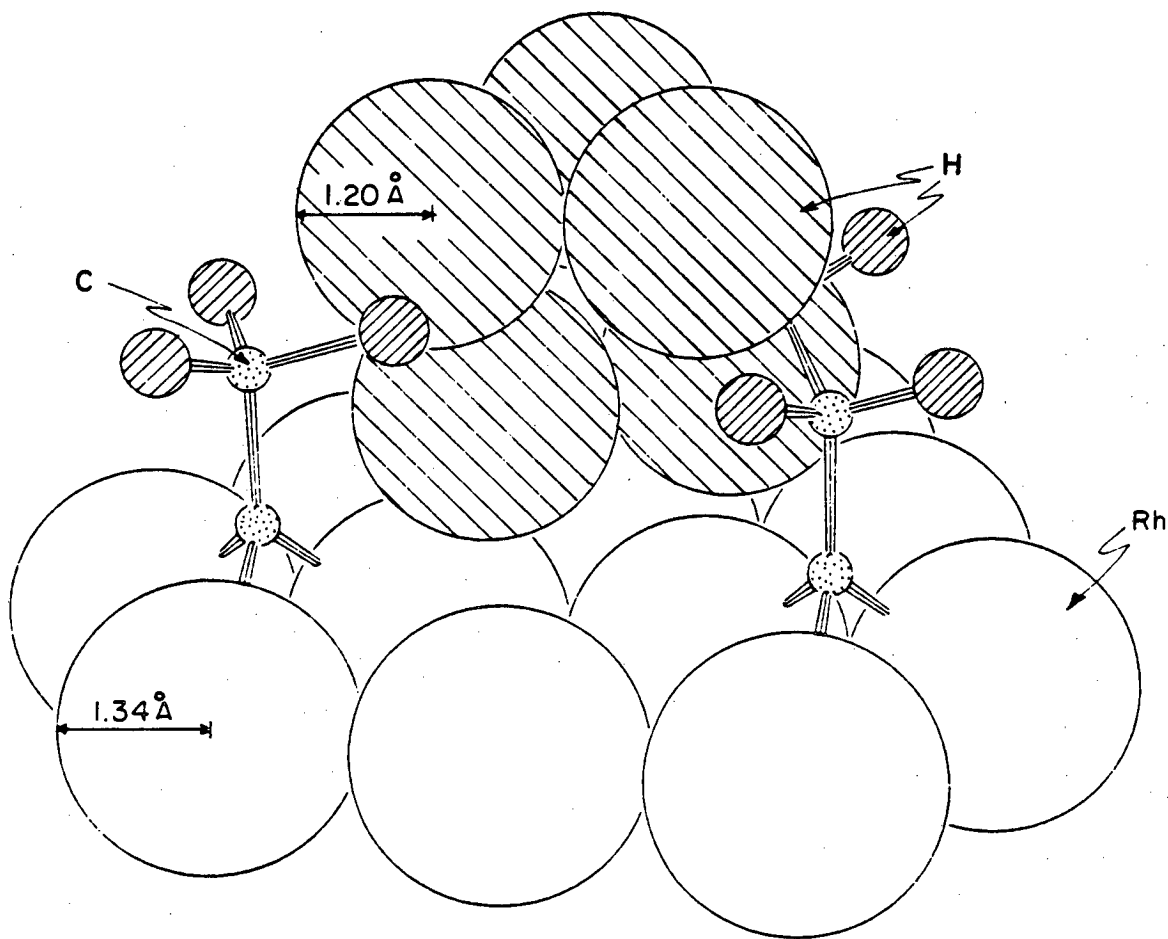


Rh(III) + c(4x2) (propylidyne) - disordered methyl groups

XBL 821-5100

Fig. 13

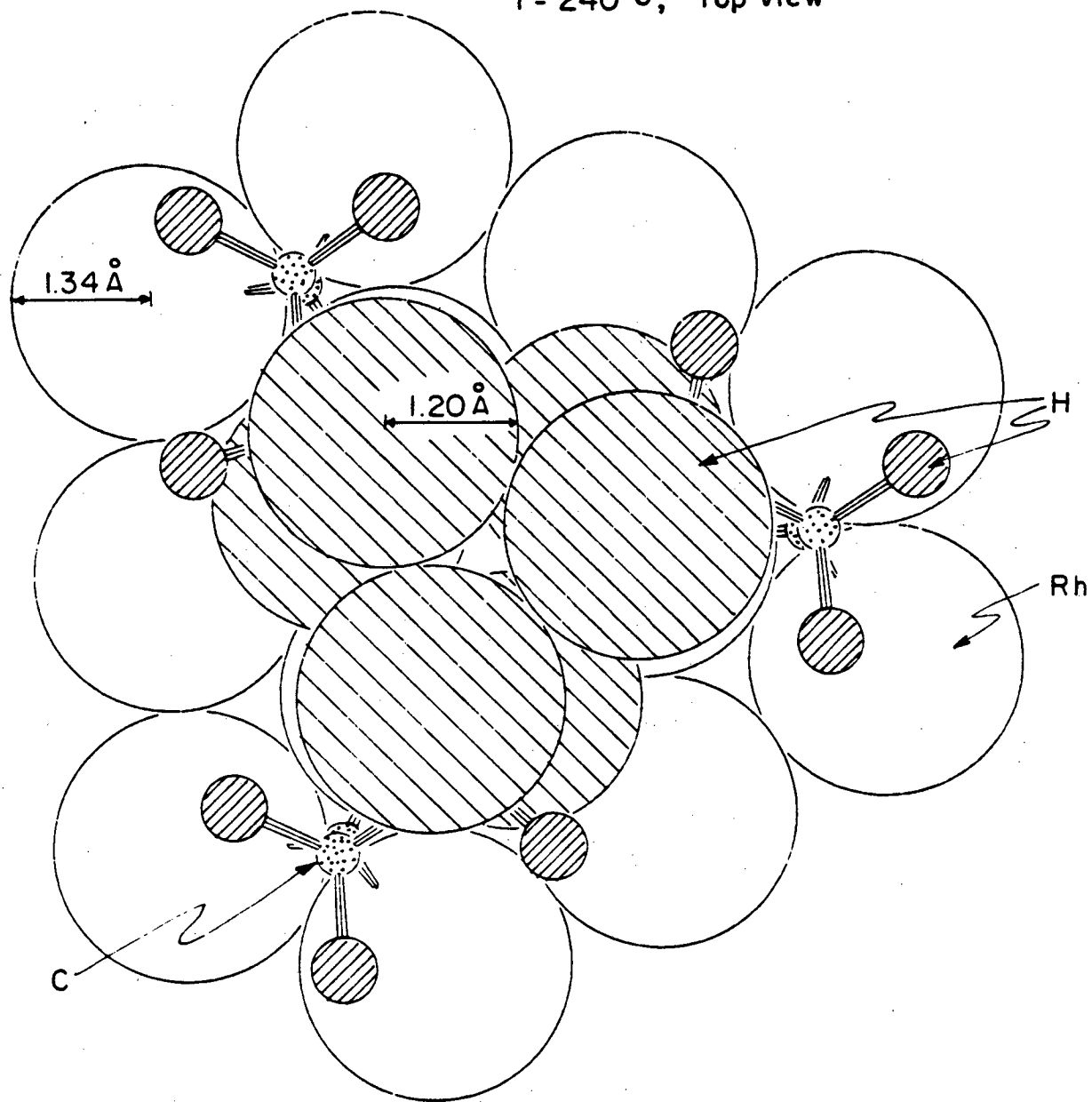
Rh(III) - $(2\sqrt{3} \times 2\sqrt{3}) R 30^\circ$ - C_3H_5
T = 240 K, Side View



XBL 827-6247

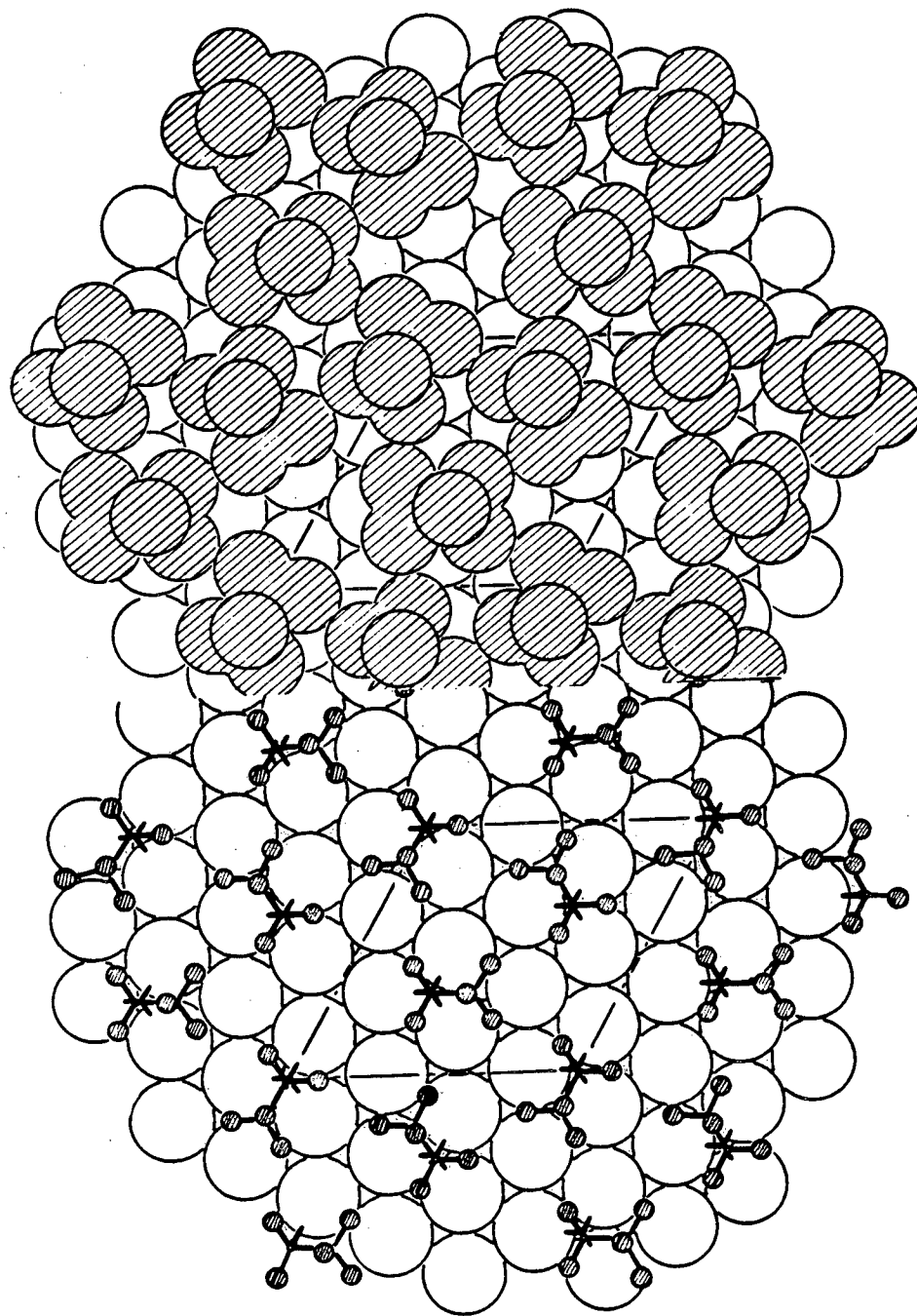
Fig. 14a

Rh(III) - $(2\sqrt{3} \times 2\sqrt{3}) R30^\circ - C_3H_5$
T = 240°C, Top View



XBL 827-6248

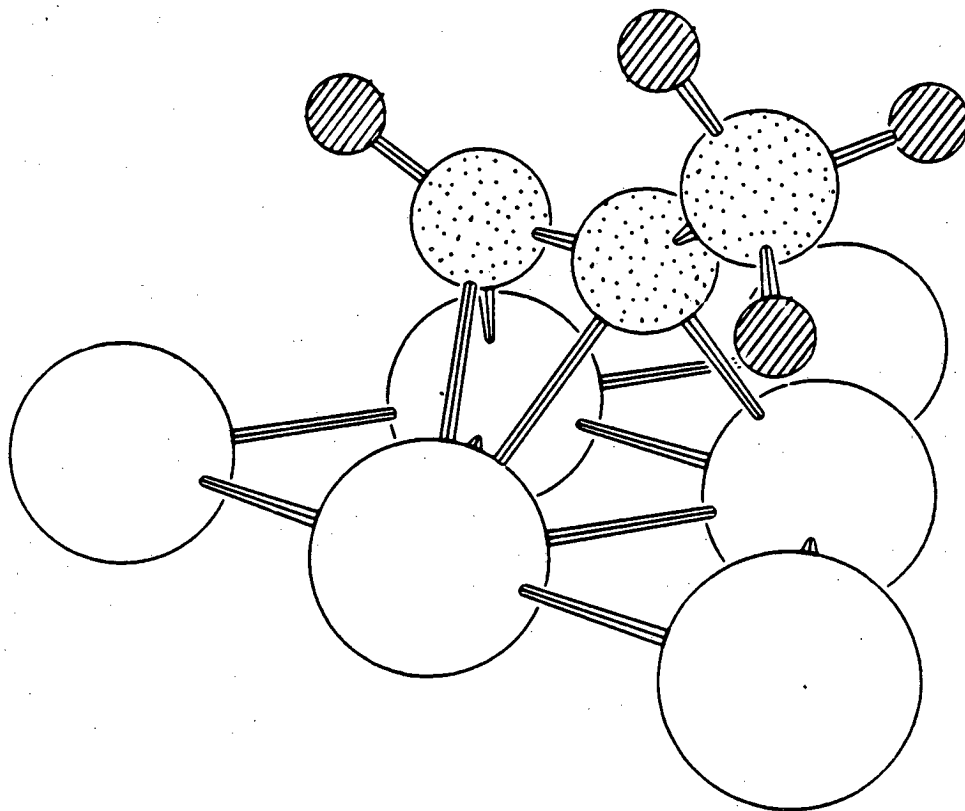
Fig. 14b



fcc (111) + $(2\sqrt{3} \times 2\sqrt{3}) R 30^\circ$ C_3H_5 (propylidyne)

XBL 813-5410

Fig. 15



Metastable methylacetylene

XBL 817-6067

Fig. 16

IX. ETHYLENE ADSORPTION ON Rh(100)

A. INTRODUCTION

In this chapter we present our preliminary results on the structure and bonding of ethylene adsorbed on the Rh(100) surface. The emphasis here will be to suggest possible structural models for this system that could help guide our ongoing research; to this end, we will also discuss other work relevant to ethylene adsorption on Rh(100).

When completed, our study should provide an interesting comparison with alkene or alkyne bonding to the Rh(111) face that was presented in Chapters VI through VIII. Such comparisons could begin to shed some light on the ancient issue of structure sensitivity in hydrocarbon catalysis.

Before discussing our experimental results, a brief summary of relevant organometallic clusters will be presented; these clusters bear some similarity to the (111) and (100) surfaces of Rh and will suggest plausible hydrocarbon structures than can form on these surfaces. Our preliminary Thermal Desorption Spectroscopy (TDS) and LEED experiments will then be introduced; the results so far indicate that ethylene probably rearranges to acetylene on the Rh(100) face near room temperature. These conclusions are based in large part on similar studies of ethylene adsorption on the reconstructed and unreconstructed Pt(100) surfaces.^{1-3,11}

Unfortunately we presently believe that a mixture of species (ethylene, ethylidyne, and acetylene) is usually present on the (100) surface simultaneously. Only at higher temperatures will an overlayer

of just acetylene form. This acetylene layer does not order well under our experimental conditions ($> 200\text{K}$) and may need to be cooled to still lower temperatures. A possible explanation for this effect is that acetylene may occupy a number of different adsorption sites above 200K . At much lower temperatures, this acetylene species could move to the lowest energy sites which would produce sufficiently long range order for a good LEED pattern to be obtained. Such a case has been reported already for the adsorption of CO on the $\text{Pt}(111)$ surface near 300K .⁴

Although a LEED intensity analysis probably can not be done on the acetylene overlayer until lower temperatures are available, we have collected intensity information for the $\text{Rh}(100)\text{-c}(2\times 2)\text{-C}$ layer that forms after the ethylene-derived layer is heated to 700K ; the carbon in this layer should have either a quarter or a half monolayer coverage. The LEED analysis of the $\text{c}(2\times 2)\text{-C}$ structure that is planned should provide the relevant bond lengths and angles for the adsorbed carbon atoms.

B. ORGANOMETALLIC ANALOGUES

Alkylidyne ($\equiv\text{C}(\text{CH}_2)_n\text{CH}_3$) overlayers seem to form on the $\text{Rh}(111)$ surface at $<240\text{-}420\text{K}$ after ethylene or propylene adsorption. The alkynes (acetylene and methylacetylene) may also produce an alkylidyne structure in the presence of hydrogen when the Rh sample is heated above 270K . A similar sequence was observed after ethylene, propylene or 2-butene adsorption on the $\text{Pt}(111)$ surface near room temperature, while the alkynes would again give an alkylidyne overlayer in the presence of hydrogen. Finally, recent HREELS experiments⁵

indicate ethylidyne formation also occurs on a Pd(111) surface after exposure to ethylene. Since these structures occur on the (111) surfaces of three different noble metals and for a number of different adsorbing molecules, the alkylidyne complex is thought to be very stable. Ethylidyne then could possibly exist on the (100) faces of these same metals even though the square lattice cannot accommodate the trivalent ethylidyne group as easily.

Organometallic clusters also demonstrate the stability of alkylidyne complexes. The trinuclear nonacarbonyl alkylidyne clusters (such as $\text{Co}_3(\text{CO})_9\text{CCH}_3$) are quite resistant to thermal decomposition or oxidation and can be easily synthesized by a variety of synthetic pathways.⁶ The relevance of these organometallic complexes is borne out by the very similar chemical transitions that are found for the clusters and that are thought to occur on the Rh, Pt, and Pd(111) surfaces. A HREELS study⁷ found that acetylene rearranges to vinylidene ($=\text{C}=\text{CH}_2$) on the Pt(111) face at 340 K. In the presence of hydrogen, this species reacts quickly to give ethylidyne. A corresponding series of acetylene complexes are observed for triosmium clusters. Acetylene reacts with $\text{H}_2\text{Os}_3(\text{CO})_9$ (I) to give $\text{HOs}_3(\text{CHCH}_2)(\text{CO})_{10}$ (II) that upon mild heating yields $\text{H}_2\text{Os}_3(\text{C}=\text{CH}_2)(\text{CO})_9$ (III).⁸ Cluster (III) is equivalent to the surface vinylidene structure identified by HREELS. After bubbling H_2 through a refluxing n-heptane solution of (III) for 24 hours, the ethylidyne complex, $\text{H}_3\text{Os}_3(\text{CCH}_3)(\text{CO})_9$ (IV),⁹

can be isolated. So both surface transitions of acetylene to vinylidene upon mild heating and of vinylidene to ethylidyne in the presence of hydrogen have parallels in Organometallic Chemistry.

With the apparent analogy between Surface and Organometallic Chemistry, can we anticipate what hydrocarbon structures will form on the Rh(100) surface from relevant cluster models? Some information can be gained from dimetal complexes recently prepared and characterized.¹⁰ Here an acetylene dimetalocycle $[\text{Ru}_2(\text{CO})(\mu\text{-CO})(\mu\text{-C}(\text{O})\text{C}_2\text{H}_2)(\text{n-C}_5\text{H}_5)_2]$ (I) forms a bridge-bonded vinylidene species $[\text{Ru}_2(\text{CO})_2(\mu\text{-CO})(\mu\text{-CCH}_2)(\text{n-C}_5\text{H}_5)_2]$ (II) upon mild heating; the vinylidene group (II) can be protonated to give an ethylidyne carbonium ion $[\text{Ru}_2(\text{CO})_2(\mu\text{-CO})(\mu\text{-CCH}_3)(\text{n-C}_5\text{H}_5)_2] [\text{BF}_4]$ (III) which easily reacts with hydride (HBF_4) to produce a bridge-bonded ethylidene ($=\text{CH-CH}_3$) cluster $[\text{Ru}_2(\text{CO})_2(\mu\text{-CO})(\mu\text{-CHCH}_3)(\text{n-C}_5\text{H}_5)_2]$ (IV). The charge on the carbonium ion (III) is delocalized onto the bridging Ru metal atoms to stabilize the cluster.

Since a dimetal ethylidene complex (IV) has been isolated in cluster chemistry, it seems very reasonable that it may also exist on the Rh(100) surface. This surface has atop and bridge sites as in the dimetal cluster in addition to fourfold hollow sites, but it does not have any three-fold hollow sites where the trivalent ethylidyne species is probably most stable. The vinylidene group (II) should be very reactive as on the (111) surface and should react with any coadsorbed hydrogen to produce either an ethylidene (IV) or ethylidyne (III) species. It is surprising that the ethylidyne carbonium ion (III) can

even be isolated as an intermediate in the synthesis of the ethylidene complex (IV). The ethylidyne species would be further stabilized on the (100) surface by bonding to a third metal atom. This bonding would probably place the α -carbon at some low symmetry position between the bridge and hollow sites.

If the analogy between Surface and Organometallic Chemistry is accepted, ethylene could reasonably form acetylene, vinylidene, ethylidyne, and ethylidene on the Rh(100) surface. The preference probably leaning towards the acetylene and ethylidyne species.

C. RESULTS AND DISCUSSION

i) Ethylene Adsorption on Rh(100) at 220 K

After adsorbing ethylene on the Rh(100) surface at 220 K, a fuzzy $c(2 \times 2)$ LEED pattern is obtained; this structure forms at probably a half-monolayer coverage of ethylene.¹ Since an earlier AES study showed slow adsorption kinetics for ethylene on Pt(100),¹ we used a wide range of gas exposures (1-500 L) that did not significantly change the quality of the LEED pattern. The pattern did improve slightly when we adsorbed ethylene at 200 rather than 220-250 K; but unfortunately it was still not adequate for intensity measurements.

Our TDS and LEED experiments for ethylene on Rh(100) have a strong similarity to those for ethylene on Pt(100). Figure 1 shows our thermal desorption spectrum for ethylene on Rh(100); while the inset illustrates the TDS spectra obtained from ethylene adsorbed on Pt(100).¹ Before discussing the TDS spectra any further, it may be helpful to consider in more detail ethylene adsorption on the reconstructed and unreconstructed Pt(100) surfaces.

An Ultraviolet Photoemission Spectroscopy (UPS) study¹ indicates that ethylene will form a mixture of species on the Pt(100) face depending on the temperature, coverage, and metal geometry. At 200 K, a mixture of ethylene, acetylene, and vinyl species ($=C=CH_2$) is thought to exist on the unreconstructed Pt(100) face; at low coverages ($\theta \leq 0.2$) only acetylene is observed while ethylene and a vinyl species appear at higher coverages ($\theta \geq .4$). Heating this hydrocarbon layer to 330 K produces only acetylene in a poorly ordered $c(2 \times 2)$ structure.

The reconstructed Pt(100) surface probably has an hexagonal array of top layer metal atoms rather than the expected square array seen for most fcc(100) faces (see Chapter IV). According to the UPS study, ethylene adsorbed on this surface at less than a half monolayer coverage resulted in a disordered ethylene phase at 200 K, a poorly ordered $c(2 \times 2)$ vinyl species at 330 K, and a poorly ordered acetylene layer (again $c(2 \times 2)$) at 473 K. Above a one half monolayer coverage, ethylene would adsorb as acetylene over the entire temperature range.

More recent High Resolution Electron Energy Loss Spectroscopy (HREELS) measurements^{11,12} indicate that ethylene does not form a vinyl species but rather ethylidyne ($\equiv C-CH_3$) on the reconstructed Pt(100) surface. Baro and Ibach¹ conclude that ethylene forms ethylidyne on the (5×20) Pt(100) surface at room temperature since the measured HREELS spectrum is identical to that found for the ethylidyne overlayer that develops on the Pt(111) face at 300 K. A similar spectrum was obtained for the (2×2) ethylidyne layer that occurs on the Rh(111) surface between $<230-270$ K;¹³ the existence of an ethylidyne

layer on Rh and Pt(111) has been confirmed by LEED intensity analyses^{14,15} and by an Angle Resolved UPS study.¹⁶

The UPS spectra of ethylidyne on Pt(111)³ are in fact identical to those measured for ethylene on the reconstructed Pt(100) face at 330 K; this further supports the claim that ethylidyne may exist on Pt(100). Originally the UPS spectrum from ethylene adsorbed on Pt(111) was thought to correspond to a vinyl species;³ and for the same reasons, the spectrum obtained for what is probably ethylidyne on the Pt(100) surface was assigned to a vinyl group.

Returning to the TDS spectra in Fig. 1, the lower trace in the inset is obtained after ethylene adsorption at room temperature on the unreconstructed (1×1) face of Pt(100). The UPS and TDS spectra of this layer were identical to those measured after acetylene adsorption at the same temperature. The upper trace corresponds to ethylene adsorption on the reconstructed (5×20) face of Pt(100). Here UPS and HREELS indicate an ethylidyne species may exist. The extra desorption peak at 430 K in the upper curve is assigned to hydrogen abstraction from the ethylidyne species; an acetylene group then forms as indicated by UPS and by the remaining section of the TDS spectrum. The area under this 430 K desorption peak is one-third of the total¹ which further supports an ethylidyne species with stoichiometry of C₂H₃.

Our TDS curve in Fig. 1 has three peaks that may also be due to acetylene decomposition. The 320, 340, and 400 K peaks that are measured after ethylene adsorption on Rh(100) are quite similar in intensity and separation to those for ethylene or acetylene on the Pt(100) surface. The striking difference is a rigid shift of about

200 K in the temperature scale; this would make the Rh(100) surface much more reactive than Pt(100) in the dehydrogenation of ethylene to acetylene. Another shoulder at 260 K appears in our TDS spectrum; this peak probably corresponds to desorption of coadsorbed hydrogen that develops during ethylene dehydrogenation to acetylene and adsorption from the ambient gas.

Ethylidyne may form on Rh(100) at lower temperatures since a similar process seems to occur on the unreconstructed Pt(100) face. The UPS spectra indicate that the hydrocarbon layer on this Pt(100) surface is inhomogeneous and may contain acetylene, ethylidyne, and ethylene. This suggests that ethylene adsorbed on the Rh(100) below 220 K may also produce an overlayer comprised of a mixture of species; the layer would not be ordered and thereby not very suitable for a LEED intensity analysis.

However, acetylene probably forms on Rh(100) after an ethylene exposure at 220 K as seen from the TDS spectrum in Fig. 1. Since this layer seems to be homogeneous, we should be able to order it. Our $c(2 \times 2)$ LEED pattern of the acetylene layer improved as the Rh crystal was cooled to the lowest temperature presently available (~ 200 K). This may be due to a small amount of decomposition that already occurs when the temperature is raised to about 260 K. However, we recall that the acetylene overlayer on the Pt(100)-(1x1) surface did not order into a very good $c(2 \times 2)$ lattice at temperatures that were far below the onset of acetylene decomposition. We believe then this effect on both the Rh and Pt(100) faces is caused by the presence of two or more

possible sites with similar adsorption energies. At a given temperature, there may be a statistical mixture following the Boltzmann distribution. With this explanation, cooling the acetylene layer that forms at 200-260 K on Rh(100) to much lower temperatures may help the ordering. A similar effect has been observed for CO adsorption on the Pt(111) surface.⁴ Here bridge or linear bonded CO molecules were separated by only a one-half kcal/mole difference in adsorption energy; so even at 170 K a sufficient number of bridge sites are populated to disorder the $(\sqrt{3}\times\sqrt{3})R30^\circ$ structure that forms at a one-third monolayer coverage.

ii) Ethylene Dehydrogenation on Rh(100) at 700 K

Ethylene was adsorbed at low temperatures (~220 K) on the Rh(100) surface; we used a gas exposure of about 30 L to reach a near saturation coverage (probably one-half of a monolayer). As reported in the previous section, a fuzzy $c(2\times 2)$ LEED pattern appears after this treatment. The crystal was then heated to 700 K for a few minutes to produce a very sharp and intense $c(2\times 2)$ pattern. During the heating period, the hydrogen in the hydrocarbon layer is completely removed since our TDS spectra show that all the hydrogen desorption takes place at temperatures below 500 K.

LEED intensity vs. voltage profiles were collected for the Rh(100)- $c(2\times 2)$ -C structure at two angles of incidence ($\theta=0^\circ$ and $\theta=10^\circ$ at $\phi=45^\circ$) with an energy range of 24-150 eV. Each set of intensity data was reproduced by a second independent adsorption experiment; the clean surface intensity curves were also obtained and checked with already published spectra.¹⁷ The analysis of these curves that is

planned should determine the structure of the carbon overlayer. One likely structure that will be tested is a carbide layer with each carbon atom above a fourfold hollow site in a $c(2\times 2)$ lattice. A recent HREELS study¹⁸ is consistent with such a geometry.

The disordered $c(2\times 2)$ structure that formed on Rh(100) after ethylene adsorption at 220 K probably has a one monolayer carbon coverage, but the $c(2\times 2)$ -C lattice may only have a half-monolayer carbon coverage. We believe the excess carbon either desorbs as acetylene or ethylene, or is disordered on the Rh surfaces. We plan to use AES to check if the carbon coverage is reduced after forming the $c(2\times 2)$ -C lattice and also to use TDS to see if any acetylene or ethylene desorbs in the formation of the $c(2\times 2)$ -C lattice.

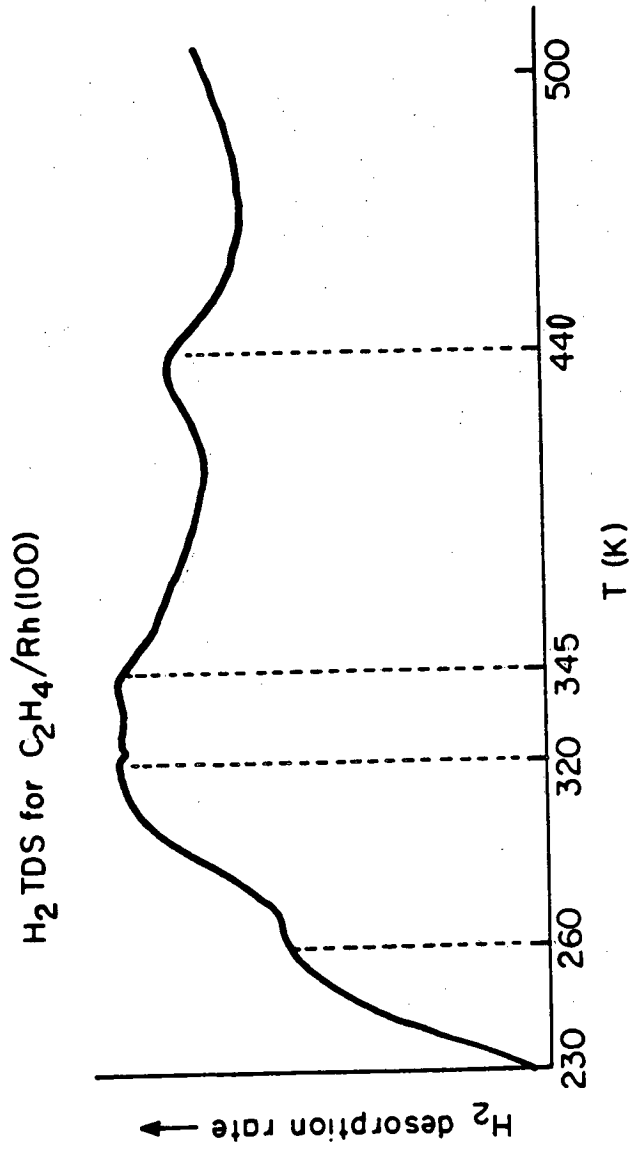
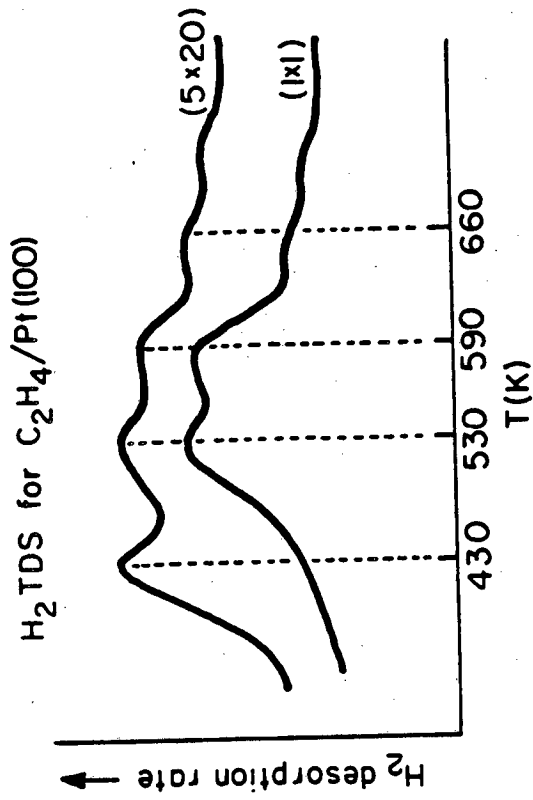
References for Chapter IX

1. T. E. Fischer and S. R. Kelemen, Surf. Sci. 69 485 (1977).
2. T. E. Fischer, S. R. Kelemen and H. P. Bonzel, Surf. Sci. 64 157 (1977).
3. J. E. Demuth, Surf. Sci. 80 367 (1979).
4. G. Ertl, M. Neumann and K. M. Streit, Surf. Sci. 64 393 (1977).
5. L. L. Kesmodel and J. A. Gates, Surf. Sci. 111 1981.
6. D. Seyferth, Adv. Organomet. Chem. 14 97 (1976).
7. H. Ibach and S. Lehwald, J. Vac. Sci. Tech. 15 407 (1978).
8. A. J. Deeming, S. Hasso and M. Underhill, J. C. S. Dalton, 1614 (1975).
9. A. J. Deeming and M. Underhill, J. C. S. Chem. Comm. 277 (1973).
10. D. L. Davies, A. F. Dyke, A. Endesfelder, S. A. R. Knox, P. J. Naish, A. G. Orpen, D. Plaas, and G. E. Taylor, J. Organomet. Chem. 198 C43 (1980).
11. A. M. Baro and H. Ibach, "Proc. Conf. on Vibrations in Adsorbed Layers," Julich, Germany (1978).
12. H. Ibach, to be published.
13. L. H. Dubois, D. G. Castner and G. A. Somorjai, J. Chem. Phys. 72 5234 (1980).
14. R. J. Koestner, M. A. Van Hove and G. A. Somorjai, accepted at Surf. Sci. (July, 1982).
15. L. L. Kesmodel, L. H. Dubois, and G. A. Somorjai, J. Chem. Phys. 70 2180 (1979).
16. M. R. Albert, L. G. Sneddon, E. W. Plummer and T. Gustaffsson, Surf. Sci. 120 (1982).

17. a) P. R. Watson, PhD thesis (University of British Columbia, Vancouver, Canada) 1978.
b) C. M. Chan, PhD thesis (California Institute of Technology, Pasadena, CA) 1979.
18. L. H. Dubois, to be published.

Figure Captions for Chapter IX

Fig. 1. An H_2 Thermal Desorption Spectrum for ethylene adsorbed on Rh(100) at 240 K is shown. The heating rate is about 10 K/sec. Similar H_2 TD spectra¹ from ethylene adsorbed on the (5×20) and (1×1) Pt(100) surfaces at 300 K are illustrated in the inset.



XBL827 - 6246

Fig. 1

X. BENZENE AND NAPHTHALENE ADSORPTION ON THE Rh(111) SURFACE

A. INTRODUCTION

To date, structural studies of benzene adlayers on noble metal surfaces have focused on the tilt of the carbon ring relative to the surface plane and on the adsorption site that is chosen. Angle-Resolved Photoemission (ARPES) measurements at normal emission indicate that benzene adsorbs parallel to the Pd(100)^{1,2} and Pt(100)³ surfaces. Further angle-resolved spectra⁴ taken at varying emission angles suggest that the benzene ring also adsorbs parallel to the Pd(111) and Ni(111) faces.

High Resolution Electron Energy Loss Spectroscopy (HREELS) experiments⁵ indicate that benzene associatively adsorbs parallel to the Ni or Pt(111) faces and further suggest that benzene occupies two different kinds of a C_{3v} symmetry sites on the surface. There are three C_{3v} sites available (atop, hcp hollow, and fcc hollow) on fcc(111) faces, but it is not clear which two are chosen. Interestingly the relative population of the two sites varied with coverage and temperature in the disordered benzene overlayers that were examined. However, HREELS studies for the ordered Ni(111)-(2 $\sqrt{3}$ ×2 $\sqrt{3}$)R30°⁶ and Rh(111)-c(2 $\sqrt{3}$ ×4)Rect⁷ benzene adlayers show that only one C_{3v} site is occupied.

The emphasis in this Chapter will be to suggest possible structural models for adsorbed benzene and naphthalene on Rh(111) that could help guide our ongoing research in this area. In addition to the

LEED, Auger Electron Spectroscopy (AES) and Thermal Desorption Spectroscopy (TDS) experiments that we have already done for benzene and naphthalene on Rh(111), I will draw upon other work done on aromatic adsorption on transition metals. (I should qualify my use of the first person plural throughout this chapter by crediting Dr. Lin Rongfu for most of the experimental work that will be described.)

Our investigation when completed should provide more detailed structural information (bond distances and angles) for aromatic adsorption on a noble metal surface than previously available by ARPES or HREELS. The Rh(111) face has two ordered layers for both benzene and naphthalene; and most of these lattices probably have only one admolecule in a relatively small primitive unit cell. This simplifies the dynamical LEED intensity calculations and gives us a good starting point in a systematic study of the structure and bonding of aromatic molecules to noble metal surfaces.

The nature of the phase transition that exists for both the benzene and naphthalene adlayers on Rh(111) will hopefully be elucidated when a structure determination for each phase has been completed. For benzene, a $\begin{pmatrix} 1 & 2 \\ 3 & -2 \end{pmatrix}$ or equivalently a $c(2\sqrt{3}\times 4)\text{Rect}$ lattice forms below 75°C ; one admolecule probably lies in the unit cell with an implied carbon coverage of $\theta_c = 3/4$. This overlayer transforms irreversibly between $90\text{--}125^\circ\text{C}$ to a (3×3) lattice with $\theta_c = 2/3$. Annealing the naphthalene overlayer at 75°C produces a mixed

phase containing both a $(3\sqrt{3}\times n\sqrt{3})R30^\circ$ [where n equals 1 or 3] and a (3×3) lattice with an expected carbon coverage of $\theta_c = 10/9$, while only the (3×3) lattice remains after the sample is heated to 125-150°C.

Similar transitions are also seen on the Pt(111) surface. Here an ordered benzene overlayer makes an irreversible transition at 50°C to a lower coverage lattice,⁸ while adsorbed azulene⁹ transforms from a mixed phase containing (3×3) and an incommensurate $(3\times 3)R30^\circ$ lattices to one containing only a (3×3) layer after heating to 180°C. This suggests that a strong parallel may exist for aromatic adsorption on the Pt(111) and Rh(111) surfaces as we already found for the alkenes and alkynes (Chapters VI-VIII).

Besides examining the phase transitions that occur with benzene and naphthalene adlayers on Rh(111), our dynamical LEED investigation will also consider the role that adsorbate-adsorbate interactions play in determining the structure of these crowded aromatic overlayers. As in our earlier investigations of the Rh(111)- (2×2) -3CO (Chapter V, Part 2) and the Rh(111)- $(2\sqrt{3}\times 2\sqrt{3})R30^\circ$ - $3C_3H_5$ (Chapter VIII) layers, direct intermolecular forces may be nearly as important as metal-adsorbate interactions in understanding the bonding of these aromatics to a metal surface.

B. EXPERIMENTAL

The cleaning of the Rh(111) sample and a description of the UHV chamber were already presented in earlier Chapters (III, V) so we will only discuss the preparation of the benzene and naphthalene gas samples here. Reagent grade benzene (Mallinckrodt) was stored in a glass

vessel that was connected to a glass and stainless steel manifold; the manifold was baked out at 80-100°C for a few hours with an ion pump before any benzene was introduced into the line. The benzene sample was degassed by three freeze-pump-thaw cycles prior to every adsorption experiment. With this treatment, the manifold pressure was less than 5 μ when the benzene was cooled to a liquid nitrogen temperature and the pumps (both sorption and ion) were valved off. The manifold was then filled to the vapor pressure (~100 torr) of benzene at room temperature just before the adsorption experiment.

Reagent grade naphthalene (J. T. Baker) was kept in a glass tube that was connected to a stainless steel manifold; the glass to metal seal was made with a torr-seal connector using viton gaskets. A copper line was also tried but some naphthalene decomposed on the walls at 80-100°C. The stainless steel manifold was first baked out at 100-120°C for a few hours using an ion pump. The naphthalene sample was then outgassed with three freeze-pump-thaw cycles; after this treatment, the line pressure was again below 5 μ with the naphthalene cooled to a liquid nitrogen temperature, the pumps valved off, and the line heated to 80-100°C. Prior to the adsorption experiment, the naphthalene sample was melted (~80°C) to get a sufficiently high vapor pressure (~10 torr) and the line was kept at 80°C to maintain this pressure at the leak valve. The vacuum side of the leak valve was not heated directly; and the naphthalene passed through 3' of 1/4" O.D. and 1" of 1/16" O.D. stainless steel tubing before being admitted into the UHV chamber near the crystal (~1").

The intensity data for the naphthalene and benzene overlayers was collected with the photographic technique described in Chapters II, III, and V. Each set of intensity data, ranging from 24-150 eV at a given crystal orientation, was taken in a 5-10 minute period; the incident LEED beam was not moved across the crystal during this time because the total intensity decay for any extra-order diffraction beam was less than 5%. All the photography was taken with the Rh(111) sample at 240-250 K.

We obtained two sets of intensity data at each sample orientation ($\theta = 0, 10, 20$ and 30° with $\phi = 0^\circ$) for the $c(2\sqrt{3}\times 4)$ Rect-benzene, (3×3) -benzene, and (3×3) -naphthalene structures. (There are two exceptions to this rule where we collected only one set of intensity data at $\theta = 20$ and 30° for the (3×3) -benzene layer.) The two sets of intensity data which were collected for almost every orientation and structure came from different adsorption experiments in order to check for reproducibility. In addition, we have obtained one set of intensity data for the mixed phase of naphthalene [$(3\sqrt{3}\times n\sqrt{3})R30^\circ + (3\times 3)$] at $\theta = 0^\circ$.

C. RESULTS AND DISCUSSION

i) Preparation of the Benzene Adlayers

A well-ordered $c(2\sqrt{3}\times 4)$ Rect-benzene layer formed at -40°C with a 30 L exposure as shown in Fig. 1a. (All exposure values have not been corrected for the ion gauge sensitivity or for the pressure difference between the gauge and sample.) However, a 15 L exposure produced only a diffuse and weak $c(2\sqrt{3}\times 4)$ Rect LEED pattern. All our intensity data for the (3×3) and $c(2\sqrt{3}\times 4)$ Rect-benzene layers were obtained after a 60 L exposure. Since the $c(2\sqrt{3}\times 4)$ Rect lattice orders already at -40°C ,

benzene should have a fairly large surface mobility at this temperature. A similar procedure using a 70 \AA exposure (which can be directly compared to ours) for a Pt(111) sample at 25°C gave a well-ordered $(2\sqrt{3}\times 4)$ Rect-benzene structure.⁸

The $c(2\sqrt{3}\times 4)$ Rect lattice is stable up to 75°C, but a mixed phase of ordered (3×3) and $c(2\sqrt{3}\times 4)$ Rect domains as illustrated in Fig. 1b can form after a short anneal (~2 minutes) at 90°C. Further heating at 100°C for ~15 minutes produced a clear (3×3) structure that is shown in Fig. 1c. Our Auger Electron Spectra did not detect any change of carbon coverage during the transition. (We obtain $C(272)/Rh(229) = 0.46\pm 0.04$ at 10V_{ptp} modulation in the dN/dE mode.) The (3×3) lattice then disordered after a ~5 minute anneal at 125-150°C. The $(2\sqrt{3}\times 4)$ Rect-benzene overlayer on Pt(111) showed a similar irreversible phase transition to a $(2\sqrt{3}\times 5)$ Rect lattice.⁸ At 50°C, the transformation to the $(2\sqrt{3}\times 5)$ -benzene layer would be completed in ~50 minutes, and well-ordered domains of both the $(2\sqrt{3}\times 4)$ and $(2\sqrt{3}\times 5)$ Rect lattices co-existed during the course of the transition.

In our preliminary adsorption experiments for benzene on Rh(111), however, a fairly disordered (3×3) layer formed already at -40°C. We believe this was caused by either CO coadsorption or a small carbon impurity present on the surface; but we have not yet investigated this point further. The (3×3) layer that formed at -40°C required annealing at 100°C for ~15 minutes to fully order.

A carbon impurity may favor the $(2\sqrt{3}\times 5)$ Rect-benzene layer on Pt(111).^{8b} When an Auger Electron Spectrum was measured for the

clean Pt(111) surface prior to benzene adsorption, the $(2\sqrt{3}\times 5)\text{Rect}$ rather than the $(2\sqrt{3}\times 4)\text{Rect}$ lattice would form initially. It is believed that the electron beam used in the AES measurement may have decomposed adsorbed CO from the background gas to give a carbon impurity. (The atomic oxygen may desorb as an ion or may react with coadsorbed CO to form CO_2 that then quickly desorbs.)

ii) Preparation of the Naphthalene Overlayers

A structure containing disordered $(3\sqrt{3}\times n\sqrt{3})\text{R}30^\circ$ and (3×3) lattices formed after a 5 L exposure (again uncorrected) of naphthalene with the Rh(111) sample at -40°C . The layer was ordered by annealing at 75°C for 5 minutes. We also tried larger exposures of naphthalene, but the quality of the LEED pattern did not improve and the Auger carbon signal did not increase. The superposition of the $(3\sqrt{3}\times n\sqrt{3})\text{R}30^\circ$ and (3×3) LEED patterns indicates that either two kinds of domains exist simultaneously on the surface or the (3×3) layer has a $(3\sqrt{3}\times n\sqrt{3})\text{R}30^\circ$ superlattice associated with it. As shown in Fig. 2a, the third-order diffraction beams were much more intense than the other extra-order reflections which implies that either a higher coverage of the (3×3) domains is present on the metal surface or the superlattice represents only a subtle structural change in the basic (3×3) cell.

Our observation that the overlayer ordered only near 75°C indicates a much lower mobility for adsorbed naphthalene than for benzene. This is consistent with naphthalene¹⁰ and azulene⁹ adsorption on Pt(111). A sharp (6×3) LEED pattern was obtained after annealing the naphthalene overlayer on Pt(111) at 100°C , while the (3×3) - and $(3\times 3)\text{R}30^\circ$ -azulene layers ordered near 125°C .

Heating the $(3 \times 3) + (3\sqrt{3} \times n\sqrt{3})R30^\circ$ phase of naphthalene on Rh(111) to 125-150°C for ~5 minutes produced a well-ordered layer as shown in Fig. 2b. This transformation seems to be irreversible; yet the $(3\sqrt{3} \times n\sqrt{3})R30^\circ$ periodicity did reappear slightly after we kept the annealed naphthalene layer at room temperature for one day. Our Auger Electron Spectra indicate that the carbon coverage does not change during the transition. (We obtain $C(272)/Rh(229) = 0.50 \pm 0.04$ at 10 V_{ptp} modulation in the dN/dE mode.) Further heating to 175°C for 5 minutes permanently disordered the (3×3) lattice. In another set of adsorption experiments, only the (3×3) domain formed after annealing the naphthalene overlayer at 50-75°C; we suspect that trace amounts of impurities (such as carbon or CO) may have caused this change, though we have not yet investigated this point further.

There is once again a strong parallel with aromatic adsorption on Pt(111). Although naphthalene forms only a (6×3) overlayer on Pt(111), azulene yields a mixed phase of (3×3) and $(3 \times 3)R30^\circ$ lattices below 190°C, a (3×3) layer between 190-200°C, and a disordered structure above 200°C.⁹ Interestingly, the mixed phase of (3×3) and $(3 \times 3)R30^\circ$ -azulene could make a reversible transition to only a (3×3) layer at 100-160°C for $\theta_c = 1.1-1.3$. We have not however seen such a reversible transition for the two ordered naphthalene phases on Rh(111).

iii) Interpretation of LEED Patterns

a) Benzene

Figure 3 shows the real space unit cells (dashed lines) of the $c(2\sqrt{3} \times 4)Rect$ and (3×3) -benzene layers above the Rh(111) surface.

HREELS experiments⁷ indicate that the benzene ring lies flat above the metal surface and may adsorb at a C_{3v} site in the $Rh(111)-c(2\sqrt{3}\times 4)Rect$ structure. On the left-hand side of Fig. 3, the benzene admolecules are placed in the $c(2\sqrt{3}\times 4)Rect$ unit cell above atop sites with two different orientations about their six-fold axis. (We do not show the other likely registries (hcp and fcc hollow sites) that allow adsorbed benzene to have C_{3v} symmetry.) The carbon positions in the upper left geometry shown in Fig. 3 are similar to those found for adsorbed acetylene on the Pt, Rh and Pd(111) surfaces,¹¹ while the hydrogen-hydrogen separation in neighboring admolecules has the largest value possible for this lattice (2.9-3.0Å). In the lower left geometry illustrated in Fig. 3 the hydrogen-hydrogen distance is 2.4Å which is close to the Van der Waals distances measured for a number of molecular crystals¹² ($2.4\pm 0.2\text{Å}$) including solid benzene I and II^{12b} (2.64 and 2.23 Å, respectively). For this reason, we favor the benzene orientation given in the lower left of Fig. 3. Now rotating each benzene shown in the upper left of Fig. 3 by 19° about its six fold axis points neighboring C-H bonds toward each other and results in the shortest possible H-H separation for this lattice (2.1 Å).

The implied carbon coverage for the $c(2\sqrt{3}\times 4)Rect$ structure is three-quarters of a monolayer ($\theta_c = 3/4$). At the right side of Fig. 3 we show a plausible benzene geometry for the (3×3) layer that forms on the $Rh(111)$ surface. The carbon coverage for this structure is probably only two-thirds of a monolayer ($\theta_c = 2/3$). Since no HREELS measurements have yet been done on the (3×3) layer, we have assumed that benzene again lies flat on the metal surface above a C_{3v}

adsorption site. A HREELS study⁵ for benzene adsorbed on Ni and Pt(111) indicated that two different C_{3v} sites are populated in a disordered layer that forms at low exposures (with C-H out-of-plane bending frequencies at 730 and $820 \pm 10 \text{ cm}^{-1}$), yet only one C_{3v} site was found in a similar study on the Ni(111)- $(2\sqrt{3} \times 2\sqrt{3})R30^\circ$ structure⁶ (with a C-H out-of-plane bending frequency at $750 \pm 10 \text{ cm}^{-1}$). This suggests to us that benzene may occupy two different C_{3v} sites in the two lattices that appear after adsorption on both the Pt and Rh(111) faces.

The particular orientation we chose for adsorbed benzene in the (3×3) structure shown at the upper right of Fig. 3 is at best only slightly favored by the Van der Waals arguments we used for the $c(2\sqrt{3} \times 4)\text{Rect}$ layer. The benzene admolecules have neighboring C-H groups pointing towards each other, but the H-H distance (that is the shortest possible for this lattice) is still significantly larger (3.1 \AA) than the optimal value (2.4 \AA). The geometry illustrated in the lower right of Fig. 3 shows another orientation of the benzene layer whereby the H-H distances are maximized (3.7 \AA). In either case, adsorbate-adsorbate interactions should not be nearly as important as we believe they are in the $c(2\sqrt{3} \times 4)\text{Rect}$ overlayer. In fact, the admolecules may be randomly oriented above the metal since the adsorbate-metal interactions may also not significantly inhibit rotation about the six-fold axis.¹³ This suggests an attractive possibility whereby the $c(2\sqrt{3} \times 4)\text{Rect}$ to (3×3) phase transition is caused by the increasing importance of the entropy term in the Gibbs Free Energy at higher temperatures ($\Delta G = \Delta H - T\Delta S$).

The benzene layers on the Pt(111) surface have a similar density to those on Rh(111). We found that a glide line symmetry exists along the longer edge of the $(2\sqrt{3}\times 5)$ Rect unit cell after carefully inspecting the photography collected by P. C. Stair.⁸ The presence of this glide line strongly suggests that there are two ad molecules in the $(2\sqrt{3}\times 5)$ Rect cell contrary to earlier findings that relied on C¹⁴ radiotraces¹⁴ (one molecule/cell) or Auger Electron Spectroscopy⁸ (three molecules/cell).

Figure 4 shows a schematic of the LEED patterns for the $(2\sqrt{3}\times 4)$ Rect and $(2\sqrt{3}\times 5)$ Rect benzene overlayers on Pt(111). In Fig. 4a, some LEED spots are missing at normal incidence for the $(2\sqrt{3}\times 4)$ Rect layer that suggests a glide line symmetry, but these spots do not unfortunately clearly reappear when the crystal is rotated by as much as 16° off-normal incidence. In Fig. 4b, the LEED spots for the $(2\sqrt{3}\times 5)$ Rect adlayer that are drawn as circles are again not present at normal incidence, but do appear when the crystal is rotated four degrees off-normal incidence. If a glide line symmetry is present in the $(2\sqrt{3}\times 4)$ Rect structure, we calculate a carbon coverage of $\theta_c = 3/4$; while the carbon coverage for the $(2\sqrt{3}\times 5)$ Rect layer is $\theta_c = 3/5$.

b) Naphthalene

The superposition of the $(3\sqrt{3}\times n\sqrt{3})R30^\circ$ and (3×3) periodicities in the naphthalene layer on Rh(111) (Fig. 2a) makes it difficult to determine n uniquely. There are two arguments however that favor $n=3$ over $n=1$. (1) The $(3\sqrt{3}\times\sqrt{3})R30^\circ$ cell is very long and narrow and does not allow an optimal packing for the naphthalene layer. (2) A $(3\sqrt{3}\times\sqrt{3})R30^\circ$ lattice would also have a LEED pattern with many single-domain

diffraction beams. As described in Chapter VIII, the Rh(111)-c(4x2)-ethylene structure produced a number of single-domain diffraction beams; and we observed that the equivalent beams from different domains had very different absolute intensities. This domain preference was attributed to the step density that exists on our Rh(111) sample. We expect that a $(3\sqrt{3}\times\sqrt{3})R30^\circ$ naphthalene lattice on the same Rh(111) sample should also give equivalent single domain diffraction beams with very different absolute intensities. However, Fig. 2a shows that the possible single domain LEED spots, which would be equivalent by the mirror plane symmetry along the (10) or (01) direction, have nearly the same absolute intensity. It is more likely then that a $(3\sqrt{3}\times 3\sqrt{3})R30^\circ$ rather than a $(3\sqrt{3}\times\sqrt{3})R30^\circ$ naphthalene periodicity exists on the Rh(111) surface.

Our Auger Electron Spectra suggest that both naphthalene layers which form on the Rh surface have the same coverage. The (3x3) phase probably has one admolecule in each primitive cell, while the $(3\sqrt{3}\times 3\sqrt{3})R30^\circ$ lattice contains three. The implied coverage for both these layer is $\theta_c = 10/9$. There are too many molecules present in the $(3\sqrt{3}\times 3\sqrt{3})R30^\circ$ cell to permit a likely structure to be drawn. However, a possible model for the (3x3) naphthalene layer is illustrated in Fig. 5. The naphthalene ring lies flat on the surface with the hydrogen atoms from neighboring admolecules meshed in a bevel gear arrangement. The smallest hydrogen-hydrogen separation is only 1.6 Å which is significantly less than the optimal Van der Waals distance of $2.4 \pm .2$ Å. The admolecule may however be somewhat

distorted (C-H tilting, for example) to reduce these repulsive Van der Waals interactions between nearest neighboring hydrogens.

Rotating the adsorbed naphthalene about an axis perpendicular to the surface will produce even shorter hydrogen-hydrogen distances than those given in Fig. 5. As drawn in our model, the two C_6 rings of naphthalene are centered 0.3 Å away from the neighboring hcp and fcc hollow sites. This would be consistent with HREELS results^{5,6} that suggest benzene on Ni and Pt(111) may be centered above a three-fold hollow in at least one of the two adsorption sites that are occupied on the metal surface.

Naphthalene adsorbs in a (6×3) lattice on the Pt(111) surface; most probably two ad molecules are located in each cell since a glide line symmetry is found along the (10) and (01) directions in the LEED pattern.¹⁰ Force field calculations,¹⁵ which assume standard Van der Waals parameters and neglect metal-adsorbate interactions, predict that the two naphthalene molecules lie flat above the metal and have a relative rotation of 60°. The packing potential energy for the layer is calculated to be a negative 5-6 kcal/mole. However, a positive potential energy of 4 kcal/mole is obtained when the relative rotation of naphthalene molecule is reduced to 0°. This latter orientation corresponds to the naphthalene overlayer illustrated in Fig. 5; but an even more repulsive interaction energy for neighboring naphthalene molecules should exist in the (3×3) lattice on Rh(111) since the Rh substrate spacing is about 4% smaller than that for Pt. Why naphthalene prefers the (3×3) cell on Rh(111) rather than a (6×3) cell

with glide lines as on Pt(111) is not at present understood in the framework of our Van der Waals arguments.

Azulene adsorbed on Pt(111)⁹ produces a mixed phase of two ordered domains ((3×3)R30° and (3×3)) that have an equal density of admolecules. A very plausible model for the azulene overlayer is similar to our naphthalene lattice shown in Fig. 5 except that the closest hydrogen-hydrogen distances are 2.0 (2 hydrogens/molecule) and 2.2Å (4 hydrogens/molecule). Force Field calculations¹⁶ in this case predict a packing potential energy of a negative 4-5 kcal/mole.

iv) Thermal Desorption Spectra

a) Benzene

Figure 6 shows the H₂ TD spectrum obtained with either the c(2√3×4)Rect or (3×3) benzene overlayers on Rh(111) and with a linear temperature ramp of 5-10°C/sec. The first hydrogen desorption peak occurs at 140°C and has a width of only 20°C, while a second broader peak appears at 300°C. The H₂ TD spectrum for benzene adsorbed on Pt(111)¹⁷ is very similar in shape, but the peak desorption temperatures are shifted to higher values (270, 380°C). The sharp first peak in the TD spectra probably signals the decomposition of the benzene molecules, while the broader second peak should then correspond to the dehydrogenation of the hydrocarbon fragments that form on the surface. An analogous sequence of decomposition and further dehydrogenation steps has been followed with HREELS and TDS for the alkylidyne layers that form on the Rh and Pt(111) surfaces (Chapters VI and VIII).

Since no H₂ desorption is detected between -40° and 100°C, benzene appears to adsorb non-dissociatively on the Rh(111) surface.

If benzene did decompose, the hydrogen that would be released should desorb near room temperature. Chemical displacement reactions support the non-dissociative adsorption of benzene on Pt(111). Trimethylphosphine ($(\text{CH}_3)_3\text{P}$) completely displaces benzene from the Pt(111) surface if the crystal temperature is kept below the onset of the thermal desorption ($<220^\circ\text{C}$)¹⁷. The same conclusion is reached for benzene adsorbed on the Ni(111) surface where the peak hydrogen desorption occurs at 180°C .¹⁸ These desorption experiments on Rh, Pt, and Ni(111) indicate that the Rh surface is the most reactive since benzene decomposition occurs at the lowest temperature on this metal; the Pt surface then turns out to be the least reactive.

A flat or π -bonded benzene ad molecule is suggested from the H_2 desorption spectra; this claim is further supported by the HREELS, ARPES, and LEED studies that have already been described. If the molecular plane of benzene was tilted away from the metal surface, we would expect either a rehybridization of the carbon atoms in the ring which would remove the energetically favorable π -resonance of benzene, or a dissociative σ -bonding of one or two carbon atoms to the metal which is also unlikely since there is no detectable hydrogen evolution below about 100°C on any of the metal surfaces discussed.

Both order-order phase transitions for benzene adsorbed on the Pt and Rh(111) surfaces leads to lower coverage structures. The $c(2\sqrt{3}\times 4)$ Rect to (3×3) lattice transformation that occurs with benzene on Rh(111) should change the carbon coverage from $\theta_c = 3/4$ to $\theta_c = 2/3$. The transition on the Pt(111) surface probably goes from a $(2\sqrt{3}\times 4)$ Rect cell ($\theta_c = 3/4$) to a $(2\sqrt{3}\times 5)$ Rect one ($\theta_c = 3/5$) since

those rectangular cells are found to probably have a glide line symmetry. If the benzene layer is initially saturated on Rh and Pt(111), the 12% (for Rh) or 20% (for Pt) reduction in the benzene density must come from either decomposition or desorption. As shown in Table 1, benzene desorption from the Pt(111) surface can occur at 100-130°C hydrogen evolution does not become appreciable until a temperature of 270°C has been reached. This suggests that the excess benzene desorbs intact during the irreversible phase transition.

Although we have not measured the benzene thermal desorption spectrum from the Rh(111) face, we believe benzene again desorbs near 100°C. To support this claim, we notice that the benzene desorption temperature is between 100-130°C for both Ni and Pt(111), even though the H₂ desorption peaks have very different temperatures (180 and 270°C). The transition from the $c(2\sqrt{3}\times 4)$ Rect to the (3×3) lattice that occurs on Rh(111) is probably caused by benzene desorption rather than decomposition even though the decomposition reaction can proceed rapidly at 140°C in this case. Our Auger Electron Spectra for the two benzene layers on Rh give the same carbon coverage. (We obtain $C(272)/Rh(229) = 0.46 \pm 0.04$.) However, the experimental uncertainty is too large (~10%) to clearly discriminate between desorption or decomposition.

It is quite surprising that the benzene transition on the Pt(111) surface can actually take place at room temperature by either leaving the sample in vacuo for 3-4 hours or continuing the benzene flux for ~30 min at 10^{-7} torr.⁸ The benzene desorption rate at room temperature is too small to account for the 20% loss in density that is

necessary, while a continued benzene exposure should saturate the benzene overlayer rather than cause a 20% reduction in density. Two possible explanations can be posed. (1) The initial benzene layer may not be fully saturated after a 70 L exposure at room temperature. This implies that there are many benzene islands with 20% of the metal uncovered; and it does not easily explain why higher benzene exposures would cause the phase transition to the $(2\sqrt{3}\times 5)$ Rect layer. (2) Or the major background gases (H_2 and CO) may remove some adsorbed benzene. CO, for example, could displace some benzene and allow the benzene lattice that remains to expand. In support of this argument, the first benzene desorption peak occurs at a much lower temperature (100-130°C) than found for CO; this implies that CO is more strongly bound to the Pt(111) surface.

b) Naphthalene

The H_2 desorption spectrum for the combined $(3\sqrt{3}\times 3\sqrt{3})R30^\circ + (3\times 3)$ phase or the (3×3) phase is illustrated in Fig. 7. A sharp peak is detected near 310°C and a broader peak at about 430°C (with a linear temperature ramp of 5-10°C/sec). We again interpret the first peak to correspond to a decomposition reaction and the higher temperature peak indicates further dehydrogenation of residual hydrocarbon fragments. As shown in Table 1, naphthalene decomposition occurs at comparable temperatures on Rh and Pt(111) (300° and 310°C, respectively) along with azulene decomposition on Pt(111) (275°C). Unfortunately, molecular desorption was not studied on any of these surfaces.

The naphthalene phase transition on the Rh(111) surface is completed in ~15 minutes at 150°C even though we measure an appreciable

decomposition probability only near 300°C. Dissociation of adsorbed naphthalene then may not cause the transformation from the $(3 \times 3) + (3\sqrt{3} \times 3\sqrt{3})R30^\circ$ phase to the (3×3) . However, decomposition of adsorbed azulene on Pt(111) is found to occur at 190°C, even though the measured H_2 desorption temperature is 275°C.⁹

D. SUMMARY

Benzene produces two different ordered overlayers on the Rh(111) surface. The $c(2\sqrt{3} \times 4)$ Rect lattice (at an implied coverage of $\theta_c = 3/4$) transforms irreversibly to a (3×3) structure (at a lower coverage of $\theta_c = 2/3$) upon heating to near 100°C. Similarly, naphthalene forms a mixture of $(3\sqrt{3} \times 3\sqrt{3})R30^\circ$ and (3×3) lattices on the Rh(111) surface (with an implied coverage of $\theta_c = 10/9$) below 125°C, while only the (3×3) phase remains after heating to 150°C. The superposition of the $(3\sqrt{3} \times 3\sqrt{3})R30^\circ$ and (3×3) LEED patterns indicates that the $(3\sqrt{3} \times 3\sqrt{3})R30^\circ$ lattice either exists as a separate domain from the (3×3) phase or occurs as a superperiodicity on the (3×3) structure.

Our Thermal Desorption Spectra (TDS) suggest that both the benzene and naphthalene layers are non-dissociatively adsorbed, while our Auger Electron Spectra do not indicate any change in carbon coverage after the $c(2\sqrt{3} \times 4) + (3 \times 3)$ -benzene or $(3\sqrt{3} \times 3\sqrt{3})R30^\circ + (3 \times 3) + (3 \times 3)$ -naphthalene transitions. We still believe however that some benzene (12%) desorbs from the surface in the $c(2\sqrt{3} \times 4) + (3 \times 3)$ transformation since our Auger Spectra have a comparable uncertainty (~10%) and such desorption without any accompanying decomposition has been found on the Pt and Ni(111) surfaces (see Table 1).

Intensity vs. voltage curves have been collected for the benzene and naphthalene layers, and a LEED determination of their surface structure has just begun. Reasonable geometries for these aromatic layers can be posed and will be tested in our dynamical LEED studies. The LEED pattern, thermal desorption spectra and High Resolution Electron Energy Loss Spectra (HREELS) suggest that benzene lies flat on the surface in the $c(2\sqrt{3}\times 4)\text{Rect}$ structure. A likely orientation of the benzene ring about its six-fold axis gives H-H contacts of 2.4\AA and carbon positions that are very similar to that found for acetylene adsorbed on Rh, Pt and Pd(111). The (3×3) -benzene layers may also be π -bonded to the metal since no H_2 desorption seems to occur in the $c(2\sqrt{3}\times 4)\text{Rect}\rightarrow(3\times 3)$ transition. The adsorbate-adsorbate interactions are probably very weak in this structure; if the metal-adsorbate interaction does not inhibit rotation about the six-fold axis, this layer may be orientationally disordered.

The (3×3) -naphthalene layer may also be π -bonded to the metal. In this case, adsorbate-adsorbate interactions should strongly inhibit any rotations about an axis perpendicular to its molecular plane. In fact, the optimal orientation (assuming no distortion of the admolecule) already gives very small H-H contacts (1.6\AA).

References for Chapter X

1. P. Hofmann, K. Horn and A. M. Bradshaw, Surf. Sci. 105 1260 (1981).
2. G. L. Nyberg and N. V. Richardson, Surf. Sci. 85 335 (1979).
3. N. V. Richardson and N. R. Palmer, Surf. Sci. 114 L1 (1982).
4. D. R. Lloyd, C. M. Quinn and N. V. Richardson, Solid State Commun. 23 141 (1977).
5. S. Lehwald, H. Ibach and J. E. Demuth, Surf. Sci. 78 577 (1978).
6. J. C. Bertolini, G. Dolmai-Imelik and J. Rousseau, Surf. Sci. 67 478 (1977).
7. B. E. Koel, private communication.
8. a) P. C. Stair, and G. A. Somorjai, J. Chem. Phys. 67 4361 (1977).
b) P. C. Stair, PhD thesis (University of California, Berkeley, 1977).
9. D. Dahlgren and J. C. Hemminger, J. Chem. Phys. 75 5573 (1981) and Surf. Sci. 114 459 (1982).
10. D. Dahlgren and J. C. Hemminger, Surf. Sci. 109 L513 (1981).
11. a) for Pt: H. Ibach and S. Lehwald, J. Vac. Sci. Tech. 15 407 (1978).
b) for Rh: L. H. Dubois, D. G. Castner, and G. A. Somorjai, J. Chem. Phys. 72 523 (1980).
c) for Pd: L. L. Kesmodel and J. A. Gates, to be published.
- 12a. L. Pauling, Nature of the Chemical Bond, (Cornell University Press, Ithaca, New York, 1980) pp. 260-261.
- 12b. G. J. Piermarini, A. D. Mighell, C. E. Weir and S. Block, Science 165 1250 (1969).

13. A. Gavezzotti and M. Simonetta, Surf. Sci. 99 453 (1980).
14. S. M. Davis, B. E. Gordon, M. Press and G. A. Somorjai, J. Vac. Sci. Tech. 19 231 (1981).
15. A. Gavezzotti and M. Simonetta, Surf. Sci. 116 L207 (1982).
16. A. Gavezzotti and M. Simonetta, submitted to Surf. Sci.
17. M. C. Tsai and E. L. Muetterties, to be published.
18. C. M. Friend and E. L. Muetterties, JACS 103, 773 (1981).

Table 1. Thermal desorption data for adsorbed aromatics.

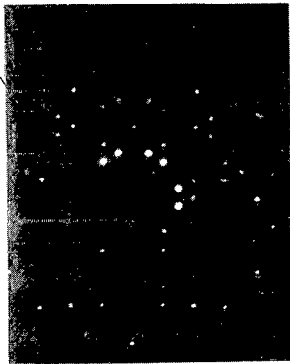
I. Benzene (C ₆ H ₆)		
<u>metal</u>	<u>H₂ desorption (T°C)</u>	<u>benzene desorption (T°C)</u>
Rh(111)	140,300	(?)
Pt(111) ¹⁷	270,380	100-130,200-220
Ni(111) ¹⁸	180,(?)	115-125,(?)
II. Naphthalene (C ₁₀ H ₈)		
<u>metal</u>	<u>H₂ desorption (T°C)</u>	<u>naphthalane desorption (T°C)</u>
Rh(111)	300,420	(?)
Pt(111)	310,360	(?)
III. Azulene (C ₁₀ H ₈)		
<u>metal</u>	<u>H₂ desorption (T°C)</u>	<u>azulene desorption (T°C)</u>
Pt(111)	275,390	(?)

Figure Captions for Chapter X

- Fig. 1. Rh(111)-benzene LEED patterns. Pattern (a) forms after adsorption at -40°C , (b) occurs after a 2-minute anneal at 90°C and (c) appears after a 15 minute anneal at 100°C .
- Fig. 2. Rh(111)-naphthalene LEED patterns. Pattern (a) forms after a 5 min anneal at 75°C and (b) appears after a 5 min anneal at $125\text{-}150^{\circ}\text{C}$.
- Fig. 3. Plausible geometries for the Rh(111)-benzene structures. We favor the lower left geometry for the $c(2\sqrt{3}\times 4)$ phase and an orientationally disordered benzene lattice for (3×3) phase.
- Fig. 4. Schematic of LEED patterns found for the Pt(111)- $(2\sqrt{3}\times 4)$ and $(2\sqrt{3}\times 5)$ -benzene structures.⁸
- Fig. 5. Plausible geometry for the (3×3) -naphthalene layer.
- Fig. 6. H_2 thermal desorption spectrum for either the Rh(111)- (3×3) or $c(2\sqrt{3}\times 4)$ Rect-benzene overlayer. The heating rate is $5\text{-}10^{\circ}\text{C}/\text{sec}$.
- Fig. 7. H_2 thermal desorption spectrum for either the $(3\sqrt{3}\times 3\sqrt{3})\text{-R}30^{\circ}+(3\times 3)$ mixed phase or (3×3) phase of naphthalene on Rh(111).

Rh(III) - C₆H₆

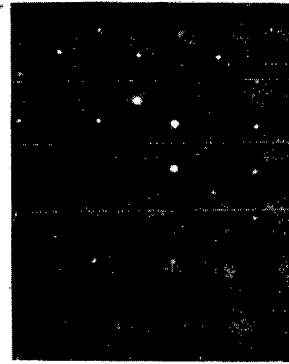
50 eV



a) $c(2\sqrt{3} \times 4)$ Rect



(b) $c(2\sqrt{3} \times 4)$ Rect + (3×3)



(c) (3×3)

XBB 829-7947

Fig. 1

Rh(III) - C₁₀H₈

50 eV



(a) $(3\sqrt{3} \times 3\sqrt{3})R 30^\circ + (3 \times 3)$



XBB 829-7946

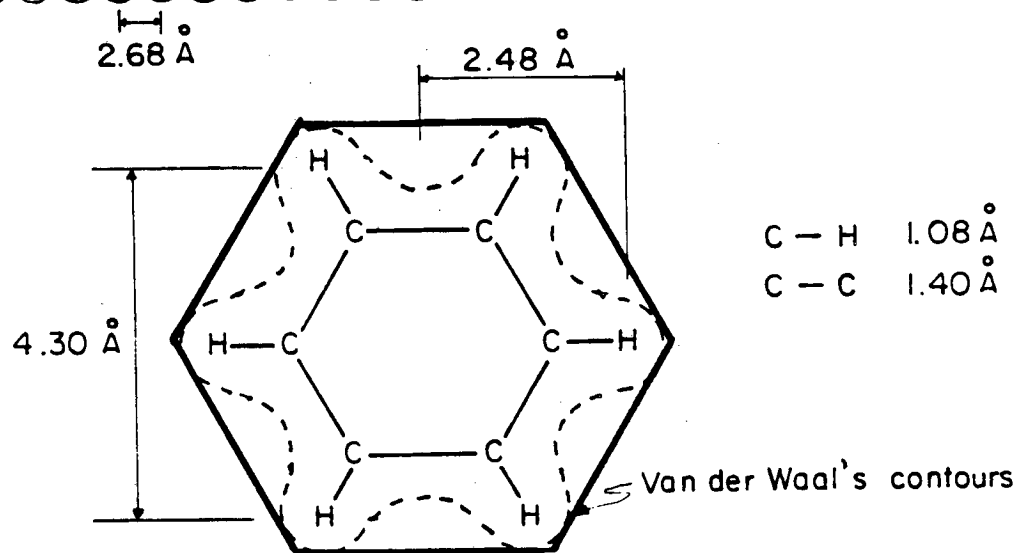
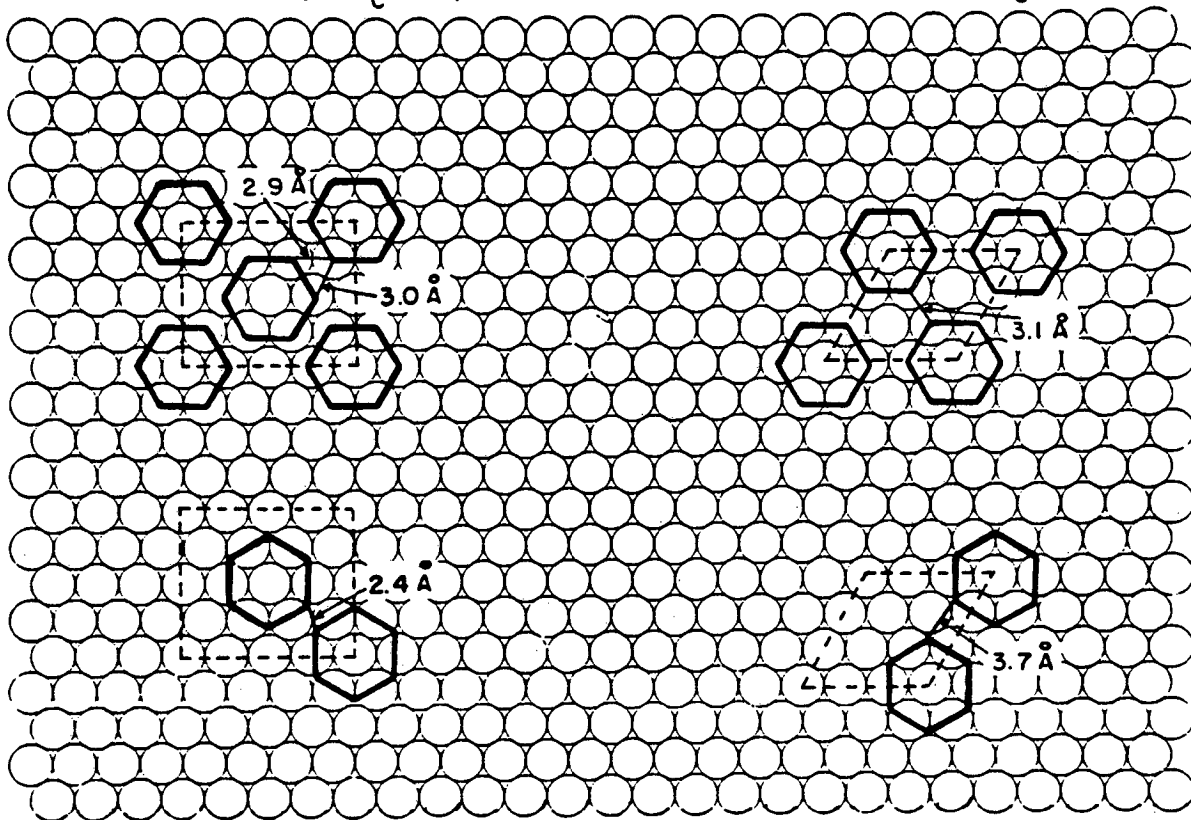
(b) (3×3)

Fig. 2

Rh(III)-C₆H₆

$c(2\sqrt{3} \times 4)$ Rect
(implied coverage, $\theta_c = 3/4$)

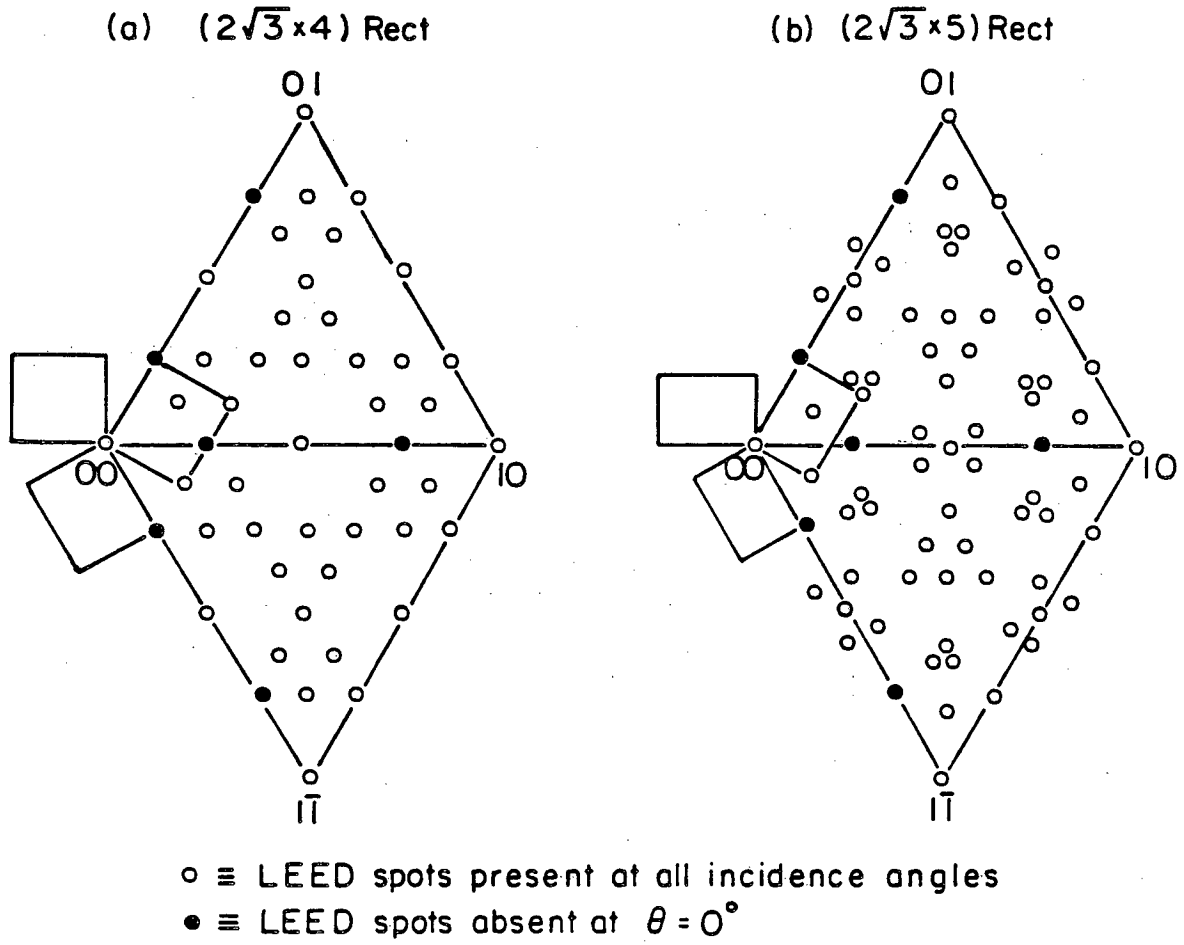
(3x3)
(implied coverage, $\theta_c = 2/3$)



XBL 828-6462

Fig. 3

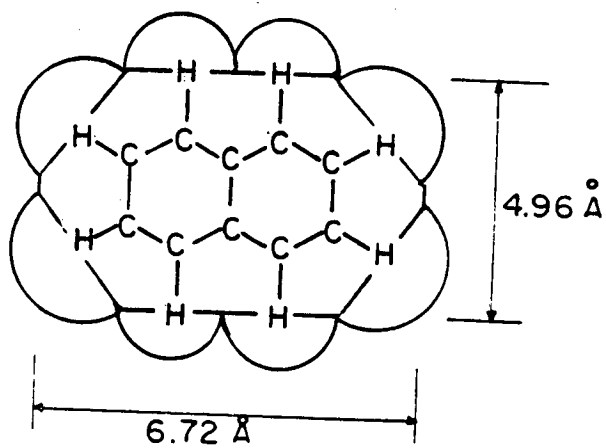
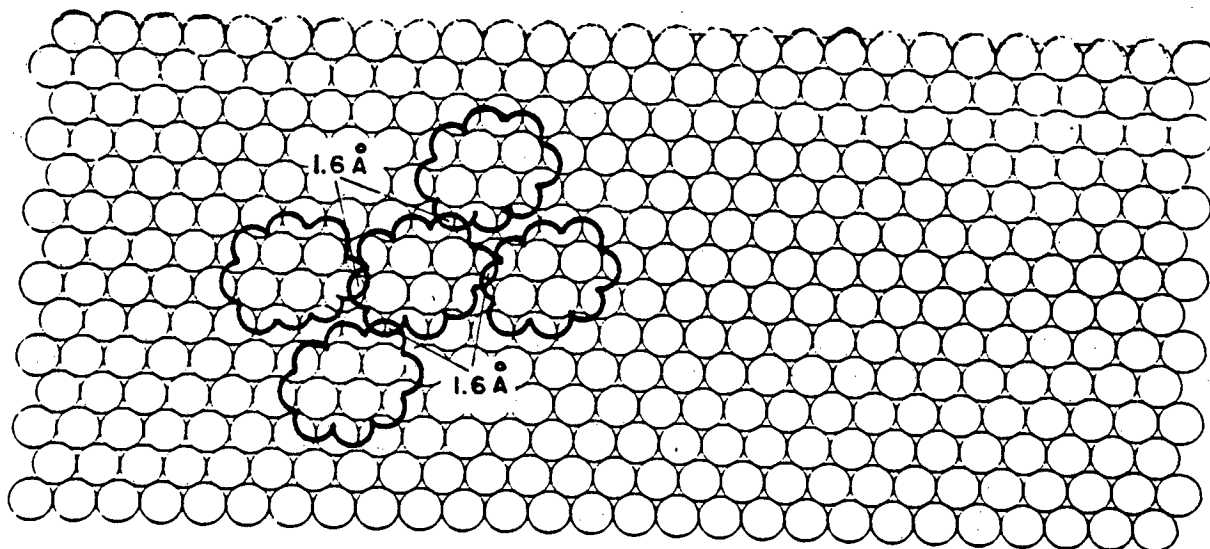
Observed Glide Line Symmetry for Pt(III)-C₆H₆



XBL 828-6461

Fig. 4

Rh(III)-C₁₀H₈
(3x3)



XBL 828-6463

Fig. 5

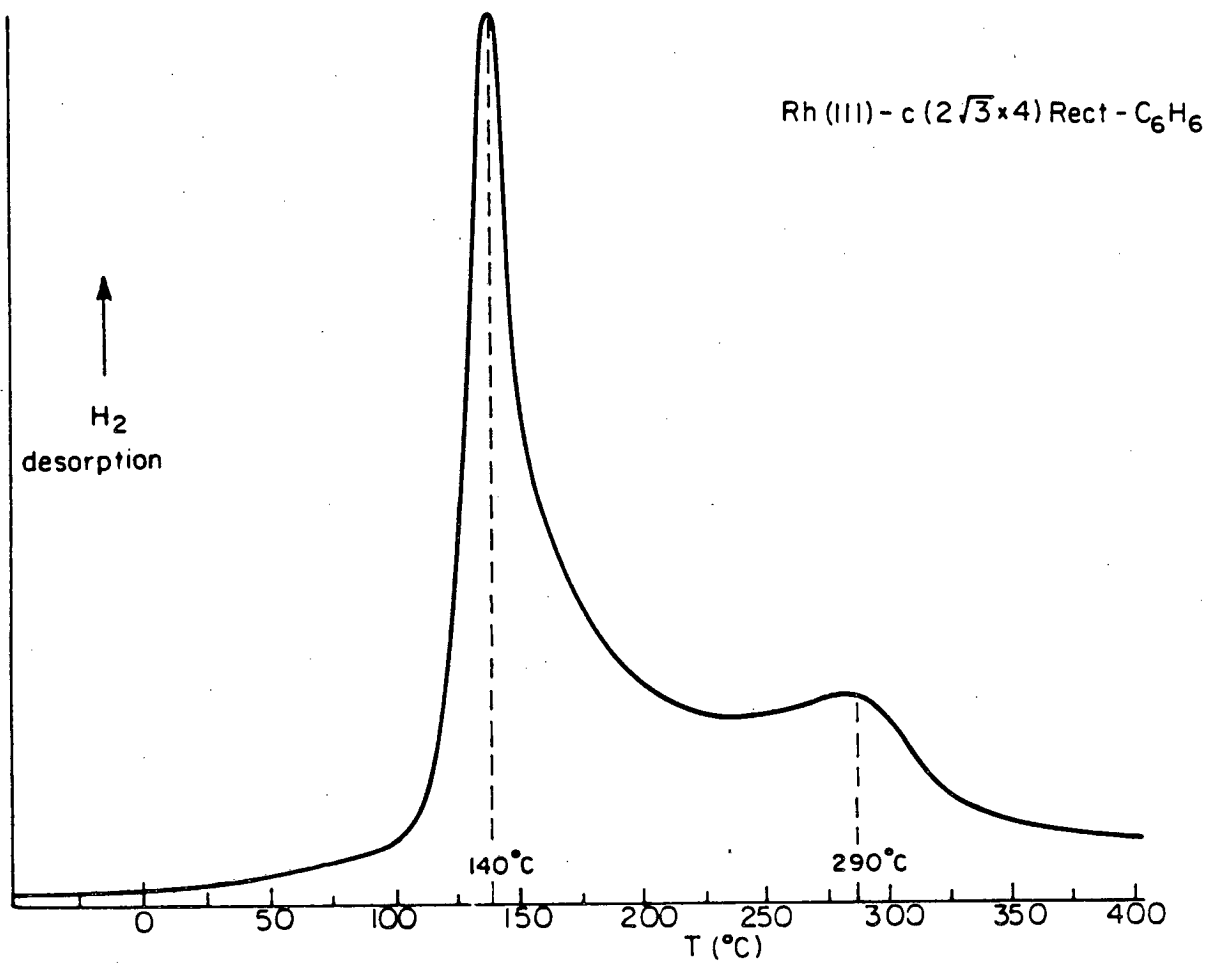
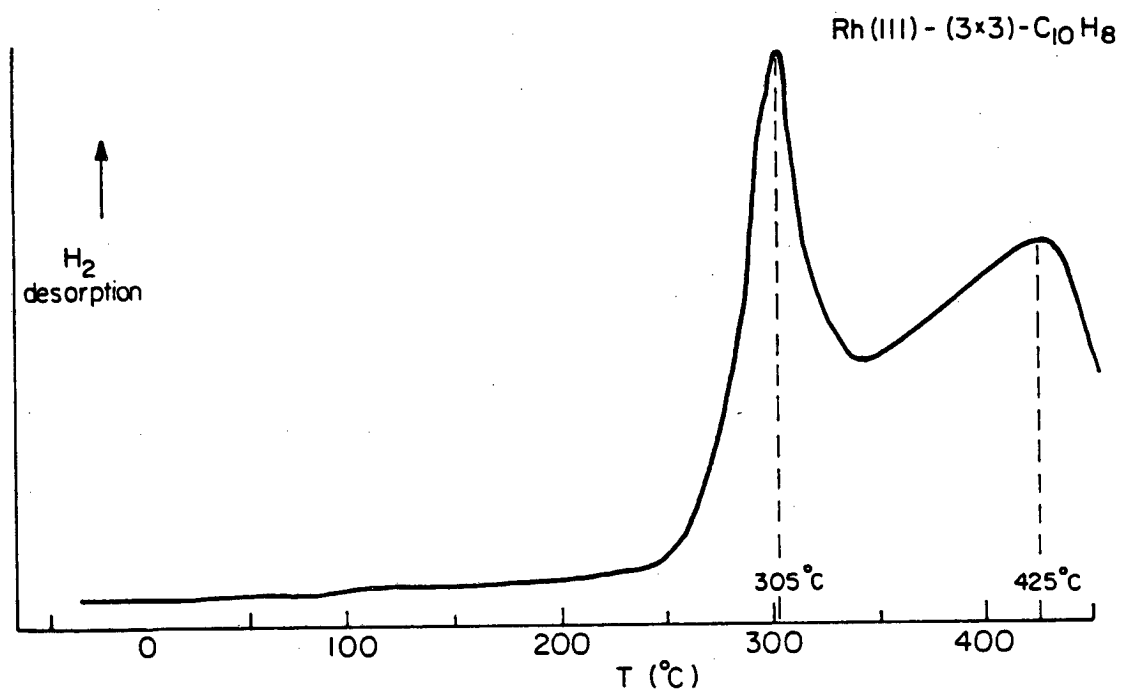


Fig. 6



XBL 828-6459

Fig. 7

APPENDIX I. EXPERIMENTAL INTENSITY CURVES

- 1) Ir(100)-(5x1)
- 2) Rh(111)
- 3) Rh(111)-($\sqrt{3}\times\sqrt{3}$)R30°-CO
- 4) Rh(111)-(2x2)-3CO
- 5) Rh(111)-(2x2)-CO-CO₂ Exposure
- 6) Rh(111)-(2x2)-C₂H₃
- 7) Rh(111)-(2x2)-C₃H₅ (low exposure)
- 8) Rh(111)-($2\sqrt{3}\times2\sqrt{3}$)R30°-C₃H₅ (high exposure)
- 9) Rh(111)-($2\sqrt{3}\times2\sqrt{3}$)R30°-C₃H₄ (high exposure)
- 10) Rh(111)-c(4x2) with C₂H₂+H, C₂H₄, C₃H₄+H, C₃H₆
- 11) Rh(111)-(3x3)-C₆H₆
- 12) Rh(111)-($3\times\sqrt{3}\times n\sqrt{3}$)R30°+(3x3)-C₁₀H₈
- 13) Rh(111)-(3x3)-C₁₀H₈
- 14) Rh(100)
- 15) Pt(111)-(2x2)-C₃H₅
- 16) Pt(111)-($2\sqrt{3}\times2\sqrt{3}$)R30°-2-C₄H₈ (high exposure)
- 17) Pt(111)-(8x8)-2-C₄H₈ (intermediate exposure)
- 18) Pt(111)-(2x2)-2-C₄H₈ (low exposure)

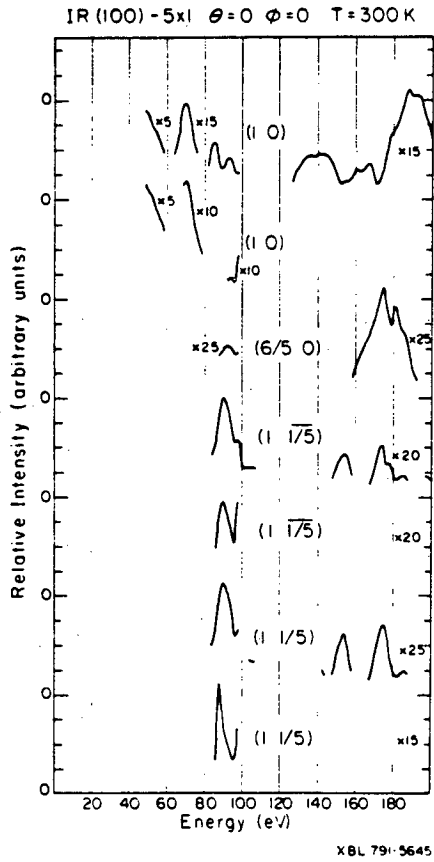


Fig. 1a

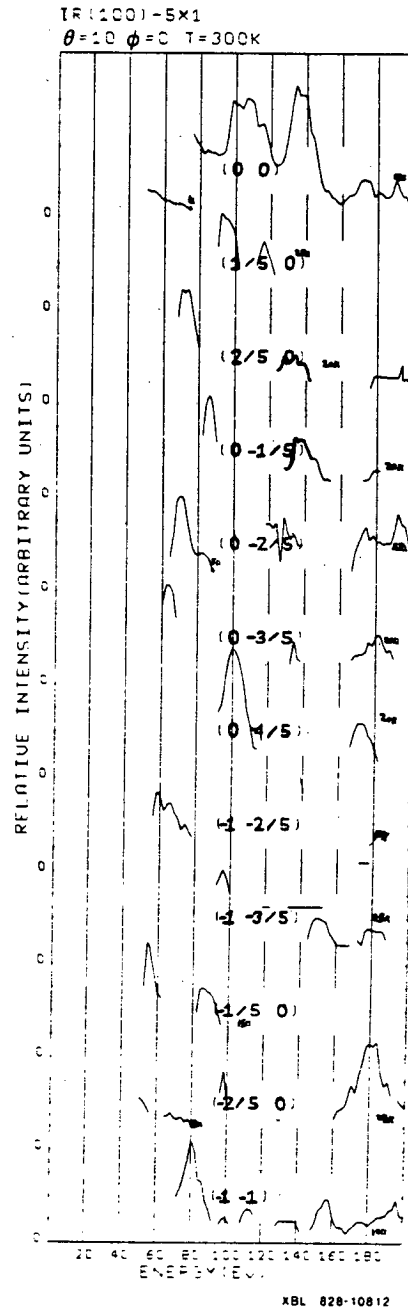
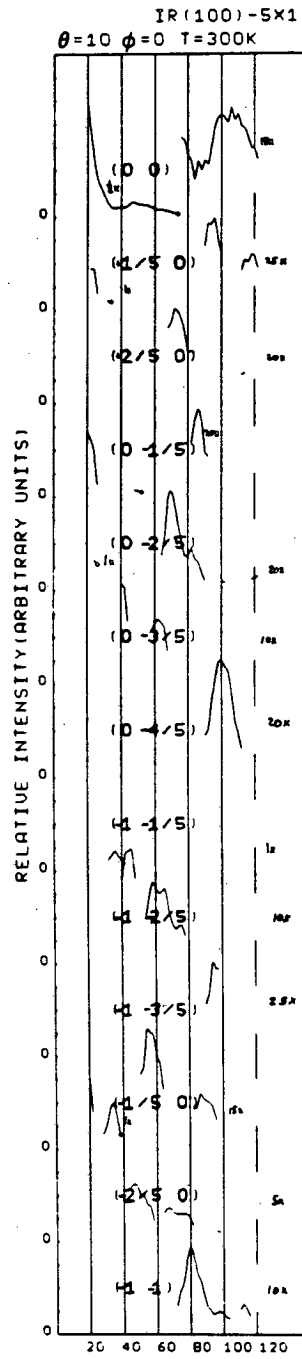


Fig. 1b

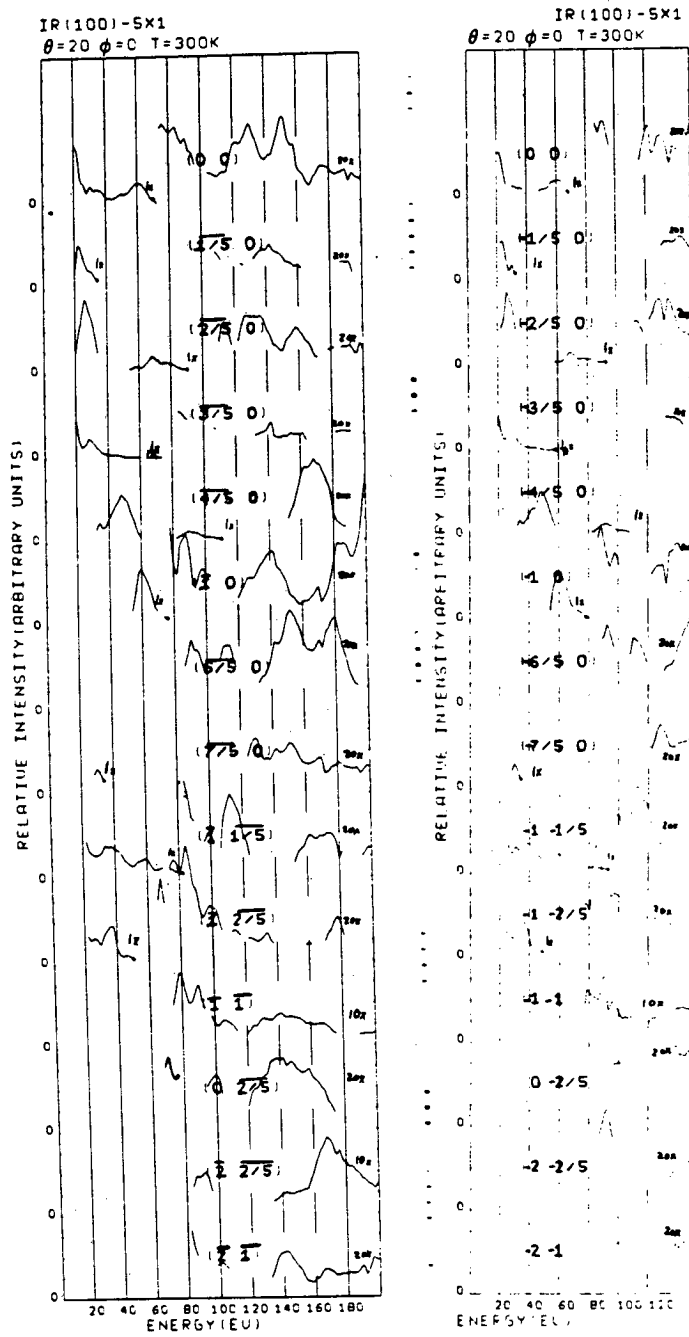
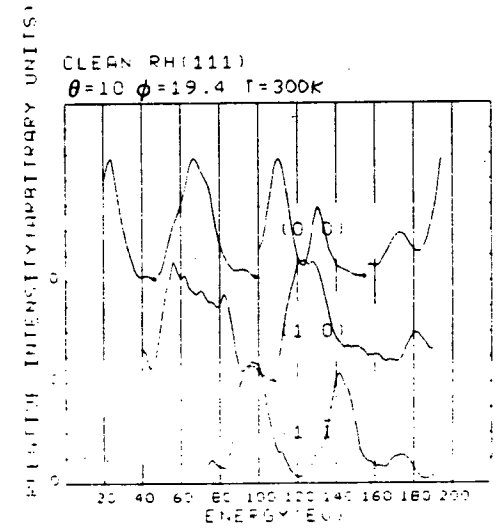
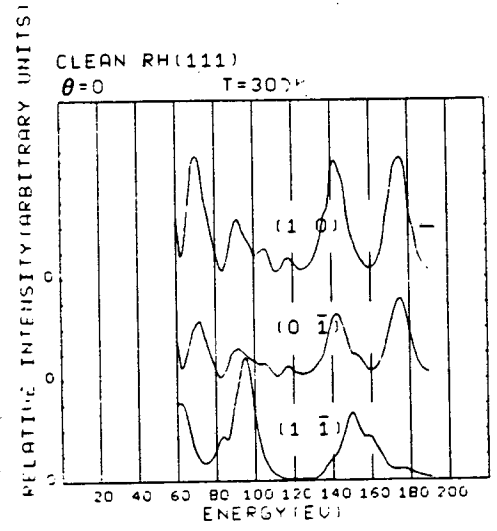
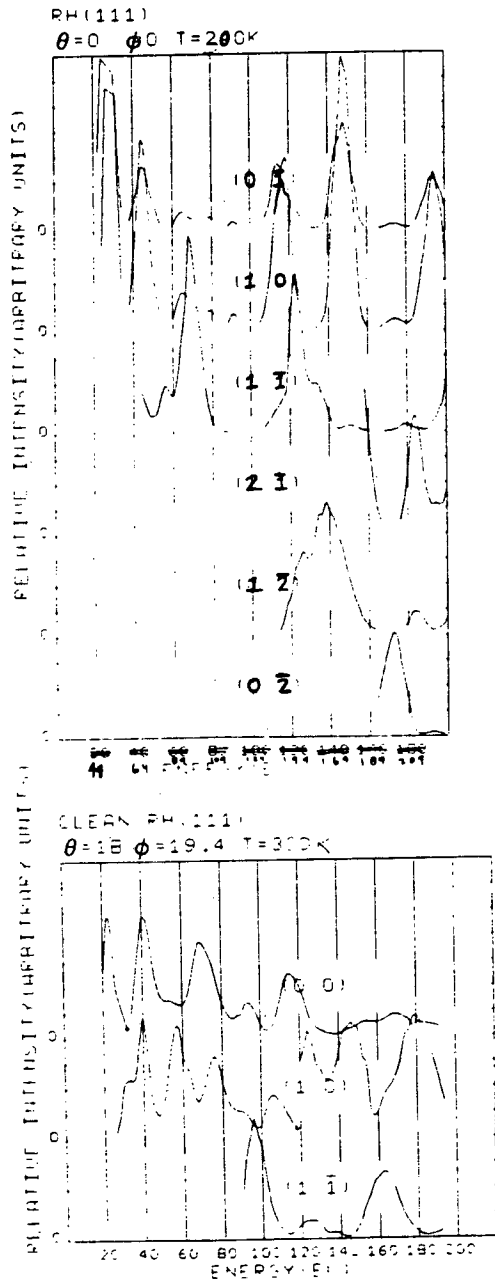


Fig. 1c



XBL 828-10809

Fig. 2

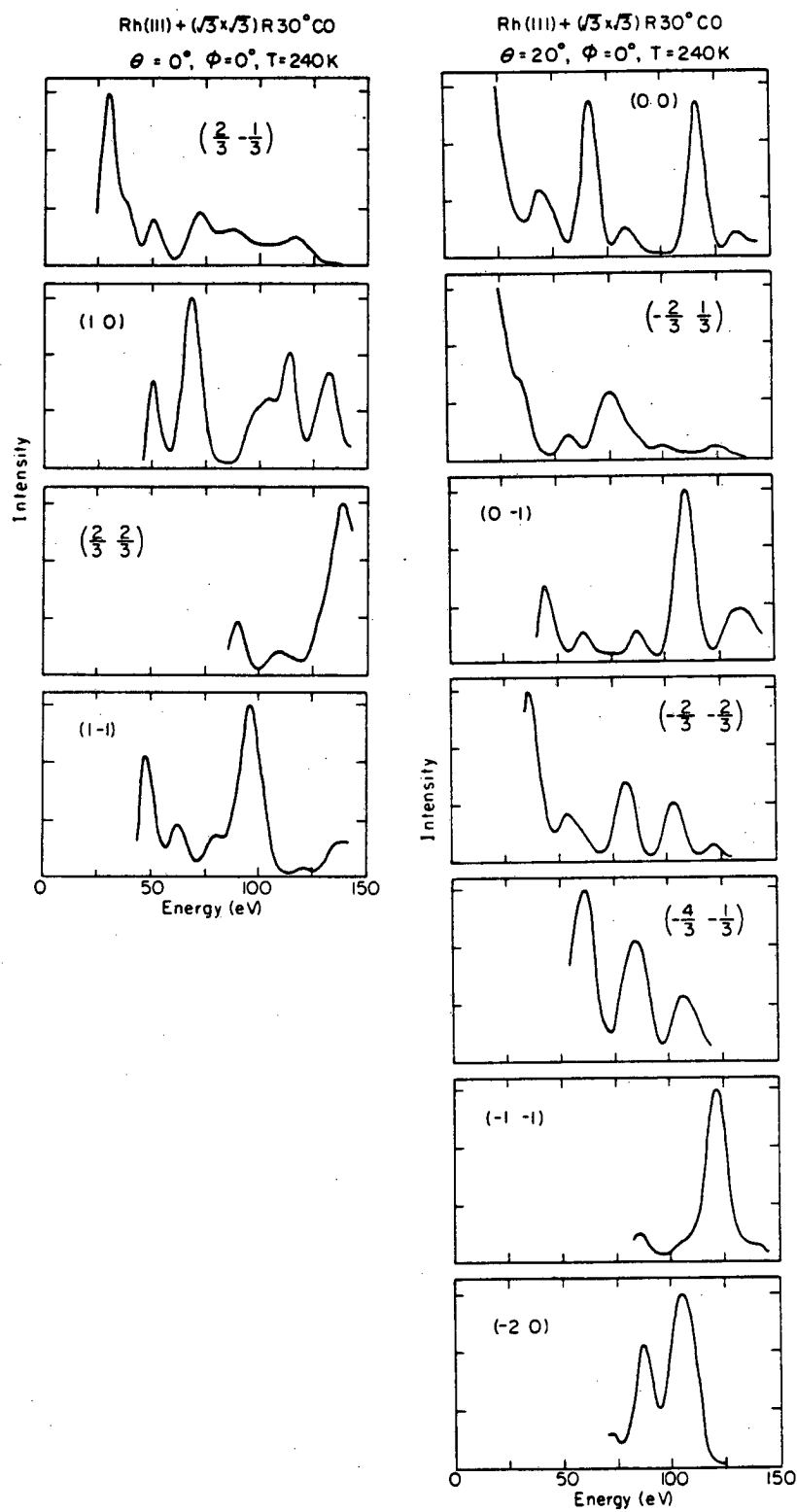


Fig.3a

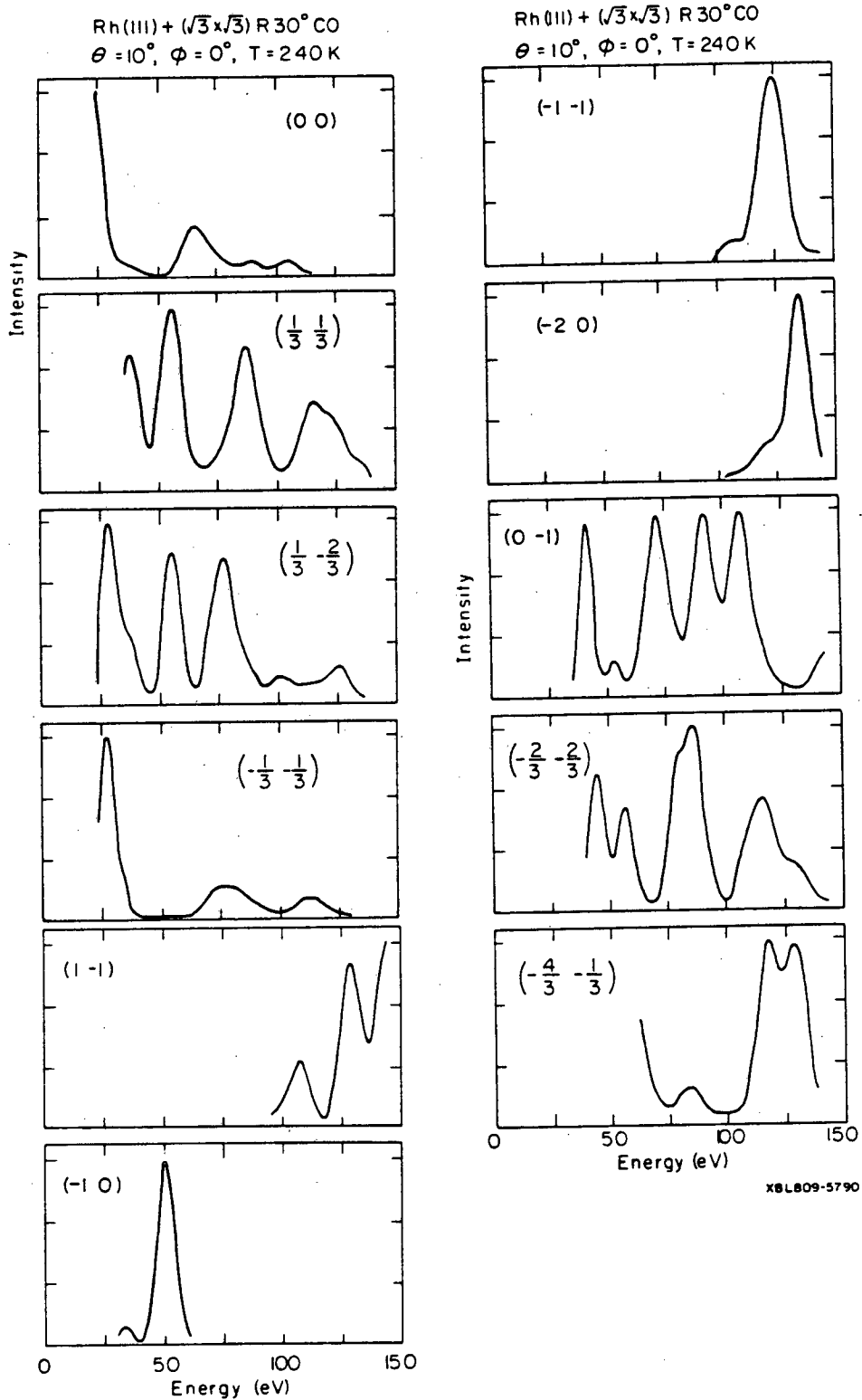
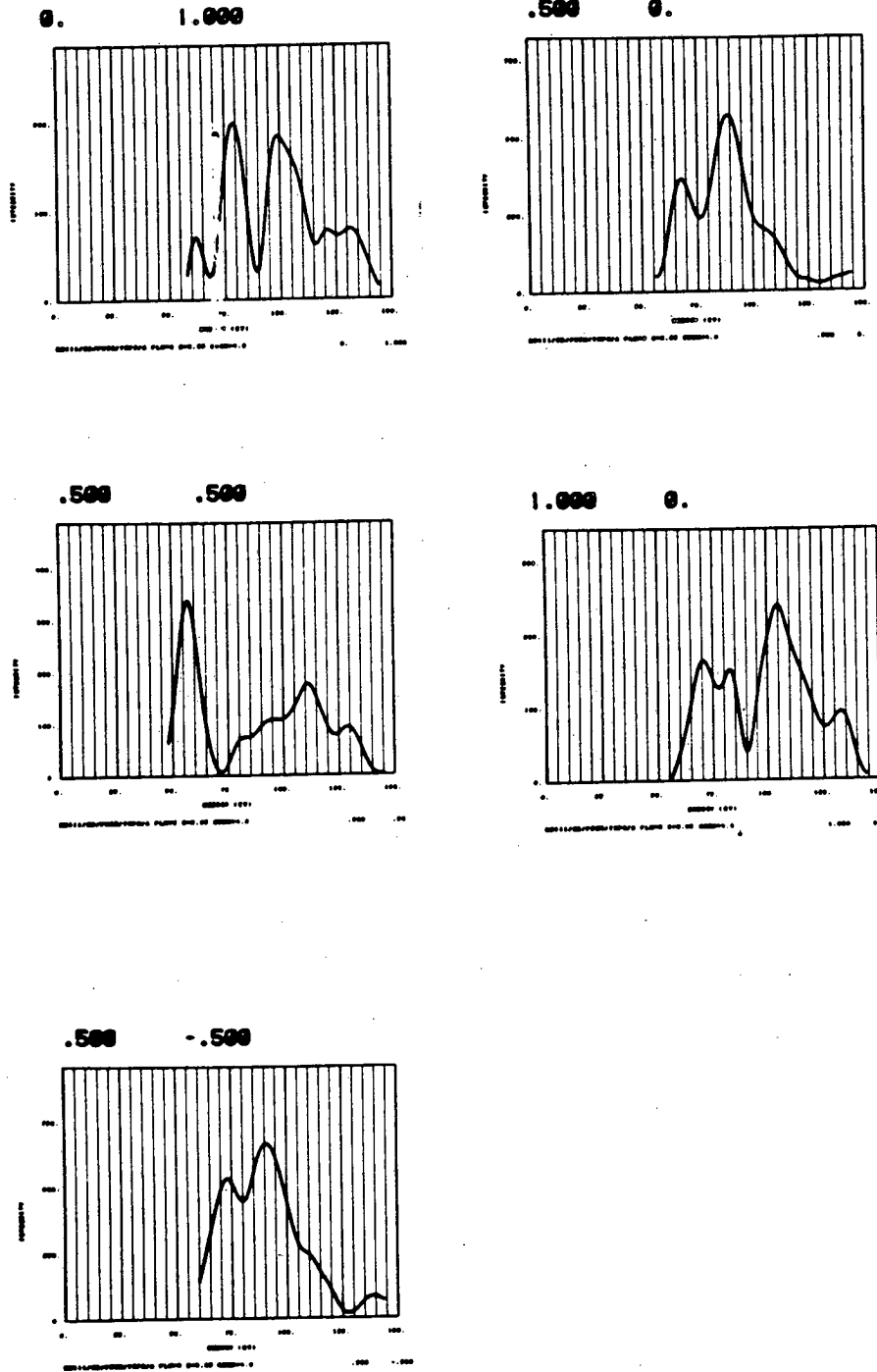


Fig. 3b

Rh(m) - (2x2) - Cu - Arun

$\Theta = 0$, $\Phi = 0$, $T = 240K$

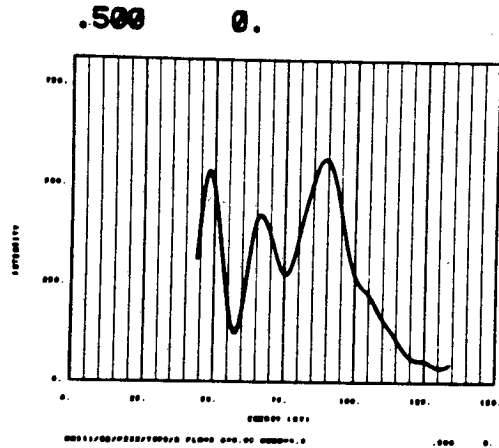
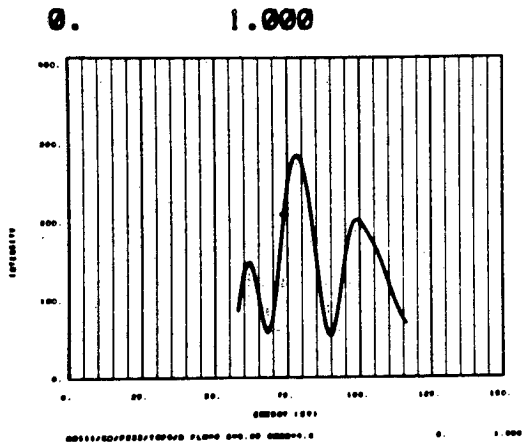
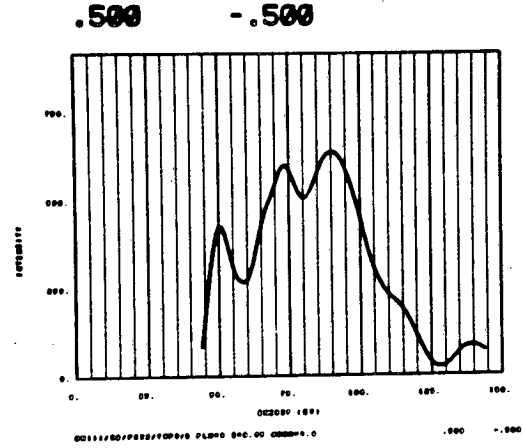
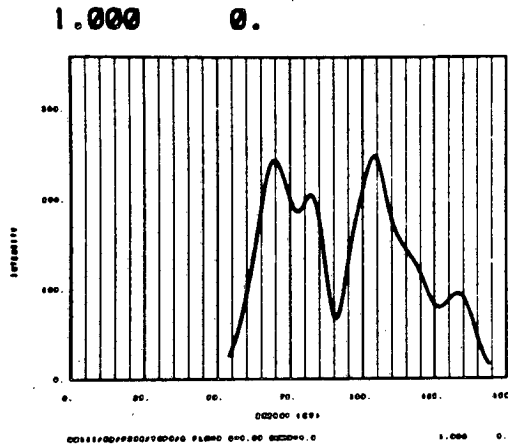


XBL 828-10992

Fig. 4a

Rh(111)-(2x2)-CO - B run

$\theta = 0$, $\phi = 0$, $T = 240K$

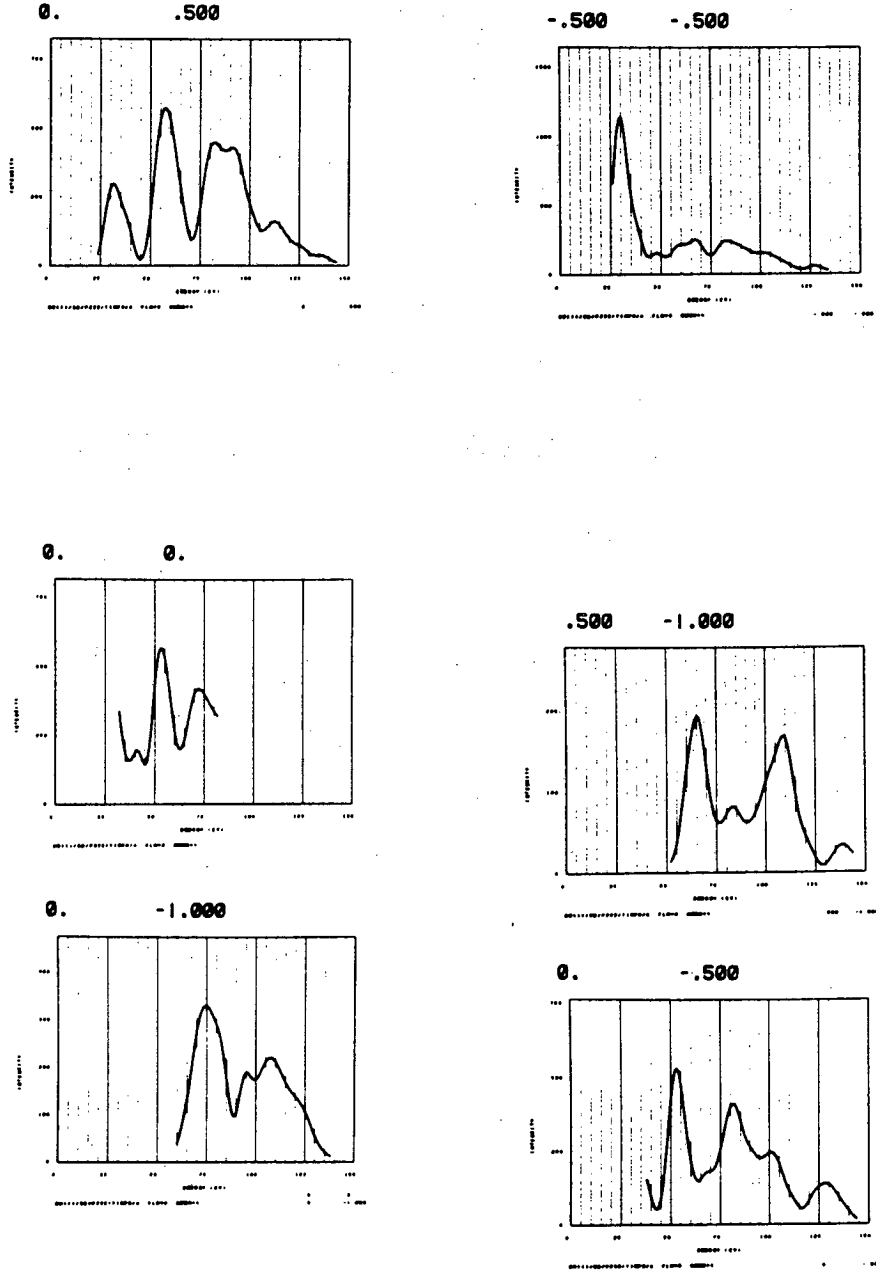


XBL 828-10994

Fig. 4b

Rh(III)-(2x2)-CD -A run

$\theta = 10, \phi = 0, T = 240K$

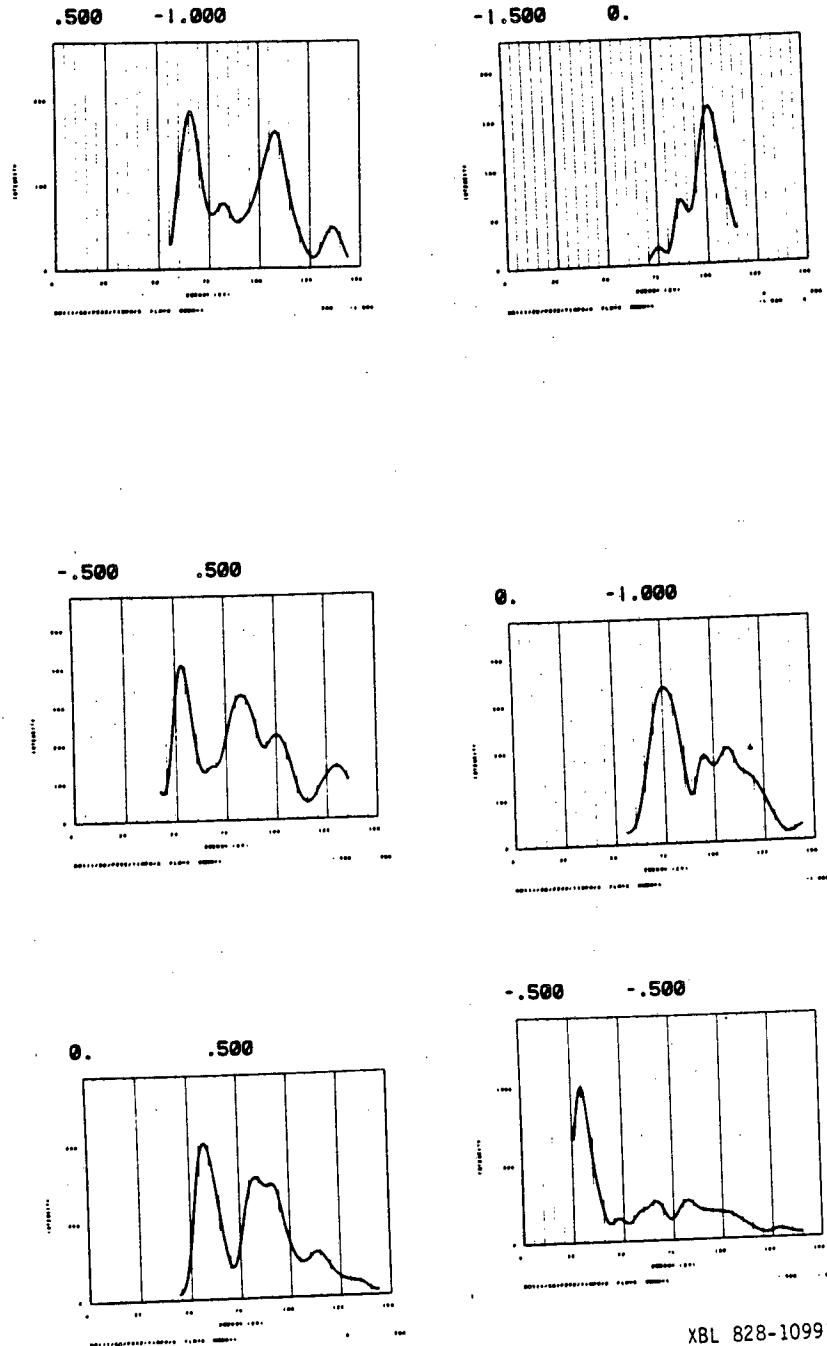


XBL 828-10993

Fig. 4c

Rh(m) - (2x2) - Co - Brun

$\Theta = 10$, $\phi = 0$, $T = 240K$

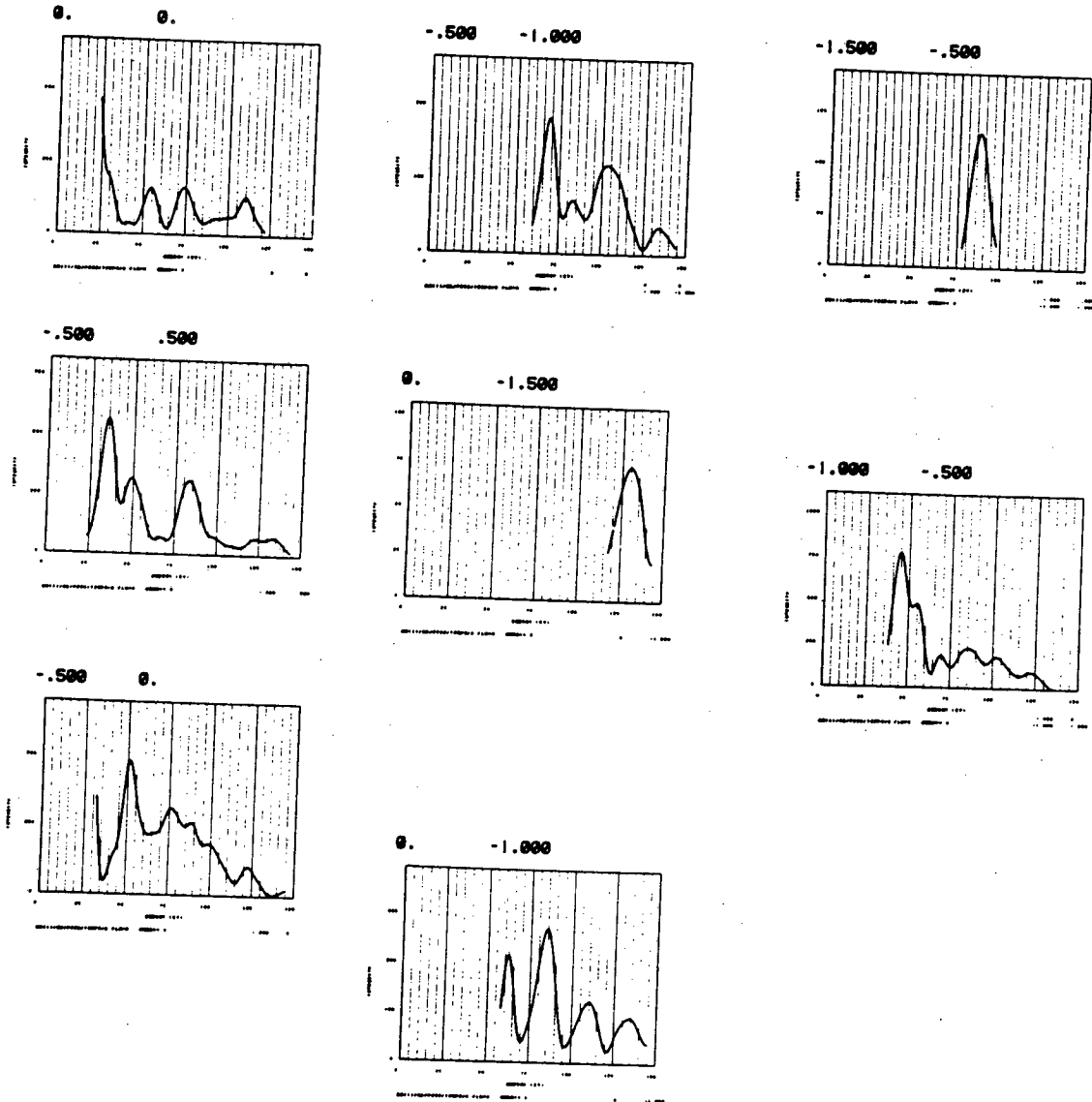


XBL 828-10991

Fig. 4d

Rh(III)-(2x2)-CO-Brun

$\Theta = 20$, $\Phi = 0$, $T = 240K$

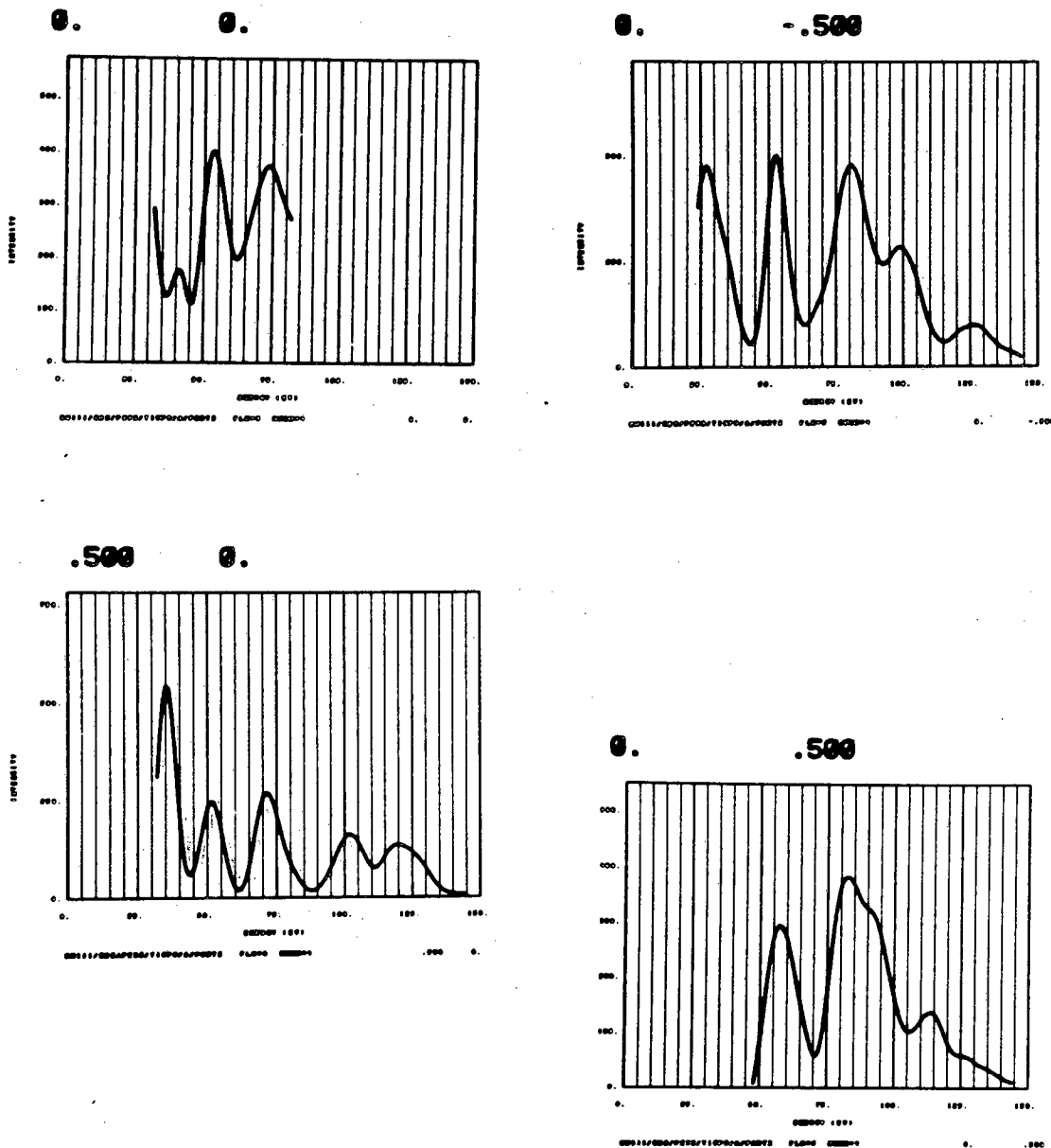


XBL 828-10981

Fig. 4f

Rh(111)-(2x2)-CO₂ - A run

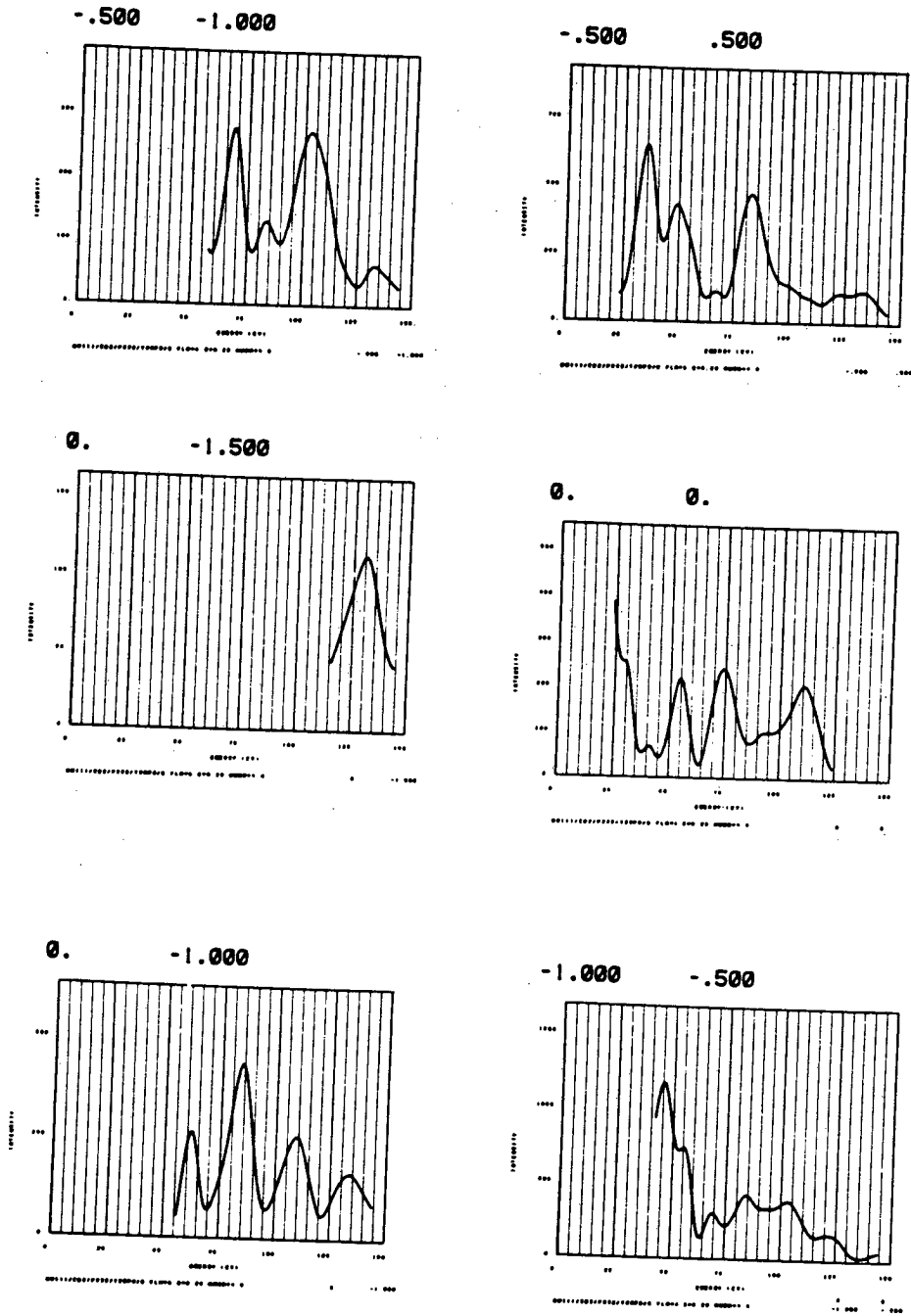
$\Theta = 10$, $\Phi = 0$, $T = 240K$



XBL 828-10995

Fig. 5a

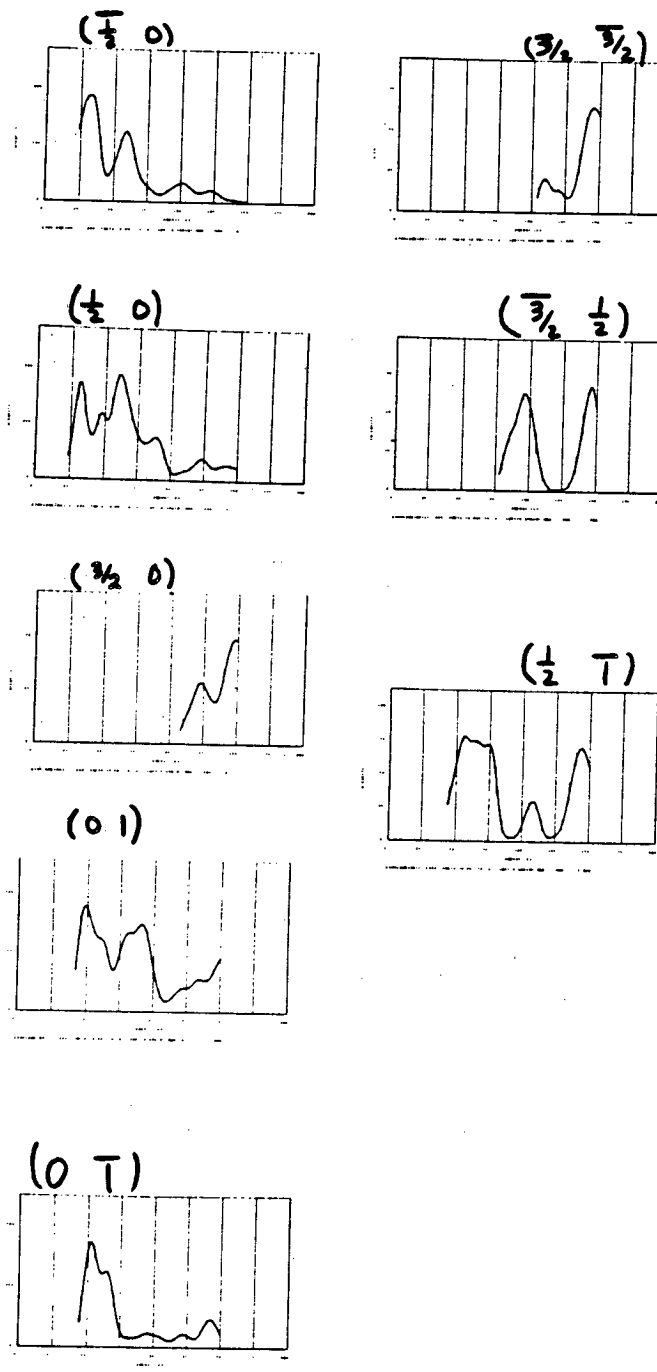
Rh(III)-(2x7) - CO₂ - B run
 $\Theta = 20, Q = 0, T = 240K$



XBL 828-10990

Fig. 5b

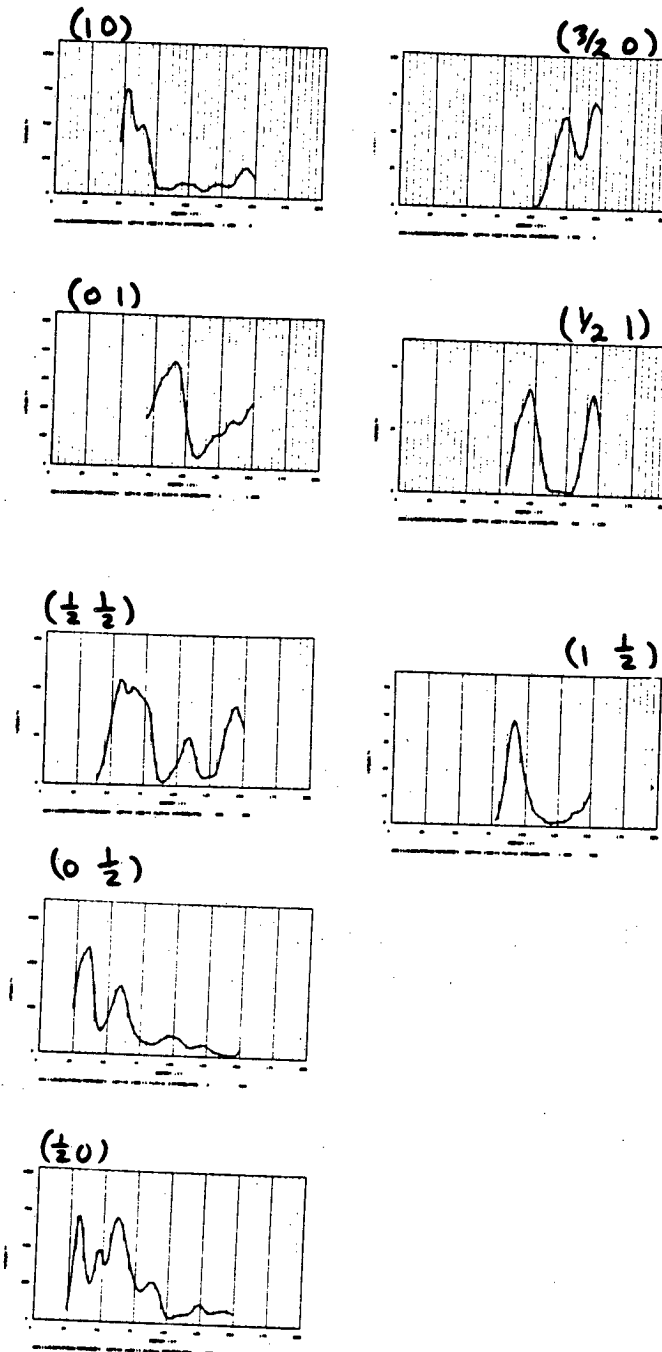
Rh(m)-(2x2)-C₂H₂-A run
 $\theta = 0$, $\phi = 0$, $T = 240K$



XBL 828-10975

Fig. 6a

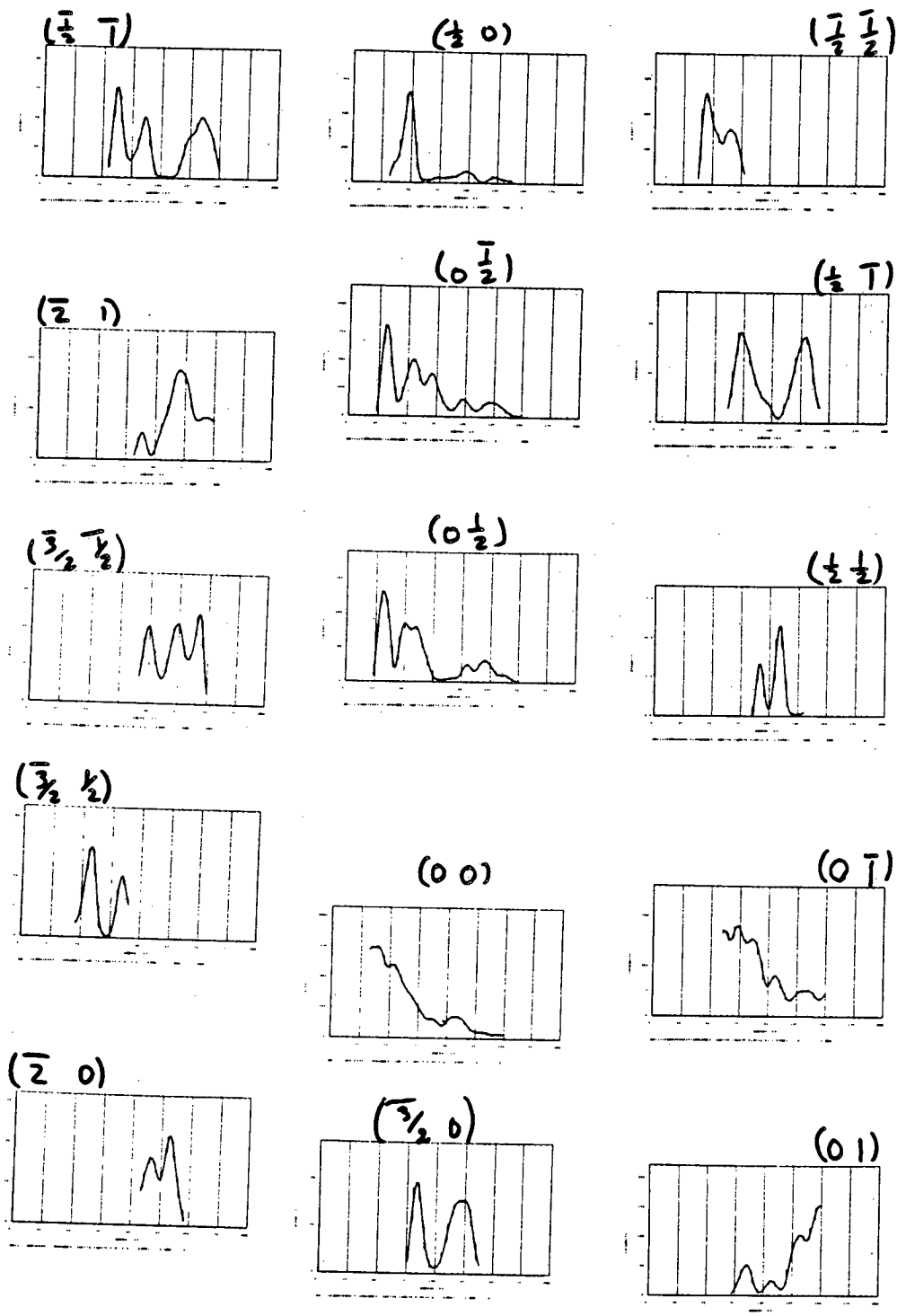
Rh(111)-(2x2)-C₂H₂-Brm
 $\theta=0$, $\phi=0$, $T=240K$



XBL 828-10984

Fig. 6b

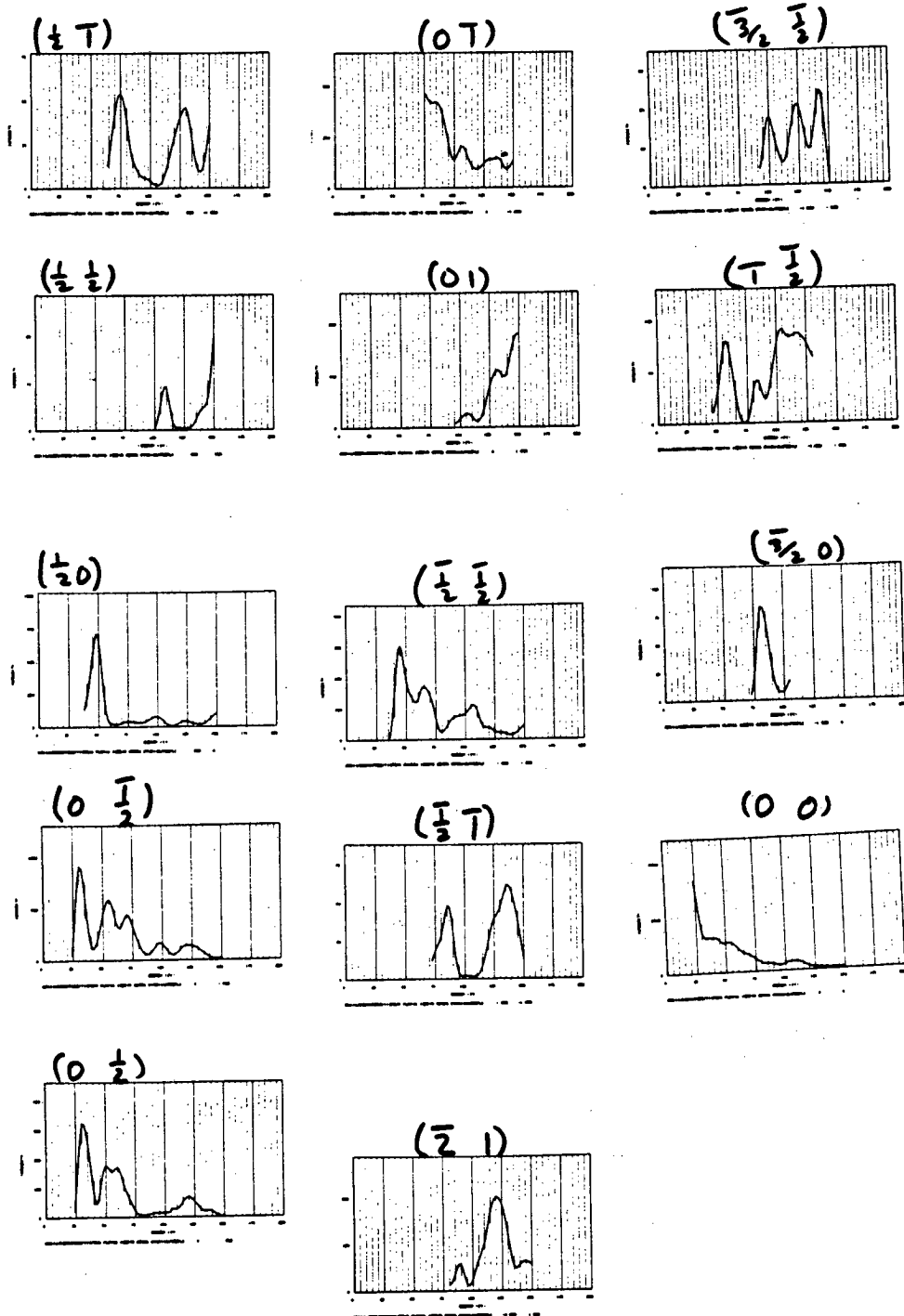
Rb(10)-(222) - C₂H₂ - 8 run
θ = 11, φ = 0, T = 240 K



XBL 828-10959

Fig. 6c

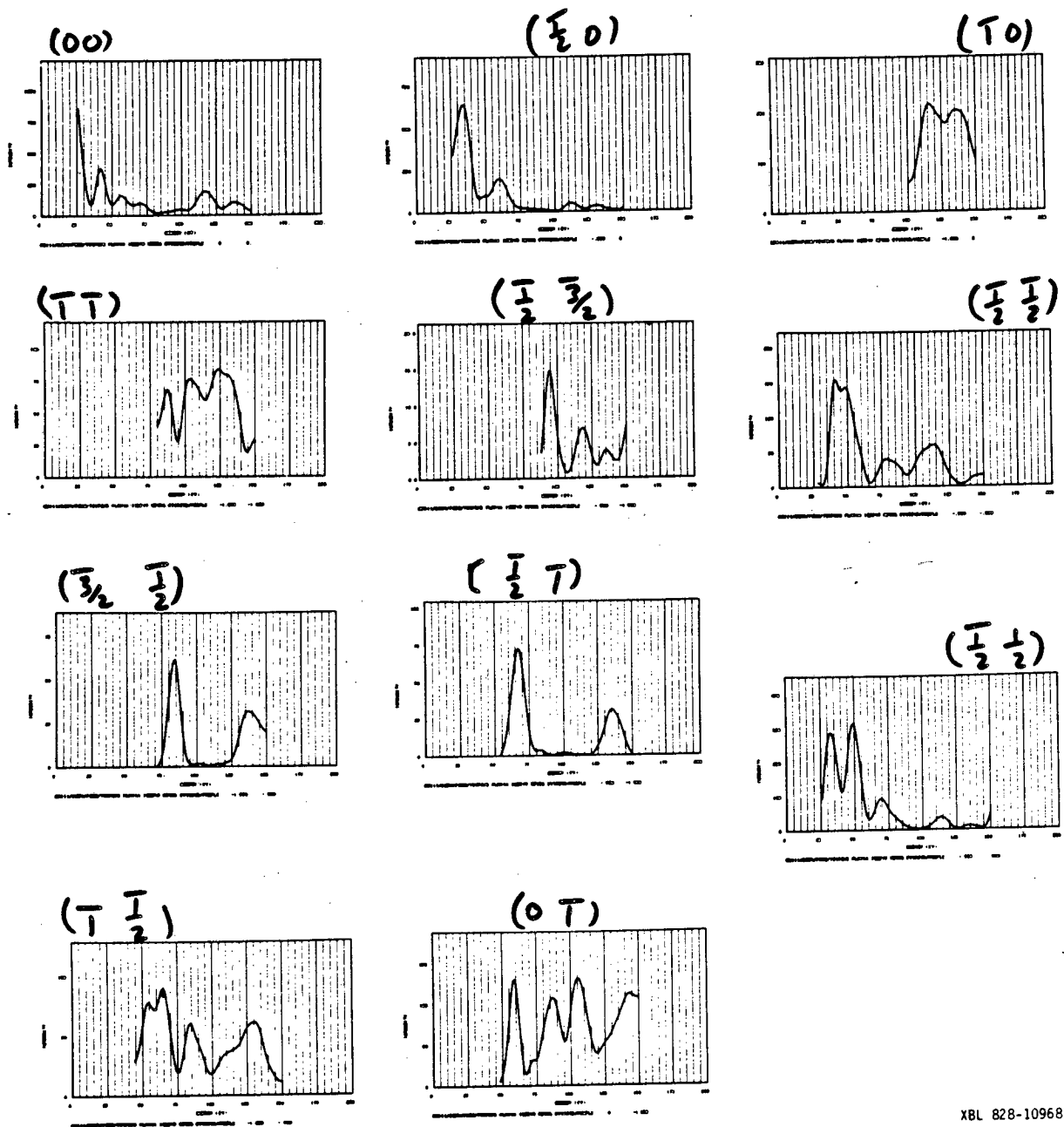
Rb(III) - (222)- C_2H_2 - Ar run
 $D=11$, $\phi=0$, $T=246K$



XBL 828-10960

Fig. 6d

Rh(III)-(b2x2)-C₂H₂ - B run
E=21, $\Phi=0$, T=240K

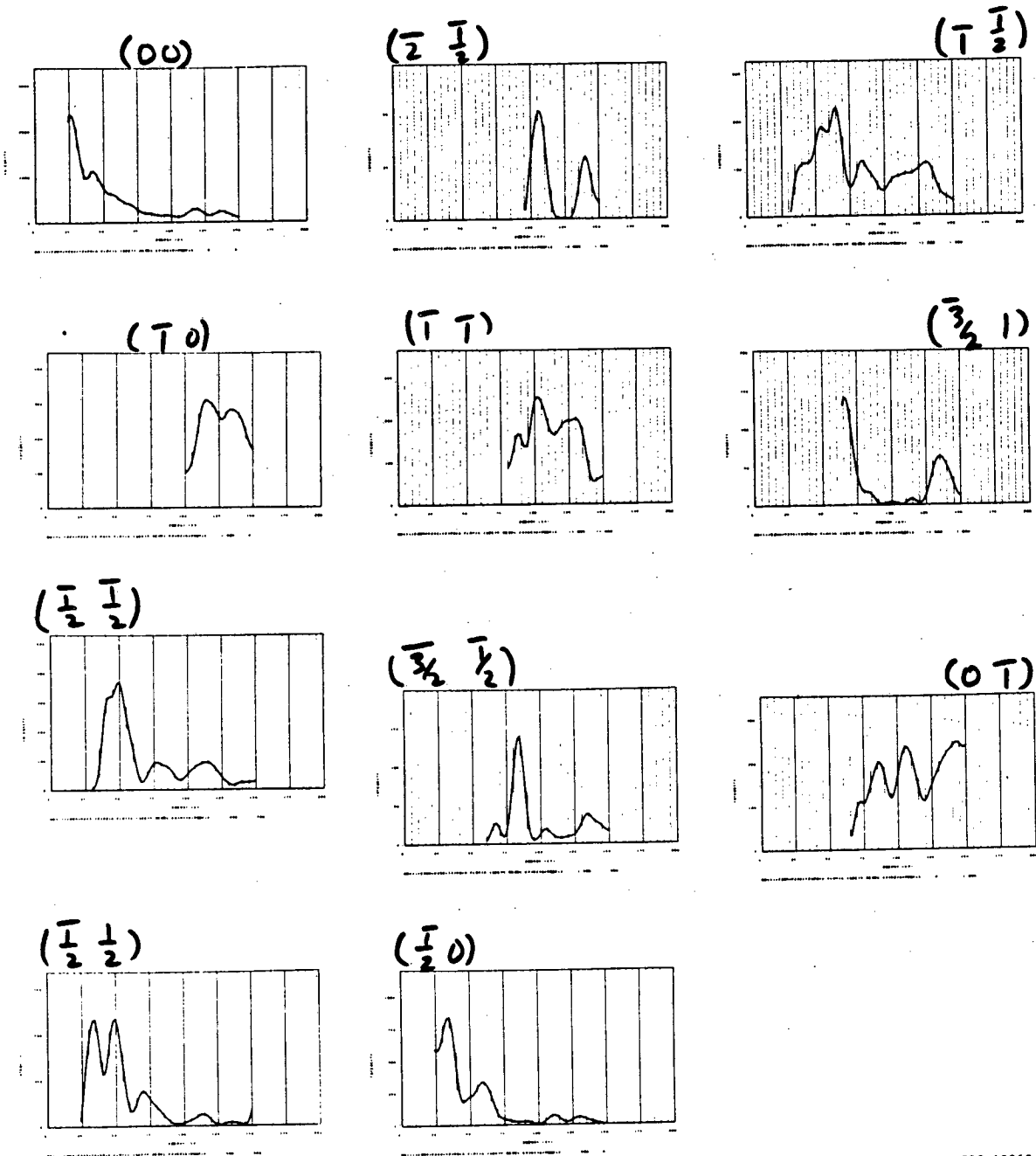


XBL 828-10968

Fig. 6e

Rh(III) (2x2) - C₂H₂ - Arun

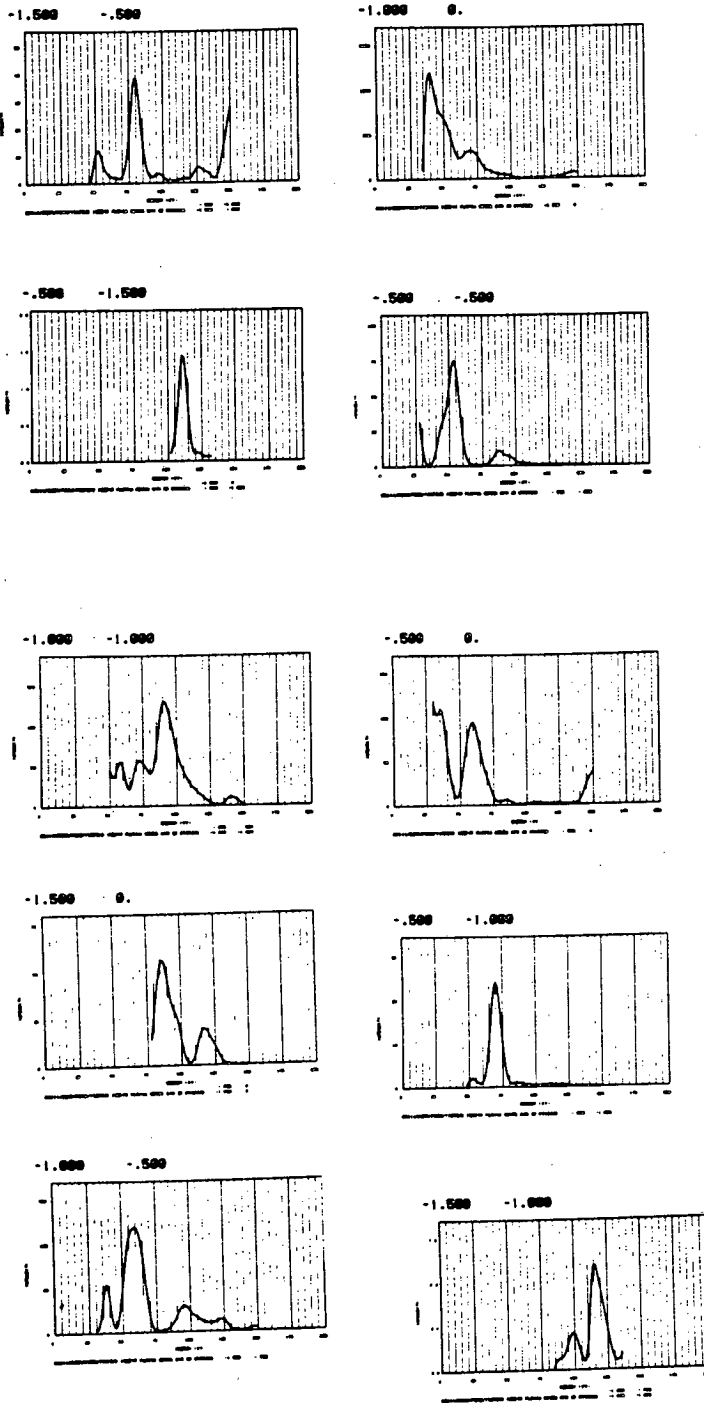
$\theta = 21$, $\phi = 0$, $T = 270K$



XBL 828-10969

Fig. 6f

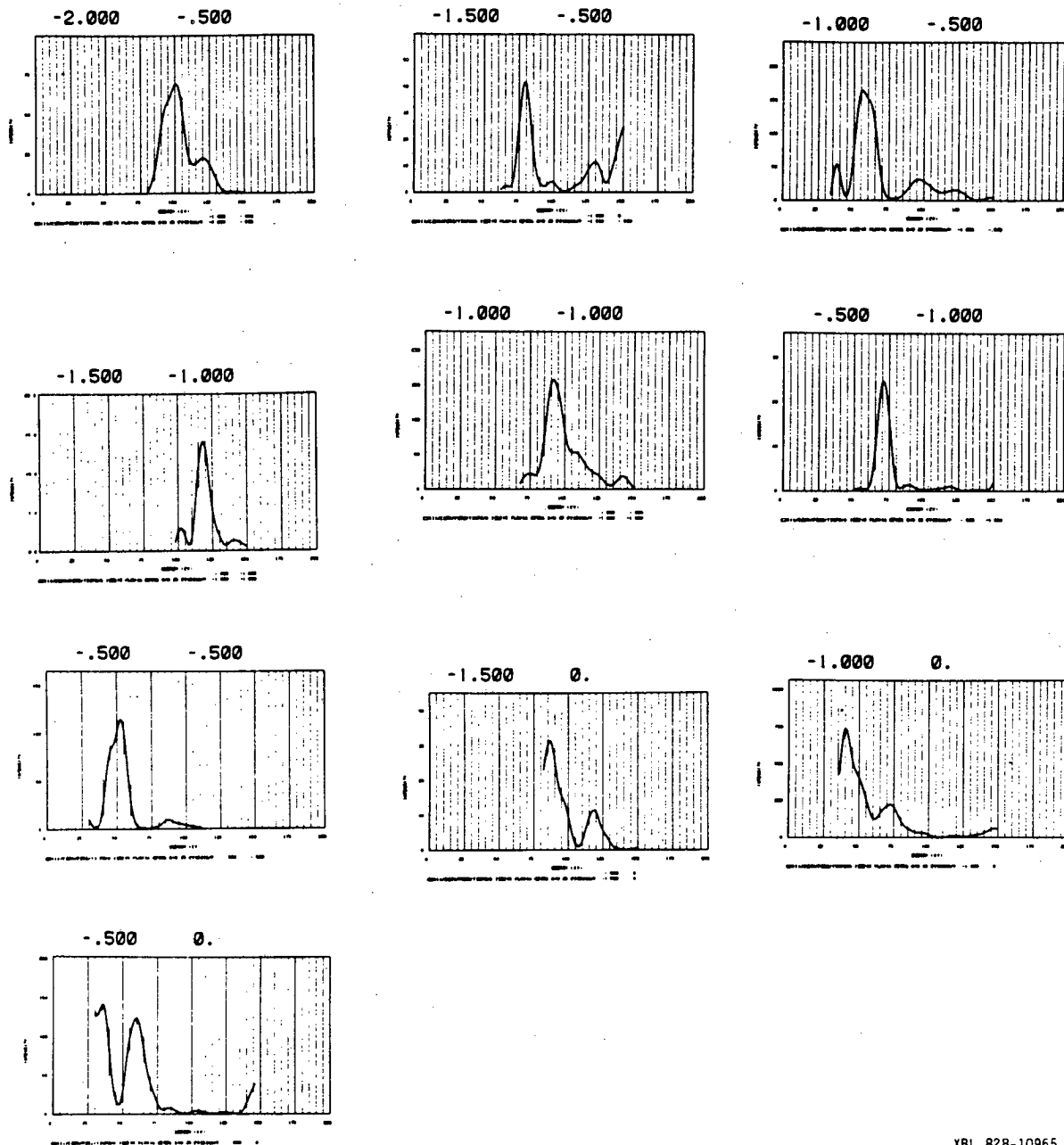
RH(11)-(2v2) - C₂H₂ - Brun
 $\theta = 31, \phi = 0, T = 240K.$



XBL 828-10977

Fig. 6g

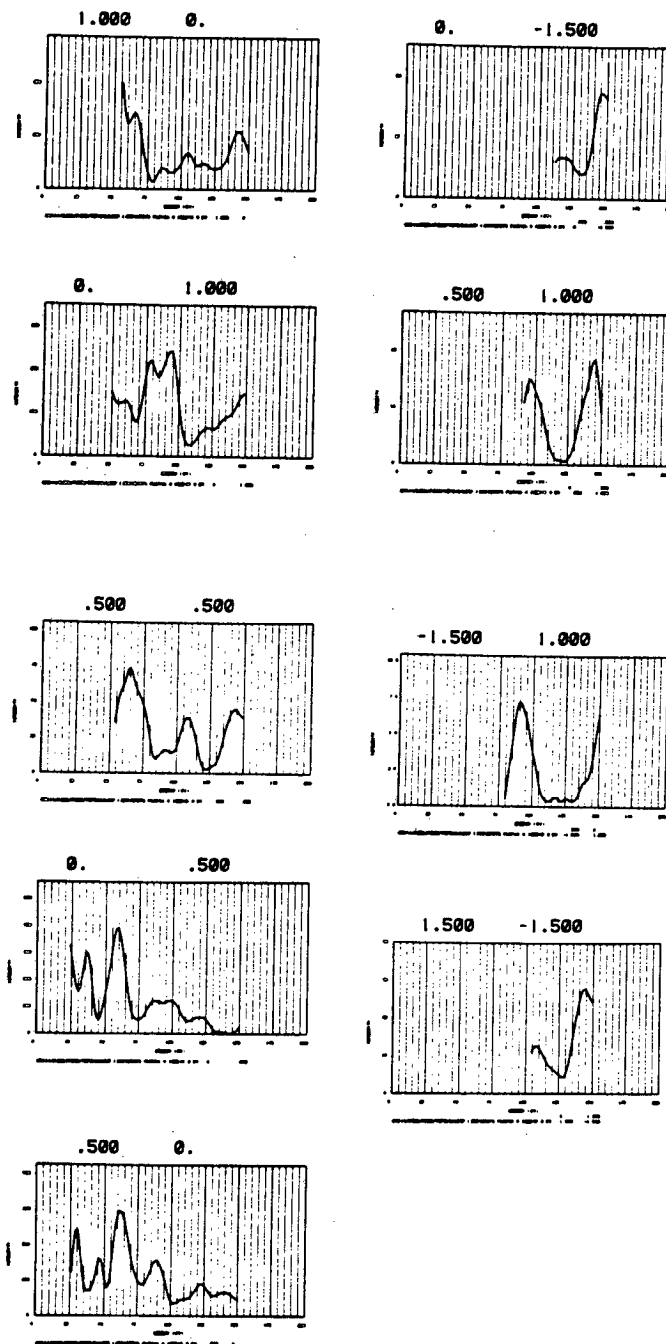
Rh(III) - (2x2) - C₂H₂ - A run
 $\Theta = 31$, $\Phi = 0$, $T = 240K$



XBL 828-10965

Fig. 6h

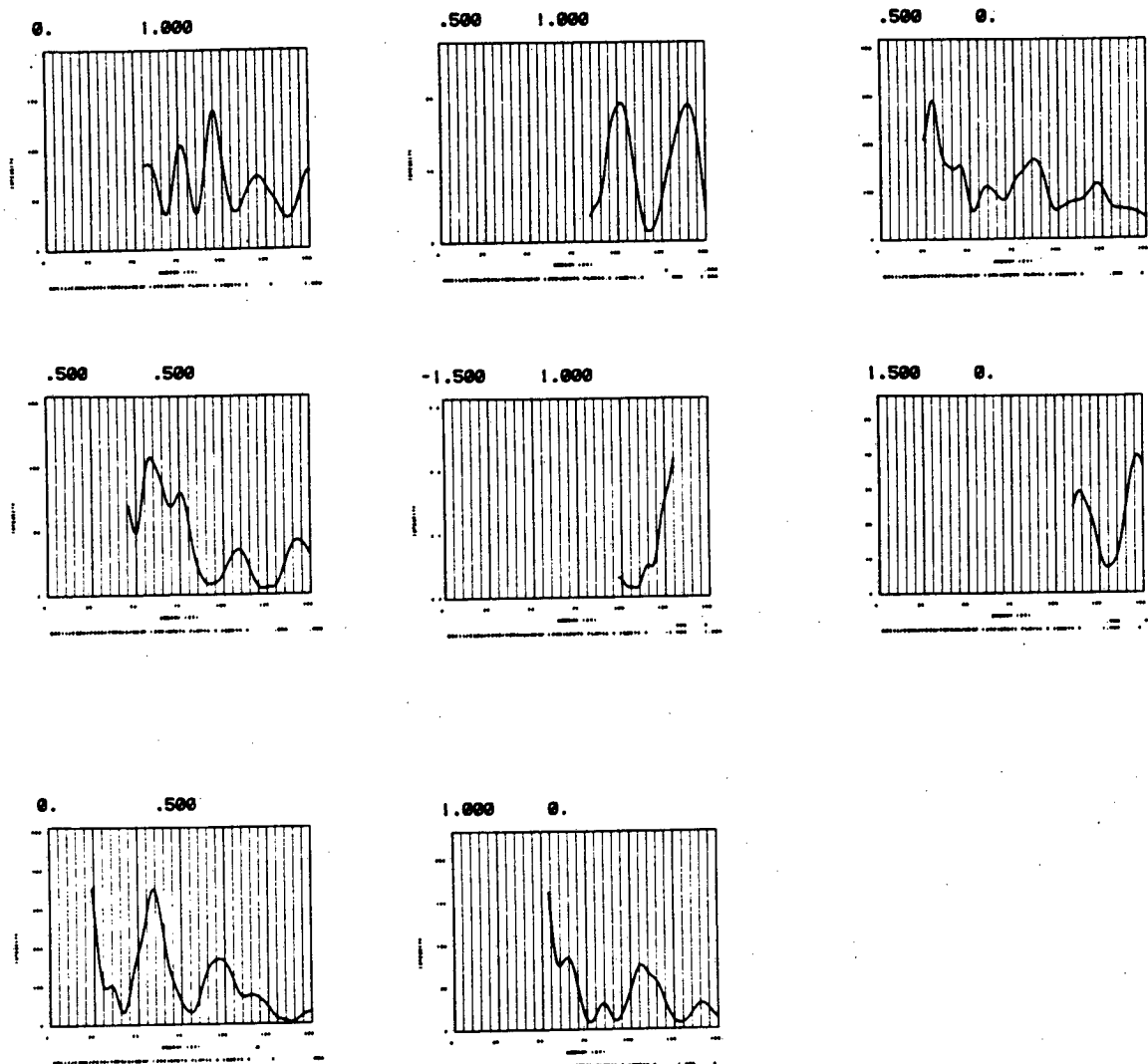
$Rh(111) - C_3H_5$ ($T=240K$)
 $\Theta=0, \Phi=0, \text{low exposure}$



xBL 828-10976

Fig. 7

Rh(111) (2.5x2.5)/R30° - C₃H₅ - A run
 $\theta = 0, \phi = 0, T = 240K$

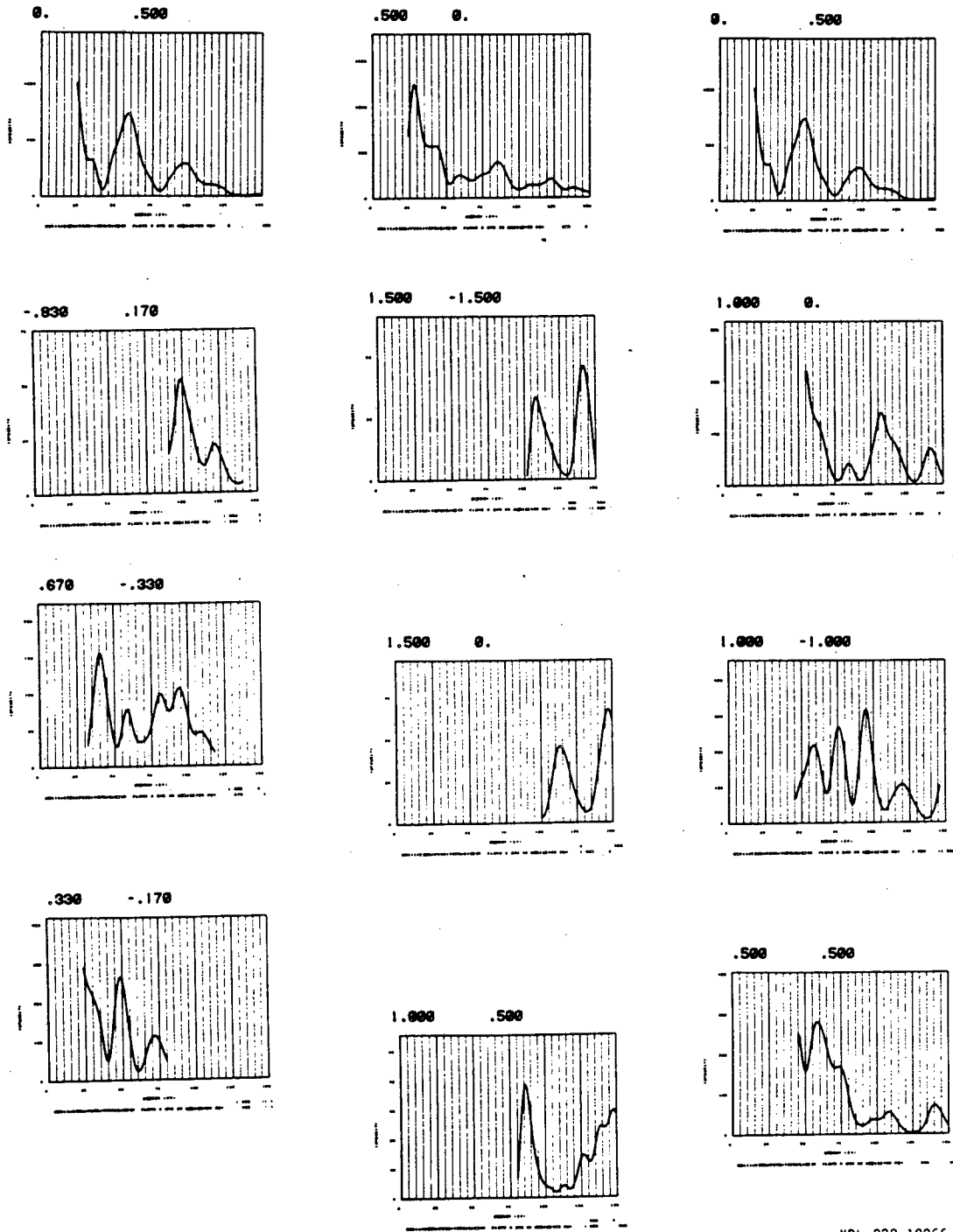


XBL 828-10980

Fig. 8a

$R_{H(11)} - (2\sqrt{3} \times 2\sqrt{3})2\pi^\circ - C_3H_5 - Br_{in}$

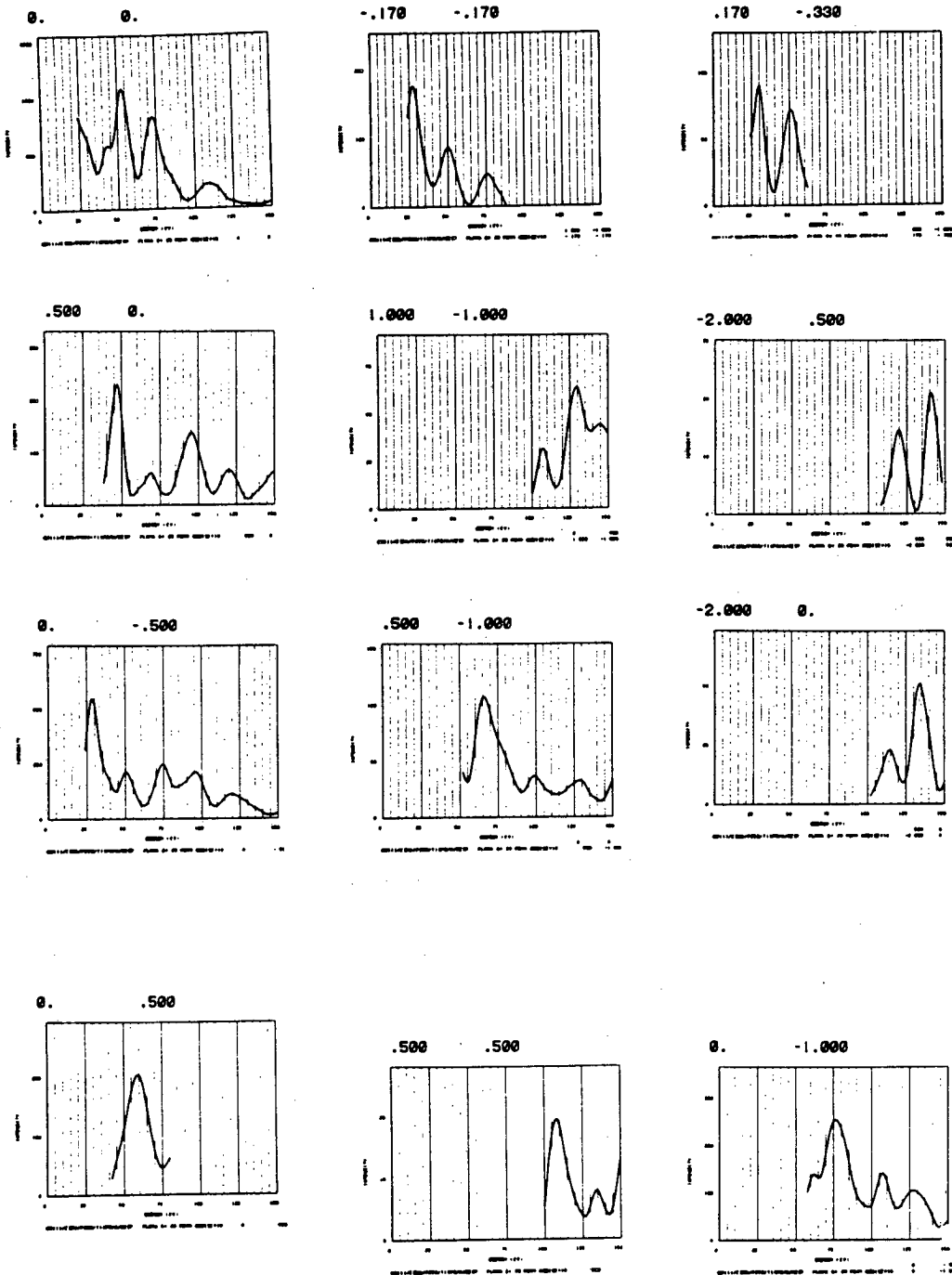
$\Theta = 0, \Phi = 0, T = 240K$



XBL 828-10966

Fig. 8b

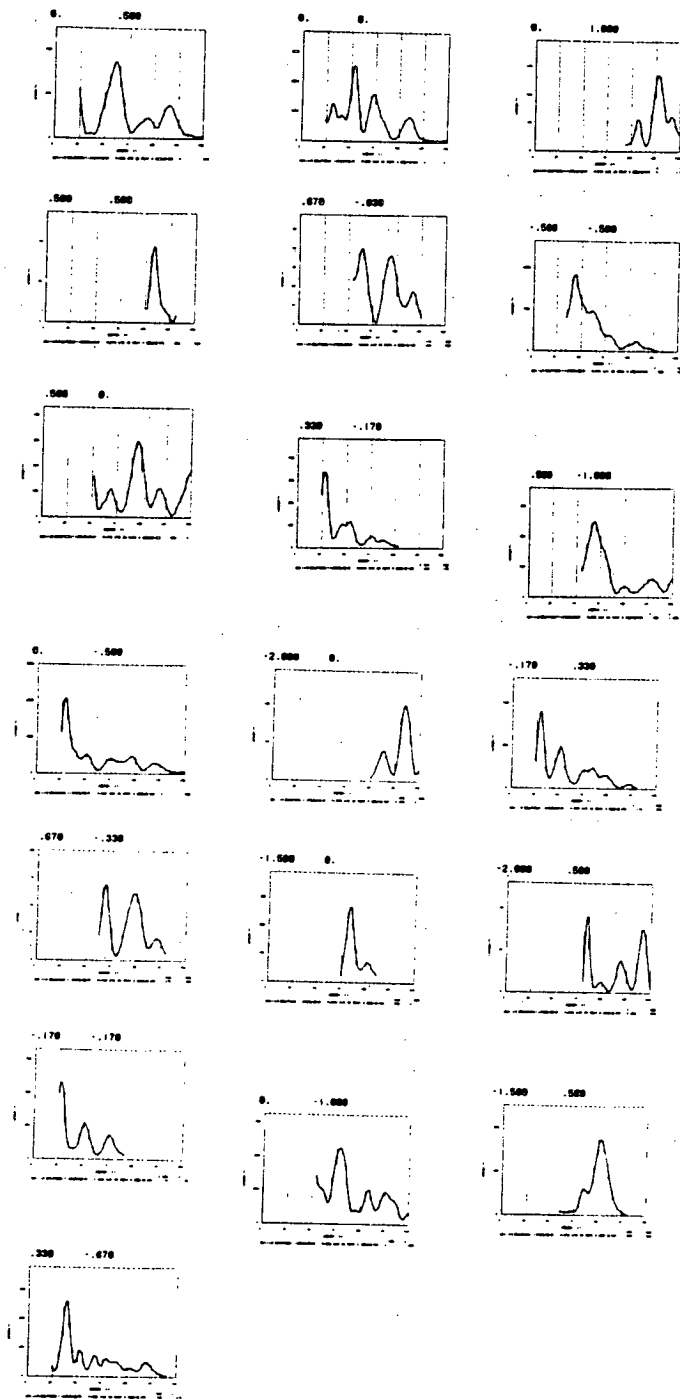
Rh(11)-(25225)R30-C₃H₅-A run
 $\Theta = 11, \Phi = 0, T = 240K$



XBL 828-10967

Fig. 8c

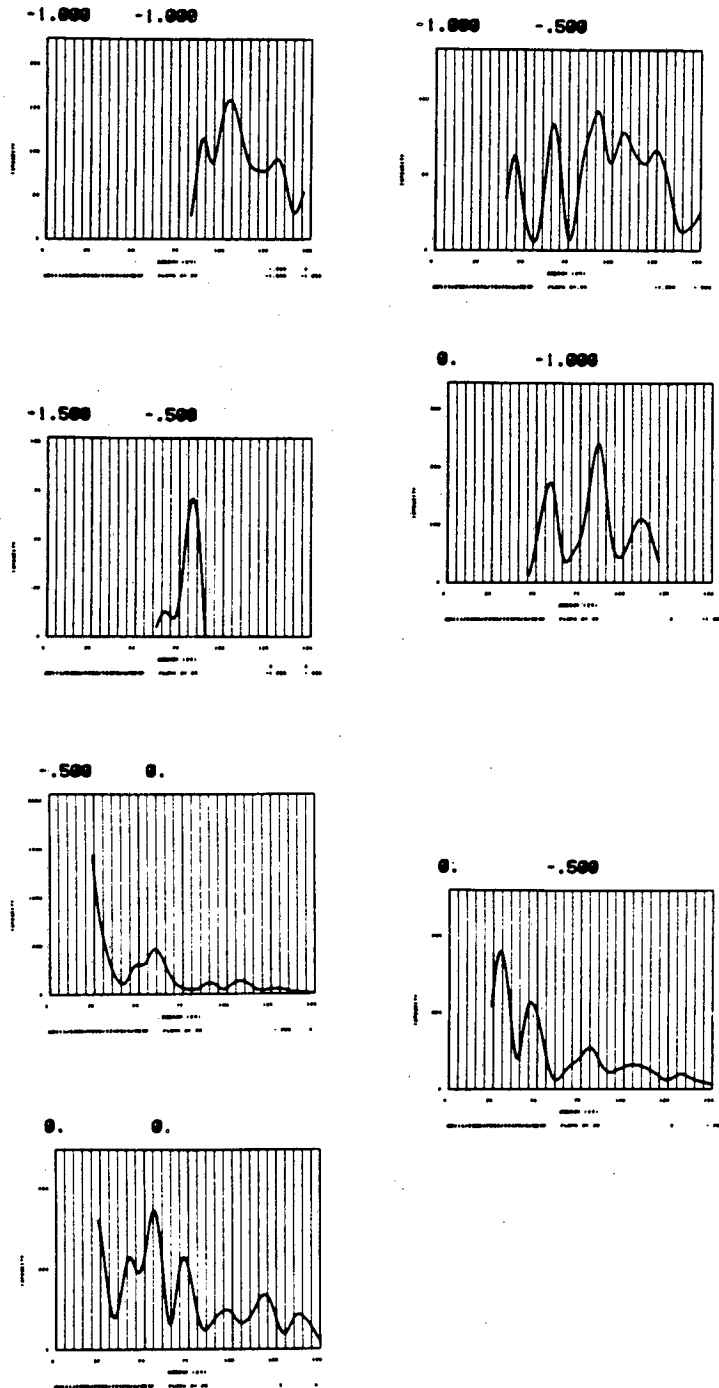
$R_{\text{H}}(\omega) = \text{Im}[\chi(\omega)] / \omega$ $\text{C}_2\text{H}_2 - \text{B}_2$
 $\theta = 11, \phi = 0, T = 240\text{K}$



XBL 828-10955

Fig. 8d

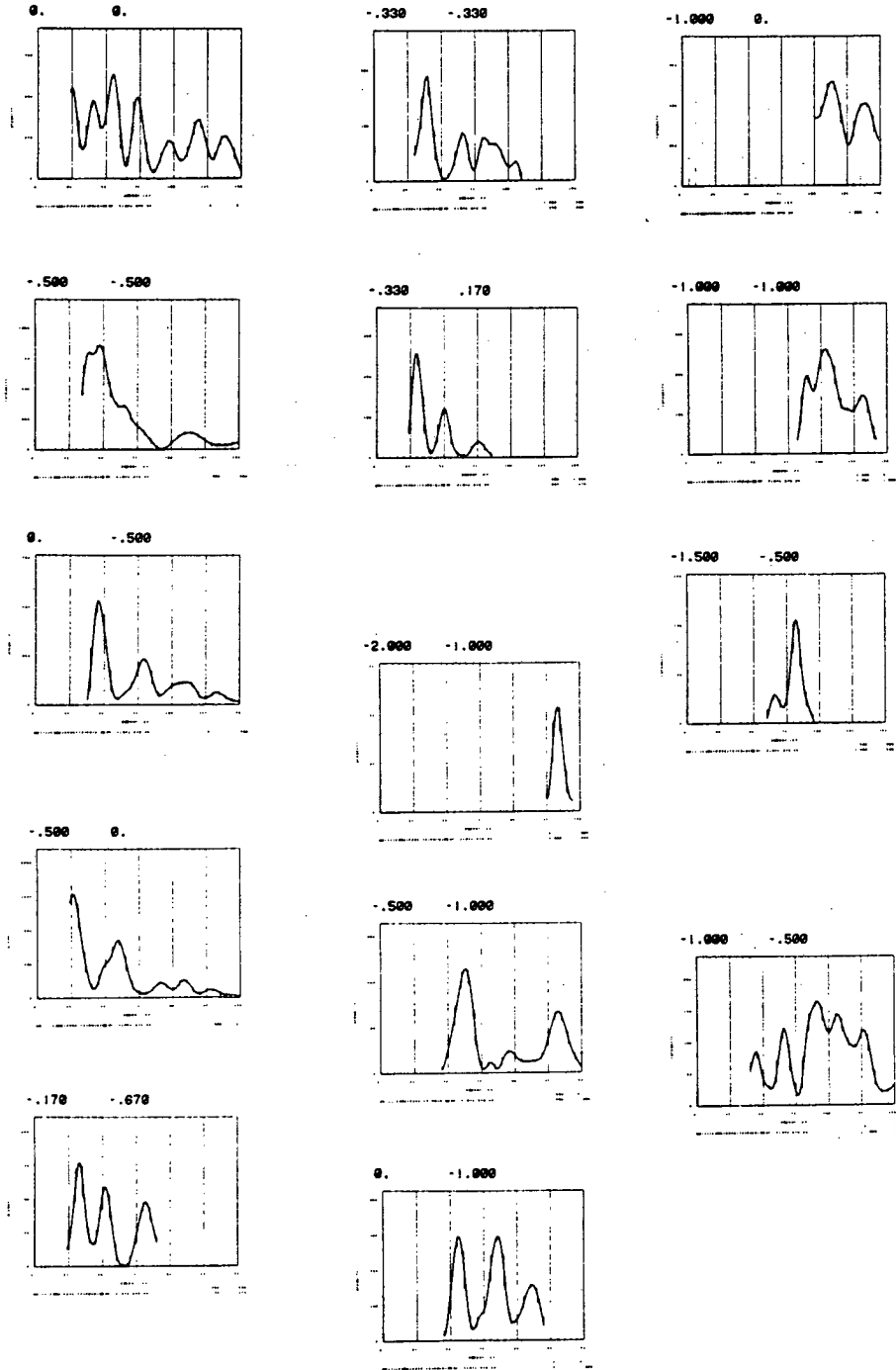
$Rh(11) - (2\sqrt{3} \times 2\sqrt{3})R30 - C_3H_5 - Ar_m$
 $\theta = 21, \psi = 0, T = 240K$



XBL 828-10978

Fig. 8e

$Rh(11) - (2\sqrt{3} \times 2\sqrt{3})R30^\circ - C_3H_5 - Br_{11}$
 $\theta = 21, \phi = 0, T = 240K$

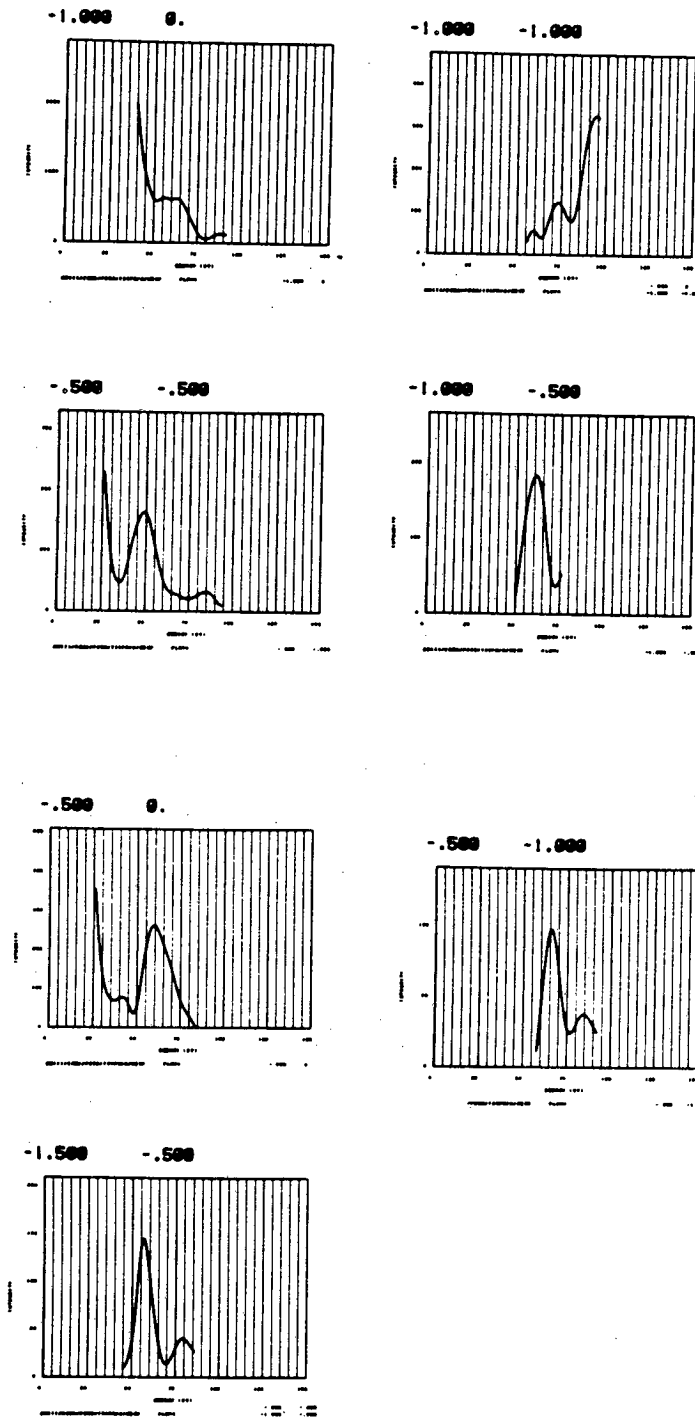


XBL 828-10961

Fig. 8f

$Rh(m) = (2.5 \times 2.5) / R_{20}^{\circ} - C_3H_5 - Arun$

$\theta = 31, \phi = 0, T = 240K$

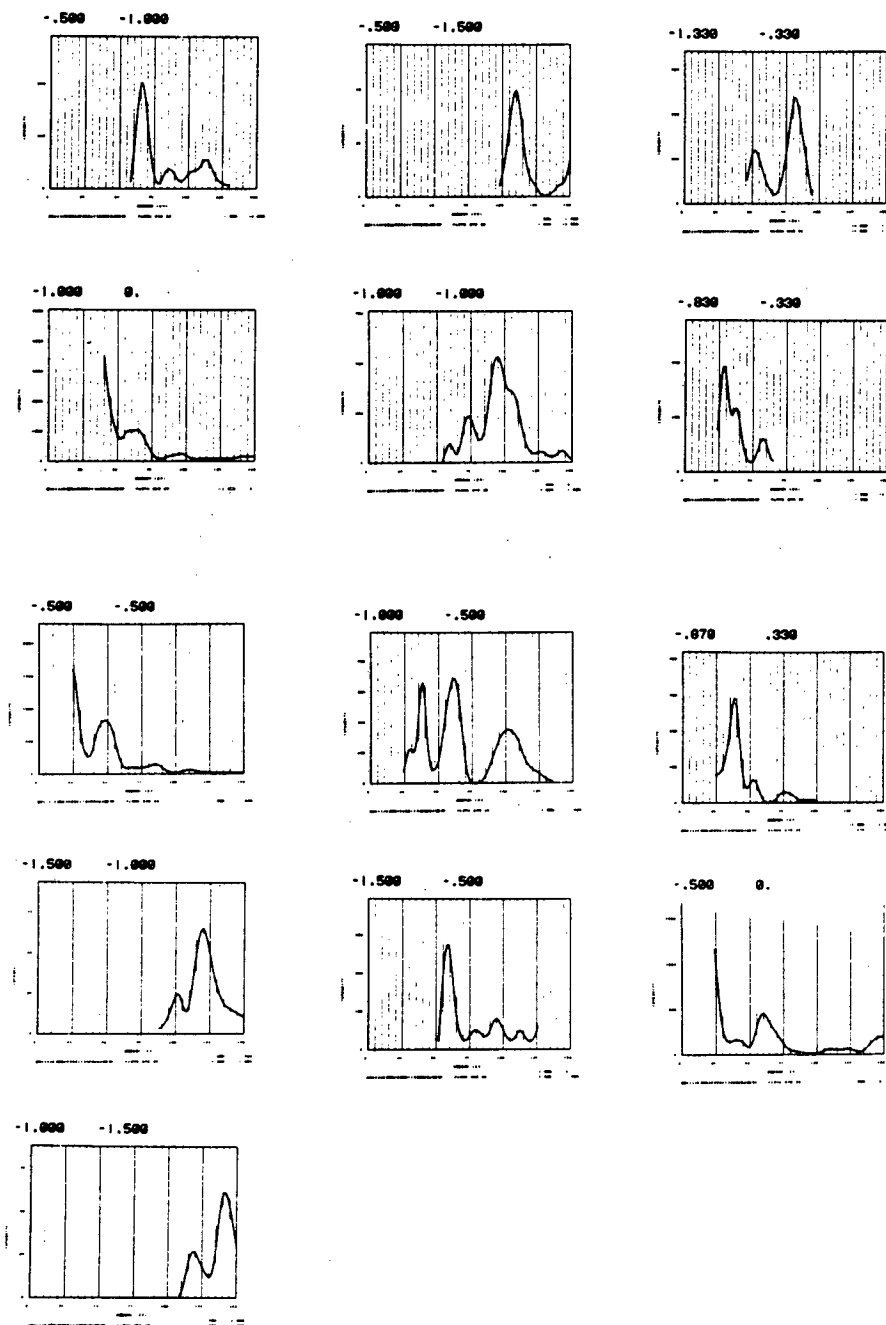


XBL 828-10979

Fig. 8g

Rh(m)-(2/3x2/5)R30°-C₂H₂-Bron

$\Theta = 31, \Phi = 0, T = 240K$

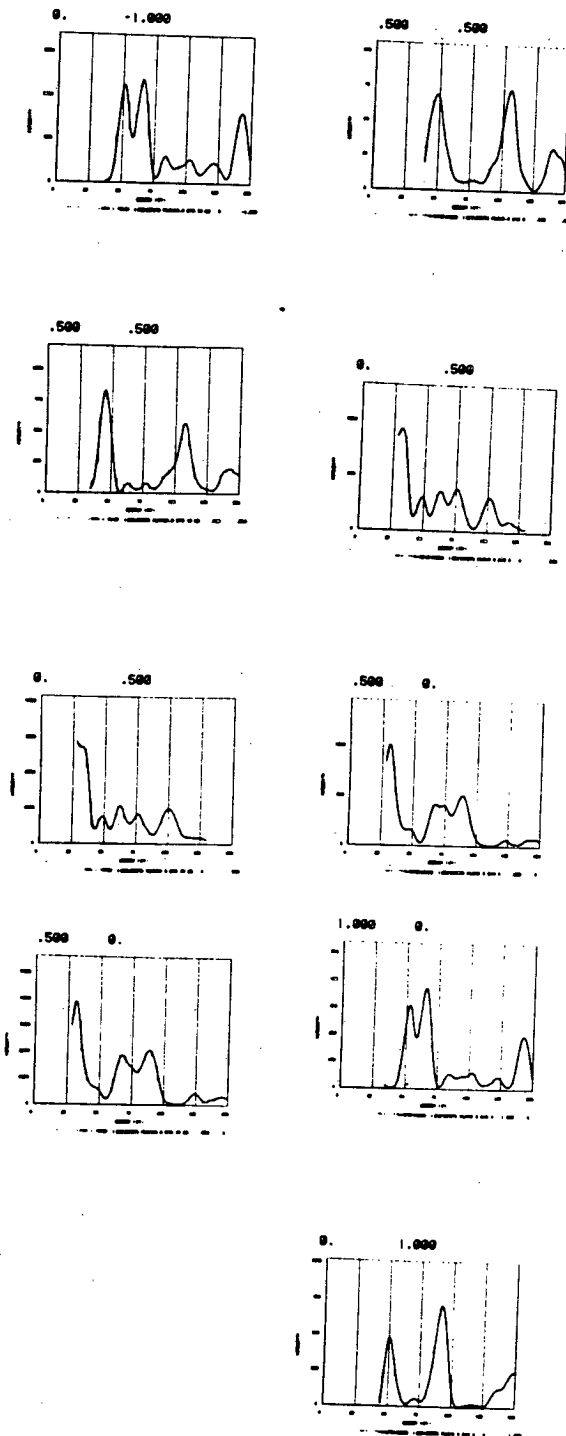


XBL 828-10962

Fig. 8h

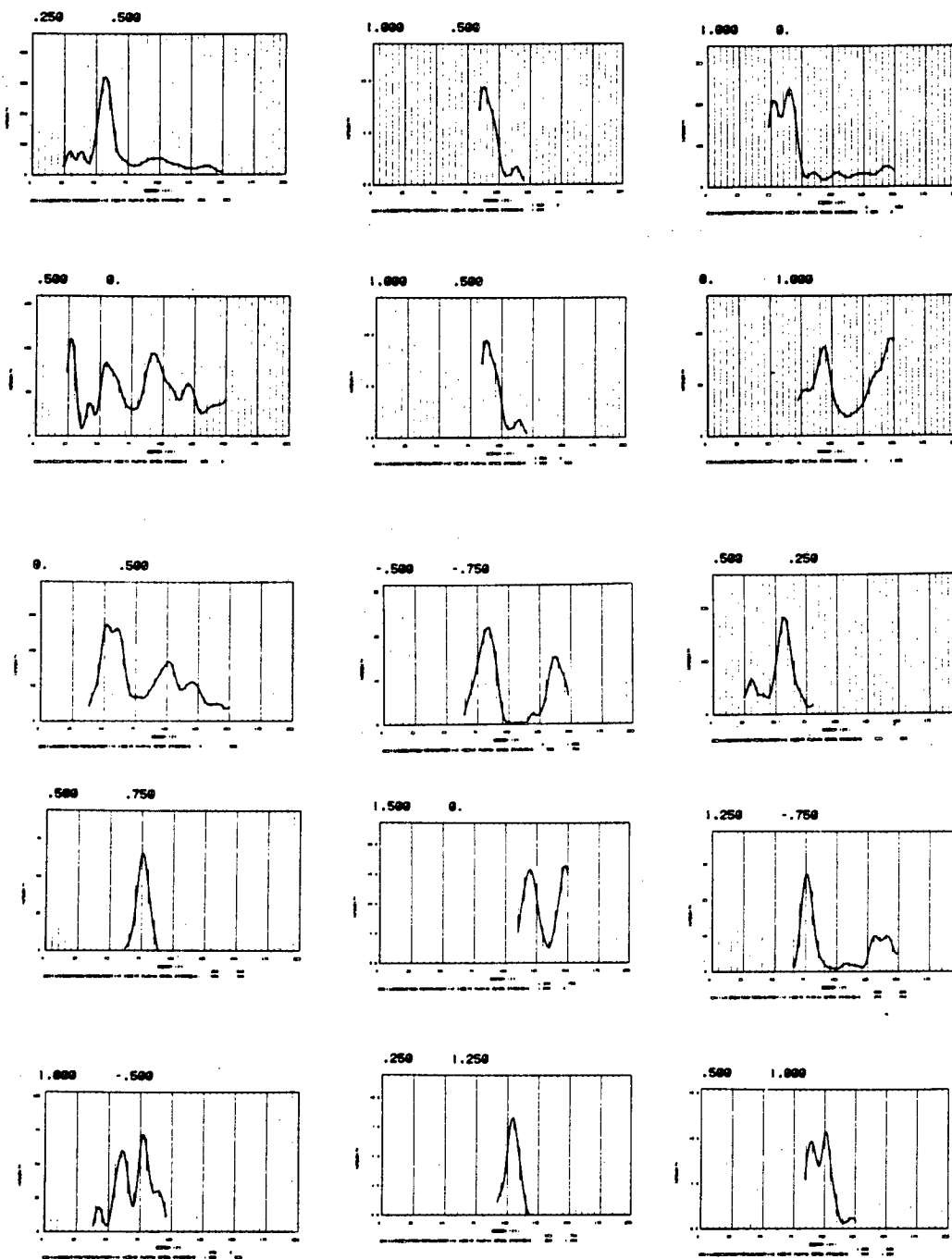
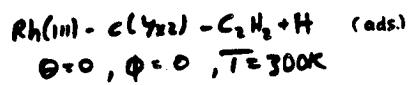
$R_h(m) - (2\sqrt{2} \lambda) B^2 - C_2 H_4 - \text{Bron}$
 $\theta = 0^\circ, T = 240K$

$R_h(m) - (2\sqrt{2} \lambda) B^2 - C_2 H_4 - \text{Arum}$
 $\theta = 0^\circ, T = 240K$



XBL 826-10985

Fig. 9

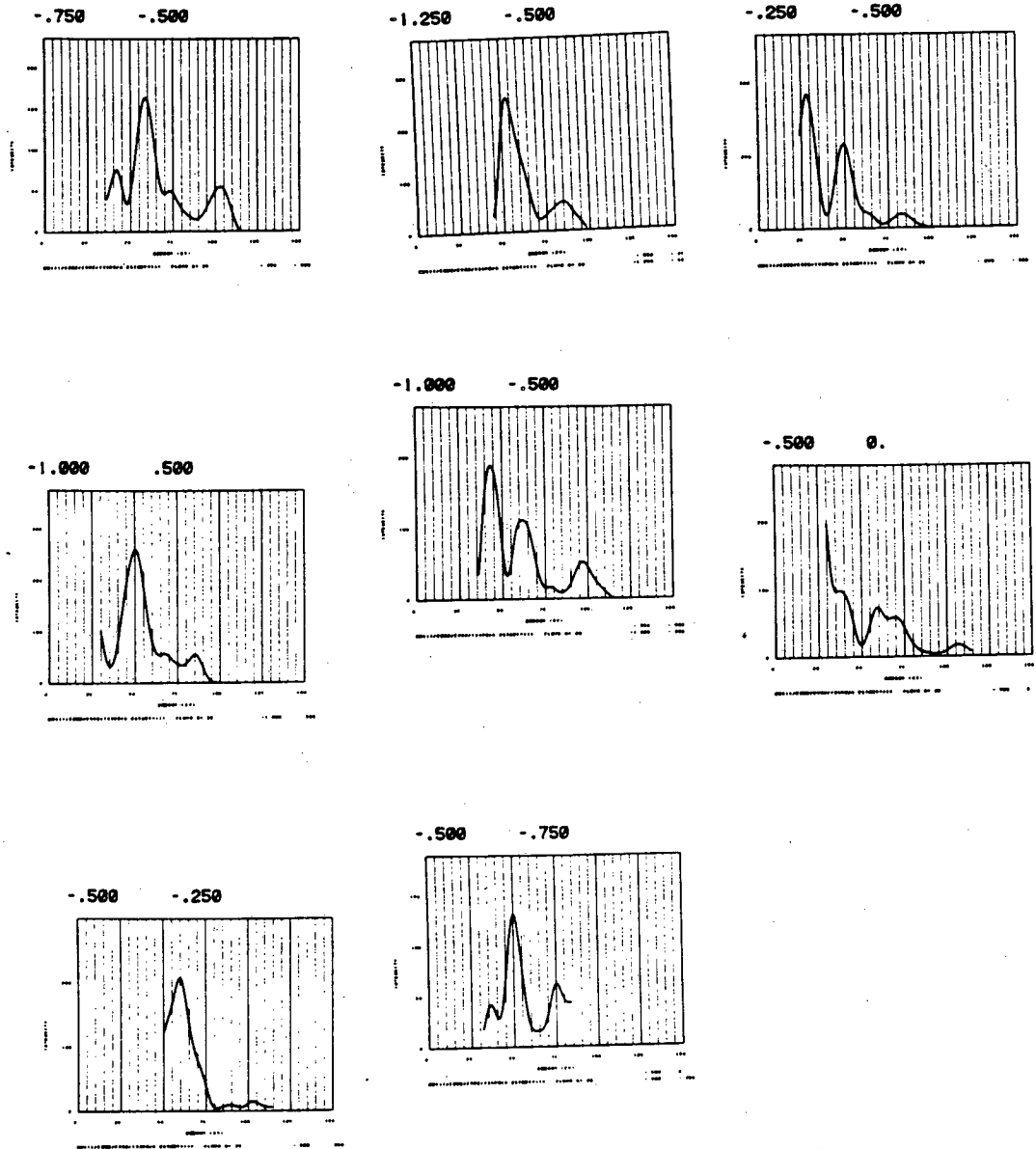


XBL 828-10963

Fig. 10a



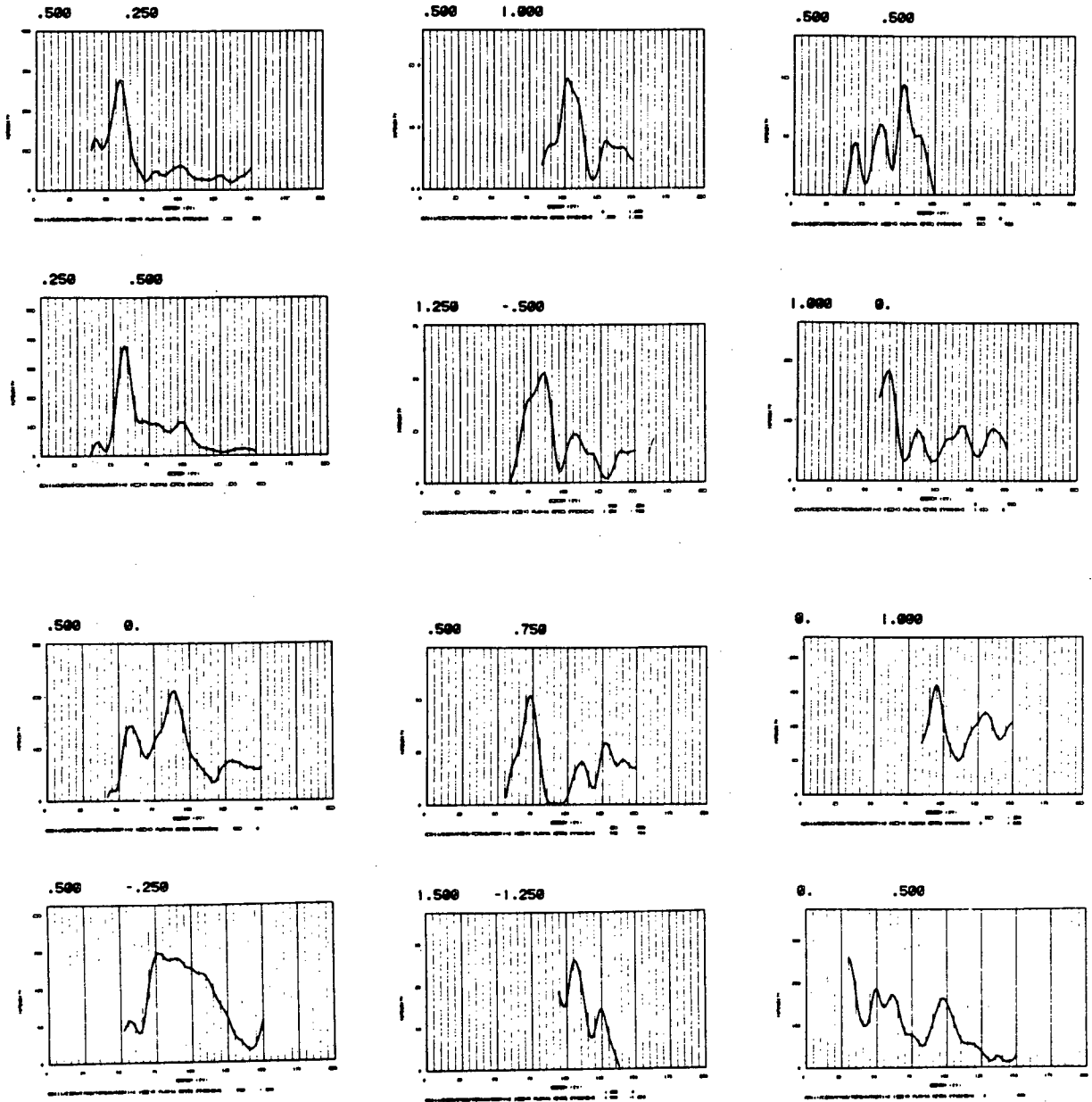
$\theta = 31, \phi = 0, T = 300K$



XBL 828-10983

Fig. 10b

Rh(111) - c(Y₂O₃) - C₂H₄ (ad 5.)
 $\theta=0, \phi=0, T=300K$

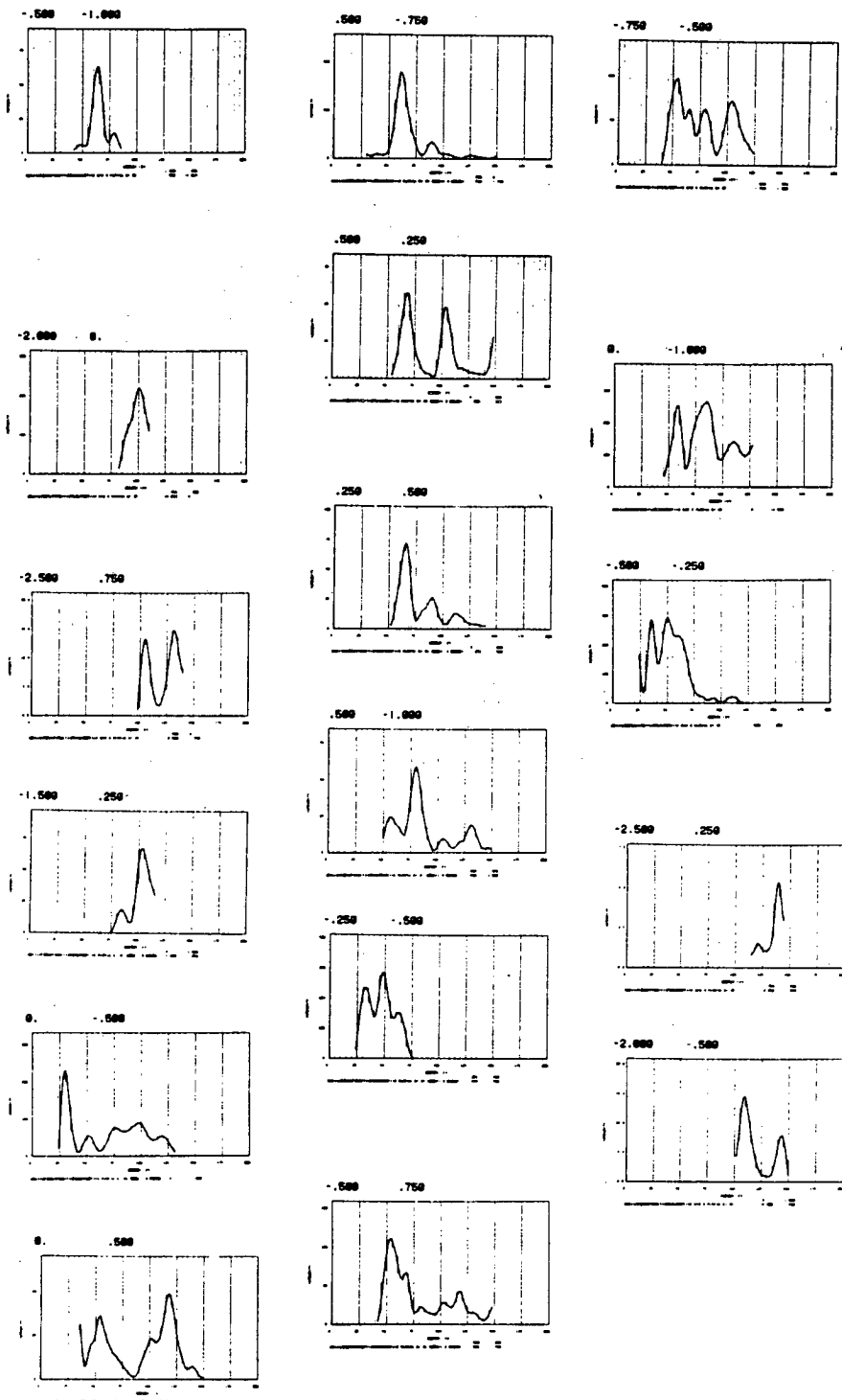


XBL 828-10970

Fig. 10c

Rh(III)-c(4M)-C₂H₄ (ads)

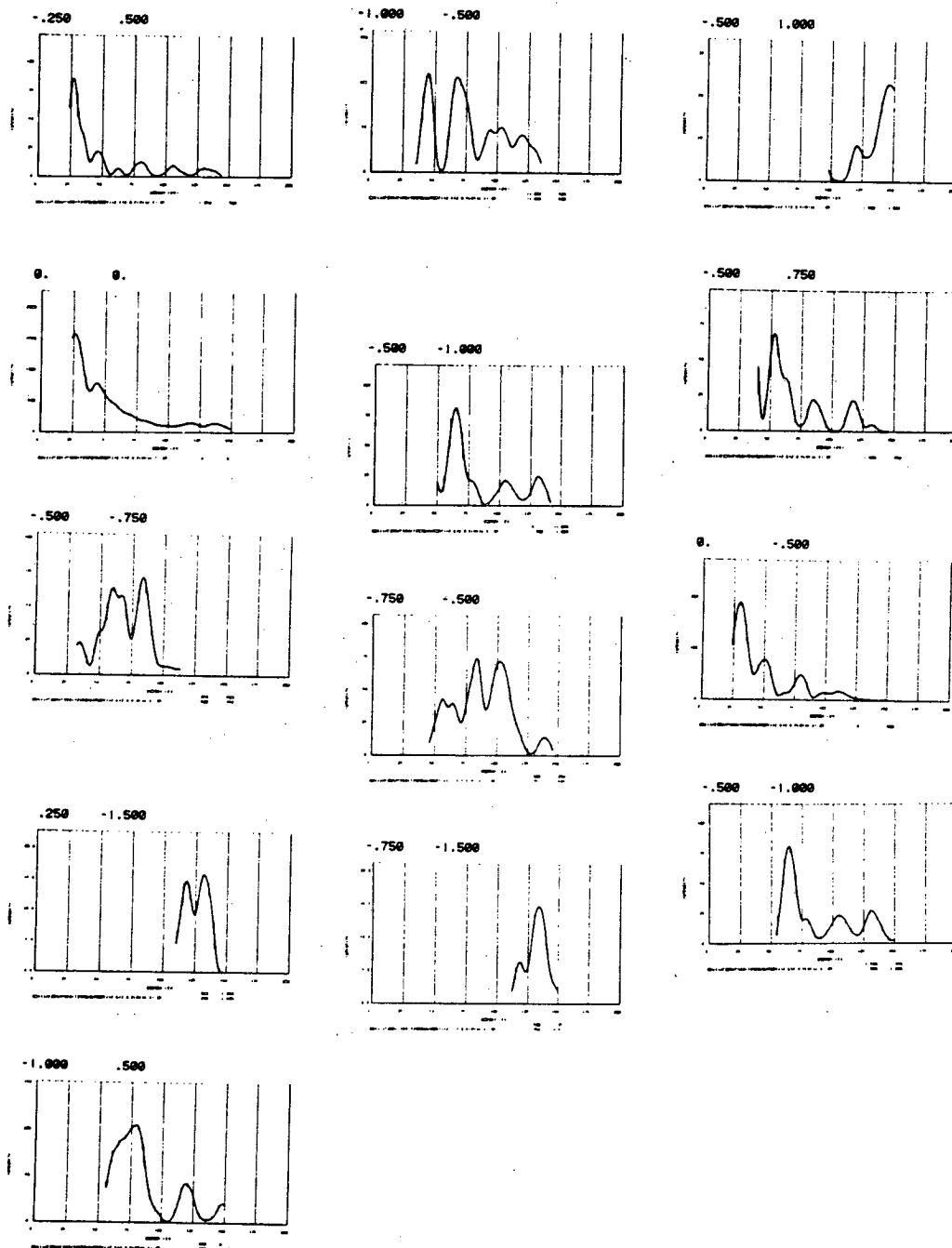
$\Theta = 11$, $\phi = 0$, $T = 300K$



XBL 828-10956

Fig. 10d

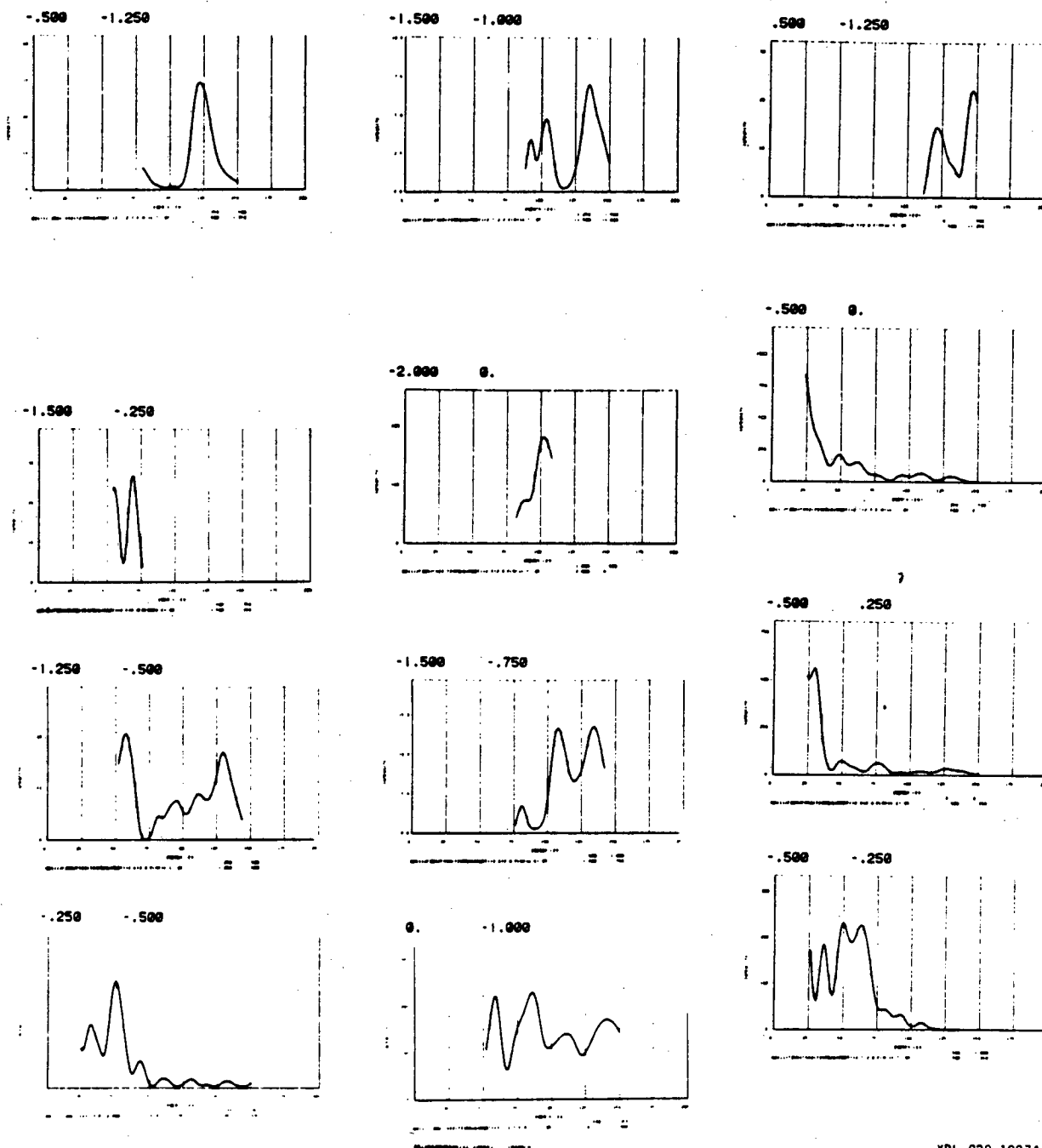
Rh(III)-c(4x2)-C₂H₄ (ads.)
 $\theta = 21, \phi = 0, T = 300K$



XBL 828-10964

Fig. 10e

Rh(III) - c(4x2) - C₂H₄ (cont'd)
 $\Theta = 21, \Phi = 0, T = 300K$

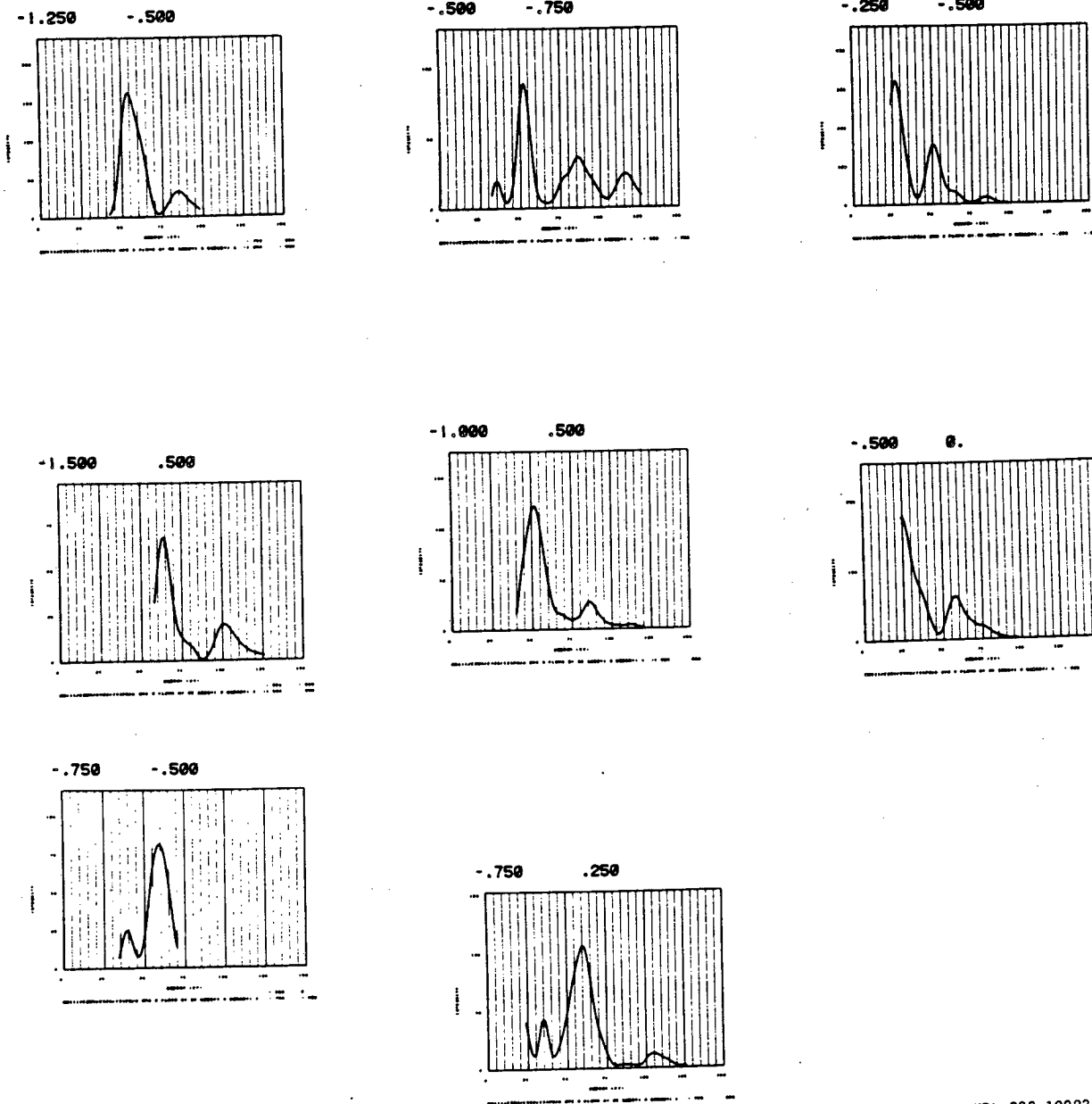


XBL 828-10974

Fig. 10f

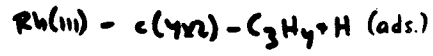
$R_h(m) - c(\gamma_0) - c_2 N_y$ (abs.)

$\Theta = 31$, $\phi = 0$, $T = 300K$

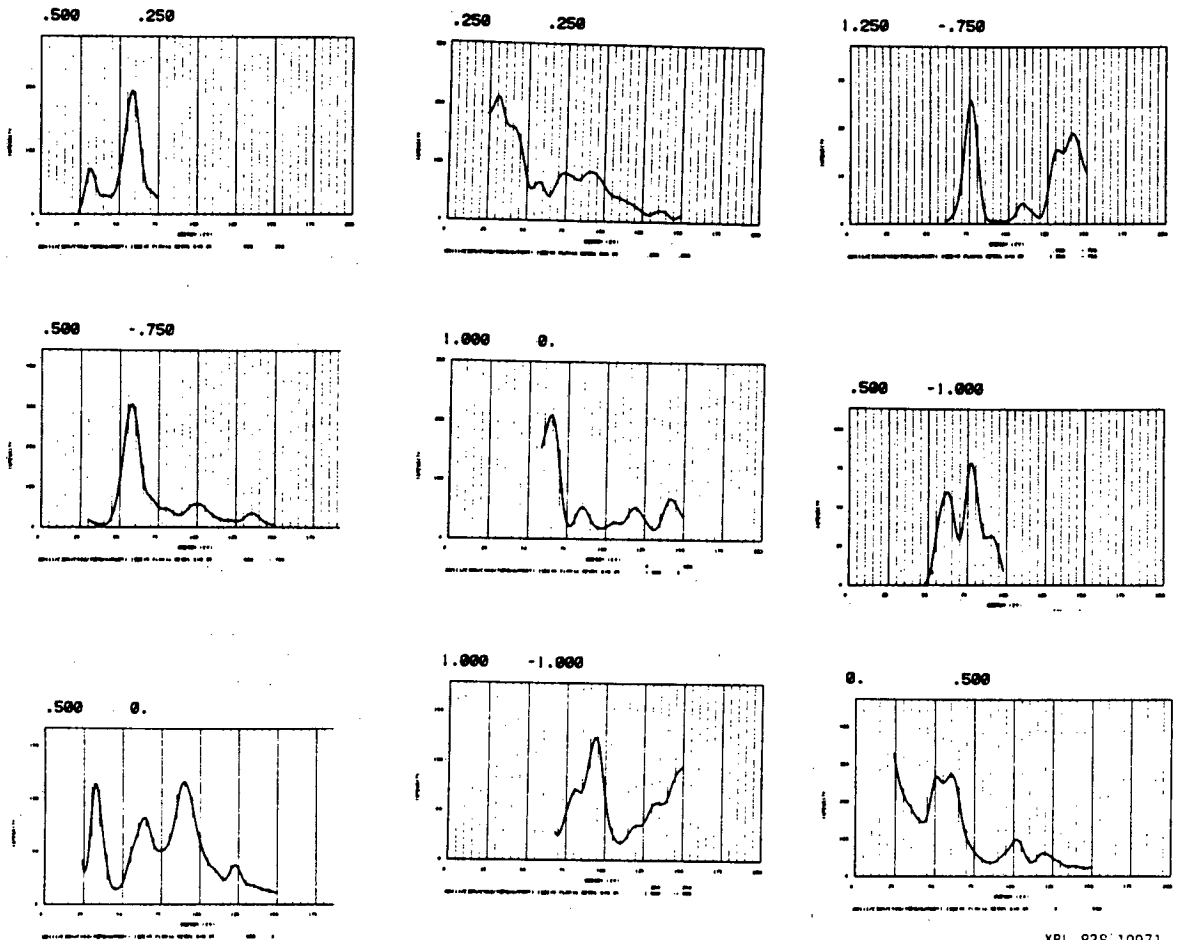


XBL 828-10982

Fig. 10g

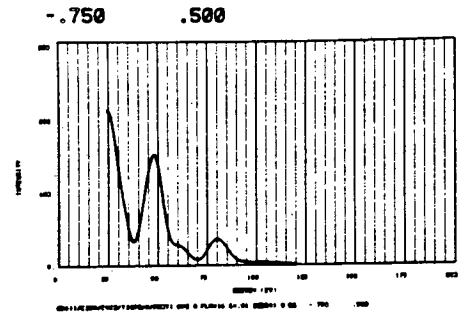
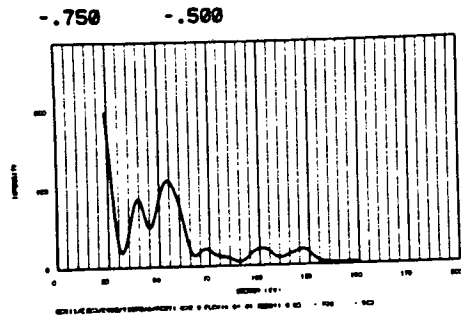
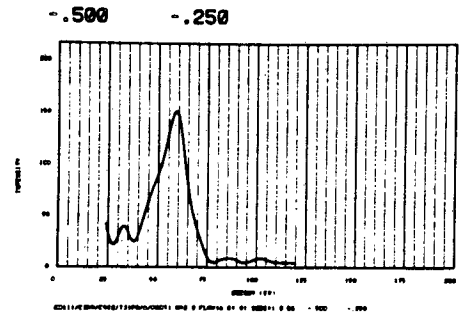
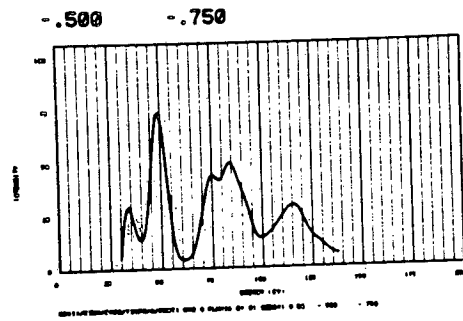
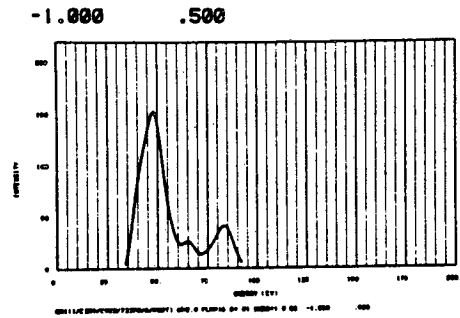
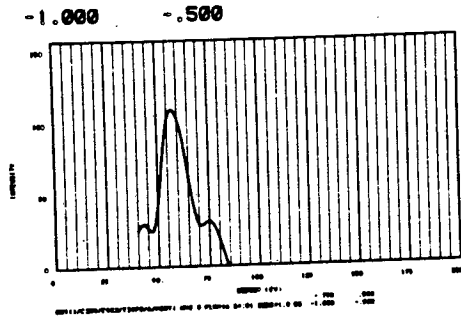
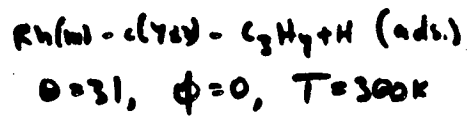


$\theta = 0, \phi = 0, T = 300K$



XBL 828-10971

Fig. 10h

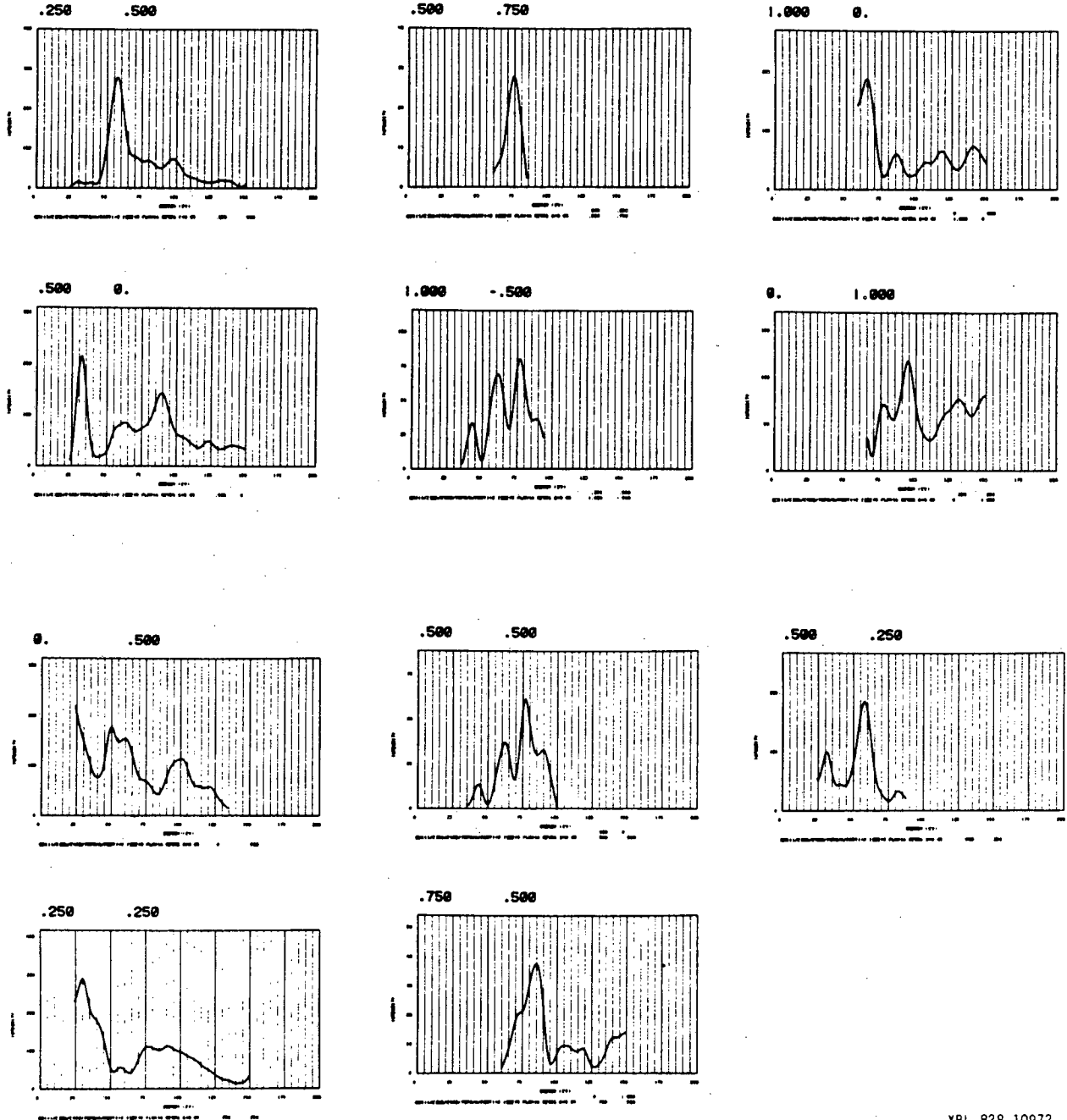


XBL 828-10989

Fig. 101

Rh (int.) - C₂H₆ (ads.)

$\theta = 0, \phi = 0, T = 300K$

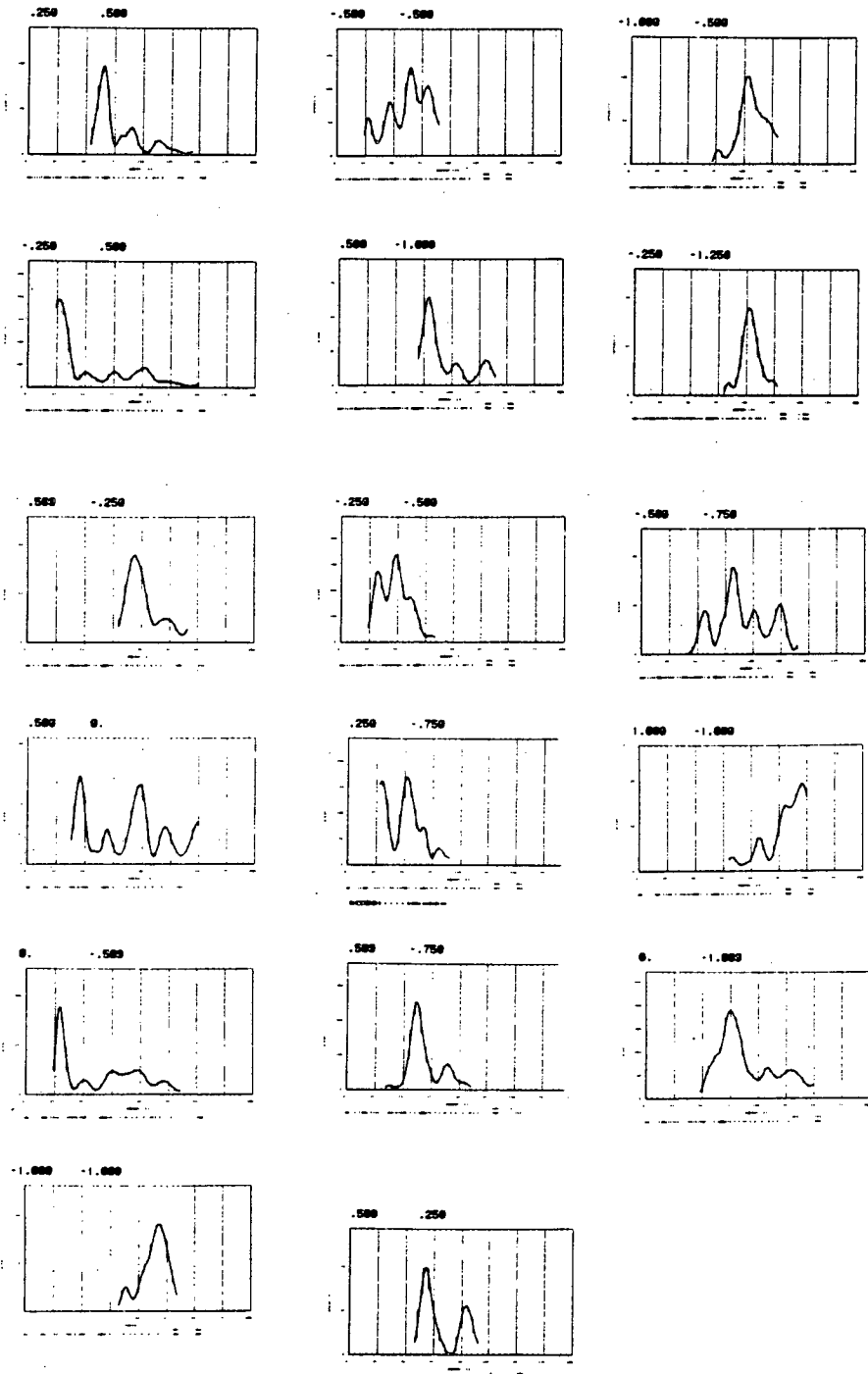


XBL 828-10972

Fig. 10j

$Rn(n) = c(V_{22}) - C_2 H_6$ (ads.)

$\Theta = 11, \phi = 0, T = 300K$

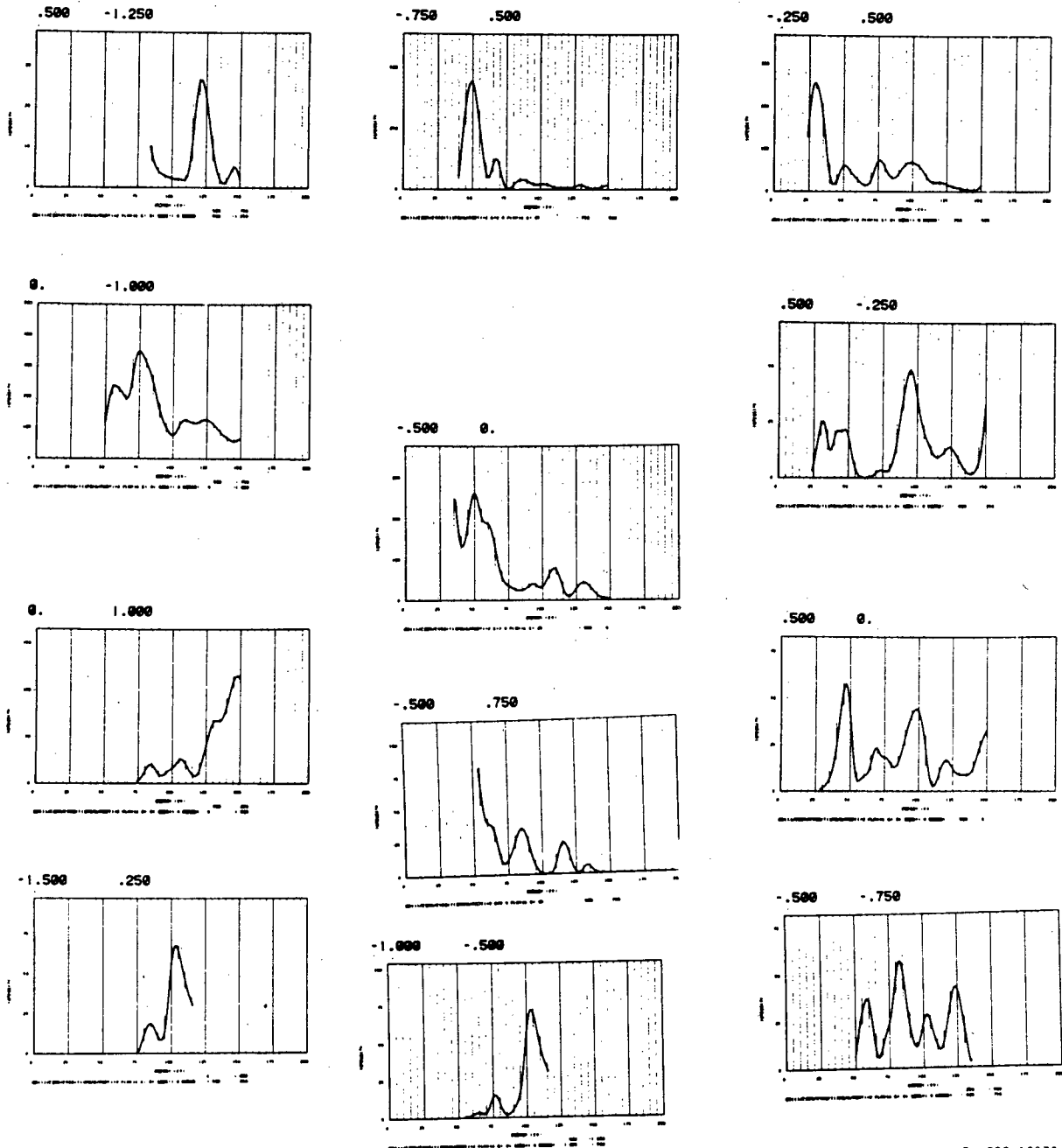


XBL 828-10958

Fig. 10k

Rh(111) - $\alpha(4 \times 2)$ - C_3H_6 (ads.)

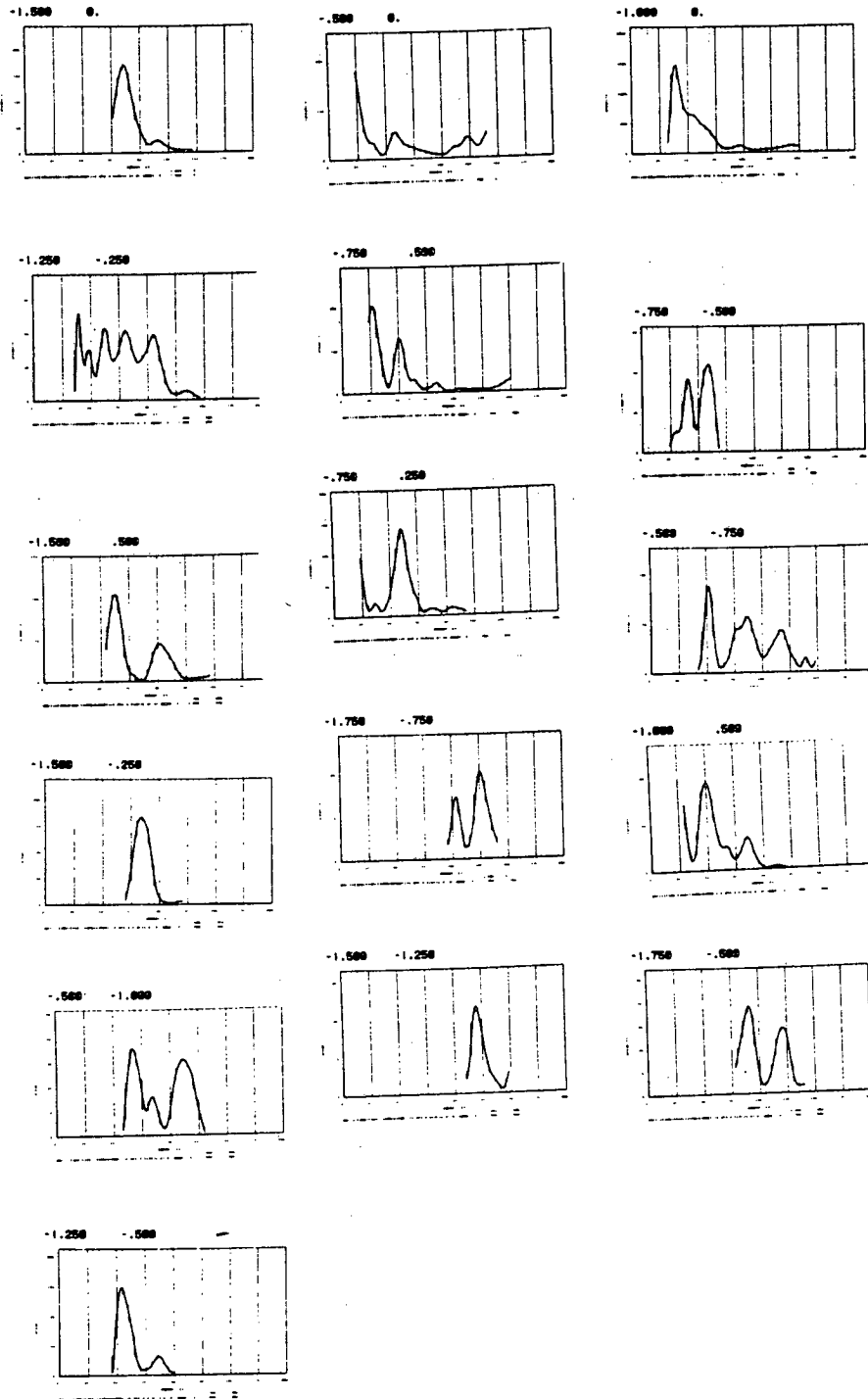
$\Theta = 21^\circ$, $\phi = 0^\circ$, $T = 300K$



xBL 828-10973

Fig. 101

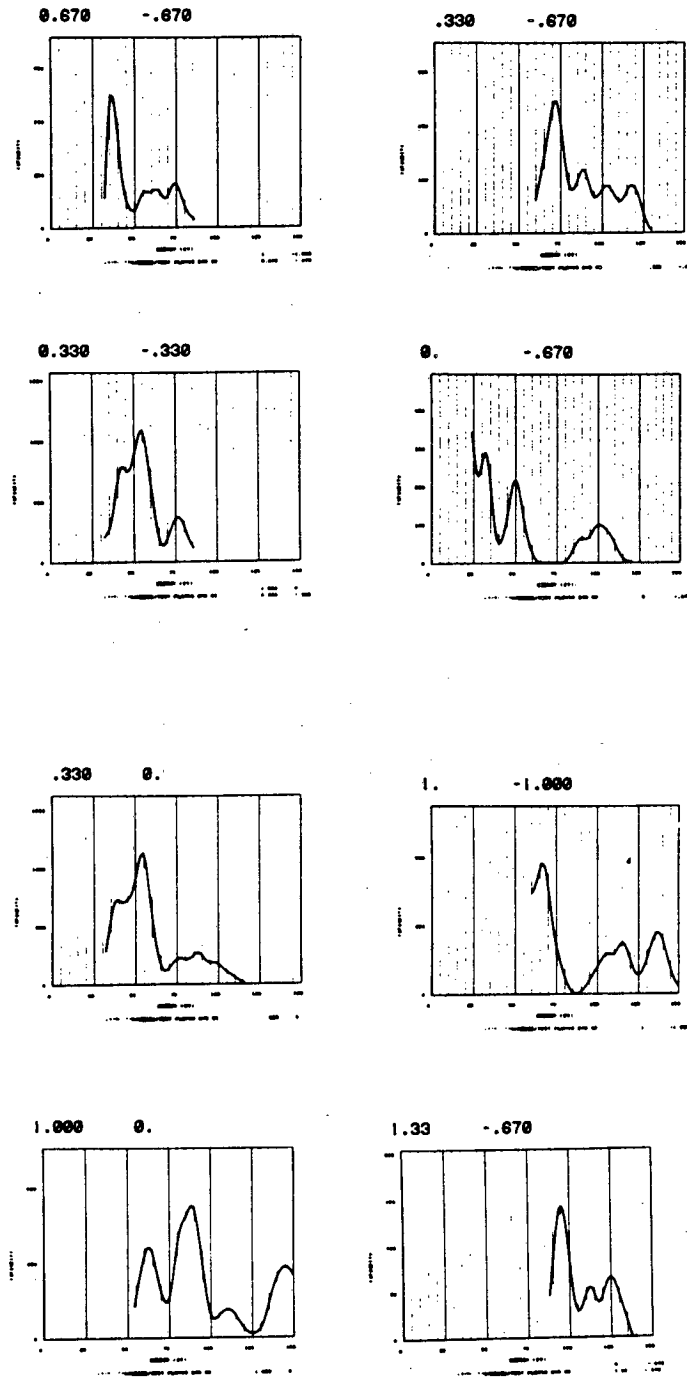
$RH(m) - c(V_{20}) - C_2H_6$ (ads.)
 $\Theta = 31, \Phi = 0, \bar{T} = 300K$



XBL 828-10957

Fig. 10m

$\text{Ph(III)}-(3\text{r3})-\text{C}_6\text{H}_6-\text{Arum}$
 $\theta=0^\circ, T=240\text{K}$

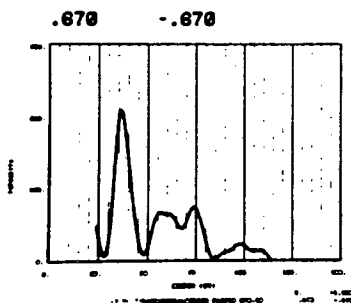
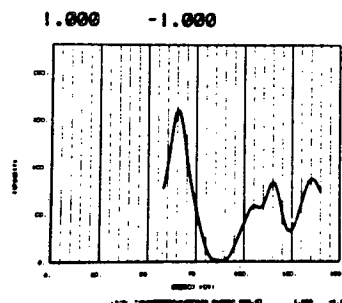
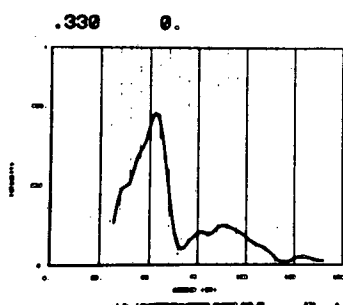
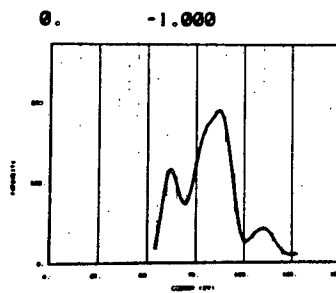
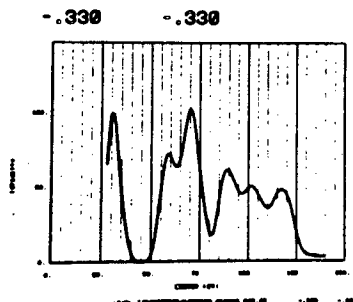


XBL 828-10986

Fig. 11a

Rh(III) - (3x3) - Benzene - Brum

$\theta = 0^\circ$, $T = 240K$

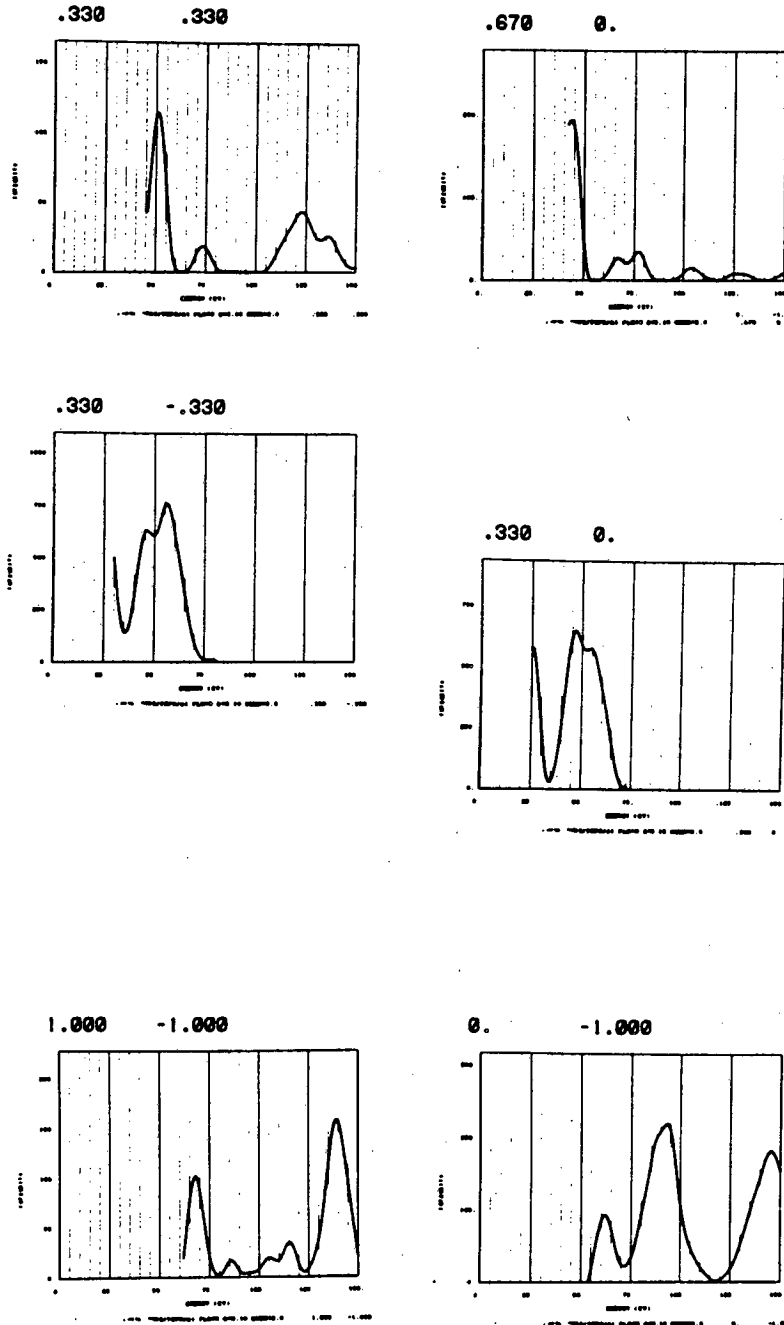


XBL 828-11078

Fig. 11b

$$R_h(m) = (3 \times 3) + (3\sqrt{3} \times n\sqrt{3})R_{30} - C_n H_8$$

$$\Theta = 0^\circ, T = 240K$$

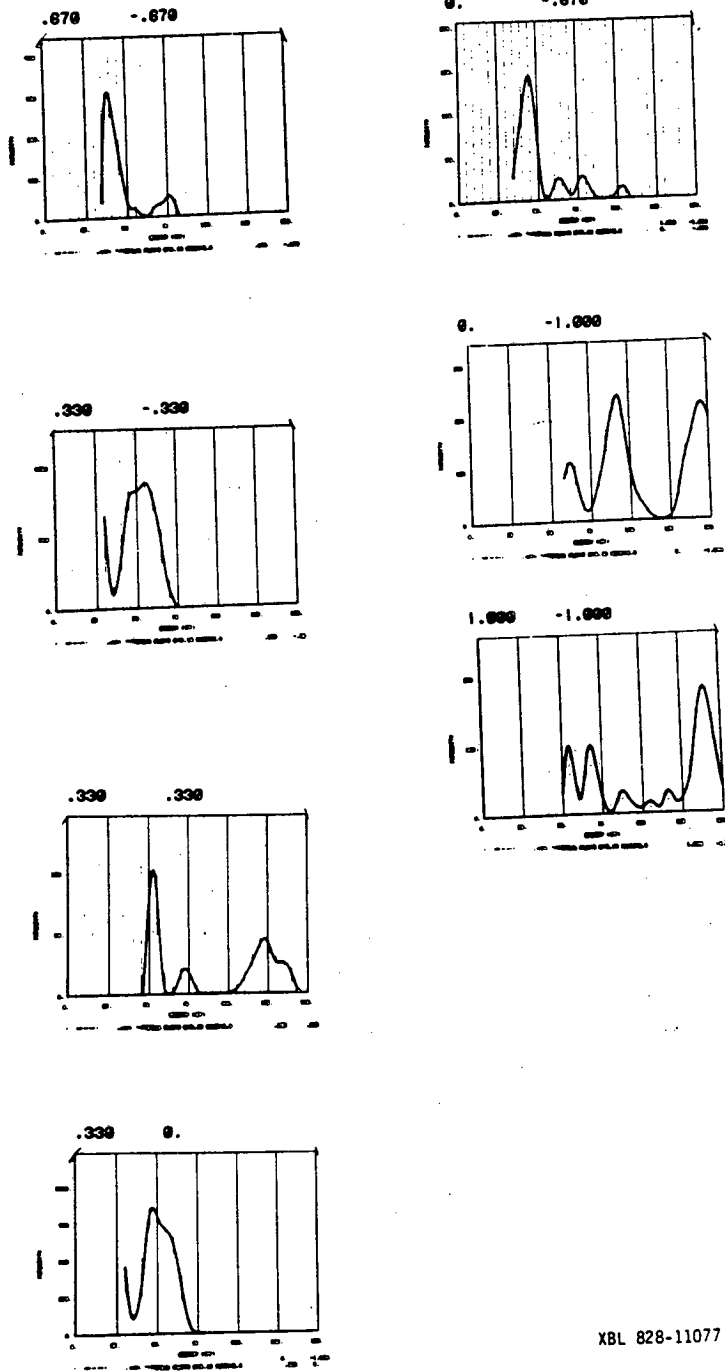


XBL 828-10988

Fig. 12

Rh(111) - (3x3) - C₁₀H₈ - SHORT
RUN

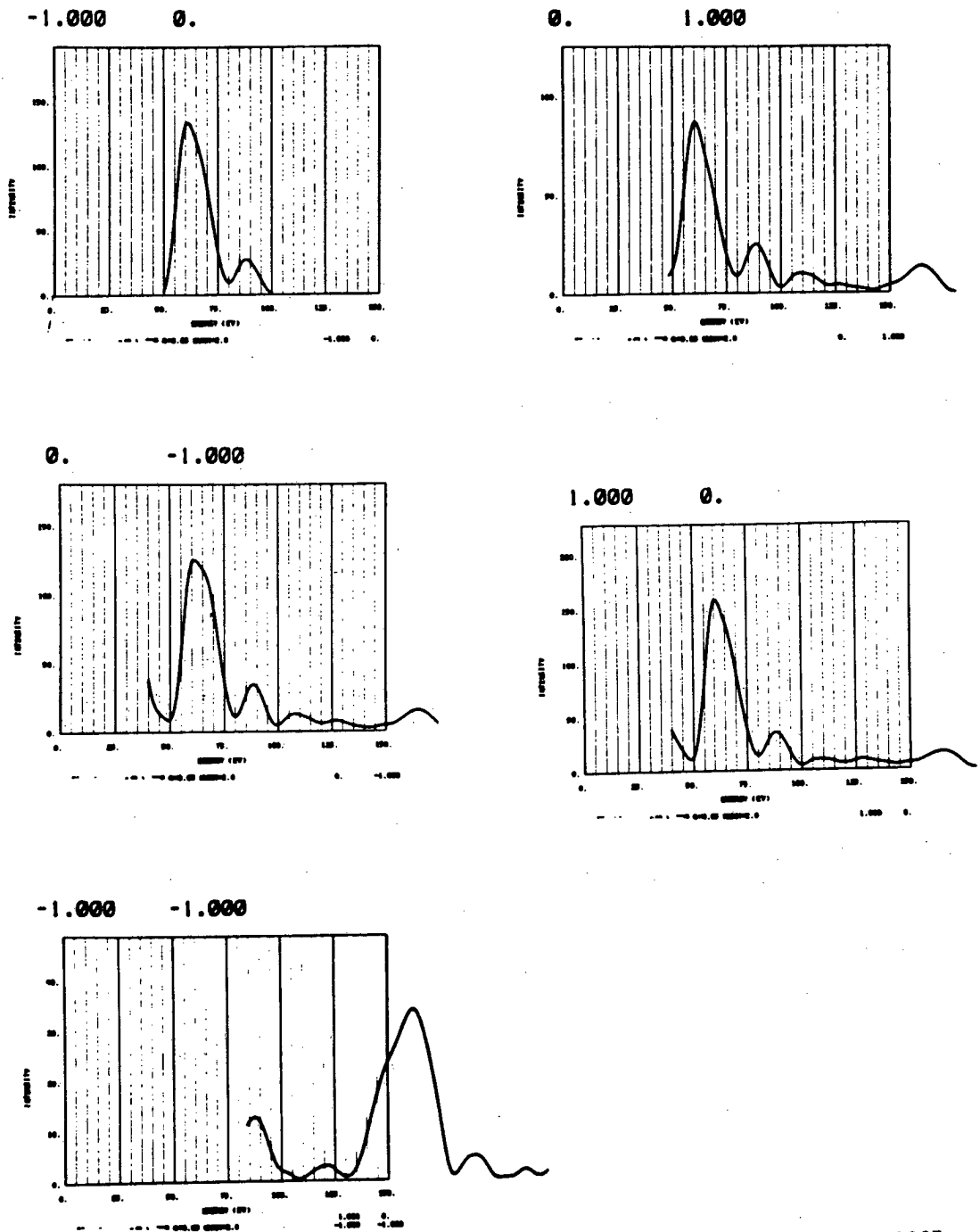
$\theta = 0^\circ$ T = 240K



XBL 828-11077

Fig. 13

clean Rh(100)
 $\theta = 0^\circ$ $T = 300K$



XBL 828-10987

Fig. 14

$F^+(111) - (2 \times 2) - C_3H_5$
 $\Theta = 0^\circ \quad T = 300k$

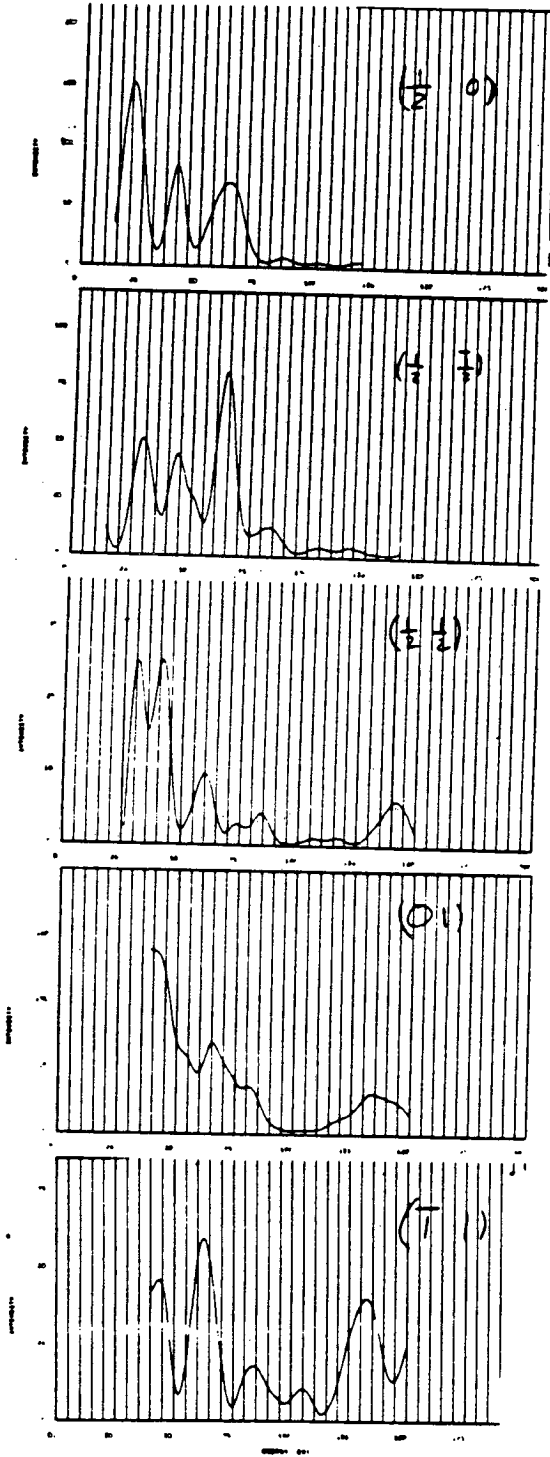
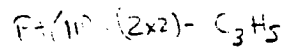
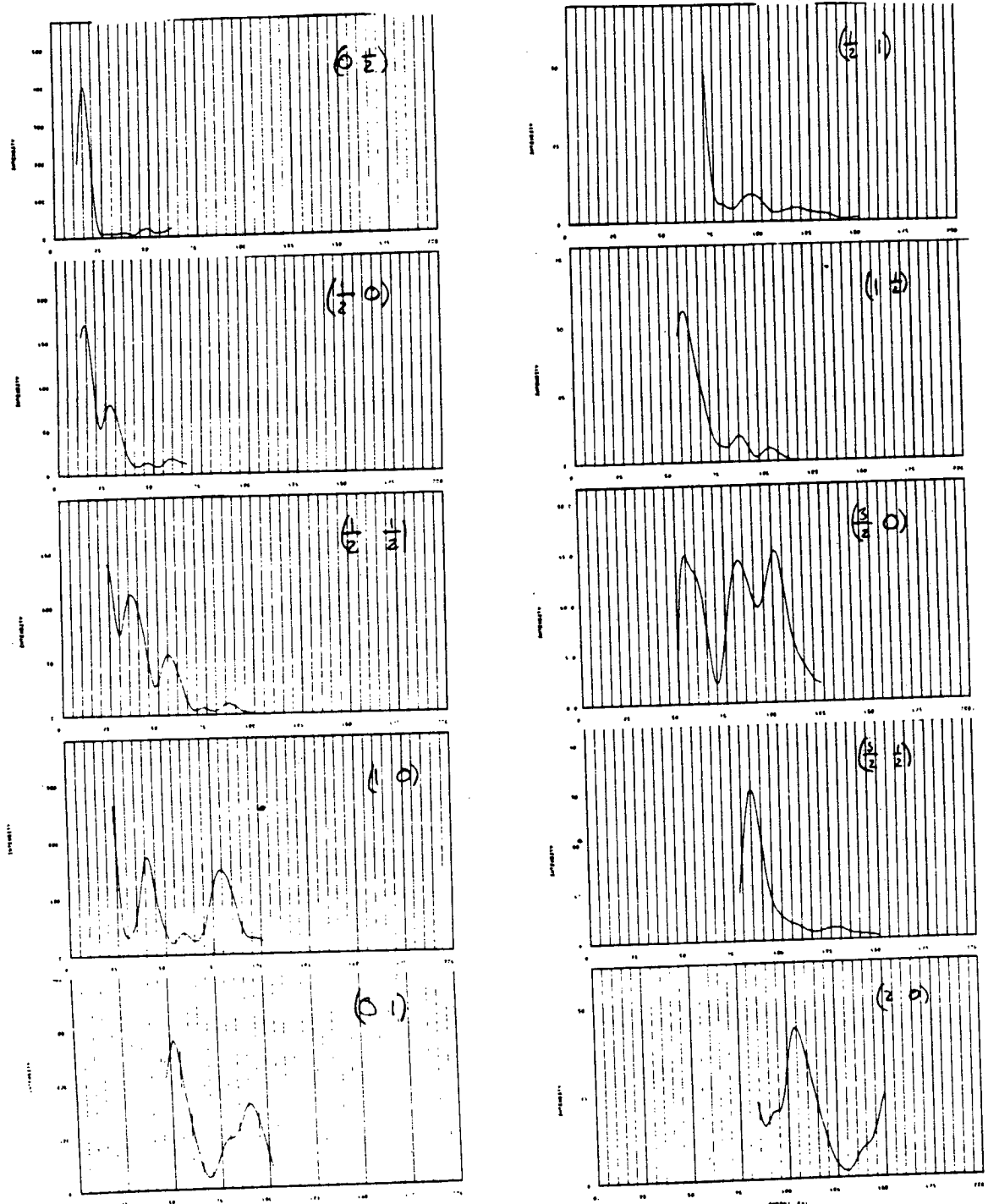


Fig. 15a



$\theta = 30^\circ (\pm 1^\circ), \phi = 30^\circ, T = 300K$



XBL 828-10810

Fig. 15b

Pt(111) - (2√3 x 2√3) R30 with 1000L
trans-2-C₄H₈

θ = 0°, T = 300K

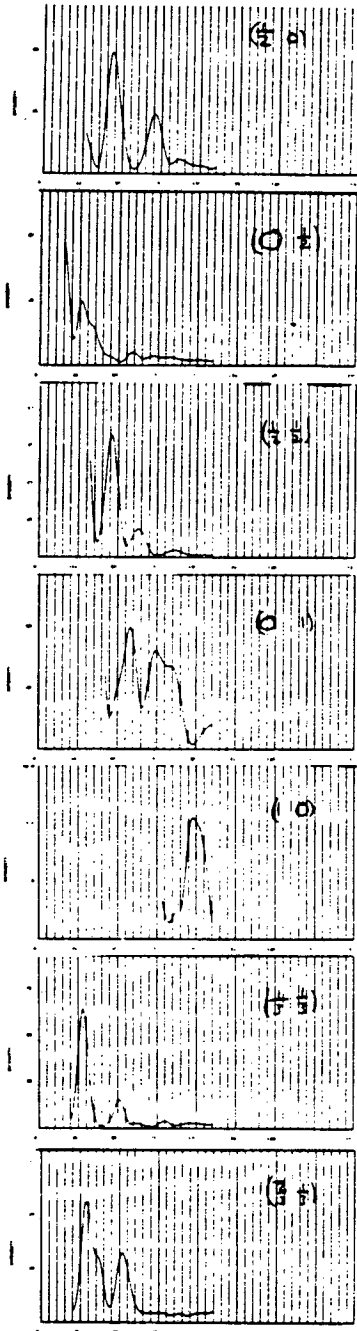


Fig. 16a

Pt(111) - (2√3 x 2√3) R30 with
1000L cis-2-C₄H₈

θ = 0°, T = 300K

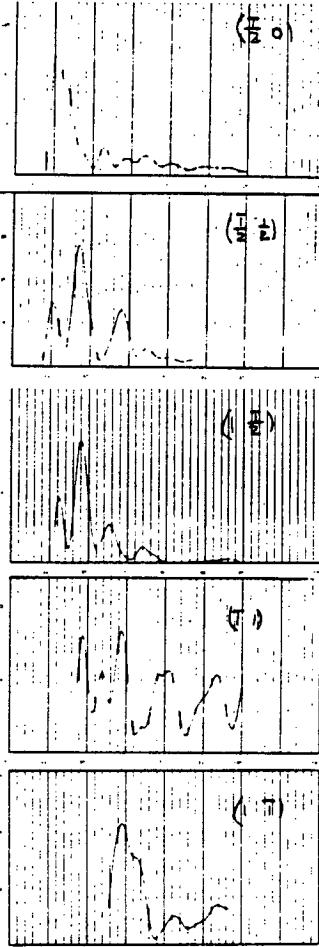


Fig. 16b

Pt(111) - (8x8) with
100L trans-2-C₄H₈

θ = 0°, T = 300K

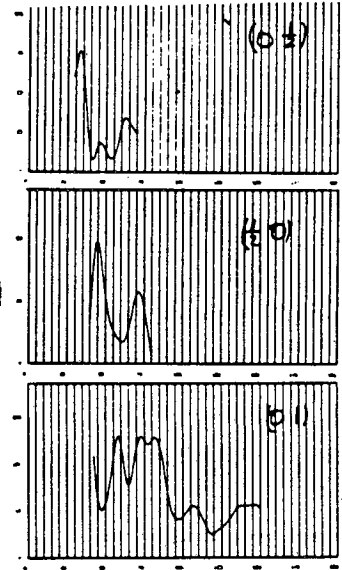
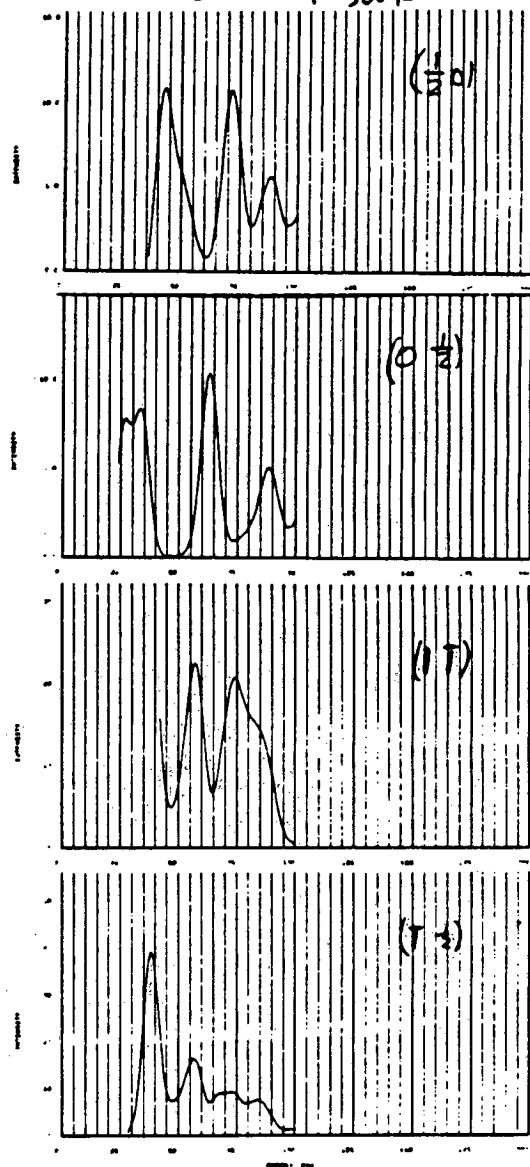


Fig. 17

$PH(111)-(2\sqrt{3} \times 2\sqrt{3})R30^\circ$ with $2L$
cis-2-C₄H₈

$\theta = 0^\circ$ $T = 300K$



XBL 928-10811

Fig. 18

APPENDIX II. LIST OF PUBLICATIONS

1. The Surface Reconstructions of the (100) Crystal Faces of Iridium, Platinum, and Gold: I. Experimental Observations and Possible Structural Models, M. A. Van Hove, R. J. Koestner, P. C. Stair, J. P. Biberian, L. L. Kesmodel, I. Bartos, G. A. Somorjai, Surface Science, 103 (1981) 189.
2. The Surface Reconstructions of the (100) Crystal Faces of Iridium, Platinum, and Gold: II. Structural Determination by LEED Intensity Analysis, M. A. Van Hove, R. J. Koestner, P. C. Stair, J. P. Biberian, L. L. Kesmodel, I. Bartos, G. A. Somorjai, Surface Science, 103 (1981) 218.
3. A Surface Crystallography Study by Dynamical LEED of the $(\sqrt{3}\times\sqrt{3})R30^\circ$ -CO Structure on the Rh(111) Crystal Surface, R. J. Koestner, M. A. Van Hove, G. A. Somorjai, 107 (1981) 439.
4. The Structures of Small Hydrocarbon Molecules on Rh(111) Studied by Low Energy Electron Diffraction: Acetylene, Ethylene, Methylacetylene, Propylene, M. A. Van Hove, R. J. Koestner, G. A. Somorjai, J. Vac. Sci. Technol., 20 886 (1982).
5. The Study of the Structure of Adsorbed Molecules on Solid Surfaces by High Resolution Electron Energy Loss Spectroscopy and Electron Diffraction, G. A. Somorjai, J. E. Crowell, R. J. Koestner, L. H. Dubois, M. A. Van Hove, Proceedings from the Ninth International Conference on Atomic Spectroscopy and the Twenty-Second Colloquium Spectroscopicum Internationale, Tokyo, Japan, August (1981).

6. R-factors in LEED: Comparison of Different R-factors, Coincidence of R-factor Minima, and Structural Search Strategies, M. A. Van Hove and R. J. Koestner, Proceedings from the Conference on Determination of Surface Structure by LEED, Plenum, New York, 1981.
7. A Surface Crystallography Study by Dynamical LEED of the (2x2)-C₂H₃ Structure on the Rh(111) Crystal Surface, R. J. Koestner, M. A. Van Hove and G. A. Somorjai, accepted at Surface Science (July, 1982).
8. Evidence for the Formation of Stable Alkylidyne Structures for C₃ and C₄ Unsaturated Hydrocarbons Adsorbed on the Pt(111) Single Crystal Surface, R. J. Koestner, J. C. Frost, P. C. Stair, M. A. Van Hove and G. A. Somorjai, Surface Science, 117 491 (1982).
9. The Structure and Bonding of Hydrocarbons Adsorbed on Transition Metal Surfaces, R. J. Koestner, M. A. Van Hove and G. A. Somorjai, submitted to Chem. Tech. (April, 1982).
10. The Molecular Structure of Adsorbed Hydrocarbons on Metal Surfaces, R. J. Koestner, M. A. Van Hove and G. A. Somorjai, submitted to J. Phys. Chem. (June, 1982).
11. A LEED Crystallography Study of the Rh(111)+(2x2)-3CO Structure, M. A. Van Hove, R. J. Koestner and G. A. Somorjai, submitted to Surface Science (July, 1982).
12. A LEED Intensity Analysis of a Surface Structure with Three CO Molecules in the Unit Cell: Compact Adsorption of CO in Simultaneous Bridge and Near-Top Sites, M. A. Van Hove, R. J. Koestner and G. A. Somorjai, submitted to Phys. Rev. Lett. (August, 1982).

13. A LEED-Intensity Analysis of the (1×5) Reconstruction of Ir(100), E. Lang, K. Muller, K. Heinz, M. A. Van Hove, R. J. Koestner, and G. A. Somorjai, submitted to Surface Science (May, 1982).
14. Benzene and Naphthalene Adsorption on the Rh(111) Surface: A LEED, TDS, and AES Study, R. F. Lin, R. J. Koestner, M. A. Van Hove and G. A. Somorjai, to be published.
15. A LEED Crystallography Study of the Rh(111)-(3×3)-Benzene Structure, M. A. Van Hove, R. F. Lin, R. J. Koestner and G. A. Somorjai, to be published.
16. A LEED Crystallography Study of the Rh(100)-c(2×2)-C Structure, M. A. Van Hove, R. J. Koestner, R. F. Lin and G. A. Somorjai, to be published.

This report was done with support from the Department of Energy. Any conclusions or opinions expressed in this report represent solely those of the author(s) and not necessarily those of The Regents of the University of California, the Lawrence Berkeley Laboratory or the Department of Energy.

Reference to a company or product name does not imply approval or recommendation of the product by the University of California or the U.S. Department of Energy to the exclusion of others that may be suitable.

TECHNICAL INFORMATION DEPARTMENT
LAWRENCE BERKELEY LABORATORY
UNIVERSITY OF CALIFORNIA
BERKELEY, CALIFORNIA 94720